Using the Geochemistry of Magnetite and Apatite to Gain Insights Into the Genesis of Kiruna-type Ore Deposits and for Exploration in Densely Covered Terrains

by

Nikita L. La Cruz

A dissertation submitted in partial fulfillment
of the requirements for the degree of
Doctor of Philosophy
(Earth and Environmental Sciences)
in the University of Michigan
2019

Doctoral Committee:

Professor Adam C. Simon, Chair
Professor Emeritus Stephen E. Kesler
Professor Rebecca Lange
Professor Sally Oey
Assistant Research Scientist Aaron S. Wolf

Nikita L. La Cruz

nlacruz@umich.edu

ORCID iD: 0000-0001-8195-9077

Dedication

For Shellon, Lloyd, Nelanie, Malika, and Nakasi.

For Vincent and Eugenie.

For Mildred and James.

For Nesta Alberta Stoll.

For Nia, Axl, Victoria, Charles, Coco, Sayyid, Maali, Elle, Amiri, Taariq, and Andre.

For my village, literal (the one I call home) and figurative (the one that raised me).

For Aunty Rhonnie, Uncle John, Uncle Sweets, Aunty Debbie, Uncle Laurel, and Uncle Peter (R.I.P.).

For little girls and boys from small villages everywhere that have a dream of leaving her/his small corner of the globe to pursue her/his education and/or dreams. You can do it!

For the ancestors who endured so much and made so many sacrifices so that I can do all that I have done and will continue to do as long as I shall live.

Acknowledgements

First, I thank God for his grace, mercy, and favour on me and my life. I thank him for his continued guidance and for the many blessings that he has bestowed upon me. I am very grateful that he blessed me with the ability and opportunity to pursue and complete this doctoral degree. It would not have been possible without him. It also would not have been possible without the many folks (some of whom I will thank below) that he sent/put in my life to help me throughout my journey.

I thank my adviser, Dr. Adam C. Simon, for all his guidance, help, and support over the last four years. Adam, thank you for giving me the opportunity to pursue this degree and my dream of doing research that would benefit Guyana and Guyanese. I am grateful that you always have my back and my best interests at heart. Thanks for always encouraging me to do things that will benefit me as an individual and professional, and for always connecting me with helpful folks. Thank you for the many, many lessons, I will take them with me as I move on from your lab. I also thank Mrs. Alicia Simon for all her help and support over the years, and for the delicious food and great hospitality every time I visited the Simon home or interacted with her.

I thank Dr. Aaron S. Wolf for his help and guidance and for teaching me how to code. Thanks for mentoring me, believing in me, and encouraging me to face my fear of coding and "sciencing", especially on those difficult days close to the end of this journey. Thanks for all your help with my dissertation research, especially my Guyana magnetite chapter, the many lessons that you taught me and serving on my dissertation committee.

I thank Dr. Steve Kesler, Dr. Rebecca (Becky) Lange, and Dr. Sally Oey for serving on my dissertation committee. Thanks for your valuable feedback and for your help and encouragement. Steve, I thank you for your willingness to always engage and converse with me and for asking all those thought-provoking questions. It's been a pleasure getting to know you and learning from you. Becky, thanks for your advice during my visit to the department in 2015, it helped me as I was making the decision to come to Michigan. Sally, thank you for all the advice; I will incorporate said advice into my life as I work towards being a "super" geologist.

Next, I thank my amazing lab family, especially my brothers: Dr. Brian "B-dawg" Konecke and Dr. Tristan "T-dawg" Childress. T-dawg and B-dawg, thanks for your friendship, love, and support over the years. Thanks for having my back and for being willing to talk to me about everything from apatite and magnetite to aliens and asteroid mining :). Additionally, I thank Daniel, Gephen, Maria, Jackie, and Justin for their help, support, friendship, and comraderie. It was great getting to know all of you and you made my time here in Ann Arbor very enjoyable. I also thank Dr. Laura Bilenker, Dr. Jaayke Knipping, Dr. Adrian Fiege, and Dr. Tom Hudgins for their friendship and for being honest with me and giving me the inside scoop about working with and for Adam during my visit to Michigan prior to starting my PhD.

I thank my sisters, Phoebe Aron and Sarah Brehm, for being integral parts of my support system over the last four years. Thanks for being my friend, for supporting me, and for taking care of me when I needed it. I couldn't have done it without the two of you! Pheebs, I also thank you for introducing me to Dylan, who is awesome. Dylan, thanks for the countless rides home and to the airport and for always being willing to spend time with me (and Sarah) even on those difficult days when we didn't really want to be around anyone.

I thank my Michigan EARTH family for the help and support during my time in Ann Arbor. Anne, I really appreciated your help, hugs, and chocolate over the years. Dale “Mr. Wizard” Austin, I thank you for all your help with illustrator and my figures over the years. Julie and Paula thanks for your help figuring out how to get things done in the department. Greg Dick and Naomi Levin, I thank you for your help and all the conversations over the year. Juliana, James, Xiaofei, Man Sam, Marlon, Prithvi, Katy, Molly, Xiaojing, Yi, Matthew, Kelly, Jenny, Derek, Sharon, Alex, Adrianna thanks for your friendship. To my officemates: Mark, Elizabeth, Laura (Motta), Aaron, thanks for being good neighbors! To my fourth floor neighbors: Jamie and Jason, I appreciated all the smiles and conversations in the hallway.

I acknowledge the love and support of my amazing family: nuclear, extended, and chosen/ not blood-related. Mom and dad, thanks for all the sacrifices you made so that Nelly and I could do all the things we wanted to do. I know it was hard to send us away so we could have access to better educational facilities but I think it was worth it. Nelly - thanks for always being there for me and for holding down the fort while I was away for these 10 years. I am eager to be back so that we can spend more time together and do everything from catching the heritage month lime, to going into the field and doing research. Love you bruv! Malika - thanks for always checking in on me and for sending the beautiful photos of Nia and Axl. They really helped me on the tough days. Nakasi - thanks for being there for me and for having my back! I am happy that you are in my life and I am patiently waiting for you to finish your study-abroad so you can join me and the girls in our dear motherland. To my cousins: Olivia, Nadea, Waneta, Shenele, and Christene, and the many, many others, thanks for checking up on me and for all the laughs and the love. I thank my uncles: Pierre, Darwin, and Chris for spoiling me and for all their help over these last four years. I am blessed and lucky to have you three as uncles. Uncle Darwin, I’m very grateful for all the time

that I was fortunate to spend with you, Aunty Maria, and Victoria. I loved every moment of it! I thank my grandparents: James, Mildred, Desiree, Vincent, and Eugenie for doing what awesome grandparents do, i.e., spoil their grandkids! Your help and support throughout my life have been invaluable. Papa and Nana, I am especially grateful for all the interactions that I was fortunate to have with you over the last 10 years; thanks for everything! Granny and grandad, I am so happy that I close enough to visit and spend time with you regularly. Shaka, Sharleen, and Karissa thank you very much for your friendship, your love, support, and of course those beautiful babies! Couldn't have done this without you! Nazima and Maria, thanks for your friendship and for all the laughs and conversation.

I thank my amazing wellness coach, Mary Jo for all her help, and guidance over the last few years. Thanks for helping me learn how to manage and deal with the stresses of grad school/a PhD and life in general. You made my graduate experience here at UMich much better!

Special shout out to my chiropractor, Dr. Tim Dehr, my acupuncturist, Jessica Walsh, and my massage therapists: Annie Kopko and Danielle Campbell for their help with my aches and pains. I am also grateful for CVS brand icy hot patches which got me through so many days when the pains tried to get the better of me.

I thank my dear friend Lennox for his love and support, and for teaching me to be patient. Big up yaself, Samples Man! <3.

I spent lots of time listening to Chronixx, Keznamdi, Jah 9, Protoje, Damian Marley, (of course) Bob Marley, so much soca music via Dj Private Ryan mixes. I thank you all for your music and for lifting my spirits on the rough days.

To the countless others who I couldn't mention, thanks for being there for me!

<3 Nik

Table of Contents

List of Tables

List of Figures

Figure 3.2: Representative backscattered electron (BSE) images of surface and drill core samples from ore bodies at El Laco. (A) Sample from Cristales Grandes containing magnetite (Mgt S1), which is altered to hematite (Hem)/martite (mar), and pyroxene (px). Craters from the LA-ICP-MS transect are visible in image. (B) Sample from San Vicente Alto showing magnetite (Mgt S2) with euhedral hexagonal iron phosphate (FePO4) intergrowths, which are paragentically early and formed pre- or syn-magnetite. The FePO4 intergrowths also contain monazite (Mnz) grains at the FePO4 grain boundaries between the magnetite and and interspersed within the grain. Finally, some FePO4 grains contain quartz (Qtz), which is paragenetically later than the FePO4 (because the FePO4 is enveloped by the quartz, as highlighted in the inset). C) Sample from Laco Norte containing magnetite, hematite, goethite (Goe) and thorite inclusions (Thr). (D) Sample from Laco Sur containing apatite (Ap) and monazite inclusions. (E) Massive magnetite grains from Rodados Negros that are subhedral and inclusion free. (F) Sample from Laco Sur containing magnetite, patches of magnetite with high Si and Mg content, and Nb-rich oxide inclusions in cracks and at the boundary of the two generations of magnetite. (G) Sample from Laco Sur containing magnetite, hematite, and goethite (Goe). (H) Sample from Laco Norte containing magnetite Mgt A and Mgt S2, and goethite (Goe). (I) Sample from deep zone of Laco Norte showing an aggregate of titanomagnetite crystals (Mgt-α) displaying trellis-textured ilmenite exsolution lamellae. (J) Sample from intermediate zone of Laco Norte showing a partially-dissolved magnetite (Mgt-X) core, which is overgrown by a later magnetite (Mgt-Y) defined by containing oscillatory textures of inclusion-rich and inclusion-poor alternating growth zones. (K-L) Samples from intermediate zones of Laco Sur that correspond to a magnetite-scapolite-pyroxene-rich zone. Thorite inclusions are common in this zone (K). (M) Sample from the deep zone of Laco Norte showing a euhedral core of inclusion-rich Magnetite-β surrounded by a rim of inclusion-poor magnetite. (N) Sample

outcrops are igneous in nature and have been altered by hydrothermal fluids. (A) BSE image of a magnetite grain from intrusion sample GY-RC-01 containing well developed ilmenite exsolution lamellae with sandwich texture and ilmenite overgrowth. Ilmenite exsolution lamellae with cloth texture are present in magnetite that exists in the regions between the ilmenite exsolutions with sandwich texture. Two small sphalerite (Sp) grains are also visible in the image. (B) Magnetite grain from a mafic intrusion showing texture dominated by sandwich-textured ilmenite exsolution lamellae. This grain contains fluorapatite and small sulfide grains (white phases in the grain). (C) Ilmenite from mafic intrusions contains magnetite as inclusions or magnetite at the boundaries of some grains. (D) Magnetite and ilmenite, which contains a chalcopyrite inclusion, from a mafic intrusion. (E) Magnetite with wavy/spongy texture; this texture was observed in grains from 2 of the pyroxenite outcrops. (F) Zoned magnetite grain with domains that contain differing Cr contents. The cores have highest Cr content and Cr content decreases towards the rim. (G) Inclusion-poor magnetite grain with hercynite (Hc) granules at the grain boundaries that is proximal to a sulfide grain, which contains pyrrhotite and pentlandite. (H) Agglomeration of magnetite grains from a pyroxenite intrusion. The grains terminate at triple junctions and an ilmenite granule is observed at the boundary of two grains. (I)Magnetite from pyroxenite intrusion with sub-micrometer trellis-textured ilmenite exsolution lamellae. (J) Magnetite from pyroxenite outcrop containing cloth-textured ilmenite exsolution lamellae. (K) Titanomagnetite grain from pyroxenite intrusion. (L) Hematite grains that meet at triple junctions. These grains were observed in three sampled outcrops. (M) Hematite grain from GY-RC-07 with Ni-S (millerite?) inclusion. (N) Ilmenite from pyroxenite samples contains magnetite exsolution lamellae and magnetite granules. (O) Polymineralic sulfide grain comprising pentlandite, pyrrhotite and chalcopyrite; this grains was observed in GY-RC-13. (P) Pyrrhotite and pyrite (Py) observed in a sampled intrusion.

Figure 4.3. This figure contains representative backscattered electron images of Fe-Cr-Ti oxides from detrital samples collected throughout Guyana. Generally, the detrital grains are texturally similar to those in the outcrop samples but also show loss of texture caused by weathering. (A) Rounded magnetite grain collected from a catchment in north-central Guyana. (B) Angular to sub-angular detrital magnetite grains collected in Guyana; inclusion-poor magnetite is the dominant texture observed in detrital grains; however, ilmenite exsolution lamellae are sometimes preserved. Some inclusion poor grains also contain hematite rims. (C) Magnetite grain with visible crevices that appears to have contained ilmenite exsolution lamellae that have been lost due to weathering; these are referred to as relic ilmenite exsolution lamellae in this study. (D) Cr-rich titanomagnetite with ilmenite exsolution lamellae. (E) Magnetite grain containing a Cr-rich titanomagnetite core, with visible ilmenite exsolution lamellae, and a Cr-poor titanomagnetite rim. An ilmenite granule is observed within the Cr-poor rim. (F, G) Detrital magnetite grains with thin (<5 μm) trellis-textured ilmenite exsolution lamellae. (H) Magnetite grain with cloth-textured ilmenite exsolution lamellae. (G) (I) Magnetite with sandwich-textured ilmenite exsolution lamellae. (J) Magnetite with wavy/spongy texture. L) Detrital chromite and weathered Cr-rich magnetite. (M) Detrital titanomagnetite grain with visible sandwich-textured ilmenite exsolution lamellae. Angular magnetite grains containing (N) chalcocite and bornite (O, P) inclusions. . (Q) Magnetite grain containing multiple bornite inclusions. (R) Ilmenite grain with pyrrhotite and tiny magnetite exsolution lamellae inclusions. (S) Pentlandite inclusion in detrital clinopyroxene grain. (T) Ilmenite grain containing polymineralic sulfide assemblage, comprising pyrite and sphalerite. (U)

probability of detection) shows how often a sample from a particular deposit type is correctly identified, and precision shows how frequently an inferred classification label is correct. IOCGs and PCDs are hampered by high false positive rates, yielding low precision values, but the model shows informatively high precision for Ni-Cu-PGE, orogenic gold, and VMS deposits. Combined with sizeable detection probabilities, the model is especially diagnostic for Ni-Cu-PGE and orogenic gold deposits. By using a non-negative least squares regression (NNLS) model that compares the characteristic overlap between the chemical signatures of magnetite from the 5 ore deposit types with that obtained when the multivariate normal model is applied to data from an unknown source, we are able to reduce the effects of the chemical overlap and determine the ore deposit source of the input data. In (B) we show the corrected/improved ore deposit source proportions obtained when the NNLS model is applied to the characteristic chemical signatures for Fe-Cr-Ti oxides from the 5 ore deposit types when they are treated as data from unknown sources. The combined use of the multivariate normal and NNLS models improves our ability to identify magnetite from the 5 ore deposit types……199

Figure 4.8. Global compilations of magnetite geochemical data from individual samples for (A) Ni-Cu-PGE, (B) VMS, (C) orogenic gold, (D) porphyry Cu-Au, and (E) porphyry Cu-Mo deposits are visualized using the discriminant plots of Dupuis and Beaudoin (2011) and Nadoll et al. (2014), where compositional fields are labeled according to nominal deposit type. When applied to individual analyses from ore deposits globally, only 24% and 5% of the global (A) Ni-Cu-PGE and (B) VMS deposit data are identified by those fields, respectively. The Al+Mn versus Ti+V discriminant plot achieves greater success rates identifying magnetite from (D) IOCG and (E, F) porphyry copper deposits than the Ni/(Cr+Mn) versus Ti+V discriminant plot. Additionally, the

<10 analyses, the intermediate symbol indicates deposits with 10 to 100 analyses, and the largest symbol indicates deposits with >100 analyses. The plot indicates that for the elements considered, individual ore deposits from each class have magnetite chemistry that deviate from the magnetite compositions of the global dataset for the particular deposit class. This deviation results in the individual ore deposit having a chemical signature similar to that for another deposit type, and high percentage of inferred contamination when the signature is compared to the chemical signature for the five deposit types using the non-negative least squares model. The non-negative least squares model reasonably identifies the proportions of the data that constitute the binary mixture of data from orogenic gold and Ni-Cu-PGE deposits (B)……263

List of Appendices

Abstract

Minerals are a key constituent of ore deposits that are the source of metals and non-metals required for our global society to function. In this dissertation, I use field and laboratory methods to understand the processes that lead to the formation of iron oxide - apatite deposits — an important source of iron — and as a tool for discovering new ore deposits. The analytical methods used include backscattered electron (BSE) imaging, cathodoluminescence (CL) imaging, and energy dispersive X-ray spectroscopy (EDS) element mapping, as well as electron probe micro-analysis (EPMA) and laser ablation inductively coupled plasma mass spectrometry (LA-ICP-MS).

Chapter 2 describes an investigation of the chemistry of apatite from the Los Colorados iron - oxide apatite deposit, in Chile, that tested existing ore genesis hypotheses. My work indicates that apatite grains in the deposit contain distinct domains with chemistries that show statistically significant differences. The major, minor, and trace element chemistry of the apatite grains are consistent with growth from silicate melt and magmatic-hydrothermal fluid. The data are supportive of ore formation via magmatic/magmatic-hydrothermal fluids, according to a new model developed at the University of Michigan.

In *Chapter 3,* I investigated the chemistry of magnetite and apatite from outcrop and drill core samples from five of the seven ore bodies at the El Laco iron - oxide apatite deposit, in Chile. Magnetite grains in the deepest samples have chemistries and textures consistent with growth of magnetite from a silicate melt, whereas the chemistries and textures of magnetite from the shallow samples and outcrops indicate growth of magnetite from magmatic-hydrothermal fluid. Apatite grains have major, minor, and trace element chemistry consistent with growth from a silicate melt

or a magmatic-hydrothermal fluid. Magnetite and apatite grains contain mineral inclusions that preserve evidence for re-equilibration with hydrothermal fluids. Together, the data suggest that the ore bodies at El Laco formed via shallow emplacement and venting of magmatic-hydrothermal fluid suspensions that contained igneous magnetite microlites.

In Chapter 4, I test the hypothesis that magnetite in stream sediment can be used as a tool for exploration in covered terrains, such as Guyana, located in the Guiana Shield. Similarities in the chemistries and textures of magnetite from outcrops and detrital grains in the same catchment indicate that the detrital grains can be used to gain insight about geological processes/sources in the catchments. However, the data also indicate changes in chemistry and loss of texture related to weathering and transport. Specifically, the concentrations of Mg, Ni, Cr, Ti, and Mn in magnetite are preserved in grains transported < 1.5 km in streams, whereas the concentrations of V and Al are preserved for transport distances up to 5 km. In order to test the hypothesis, I developed a new model that predicts the ore deposit sources of magnetite grains collected in streams in Guyana, using the compositions of magnetite from nickel-copper-platinum group element (Ni-Cu-PGE), orogenic gold, volcanogenic massive sulfide (VMS), iron oxide - copper - gold (IOCG), and porphyry copper deposits. The results indicate prospectivity for orogenic gold and Ni-Cu-PGE deposits in the sampled catchments. Additionally, sulfides present in detrital grains in the sampled catchments support the ore deposit source(s) inferred from magnetite geochemistry. This work demonstrates the utility of detrital magnetite geochemistry as a tool for exploration in covered terrains.

Chapter 1
Introduction

My dissertation focuses on advancing society's understanding of mineral deposits—regions in the Earth's crust where the concentration of one or more elements is anomalously higher than average crustal concentrations. Mineral deposits that contain anomalous concentrations of minerals that can be removed from the Earth's crust in an economically feasible way are considered ore deposits. For minerals to be considered ore, they must be present in large amounts/tonnage, at high grades (i.e., the ratio of the mineral/element of interest to other minerals should be low), and be easily accessible/mineable (Mungall, 2013). Our global society is heavily dependent on the extraction of base (iron, copper, manganese, zinc), precious (gold, platinum), and strategic (rare earth elements) metals to sustain the lifestyles, including continual supplies of electricity, potable water, and technological advancements, that humans in developed countries are accustomed to, and that those in developing countries aspire to. Without mining, we would be unable to construct and power our homes, drive our cars, cook our food, or maintain global communication. Critical advances in technology, health care, and research in many fields would also not be possible if the metals and non-metals hosted in ore deposits were not readily available.

The current global mining industry is a huge business that is fueled by society's demand. In 2018, the estimated value of nonfuel minerals produced in mines in the United States was approximately $82 billion (USGS, 2019). As a global society, we mine metals and non-metals on all continents except Antarctica. However, due to our long history of mining, many mining districts globally are becoming mature, and the extraction of ore is becoming difficult and expensive. For

instance, mines such as Chuquicamata, Chile, Bingham Canyon, Utah, USA, and the Kiruna mine, Sweden have been operating for over 100 years (Ossandón et al., 2001; Emel and Huber, 2011; Granås, 2012). While these mines have been able to sustain mine lives of greater than 100 years, this is not the case of all mines. In fact, such extensive mine lives are very rare, and it is becoming increasingly difficult to discover new ore deposits that contain enough ore to warrant the construction of new mines. Globally, there have been fluctuations in the amount of money spent on exploration for all commodities since the start of the 20th century; however, the general trend in expenditure on exploration is a downward one (Paterson, 2003). For specific commodities, such as gold, Schodde (2011) reports that there has been an overall decrease in the discovery of gold deposits with endowments that exceed 1 million ounces despite increased cost of exploration.

Economic geology is the branch of geology focused on understanding the geological processes that result in the formation of ore deposits. This field is interdisciplinary in nature and utilizes knowledge from petrology, geochemistry, geophysics, and structural geology to better understand how metals and non-metals are transferred from their sources to the Earth's crust, where they form mineral/ore deposits. Understanding the process that led to the formation of an ore deposit in one location provides insights that can be used to explore for and discover the same type of ore deposit in another region where similar geological processes might have occurred. The research that is conducted by economic geologists is, therefore, integral to ensuring increased success in discovering ore deposits in areas where exploration has been done before, or in new areas where there has been limited exploration.

1.1 Mineral Geochemistry

Minerals are the building blocks of rocks, and are key constituents in ore deposits. They are defined as inorganic substances with fixed chemical composition and chemical structure (Deer

et al., 1992). While it is true that minerals have specific stoichiometric chemistries, imposed by the constraints of their atomic-scale structure, many researchers have shown that elements that are not structural components of a mineral can substitute in as minor or trace components (Goldschmidt, 1937; Onuma et al., 1968; Jensen, 1973; Philpotts, 1978; Smyth and Bish, 1988). To first order, an element can substitute for another element in the crystal lattice of a mineral provided that the elements have similar size (i.e., the ionic radii of the elements are within 15% of each other), or charge (Goldschmidt, 1937). Coupled substitution, where two elements substitute into the crystal lattice of a mineral is also common as a mechanism to balance charge so that the overall structure maintains charge-neutral.

The substitution of elements into the crystal lattice of a mineral depends not only on cation size and charge constraints, but also critically on the distribution (i.e., partitioning) of elements between the mineral and the fluid and/or melt from which it is growing. The partitioning of an element between a mineral and a fluid is a direct consequence of thermodynamics and kinetics, and thus varies depending on element and mineral type and is largely controlled by the composition of the fluid, temperature, oxygen fugacity, and competition from the growth of other minerals (Candela and Piccoli, 1995; Blundy and Wood, 2003). Through many years of research geochemists have developed an understanding of how particular elements behave during geological processes, and this has led to the use of minor and trace element compositions of rocks and minerals to gain insights about geological processes (McIntire, 1963; Irvine, 1965; Hanson, 1978, 1980). More recently, researchers have noticed the utility of particular minerals as tracers of geological processes (e.g. apatite and magnetite in the case of ore-deposits). For instance, Konecke (2019) showed that sulfur in apatite is a useful proxy for understanding redox and degassing processes in magmatic environments. Dare et al. (2012) showed that the concentrations of minor

and trace elements in magnetite (i.e., Ti, V, Cr, Ni) that crystallizes from a fractionating sulfide liquid reflect the composition of the sulfide liquid. In this dissertation, I investigate the chemistry of apatite and magnetite to gain insight into the ore forming processes in iron – oxide apatite deposits.

1.2 Apatite Geochemistry as a Tool for Invesitgating Ore Forming Processes

Apatite is a common phosphate mineral in many geological environments and has the chemical formula $A_{10}(XO_4)_3(Z)_2$. Owing to its crystal structure, more than 40 elements can substitute into the apatite structure, apart from the most common structural components of Ca, P, F, Cl, and OH. (Piccoli and Candela, 2002; Harlov, 2015; Hughes and Rakovan, 2015; Webster and Piccoli, 2015). Of the three endmembers, fluorapatite ($Ca_{10}(PO4)_3(F)_2$) is the most common variety reported in terrestrial and extra-terrestrial environments (Piccoli and Candela, 2002); however, chlorapatite ($Ca_{10}(PO4)_3(Cl)_2$), has been reported in some environments (Boudreau et al., 1995; Marks et al., 2012). In addition to F, Cl, and OH, apatite incorporates redox sensitive elements (e.g., S, Fe, Mn, and C), and other elements (e.g., rare earth elements (REEs) and Sr) which can be used to gain insights about the pressure, temperature, and oxygen and sulfur fugacity conditions when apatite crystallized (Konecke et al., 2017a,b). Additionally, the chemistry of apatite has been shown to vary depending on the ore deposit environment in which it crystallizes (Belousova et al., 2002; Bouzari et al., 2016; Mao et al., 2016).

Apatite is a common phase in Kiruna-type iron-oxide apatite (IOA) deposits, which are an important source of iron and a potential source of rare earth elements, which can be concentrated in apatite in these deposits. Though IOA deposits have been mined since the 1800s, the ore forming processes for these deposits remain heavily debated. The ore in IOA deposits typically contains greater than 90% magnetite with minor apatite and actinolite, and ore bodies are typically present

in crustal scale faults (Sillitoe, 2003). There are six ore genesis hypotheses for IOA deposits that generally propose magmatic or hydrothermal origin for these deposits. The ore genesis hypotheses include: (1) precipitation of ore minerals from basinal brines (Barton and Johnson, 1996, 2004; Rhodes and Oreskes, 1999; Rhodes et al., 1999; Barton, 2013), or (2) metamorphic aqueous fluids (Williams, 1994; de Jong et al., 1998); (3) replacement of volcanic and hypabyssal rocks by magmatic-hydrothermal fluids (Sillitoe and Burrows, 2003); (4) precipitation of ore minerals from immiscible Fe-rich magma (Nyström and Henríquez, 1994; Naslund et al., 2002; Tornos et al., 2016; Velasco et al., 2016; Broughm et al., 2017); (5) precipitation from orthomagmatic fluid (Weis, 2013; Jonsson et al., 2013; Hofstra et al., 2016), and (6) precipitation from magmatic/magmatic-hydrothermal fluid suspensions (Knipping et al., 2015a). This dissertation work aims to provide a better understanding of the ore forming processes for archetype IOA deposits, to ultimately inform future exploration for this class of deposits.

Los Colorados is one of seven IOA deposits which contain greater than 100 million tons of iron ore located in the Chilean Iron Belt (CIB). The CIB is a 1000 km long nearly continuous volcanic belt that is located along the Chilean coast and contains approximately 50 IOA deposits, in addition to iron oxide copper gold (IOCG) deposits. Magnetite from the ore bodies at Los Colorados were the focus of the study of Knipping et al. (2015 a), which highlighted the usefulness of geochemistry for elucidating IOA ore forming processes. This study focused on using the major, minor, and trace element chemistry of magnetite, which constitutes the majority of the ore deposit in order to constrain deposit formation. They also used the Fe, O, and H stable isotope signatures of magnetite to further fingerprint the source of the ore forming fluid and proposed a model that explains the geochemical and geological observations for this deposit. According to the model of Knipping et al. (2015a), (1) magnetite crystallizes as a liquidus phase during the cooling of a

magma with intermediate composition and causes exsolution of a volatile phase — this magnetite is enriched in trace elements, e.g., Ti, V, Al, Mn, (2) fluid bubbles nucleate on magnetite microlites as the melt attains volatile saturation, giving rise to a magnetite-fluid suspension which sweeps through the cooling magma body and scavenges fluid mobile elements from the magma — magnetite growing from this hydrothermal fluid has chemistry different to that which crystallized earlier from the magma, (3) the fluid suspension ascends through the crust along regional crustal scale faults during regional extension to give rise to an ore body.

In Chapter 2, I investigate the chemistry of apatite from the Los Colorados IOA deposit. The apatite grains investigated are intimately intergrown with the magnetite investigated by Knipping et al. (2015), thus the goal of this project is to use the chemistry of apatite to test the ore genesis hypothesis of Knipping et al. (2015), in addition to the existing hypotheses. I used backscattered electron imaging, cathodoluminescence imaging, and energy dispersive X-ray spectroscopy (EDS) element mapping to investigate apatite grains prior to quantitatively determining the major, minor, and trace element chemistry of the grains using electron-probe micro-analyses (EPMA) and laser ablation inductively coupled plasma mass spectrometry (LA-ICP-MS). Imaging analyses revealed that individual apatite grains contained distinct domains within them, and that monazite and thorite were present as inclusions in some grains. Additionally, quantitative analyses determined that the concentrations of major (F and Cl), minor, and trace (Sr, Mn, REEs) elements are distinct within these individual domains in apatite grains. Specifically, the concentration of F was high in the inner domains of grains, while the concentration of Cl, Sr, and Mn were higher in the outer domains of individual apatite grains. Statistical analyses reveal statistically significant chemical variability within the domains in individual apatite grains, refuting hypotheses involving growth of apatite from a single fluid. Knipping et al. (2015) found

that the magnetite grains at Los Colorados were chemically zoned, and have cores with chemistry similar to magnetite which grows from a silicate melt (e.g., elevated Ti, V, Al, Mn content), and rims which have chemistry similar to magnetite which grows from a magmatic hydrothermal fluid. The statistically distinct chemical compositions of apatite from Los Colorados are consistent with the growth of the inner domains of apatite from a silicate melt and growth of the outer domains of apatite from a magmatic-hydrothermal fluid. The investigation of the chemistry of apatite from the Los Colorados IOA deposits, therefore, supports ore genesis of this deposit and other IOA deposits according to the magmatic/magmatic-hydrothermal flotation model of Knipping et al. (2015). This chapter is published in *Mineralium Deposita* **2019**, 1-14.

1.3 Magnetite Geochemistry as a tool for Investigating Ore Forming Processes

Magnetite is an iron oxide mineral with the chemical formula Fe_3O_4. Like apatite, magnetite is present in a variety of geologic and ore deposit environments, including igneous, sedimentary, and metamorphic rocks, as well as IOA, iron oxide copper gold (IOCG), porphyry copper gold, nickel copper platinum group element (Ni-Cu-PGE), volcanogenic massive sulfide (VMS), sedimentary exhalative (SEDEX), banded iron formation (BIF), and skarn deposits (Dupuis and Beaudoin, 2011). Magnetite is a spinel group mineral and forms solid solutions with other spinel group minerals, including, ulvöspinel, chromite, hercynite, jacobsite, and coulsonite due to substitutions of Ti, Cr, Al, Mn, and V, for Fe in the magnetite structure (Deer, 1992). This trace element substitution is controlled by temperature, oxygen, and sulfur fugacity, and fluid composition (Nadoll et al., 2014). Grigsby (1990) showed that the chemistry of detrital magnetite is useful as a tool for determining petrogenesis. More recently, Dupuis and Beaudoin (2011) and Nadoll et al. (2014) showed that the chemistry of magnetite can be used to discriminate magnetite from a variety of igneous and hydrothermal ore deposits.

The debate regarding ore genesis of IOA deposits can be thought of as a debate surrounding the nature of the fluids that form them. The basinal brines, metamorphic fluid, and the metasomatic replacement hypotheses argue that the ore fluids are hydrothermal in nature. However, there is disagreement about the source — and by extension the temperature — of the hydrothermal fluids (Barton and Johnson, 1996, 2004; Williams, 1994; de Jong et al., 1998; Rhodes and Oreskes, 1999; Rhodes et al., 1999; Sillitoe and Burrows, 2003; Barton, 2013). The orthomagmatic and immiscible iron rich melt hypotheses argue that the ore forming fluids are purely igneous/magmatic but there is disagreement about how the fluid gives rise to the formation of the ore bodies (Henriquez and Martin, 1978; Nystrom and Henriquez, 1994; Naslund et al., 1997; 1998; 2002; Weis, 2013; Jonsson et al., 2013; Hofstra et al., 2016). The magmatic/magmatic-hydrothermal hypothesis argues that the ore forming fluid is a magmatic-hydrothermal fluid that contains igneous magnetite microlites that exsolve from a cooling silicate melt (Knipping et al., 2015a). Since the chemical signatures of magnetite reflect the temperature at which magnetite crystallized, investigations of the chemistry of magnetite from IOA deposits will provide insights about the nature and temperature of the ore forming fluids (Nadoll et al., 2014).

The various IOA ore genesis hypotheses are usually supported by field evidence, and the El Laco IOA deposit has been used by the proponents of most hypotheses to explain the various models. El Laco is the youngest and best preserved IOA deposit and has been intensively studied since it was first described as a "magnetite flow" by Park (1961). Of the IOA ore genesis hypotheses, those proposed for El Laco are (1) precipitation from an immiscible iron rich melt (Nystrom and Henriquez, 1994; Naslund et al., 2002; Tornos, 2016), (2) metasomatic replacement of the andesite host rock by a hydrothermal fluid (Sillitoe and Burrows, 2002; Dare et al., 2015), (3) precipitation from basinal brines (Rhodes and Oreskes, 1992; Barton, 2013), and (4)

precipitation from magnetite-bearing fluid suspensions mobilised during volcanic edifice collapse (Ovalle et al., 2018). For proponents of the magmatic liquid immiscibility hypothesis, the strongest lines of evidence for ore genesis according to this model are: (1) the unequivocally volcanic textures preserved in the ore bodies (i.e., pahoehoe and aa flow surfaces, abundant gas escape tubes, coarse, spherulitic, and dendritic magnetite crystals, razor-sharp chilled contacts; vesicular textures with open vesicles; friable, pyroclastic ore material, including iron oxide ash) (Henriquez and Martin, 1978; Nystrom and Henriquez, 1994; Naslund et al., 1997; 1998; 2002); (2) the igneous $\delta^{18}O$ isotopic signatures of the iron oxide ores (Rhodes et al. 1999; Naslund et al. 2002; Nystrom et al., 2002); (3) the high (>700 °C) homogenization temperatures of fluid inclusions hosted in multiple phases from multiple ore bodies at the deposit (Sheets et al., 1997; Rhodes et al., 1999; Rhodes and Oreskes, 1999; Broman et al., 1999); (4) the igneous chemical signatures of minerals, e.g., pyroxene, apatite, and magnetite, and the rare earth element signatures of these minerals (Nystrom and Henriquez, 1994; Rhodes et al., 1999; Naslund, 2002); and (5) the presence of melt inclusions containing immiscible iron oxide and silicate melts in the host andesite (Velasco et al., 2016). Proponents of the hydrothermal replacement model highlight: (1) layers of magnetite which mimic the morphology of andesite flow layers in the deposit; (2) porous textures in magnetite, which resemble andesite breccia fragments that were partially or completely replaced by magnetite; (3) the observed replacement of diopside by magnetite and apatite; (4) evidence of hydrothermal activity during mineralization, including: coarse grained magnetite octahedra encrustations, magnetite veins containing drusy quartz, brecciation, geyser-like magnetite terraces, and fumarole-like tube structures; (5) the trace element chemistry of magnetite, which is consistent with that of magnetite which forms from magmatic-hydrothermal fluids (Dare et al., 2015), as evidence for ore genesis via metasomatic replacement of the host rocks by a hydrothermal ore

fluid. The main line of evidence for the involvement of basinal brines in ore genesis at El Laco is the heavy $\delta^{18}O$ isotopic signatures of the iron oxide ores that can be explained by an ore fluid that has interacted with buried evaporite deposits or a closed-basin fluid that has undergone significant evaporation (Rhodes et al., 1999). Interestingly, although the El Laco deposit comprises 7 individual ore bodies, most of the aforementioned studies are focused on samples from just two of them, thus, the understanding of these studies are biased. Attaining a holistic understanding of the ore forming processes at El Laco is important as it will likely allow the economic geology community to achieve consensus about the formation of IOA deposits.

1.4 Using Magnetite and Apatite Geochemistry to Elucidate Ore Genesis at the El Laco IOA Deposit

In *Chapter 3*, I investigate the chemistry of minerals from the enigmatic El Laco IOA deposit to test the IOA ore forming hypotheses. This study is different from previous studies at the deposit in that I assess the major, minor, and trace element chemistry of magnetite from surface to depth at two ore bodies, in addition to assessing the major, minor, and trace element chemistry of magnetite and apatite from surface samples at three other ore bodies. Lastly, Childress (2019) determined the stable Fe, O, H isotopic signatures of aliquots of the same samples. The data produced by BSE imaging, EDS elemental mapping, cathodoluminescence imaging (for apatite), EPMA, and LA-ICP-MS in this study indicate that magnetite in the deep roots of the ore deposit has chemistry and textures consistent with growth from a silicate melt, and magnetite from surface outcrops has chemistry and textures consistent with growth from a magmatic-hydrothermal fluid. Apatite grains in the ore bodies have chemistry consistent with growth from a magmatic hydrothermal fluid. Together, the data for magnetite and apatite are consistent with ore genesis at

El Laco via precipitation from magnetite-fluid suspensions, according to Ovalle et al. (2018). This chapter is accepted for publication in *Economic Geology* pending revisions.

1.5 Magnetite Geochemistry as a Tool for Exploration

A desired outcome of my doctoral education was to do research that directly benefits the mining industry in my home country Guyana. Guyana is located in the Guiana Shield, a Precambrian geologic province located in northern South America. The geology of the Guiana Shield is similar to that of other Precambrian Shields, e.g, the Birimian Shield in West Africa, however, it is underexplored in comparison (Delor et al., 2003). The underexplored nature of this region coupled with the similarities in geology between this Shield and the Birimian Shield, where large amounts of gold and other deposit types have been discovered, provide motivation for targeted exploration for gold and other commodities in this region. Exploration in the Shield is hampered by limited road accessibility, the thick forest cover and weathering profile, and lack of outcrops, but the use of geochemical and geophysical exploration strategies have led to the discovery of greater than 100 million ounces of gold in this region (Bardoux et al., 2018). During geochemical surveys, heavy mineral concentrates which contain magnetite, ilmenite, and other phases are routinely collected. Previous studies highlight the general utility of magnetite geochemistry as a tool for investigating petrogenesis and ore deposit potential, motivating potential application of this technique in the Guiana Shield (Grigsby, 1990; Dupuis and Beaudoin, 2011; Nadoll et al., 2014).

An important finding of my study in *Chapter 3* was that magnetite from a single ore deposit plots in multiple fields on some discriminant diagrams, and that the existing discriminant diagrams, e.g. Al+Mn versus Ti+V (Nadoll et al., 2014) successfully indicate the temperature of formation of magnetite, rather than identify the ore deposit source of magnetite grains. However, there have

been many recent studies which highlight the utility of using statistical analyses, in addition to a larger number of trace and minor elements, to identify magnetite from different ore deposit environments (Makvandi et al., 2016; Pisiak et al., 2017; Dmitrijeva et al., 2018; Huang et al., 2019a, b).

In *Chapter 4*, I test the hypothesis that the chemistry of detrital magnetite can be used as a tool for exploration in covered terrains. Due to the limited success of existing discriminant diagrams (especially when applied to samples of unknown origin), I develop a new model that uses the chemistry of magnetite obtained via EPMA to predict the ore deposit source(s) (i.e., Ni-Cu-PGE, orogenic gold, VMS, IOCG, and porphyry copper deposits) of magnetite samples collected during exploration campaigns. This new discriminant model more successfully identifies magnetite from Ni-Cu-PGE, VMS, IOCG, and porphyry copper deposits than existing geochemical discriminant methods and allows identification of orogenic gold deposits which is not possible using existing discriminant diagrams.

As a first application, I use the model on outcrop and detrital stream sediment samples collected in catchments throughout the greenstone belts of Guyana. Backscattered electron imaging of the grains reveal textural similarities between the grains from outcrops and detrital samples, indicating that the detrital grains are sourced from the outcrops in the catchments and thus are useful for obtaining insight into the geology of the sampled catchments. Textural analyses also indicated that textures can be lost due to weathering and transport by streams. Geochemical data for magnetite were obtained via EPMA and comparison of the data for grains from outcrop and stream sediment samples indicate that the concentrations of measured elements are higher in outcrop samples as compared to detrital grains. The concentrations of Mg, Ni, Cr, Ti, and Mn decrease rapidly as grains are weathered and transported by streams. Further analyses indicate that

chemical signatures of the aforementioned elements are lost when grains are transported to distances greater than 1.5 km away from the source outcrop, but that the concentrations of V and Al in grains are preserved for transport distances up to 5 km. Application of the model to the data for samples from Guyana indicate the detrital grains are sourced from orogenic gold deposits and also indicate the potential for Ni-Cu-PGE deposits in some catchments. Additionally, the presence of sulfide inclusions in magnetite or other detrital phases in the sampled catchments support the ore deposit source inferred from the model for the sampled catchments.

1.6 References

Bardoux, M., Moroney, M., and Robert, F., 2018, Gold mineralization in the Guiana Shield, Guiana and Suriname, South America: a field trip to the 14th Biennial Society for Geology Applied to Mineral Deposits (SGA) meeting: Geological Survey of Canada, Open File 8351, p. 28 https://doi.org/10.4095/306546

Barton, M.D., 2013, Iron Oxide(-Cu-Au-REE-P-Ag-U-Co) Systems. In: Turekian, K.K., and Holland, H.D., ed., Treatise on Geochemistry, 2nd ed. Elsevier, Amsterdam, p. 515 - 541.

Barton, M.D., and Johnson, D.A., 1996, Evaporitic-source model for igneous-related Fe oxide–(REE-Cu-Au-U) mineralization: Geology, v. 24(3), p. 259-262.

Barton, M.D., and Johnson, D.A., 2004, Footprints of Fe-oxide(-Cu-Au) systems: University of Western Australia Special Publications, v. 33, p. 112-116.

Belousova, E.A., Griffin, W.L., O'Reilly, S.Y., and Fisher, N.I., 2002, Apatite as an indicator mineral for mineral exploration: Trace-element compositions and their relationship to host rock type: Journal of Geochemical Exploration, v. 7, p. 45–69.

Boudreau, A.E, Love, C., and Prendergast, M.D., 1995, Halogen geochemistry of the Great Dyke, Zimbabwe: Contributions to Mineralogy and Petrology, v. 122, p. 289-300.

Bouzari, F., Hart, C.J., Bissig, T., and Barker, S., 2016, Hydrothermal alteration revealed by apatite luminescence and chemistry: a potential indicator mineral for exploring covered porphyry copper deposits: Economic Geology, v. 111(6), p.1397-1410.

Broman, C., Nyström, J.O., Henríquez, F, and Elfman, M., 1999, Fluid inclusions in magnetite-apatite ore from a cooling magmatic system at El Laco, Chile: Gff, v. 121(3), p.253-267.

Broughm, S.G., Hanchar, J.M., Tornos, F., Westhues, A., and Attersley, S., 2017, Mineral chemistry of magnetite from magnetite-apatite mineralization and their host rocks: examples from Kiruna, Sweden, and El Laco, Chile: Mineralium Deposita, v. 52 p. 1223-244.

Candela, P.A., and Piccoli, P.M., 1995, Model ore-metal from melts into vapor and vapor/brine mixtures, in Thompson, J.F.H., ed., Magmas Fluids and Ore Deposits, Vol. 23: Victoria, University of British Columbia, p. 101-127

Childress, T., 2019, Fingerprinting Source Fluids of Iron Oxide-Copper-Gold and Iron Oxide-Apatite Deposits Using Traditional and Non-Traditional Stable Isotope Geochemistry, Unpublished Doctoral dissertation, Ann Arbor, Michigan, The University of Michigan.

Dare, S.A., Barnes, S.J., and Beaudoin, G., 2012, Variation in trace element content of magnetite crystallized from a fractionating sulfide liquid, Sudbury, Canada: implications for provenance discrimination: Geochimica et Cosmochimica Acta, v. 88, p.27-50.

Dare, S.A., Barnes, S.J., and Beaudoin, G., 2015, Did the massive magnetite "lava flows" of El Laco (Chile) form by magmatic or hydrothermal processes? New constraints from magnetite composition by LA-ICP-MS: Mineralium Deposita, 50(5), p. 607-617.

Delor, C., de Roever, E.W.F., Lafon, J-M., Lahondère, D., Rossi, P., Cocherie, A., Guerrot, and C., Potrel, A., 2003, The Bakhuis ultra-high-temperature granulite belt (Suriname): II. Implications for the late Transamazonian crustal stretching in a revised Guiana Shield framework: Geologie de la France, v. 2-3-4, p. 207-230.

de Jong, G., Rotherham, J., Phillips G.N., and Williams, P.J., 1998, Mobility of rare-earth elements and copper during shear-zone-related retrograde metamorphism: Geology en Mijnbouw, v. 76, p. 311-319.

Dmitrijeva, M., Metcalfe, A.V., Ciobanu, C.L., Cook, N.J., Frenzel, M., Keyser, W.M., Johnson, G., and Ehrig, K., 2018, Discrimination and variance structure of trace element signatures in Fe-Oxides: A Case Study of BIF-Mineralisation from the Middleback Ranges, South Australia: Mathematical Geosciences, 50(4), p. 381-415.

Dupuis, C., and Beaudoin, G., 2011, Discriminant diagrams for iron oxide trace element fingerprinting of mineral deposit types: Mineralium Deposita, v. 46(4), p.319-335.

Emel, J., and Huber, M.T., 2011, The Richest Hole on Earth? Nature, Labor and the Politics of Metabolism at the Bingham Canyon Copper Mine, in Brunn, S., ed., Engineering Earth, Dordrecht , Springer, p. 353-366.

Goldschmidt, V.M., 1937. The principles of distribution of chemical elements in minerals and rocks. The seventh Hugo Müller Lecture, delivered before the Chemical Society on March 17th, 1937. Journal of the Chemical Society (Resumed), p.655-673.

Granås, B., 2012, Ambiguous place meanings: living with the industrially marked town in Kiruna, Sweden: Geografiska Annaler: Series B, Human Geography, v. 94(2), p.125-139.

Grigsby, J.D., 1990, Detrital magnetite as a provenance indicator. Journal of Sedimentary Research, v. 60(6), p.940-951.

Hanson, G.N., 1978, The application of trace elements to the petrogenesis of igneous rocks of granitic composition: Earth and planetary science letters, v. 38(1), p.26-43.

Hanson, G.N., 1980, Rare earth elements in petrogenetic studies of igneous systems: Annual Review of Earth and Planetary Sciences, v. 8(1), p.371-406.

Harlov, D.E., 2015, Apatite: A Fingerprint for Metasomatic Processes: Elements, v. 11, p.171–176.

Henriquez, F., and Martin, R.F., 1978, Crystal-growth textures in magnetite flows and feeder dykes, El Laco, Chile: The Canadian Mineralogist, v. 16(4), p.581-589.

Hofstra, A.H., Meighan, C.J., Song, X., Samson, I., Marsh, E.E., Lowers, H.A., Emsbo, P., and Hunt, A.G., 2016, Mineral thermometry and fluid inclusion studies of the Pea Ridge iron oxide-apatite–rare earth element deposit, Mesoproterozoic St. Francois Mountains terrane, southeast Missouri, USA.: Economic Geology, v. 111, p. 1985–2016.

Huang, X.W., Boutroy, É., Makvandi, S., Beaudoin, G., Corriveau, L. and De Toni, A.F., 2019a, Trace element composition of iron oxides from IOCG and IOA deposits: relationship to hydrothermal alteration and deposit subtypes: Mineralium Deposita, v. 54(4), p. 525-552..

Huang, X.W., Sappin, A.A., Boutroy, É., Beaudoin, G. and Makvandi, S., 2019b, Trace Element Composition of Igneous and Hydrothermal Magnetite from Porphyry Deposits: Relationship to Deposit Subtypes and Magmatic Affinity: Economic Geology, v. 114(5), p.953-979. doi.org/10.5382/econgeo.4651

Hughes, J.M., and Rakovan, J.F., 2015, Structurally robust, chemically diverse: apatite and apatite supergroup minerals: Elements, v. 11, p.165–170.

Irvine, T.N., 1965, Chromian spinel as a petrogenetic indicator: Part 1. Theory: Canadian Journal of Earth Sciences, 2(6), p. 648-672.

Jensen, B.B., 1973, Patterns of trace element partitioning: Geochimica et Cosmochimica Acta, v. 37(10), p.2227-2242.

Jonsson, E., Troll, V.R., Högdahl, K., Harris, C., Weis, F., Nilsson, K.P., and Skelton, A., 2013, Magmatic origin of giant 'Kiruna-type' apatite-iron-oxide ores in central Sweden: Scientific Reports, v. 3 (1644), p. 1 – 8.

Knipping JL, Bilenker LD, Simon AC, Reich M, Barra F, Deditius AP, Lundstrom C, Bindeman I, Munizaga R (2015a) Giant Kiruna-type deposits form by efficient flotation of

magmatic magnetite suspensions. Geology 43:591–594.
Knipping, J.L., Bilenker, L.D., Simon, A.C., Reich, M., Barra, F., Deditius, A.P., Wälle, M., Heinrich, C.A., Holtz, F., and Munizaga, R., 2015b, Trace elements in magnetite from massive iron oxide-apatite deposits indicate a combined formation by igneous and magmatic-hydrothermal processes: Geochimica et Cosmochimica Acta, v. 171, p. 15–38.
Konecke, B., 2019, Sulfur in Apatite as a Volatile and Redox Tracer in Magmatic and Magmatic-Hydrothermal Systems: Unpublished Doctoral dissertation, Ann Arbor, Michigan, The University of Michigan.
Konecke, B.A., Fiege, A., Simon, A.C., Parat, F., and Stechern, A., 2017a, Co-variability of S^{6+}, S^{4+} and S^{2-} in apatite as a function of oxidation state: Implications for a new oxybarometer: American Mineralogist, v. 102(3), p. 548-557. doi.10.2138/am-2017-5907
Konecke, B., Fiege, A., Simon, A.C., and Holtz, F., 2017b, Cryptic metasomatism during late-stage lunar magmatism implicated by sulfur in apatite: Geology, v. 45, p. 739-742.
Makvandi, S., Ghasemzadeh-Barvarz, M., Beaudoin, G., Grunsky, E.C., McClenaghan, M.B., and Duchesne, C., 2016, Principal component analysis of magnetite composition from volcanogenic massive sulfide deposits: Case studies from the Izok Lake (Nunavut, Canada) and Halfmile Lake (New Brunswick, Canada) deposits: Ore Geology Reviews, 72, p. 60-85.
Mao, M., Rukhlov, A.S., Rowins, S.M., Spence, J., and Coogan, L.A., 2016, Apatite trace element compositions: A robust new tool for mineral exploration: Economic Geology, v. 111, p. 187–1222.
Marks, M.A., Wenzel, T., Whitehouse, M.J., Loose, M., Zack, T., Barth, M., Worgard, L., Krasz, V., Eby, G.N., Stosnach, H., and Markl, G., 2012, The volatile inventory (F, Cl, Br, S, C) of magmatic apatite: An integrated analytical approach: Chemical Geology, v. 291, p.241-255.
McIntire, W.L., 1963, Trace element partition coefficients—a review of theory and applications to geology: Geochimica et Cosmochimica Acta, v. 27(12), p.1209-1264.
Mungall, J.E., 2013. Geochemistry of magmatic ore deposits, in In: Turekian, K.K., and Holland, H.D., ed., Treatise on Geochemistry, 2nd ed. Elsevier, Amsterdam, p. 195–218. doi:10.1016/B978-0-08-095975-7.01108-6
Nadoll, P., Angerer, T., Mauk, J.L., French, D., and Walshe, J., 2014, The chemistry of hydrothermal magnetite: a review: Ore geology reviews, v. 61, pp.1-32.
Naranjo, J.A., Henríquez, F., and Nyström, J.O., 2010, Subvolcanic contact metasomatism at El Laco volcanic complex, central Andes: Andean Geology, v. 37(1), p. 110 – 120.

Naslund, H.R., Henríquez, F., Nyström, J.O., Vivallo, W., and Dobbs, F.M., 2002, Magmatic iron ores and associated mineralization: examples from the Chilean High Andes and Coastal Cordillera, in: Porter, T.M., ed., Hydrothermal iron oxide copper-gold and related deposits: A global perspective, 2nd ed.: Adelaide, PGC Publishing, p. 207-226.
Naslund, H.R., Dobbs, F.M., Henriquz, F.J., and Nystrom, J.O., 1998. Evidence for iron-oxide magmas at El Laco, Chile. In Geological Society of America Abstracts with Programs (Vol. 30, p. 91).
Naslund, H.R., Dobbs, F.M., Henríquez, F.J., and Nyström, J.O., 1997. Irrefutable evidence for the eruption of iron-oxide magmas at El Laco Volcano, Chile: EOS, Transaction of the American Geophysical Union, v. 78(17), p.S333.

Nyström, J.O., and Henríquez, F., 1994, Magmatic features of iron ores of the Kiruna type in Chile and Sweden: ore textures and magnetite geochemistry: Economic Geology, v. 89, p. 820–839.
Nyström, J.O., Vergara, M., Morata, D., and Levi, B., 2003. Tertiary volcanism during extension in the Andean foothills of central Chile (33 15′–33 45′ S): Geological Society of America Bulletin, v. 115(12), pp.1523-1537.
Ossandón C, G., Fréraut C, R., Gustafson, L.B., Lindsay, D.D., and Zentilli, M., 2001, Geology of the Chuquicamata mine: A progress report: Economic Geology, v. 96(2), pp.249-270.
Onuma, N., Higuchi, H., Wakita, H., and Nagasawa, H., 1968, Trace element partition between two pyroxenes and the host lava: Earth and Planetary Science Letters, v. 5, p.47-51.
Ovalle, J.T., La Cruz, N.L., Reich, M., Barra, F., Simon, A.C., Konecke, B.A., Rodriguez-Mustafa, M.A., Deditius, A.P., Childress, T.M., and Morata, D., 2018, Formation of massive iron deposits linked to explosive volcanic eruptions: Scientific reports, v. 8(1), p.14855.
Paterson, N.R., 2003, Geophysical developments and mine discoveries in the 20th century: The Leading Edge, v. 22(6), p.558-561.
Philpotts, A.R., 1978, Textural evidence for liquid immiscibility in tholeiites: Mineralogical Magazine, v. 42(324), p.417-425.
Piccoli, P.M. and Candela, P.A., 2002, Apatite in igneous systems: Reviews in Mineralogy and Geochemistry, v. 48(1), pp.255-292.
Pisiak, L.K., Canil, D., Lacourse, T., Plouffe, A., and Ferbey, T., 2017, Magnetite as an indicator mineral in the exploration of porphyry deposits: a case study in till near the Mount Polley Cu-Au deposit, British Columbia, Canada: Economic Geology, 112(4), p. 919-940.
Rhodes, A.L., and Oreskes, N., 1999, Oxygen isotope composition of magnetite deposits at El Laco, Chile: evidence of formation from isotopically heavy fluids: Society of Economic Geology Special Publications, v. 7, p. 333-351.
Rhodes A.L., Oreskes N., and Sheets S., 1999, Geology and rare earth element geochemistry of magnetite deposits at El Laco, Chile: Society of Economic Geology Special Publication, v. 7, p. 299-332.
Schodde, R., 2011, November. Recent trends in gold discovery. In NewGenGold Conference, Perth (Vol. 2).
Sillitoe R.H., 2003, Iron oxide-copper-gold deposits: An Andean view: Mineralium Deposita, v. 38, p. 787–812.
Sillitoe, R.H., and Burrows, D.R., 2002, New field evidence bearing on the origin of the El Laco magnetite deposit, northern Chile.: Economic Geology, v. 97(5), p. 1101-1109.
Smyth, J.R., and Bish, D.L., 1988, Crystal structures and cation sites of the rock-forming minerals: Boston: Allen & Unwin, p. 332.
Tornos, F., Velasco, F., and Hanchar, J.M., 2016, Iron-rich melts, magmatic magnetite, and superheated hydrothermal systems: The El Laco deposit, Chile: Geology, v. 44, p. 427–430.
U.S. Geological Survey, 2019, Mineral commodity summaries 2019: U.S. Geological Survey, p.1-200, https://doi.org/10.3133/70202434.
Velasco, F., Tornos, F., and Hanchar, J.M., 2016, Immiscible iron-and silica-rich melts and magnetite geochemistry at the El Laco volcano (northern Chile): Evidence for a magmatic origin for the magnetite deposits: Ore Geology Reviews, v. 79, p. 346-366.

Webster, J.D., and Piccoli, P.M., 2015, Magmatic apatite: a powerful, yet deceptive, mineral: Elements, v. 11, p. 177–182.
Weis, F., 2013, Oxygen and Iron Isotope Systematics of the Grängesberg Mining District (GMD), Central Sweden: Unpublished M.Sc. thesis, Uppsala, Sweden, Uppsala University.
Williams, P.J., 1994, Iron mobility during synmetamorphic alteration in the Selwyn Range area, NW Queensland: implications for the origin of ironstone-hosted Au-Cu deposits:
Mineralium Deposita, v. 29(3), p. 250-260.

Chapter 2

The Geochemistry of Apatite From the Los Colorados Iron Oxide – Apatite deposit, Chile: Implications for Ore Genesis

Co-authors: Adam C. Simon, Aaron S. Wolf, Martin Reich, Fernando Barra, Joel E. Gagnon

Published in *Mineralium Deposita* (2019), 1-14.

2.1 Abstract

Apatite grains from the Los Colorados iron oxide – apatite (IOA) deposit, the largest IOA deposit in the Chilean Iron Belt (CIB), exhibit significant intracrystalline spatial variability with respect to the concentrations of F, Cl, and OH and trace elements. Statistical interrogation of the compositional data indicates that individual apatite grains contain spatially discrete F-rich and Cl-rich domains. The chemical composition of the F-rich domains is consistent with apatite growth from silicate melts, whereas the chemical composition of the Cl-rich domains is consistent with apatite growth from a magmatic-hydrothermal fluid that cooled as it percolated outward from the Los Colorados fault — the structural control for emplacement of the ore body — into the surrounding brecciated diorite and andesite host rocks.

Apatite in the deposit is intimately intergrown with magnetite and actinolite for which trace element, Fe, H and O stable isotope data indicate a combined magmatic/ magmatic-hydrothermal genesis for the deposit. The compositional data for apatite are consistent with a genetic model wherein F-rich apatite cores crystallized with magnetite from silicate melt, followed by exsolution

of a magmatic-hydrothermal fluid during decompression of the parent magma. Experimental studies demonstrate that magmatic-hydrothermal volatile phase bubbles preferentially nucleate and grow on the surfaces of apatite and magnetite microlites during decompression of a magma body. Continued degassing of the melt results in the volatile phase sweeping up apatite and magnetite microlites, and forming a magnetite-apatite-fluid suspension that is buoyant in the magma chamber, and ascends from the source magma along faults during regional extension. Halite-saturated fluid inclusions in magnetite, which is paragenetically equivalent to apatite at Los Colorados, indicate that the magmatic-hydrothermal fluid was a brine, which allows this fluid to efficiently scavenge Cl, P, rare earth elements, and other fluid-compatible elements from the silicate melt. During ascent, the X_{Cl}/X_F ratio of apatite increases as it grows from the evolving Cl-rich magmatic-hydrothermal fluid during decompression and cooling.

2.2 Introduction

Kiruna-type iron oxide – apatite (IOA) deposits are an important source of iron (Fe), and are potential rare earth element (REE) resources owing to light REE-enrichment of apatite in many deposits (Frietsch 1978; Hitzman et al. 1992; Barton 2013). IOA deposits and their Cu- and Au-rich counterparts, the iron oxide – copper – gold (IOCG) deposits, are spatially and temporally related to one another in many districts, and have been suggested to be cogenetic end-members of iron-rich ore systems (Hitzman et al. 1992; Davidson and Large 1994; Frietsch and Perdahl 1995; Sillitoe 2003; Pirajno and Bagas 2008; Groves et al. 2010; Knipping et al. 2015a, b; Reich et al. 2016; Barra et al. 2017; Simon et al. 2018). IOA deposits are dominated by magnetite (50 – 90 modal %) with apatite and actinolite comprising the bulk of the remainder of the ore (Frietsch and Perdahl 1995), whereas IOCG deposits are dominated modally by magnetite and (specular)

hematite in addition to chalcopyrite, pyrite, bornite, and gangue minerals such as K-feldspar, biotite and sericite, among others (Sillitoe 2003; Williams et al. 2005; Barton 2013).

There is no accepted genetic model for the formation of IOA deposits. Working hypotheses that explain the formation of IOA deposits include (i) magmatic-hydrothermal replacement of volcanic and hypabyssal rocks (Sillitoe and Burrows 2002); (ii) precipitation from basinal brines (Barton and Johnson 1996, 2004; Rhodes and Oreskes 1999; Rhodes et al. 1999; Barton 2013) or (iii) metamorphic aqueous fluids (Williams 1994; de Jong et al. 1998); (iv) formation from Fe-oxide rich immiscible magma (Nyström and Henríquez 1994; Naslund et al. 2002; Tornos et al. 2016; Velasco et al. 2016; Broughm et al. 2017); (v) precipitation from orthomagmatic fluid (Weis 2013; Jonsson et al. 2013; Hofstra et al. 2016; Westhues et al. 2016, 2017a, b); or (vi) formation by precipitation from a magmatic/magmatic-hydrothermal fluid suspension (Knipping et al. 2015a; Simon et al. 2018).

Here, we focus on the chemistry of apatite from the Los Colorados IOA deposit in the Chilean Iron Belt (CIB). Several studies focused exclusively on magnetite, actinolite and pyrite from Los Colorados (Knipping et al. 2015a, b; Bilenker et al. 2016; Reich et al. 2016). Those studies used the trace element chemistry of magnetite and pyrite, the Fe, H, and O stable isotope compositions of magnetite, and the O and H stable isotope signatures of actinolite to develop a new magmatic/magmatic-hydrothermal model to explain the origin of the Los Colorados deposit. The new genetic model proposed by Knipping et al. (2015a) for IOA deposits invokes crystallization of magnetite microlites from a silicate melt, and the formation of a magmatic magnetite-fluid suspension that transports magnetite from the source magma into the overlying crust via pre-existing fault structures that are reactivated by crustal extension. Textural observations of samples from Los Colorados indicate that apatite is paragenetically equivalent to

magnetite and actinolite. Thus, the chemistry of apatite in the deposit should be consistent with the genetic model proposed by Knipping et al. (2015a).

Apatite is a ubiquitous phase in IOA deposits, and is a common accessory mineral in terrestrial and extraterrestrial environments. Apatite ($Ca_{10}(PO_4)_6(F,Cl,OH)_2$) can structurally accommodate nearly half of the elements in the periodic table (Piccoli and Candela 2002; Harlov 2015; Hughes and Rakovan 2015; Webster and Piccoli 2015), and the observed systematic variation of the halogen and trace element chemistry of apatite, as a function of P-T-X conditions at the time of apatite crystallization, or re-equilibration during metasomatism, allows the chemistry of apatite to be used to assess the chemical evolution of geologic systems (Streck and Dilles 1998; Belousova et al. 2002; Parat et al. 2011; Mao et al. 2016; Bouzari et al. 2016; Konecke et al. 2017a, b; Webster et al. 2017). In this study, we combine cathodoluminescence (CL) imaging, energy dispersive X-ray spectroscopy (EDS) element mapping, electron probe micro-analyses (EPMA), and laser ablation inductively coupled plasma mass spectrometry (LA-ICP-MS) to investigate the chemistry of apatite from the Los Colorados IOA deposit. The systematic variation of halogen and trace element compositions of apatite are shown to be consistent with the flotation model proposed by Knipping et al. (2015a), and provide evidence that apatite, along with magnetite, record a transition from magmatic to magmatic-hydrothermal conditions during ore genesis.

2.3 Geological Setting

Los Colorados is the largest IOA deposit in the 1000 km-long CIB, which hosts ~50 IOA deposits, including seven that contain >100 million tons (Mt) of high grade Fe ore (Fig. 2.1A). The regional geology and the tectonic history of the CIB are described in detail by Pichon (1980), Oyarzún and Frutos (1984), and Oyarzún et al. (2003). Los Colorados formed during the Cretaceous (~110 Ma) and is located ~35 km north of Vallenar, Chile (Fig. 2.1A; Pichon 1980;

Oyarzún and Frutos 1984). Los Colorados has proven resources of ~900 Mt of ore with an average grade of 34.6% Fe (CAP Annual Report 2015). At Los Colorados, high grade magnetite ore was mined from three ore bodies, which are hosted in the diorite and andesite of the Punta del Cobre Formation (Pincheira et al. 1990). The main ore bodies at Los Colorados are the western ore body, which is ~900 m long and ~280 m wide, and the eastern ore body, which is ~780 m long and ~50 m wide (Fig. 2.1B). The western and eastern ore bodies are tabular, sub-parallel and sub-vertical, and contain ≥90 modal % magnetite with lesser amounts of apatite, actinolite, and pyrite. The ore grades of the western and eastern ore bodies are 65-60% Fe, and 62-57% Fe, respectively. The emplacement of the ore bodies was structurally controlled by the district-scale Los Colorados fault, which is part of the Atacama Fault System (Pichon 1980; Oyazún and Frutos 1984; Reich et al. 2016). The third ore body at Los Colorados consists of lower-grade disseminated and veinlet magnetite (up to 5 modal %), pyrite (up to 5 modal %), and sparse chalcopyrite (Fig. 2.1B; Reich et al. 2016). Previous studies report moderate argillic alteration in the diorite, and lack of potassic and sodic alteration in the ore bodies (Knipping et al. 2015a, b; Reich et al. 2016).

2.4 Analytical Methods and Data Analysis

2.4.1 Sample Selection

A total of 43 apatite grains were studied from drill core LC-04, collected at a depth of 99.5 m from the surface in the tabular, western ore body, and one sample collected in the pit from freshly blasted (disaggregated) material on the eastern edge of the western ore body (Fig. 2.1B). This latter zone showed a gradation from the massive ore body into the magnetite breccia body, i.e., a halo composed of magnetite intergrown with centimeter-scale crystals of actinolite and apatite (Fig. 2.1B). The compositions of magnetite, actinolite, and pyrite in these samples are described in detail in Knipping et al. (2015a, b), Bilenker et al. (2016), and Reich et al. (2016),

respectively. Apatite grains in thin sections and epoxy mounts were analyzed. The apatite grains mounted in epoxy were obtained by separating apatite from magnetite and actinolite following standard mineral separation protocols.

2.4.2 Element mapping and cathodoluminescence imaging

The apatite grains were investigated by using a combination of back-scattered electron (BSE) imaging, energy-dispersive X-ray spectroscopy (EDS) element mapping, and cathodoluminescence (CL) imaging. Qualitative elemental EDS maps of apatite grains were made by using a JEOL JSM – 7800 FLV Field Emission Scanning Electron Microscope (FE-SEM). An accelerating voltage of 20 kV was used to generate EDS maps of Ca, P, Cl, and F. A Gatan ChromaCL2 CL imaging detector on the FE-SEM was used to obtain CL images of apatite grains. A 20 kV accelerating voltage was used to generate the CL images.

2.4.3 Electron probe micro-analysis (EPMA)

Concentrations of Ca, P, F, Cl, S, Si, Na, Mg, and Al in apatite grains were measured via wavelength-dispersive X-ray spectrometry (WDS) by using a Cameca SX100 electron probe micro-analyzer (EPMA). Line transects and spot analyses were performed on apatite grains in thin sections and on individual grains in epoxy mounts. EDS element maps and CL images were used to guide the EPMA analyses. WDS measurements were made by using an excitation voltage of 15 keV, a beam current of 10 nA, and a beam diameter of 2 μm. Synthetic fluorapatite and chlorapatite grains (cf. Schettler et al. 2011) were used as the primary standards for Ca Kα, Cl Kα, F Kα, P Kα, and natural silicates and an anhydrite sample were used as the primary standards for Na Kα, Si Kα, Mg Kα, Al Kα and S Kα (Table 2A-1). Major elements in apatite (Ca, P, Cl, F) were analyzed first in the analytical sequence as suggested by Goldoff et al. (2012). A counting time of 20 s was used for major elements (Ca, P, F, Cl), and a counting time of 30 s was used for minor elements

(Na, S, Si, Mg, Al) following the analytical protocol of Pyle et al. (2002). The hydroxide (OH) content of apatite for each individual spot analysis was calculated by mass balance using the quantitatively determined F and Cl concentrations, and the constraint that the halogen site in apatite is occupied by $X_F + X_{Cl} + X_{OH} = 1$ (Hughes and Rakovan 2015). We used the spreadsheet of Ketcham et al. (2015) to calculate OH concentrations in apatite.

2.4.4 Laser ablation inductively coupled plasma mass spectrometry (LA-ICP-MS) analyses

The concentrations of Ti, V, Mn, Ni, Sc, Sn, W, Cu, Zn, Sr, Ba, Zr, Cr, Ge, As, Th, U, Pb, Y, and all rare earth elements (REEs) except Pm were measured by using a Photon Machines 193 nm short-pulse-width Analyte Excite ArF excimer laser ablation system attached to an Agilent 7900 fast scanning inductively coupled plasma quadrupole mass spectrometer (ICP-QMS). The LA-ICP-MS analyses were performed along the same transects, but slightly offset, within apatite grains that were previously analyzed by EPMA. The analyses were performed by using a laser beam with an energy of 4.1 mJ/ pulse, for a calculated fluence of 2.54 J/cm^2. Beam diameters of 15 μm and 20 μm, respectively, were used for spot analyses of apatite grains in the epoxy mounts and thin sections. There were 800 laser pulses at a frequency of 20 Hz during each analysis, and each individual analysis consisted of first measuring the gas background for 30 s followed by ablation of apatite for 40 s. The Ca concentration of apatite, which was previously quantified by using EPMA, was used as the internal standard for LA-ICP-MS calibration, and the NIST-610 reference glass was used as the bracketing external calibration standard. The NIST-610 glass was analyzed periodically as an unknown during the analytical session to evaluate the accuracy of the analyses. The concentrations of the elements analyzed and their associated limits of detection were determined by using the SILLS software package (Guillong et al. 2008), which calculates the detection limit following Pettke et al. (2012). Each LA-ICP-MS transient signal was evaluated for

the presence of inclusions, and only inclusion-free signals were processed. The concentrations of all elements measured in the NIST-610 standard glass, when treated as an unknown, agree within analytical error with the concentrations reported by Jochum et al. (2011).

2.5 Results

2.5.1 Element mapping and cathodoluminescence imaging

Representative BSE, EDS Kα maps, and CL images for apatite grains from Los Colorados are presented in Fig. 2.2, and Figs. 2A.1, and 2A.2. The BSE images reveal the presence of apatite-hosted inclusions that EDS point analyses indicate are monazite ($[Ce,La,Nd]PO_4$) and $ThSiO_4$ (Figs. 2A.3, 2A.4). The EDS element maps indicate that Ca and P are homogeneously distributed in the apatite grains (Figs. 2A.1C and 2A.D, 2A.2C and 2A.2D). Additionally, the EDS maps reveal variability in the distribution of Cl within individual apatite grains (Fig. 2.2B; Figs. 2A.1E, 2A.2E). The EDS maps do not provide insight about the distribution of F owing to the high limit of detection for F on the EDS detector.

The CL images indicate chemical heterogeneities that manifest as variability in luminescence color and intensity within individual apatite grains (Fig. 2.2C; Figs. 2A.1B, 2A.2B). The variations observed in the CL images correlate with the variations in Cl distribution revealed in the EDS elemental maps (Figs. 2.2B and C; Figs. 2A.1B and 2A.1E, and 2A.2B and 2A.2E). In all apatite grains from the pit sample (Fig. 2A.1), the brightest luminescence is observed in the regions of apatite with low Cl concentration. On the contrary, in most grains from the drill core, the brightest luminescence is observed in regions of apatite grains that are enriched in Cl (Fig. 2A.2). However, there are also apatite grains from the drill core samples where, as observed for the pit samples, the brightest luminescence is observed in Cl-poor regions of apatite (Fig. 2.2B and C).

2.5.2 Major, minor, and trace element concentrations of apatite

A total of 285 spot analyses were performed by using both EPMA and LA-ICP-MS. The number of individual spot analyses per apatite grain ranged from 1 on small grains, to as many as 20 on large grains. Compositional data for all apatite grains are reported in Table 2A2. The average concentrations (±1σ) of CaO and P_2O_5 for all apatite grains are 54.5 ± 0.6 wt% and 41.6 ± 0.8 wt%, respectively. The concentration of Cl in apatite grains ranges from 0.40 to 4.03 wt% (X_{Cl} = 0.12 to 1.16) for the pit sample, 0.80 to 5.76 wt% (X_{Cl} = 0.02 to 1.68) for drill core sample LC-04-99.5A, and 0.82 to 5.52 wt% (X_{Cl} = 0.24 to 1.64) for drill core sample LC-04-99.5B. The average concentrations of Cl in the cores and rims, respectively, of apatite grains are 1.44 wt% (X_{Cl} = 0.46), and 3.15 wt% (X_{Cl} = 0.88) for the pit samples, and 1.79 wt% (X_{Cl} = 0.57) and 3.86 wt% (X_{Cl} = 1.12) for the drill core samples. The concentration of F in apatite grains ranges from below detection limit (BDL) to 2.3 wt% (X_F = BDL to 1.62) for the pit sample, BDL to 2.6 wt% (X_F = BDL to 1.40) for drill core sample LC-04-99.5A sample, and BDL to 2.51 wt% (X_F = BDL to 1.34) for drill core sample LC-04-99.5B. The average F concentrations in the cores and rims, respectively, of the apatite grains are 1.60 wt% (X_F = 0.79) and 0.29 wt% (X_F = 0.19) for the pit sample, and 1.24 wt% (X_F = 0.55) and 0.34 wt% (X_F = 0.18) for the drill core sample. Fluorine concentrations were below detection limit for many of the analyses of apatite grains (Table 2A2). Calculated OH concentrations in apatite grains range from 0.18 to 1.94 wt% (X_{OH} = 0.12 to 1.28) for the pit sample, 0.09 to 1.52 wt% (X_{OH} =0.14 to 1.76) for drill core sample LC-04-99.5A, and 0.22 to 1.27 wt% (X_{OH} = 0.26 to 1.52) for drill core sample LC-04-99.5B. The average calculated OH concentrations in the cores and rims, respectively, of the apatite grains are 0.53 wt% (X_{OH} = 0.74), and 0.75 wt% (X_{OH} = 0.93) for the pit samples, and 0.71 wt% (X_{OH} = 0.89) and 0.70 wt%

(X_{OH} = 0.70) for the drill core samples. The concentrations of F and Cl are negatively correlated (Figs. 2.3A, B), whereas the relationship between calculated OH and Cl is unclear (Fig. 2A.5).

The variations in Cl, F, and calculated OH concentrations found in apatite grains were also observed within individual apatite grains (Fig. 2.4A). This is consistent with the Cl Kα EDS maps (Fig. 2.2B; Figs. 2A.1E, 2E). For instance, the X_{Cl}/X_F ratio for the apatite grain in Fig. 2.2, which corresponds to the red circles in Fig. 2.4A, varies across the apatite grain. From top left to bottom right on the transect shown in Fig. 2.2, the X_{Cl}/X_F ratio varies from 4.62 to 5.14, decreases to 0.54 and 0.23, followed by an increase to 2.92, then decreases to 0.21, and finally increases to 3.16 and 4.54 as the transect reaches the edge of the apatite grain.

The concentrations of Na_2O, MgO, Al_2O_3, S, and SiO_2 in apatite are generally low, and are similar among apatite grains from the pit and drill core samples (Table 2A2). The concentrations of the following trace elements are consistently above the limit of detection: As, Mn, Sr, Ti, V, Y, La, Ce, Pr, Nd, Sm, Eu, Gd, Tb, Dy, Ho, Er, Tm, Yb, and Lu (Table 2A2). The concentrations of Ho, Eu, Tm, Yb, and Lu are similar in apatite grains from all three samples (Table 2A2). Chondrite-normalized mean concentrations of REEs in apatite from the pit and drill core samples indicate enrichment of light rare earth elements (LREEs) compared to heavy rare earth elements (HREEs) (Fig. 2.5). The concentrations of Sc, Zr, Ni, Cu, Co, Zn, Sn, Ba, W, Th, Pb, and U were consistently close to, or below the limit of detection (Table 2A2). The concentration of Ge was above the limit of detection for some of the apatite grains from the drill core samples (BDL - 31ppm), but below the limit of detection for apatite grains from the pit sample.

2.5.3 Data Analysis

We customized analysis scripts in the Python programming language to quantitatively assess the observed spatial variability of F and Cl concentrations and all measured trace elements

within individual apatite grains (Appendix 2.1). Specifically, Gaussian interpolation was utilized to smooth the maps and better highlight the observed variability of Cl intensity within the apatite grains. Histograms of the smoothed Cl maps reveal three statistically distinct domains within apatite grains: a F-rich (Cl-poor) domain, a Cl-rich (F-poor) domain, and a domain consisting of intermediate Cl that exists between the F-rich and Cl-rich domains (Figs. 2.6A, B, C). Spatially, F-rich domains are located away from apatite grain boundaries; we refer to these domains as apatite cores (Figs. 2.6D, E, F; 2.4C). The Cl-rich domains are located in the outer region of apatite grains and proximal to cracks within grains; we refer to these domains as apatite rims (Figs. 2.6D, E, F; 2.4D). The third population of domains exists spatially between the Cl-rich rims and the F-rich cores of apatite grains; we refer to these domains as boundary regions. The data analysis did not reveal whether the boundary zones belonged to the core or rim domains, most likely because the smoothing required to average over the high spatial variability of Cl concentrations along the core-rim boundary would necessarily involve averaging over both core and rim pixels in the Cl Kα EDS maps (Fig. 2 6D, E, F).

The concentrations of representative major, minor, and trace elements in apatite cores, rims, and boundary zones are plotted against Cl in Fig. 2.3 and Fig.2A.7. The figures indicate that the elemental concentrations for the drill core samples are similar; thus, we combined the results for these two samples for the rest of the statistical analyses (Appendix 2.1). The statistical analyses of the minor and trace element chemistry reveal significant differences ($p<0.05$) between the mean concentrations in the cores and rims for many minor and trace elements in apatite grains for the pit samples (including Sr, Ce, Nd, Y, V, Mn, and As) (Fig. 2A.8A). On the contrary, the mean concentrations in the core and rim for many minor and trace elements in apatite grains from the drill core samples are statistically indistinguishable, except for Mn, which shows a difference at

the p=0.038 level (Fig. 2A.8). Comparison of the distribution of elements in the cores of apatite from the pit and drill core samples shows that F-rich cores of apatite from the drill core are significantly elevated in nearly every minor and trace element examined (except for Si and S), including Sr, Ce, Nd, Lu, Y, V, Ti, Na, Mn, and As (Fig. 2.7). The Levene test for variance in elemental concentrations in the core and rim of apatite grains indicates that for the pit sample, the variance for all elements, except Ti, is statistically indistinguishable, while the variance for all elements, except As, is statistically indistinguishable for the drill core sample (Table 2A3).

2.6 Discussion

2.6.1 Halogen concentrations in apatite and the causes of variability

In igneous systems where apatite is commonly a near-liquidus phase, it is well documented that apatite is initially enriched in F owing to the high apatite/melt partition coefficient for F relative to Cl (Harlov 2015; Webster and Piccoli 2015). During progressive crystallization of the melt, the F/Cl ratio of the melt decreases owing to the crystallization of apatite, and results in progressive Cl enrichment of apatite. This is not what we observe for apatite grains from Los Colorados, where F-rich apatite cores are statistically distinct from Cl-rich rims, such that, there is no continual core to rim gradation from F-rich to Cl-rich apatite. In Fig. 2.4B, the F-Cl-OH concentrations of apatite grains from Los Colorados are plotted with fields from Boudreau et al. (1995) that represent the F-Cl-OH compositions of apatite grains from mafic igneous systems. Those authors report that apatite analyses that plot closer to the F apex of the F-Cl-OH ternary diagram represent apatite grown from unfractionated silicate melt at near-liquidus temperatures, whereas analyses that plot closer to the Cl apex represent apatite grown from, or re-equilibrated with, a Cl-bearing magmatic-hydrothermal fluid (Brown and Peckett 1977; Boudreau et al. 1986; Boudreau 1993; Piccoli and Candela 2002; Boudreau and Simon 2007; Webster and Piccoli 2015).

The F-Cl-OH compositions of some apatite grains from Los Colorados plot in the field for apatite that crystallized from, and grew in equilibrium with, a mafic silicate melt (e.g., Munni Munni, Duluth, Great Dyke), whereas other apatite analyses plot in the field for apatite that grew in the presence of a Cl-bearing magmatic-hydrothermal fluid (e.g., Stillwater and Bushveld below major PGE zones) (Fig. 2.4B). The statistically distinct F-rich cores (Fig. 2.4C) and Cl-rich rims (Fig. 2.4D) observed in all apatite grains from Los Colorados are consistent with initial growth of apatite from a silicate melt followed by growth from a Cl-rich magmatic-hydrothermal fluid. This explains the absence of a gradual change of F/Cl ratio from the F-rich domains to the Cl-rich domains, and is consistent with the core-to-rim chemistry of paragenetically equivalent magnetite, as discussed below and by Knipping et al. (2015a, b).

2.6.2 Trace and minor element concentrations in apatite

Generally, the concentrations of trace elements are higher in the core of apatite grains from the drill core relative to the core of apatite grains from the pit sample (Table 2A2; Fig. 2.7). The most plausible explanation for the compositional differences is the temperature of the mineralizing fluid, which was hotter during formation of the massive magnetite eastern ore body (Fig. 1B). This is consistent with published concentrations of [Mg+Mn] vs [(Si+Al)/(Mg+Mn)] that decrease systematically in paragenetically equivalent magnetite as one moves from the massive magnetite eastern ore body, the source of the drill core sample, into the disseminated mineralization in the brecciated host rock, the source of the pit sample (Knipping et al. 2015a, b; Deditius et al. 2018). Further, comparison of magnetite chemistry at Los Colorados with that from the global study of Nadoll et al. (2014) indicates that the temperature of mineralization was higher for the massive magnetite ore body than the disseminated mineralization in the host rock. The only direct constraint on the temperature of mineralization is provided by O-isotope thermometry for

paragenetically equivalent magnetite and actinolite, intergrown with apatite, from the drill core sample, and indicates a minimum temperature of 640 °C for mineralization of the massive magnetite ore body (Bilenker et al. 2016). Finally, the chemistry of disseminated pyrite in the brecciated ore body east of the main massive magnetite ore body also indicates a cooler temperature for the magmatic-hydrothermal fluid as it percolated from the massive magnetite ore zone to into the host rocks (Reich et al. 2016).

The concentrations of Mn and REEs in apatite are consistent with the CL images presented in Fig. 2.2, and Figs. 2A.1, and 2. Cathodoluminescence in apatite is the result of trace element substitutions into the apatite structure (Waychunas 2002). The intensity and perceived color of the luminescence are caused by the presence of specific ions or groups of ions, most commonly Mn^{2+}, which causes yellow luminescence, and REE^{3+} which causes violet-blue luminescence (Götze et al. 2001; Waychunas 2002; Kempe and Götze 2002; Götze 2012). Variations in the concentrations of Mn^{2+} and REE^{3+} at the ppm level cause observable changes in the CL intensity (Gros et al. 2016). The LA-ICP-MS data for apatite from Los Colorados indicate that the CL activators Mn^{2+} and REE^{3+} are present in apatite, and the concentrations of these CL activators correlate spatially with CL intensity. In apatite grains from the pit sample, the cores, which exhibit bright luminescence, are enriched in REEs (La, Ce, Nd, Dy, Yb) relative to the rims, which are enriched in Mn, and exhibit darker luminescence (Figs. 2A.1B; 8A). The luminescence for samples from the drill core is more complex; for some grains the core exhibits bright luminescence, while for others, the rim exhibits bright luminescence (Fig. 2.2C; Fig. 2A.2B). The data indicate that for apatite grains from the drill core, the rims are depleted in Mn relative to the cores, and the concentrations of the REEs (Ce, Lu, Dy, La, Yb and Nd) are similar in both the cores and the rims (Fig. 2A.8B). The differences in the color and intensity of the luminescence for the apatite grains

at Los Colorados, in addition to the spatial variability of halogens, therefore, indicate differences in the chemistry of the fluids from which the individual domains of apatite grew.

Fluid mobile elements such as Sr, Mn, and As are enriched in the rim of the apatite grains from the pit samples (Table 2A2; Fig. 2A.8A). The ability of Cl-bearing hydrothermal fluids to transport Sr, Mn, and As is well documented by field and experimental studies (Reed et al. 2000; Williams-Jones and Heinrich 2005; Simon et al. 2007). The concentration of S is also marginally higher in the Cl-rich rim, compared to the Cl-poor core, of apatite grains from both the pit and drill core samples (Table 2A2; Fig. 2A.8). The higher S contents in the Cl-rich rims is consistent with incorporation of sulfate in the apatite structure (Konecke et al. 2017a).

2.6.3 Comparison to apatite from other IOA deposits and igneous rocks

The chemistry of apatite from Los Colorados is consistent with data for other IOA deposits in the Chilean Iron Belt. Treloar and Colley (1996) report that most apatite grains from the Mina Carmen and Fresia deposits exhibit zonation from F-rich core to Cl-rich rim. Rojas et al. (2018) report that apatite in the deeper zones of the El Romeral deposit is F-rich, whereas hydroxyapatite is present at shallow levels. The Cl contents of both the fluorapatite and hydroxyapatite are low (<0.5 wt%); however, the Cl content of the hydroxyapatite is higher (up to 0.24 wt%) than that for the fluorapatite (0.1-0.13 wt%). Naslund et al. (2002) report that apatite from the El Laco IOA deposit in northern Chile is F-rich, which is consistent with data for the Cerro de Mercado IOA deposit, Durango, Mexico (Young 1969), IOA deposits in the Kiruna district, Sweden (Frietsch 1978; Harlov et al. 2002a; Jonsson et al. 2016), IOA deposits in the Bafq district, Iran (Torab and Lehman 2007; Bonyadi et al. 2011), and the Pea Ridge IOA deposit in Missouri, USA (Harlov et al. 2016).

The trace element concentrations for apatite from Los Colorados are also similar to those reported for other IOA deposits. For example, in Fig. 2.8, the concentrations of V vs. Sr and Mn vs. Yb, in apatite from Los Colorados, are plotted along with data for apatite from the Aoshan (China), Great Bear (Canada), and Durango/ Cerro de Mercado (Mexico) IOA deposits (Mao et al. 2016). The trace element data for all of these deposits overlap, although generally apatite from Los Colorados exhibit a larger spread of concentrations. The concentrations of REEs in apatite from Los Colorados are similar to those reported for apatite grains from Carmen and Fresia in the CIB (Treloar and Colley 1996; Konecke et al. 2017a), and apatite grains from Fresia have cores that are enriched in LREEs, specifically Ce, La, and Nd (Treloar and Colley 1996), consistent with the core of apatite grains from the pit sample at Los Colorados (Table 2A.2; Fig. 2A.8A). The concentrations of REEs in apatite at Los Colorados are, on average, lower than those reported for apatite grains from IOA deposits in the Kiruna, Great Bear, Grängesberg and Bafq districts, and the Pea Ridge IOA deposit (Harlov et al. 2002a; Torab and Lehmann 2007; Jonsson et al. 2016; Mao et al. 2016; Harlov et al. 2016).

The trace element compositions of the F-rich domains (cores) and Cl-rich domains (rims) of apatite from Los Colorados are compared in Figs. 2A.9 and 10 with the global compilation of apatite trace element data reported by Piccoli and Candela (2002). The Mn-Na-Ca compositions of apatite cores from Los Colorados overlap apatite from mafic (Fig. 2.A9-A), and a subset of the apatite compositions from felsic rocks, although the spread of compositions for felsic rocks is larger than that for apatite from Los Colorados. The rims of apatite from Los Colorados also overlap the compositions of apatite from mafic and felsic rocks in Mn-Na-Ca space (Fig. 2A.9B). Similarly, the concentrations of Si, S, and P in apatite cores and rims from Los Colorados overlap apatite from felsic rocks (Fig. 2A.10).

2.6.4 Formation of REE-phosphate ([REE]PO_4) AND $ThSiO_4$ inclusions in apatite

At Los Colorados, monazite inclusions are present within apatite at the boundary of F-rich and Cl-rich domains, whereas $ThSiO_4$ inclusions are observed on grain boundaries of apatite and actinolite. These observations are consistent with studies of IOA deposits in the Durango, Kiruna, and Bafq districts (Harlov et al. 2002a; Torab and Lehman 2007; Bonyadi et al. 2011), the Carmen IOA deposit in Chile (Konecke et al. 2017a), and the Olympic Dam IOCG deposit, Australia (Krneta et al. 2016). Knipping et al (2015a, b) reported that the hydrothermal fluid at Los Colorados was a Na-K-Fe-rich brine, which based on the experimental results of Harlov and Förster (2003) eliminates coupled dissolution–reprecipitation reactions as a plausible explanation for the growth of monazite and $ThSiO_4$ inclusions in apatite. We suggest that monazite and $ThSiO_4$ inclusions formed as a result of local supersaturation of the fluid, and that nucleation of monazite and $ThSiO_4$ on grain boundaries that were overgrown by Cl-enriched apatite that grew from the cooling hydrothermal fluid.

2.6.5 Genesis of the Los Colorados mineral deposit

The chemistry of apatite from Los Colorados is consistent with the magmatic flotation model proposed by Knipping et al. (2015a) for the Los Colorados IOA deposit. Trace element data (Ti, V, Mn, and Al concentrations) and $\delta^{56}Fe$ and $\delta^{18}O$ stable isotope data for magnetite (Knipping et al. 2015a; Bilenker et al. 2016), as well as δD for magnetite and actinolite from the ore bodies at Los Colorados (Bilenker et al. 2016), trace element data for disseminated pyrite (Reich et al. 2016) trace element data for late-stage, disseminated magnetite in the brecciated diorite and andesite host rocks (Deditius et al. 2018) indicate that the mineralizing fluid at Los Colorados was sourced from a silicate magma of mafic to intermediate composition, and that the chemistry of magnetite and pyrite record growth of these phases from a cooling magmatic-hydrothermal fluid.

The model presented by Knipping et al. (2015a) invokes crystallization of magnetite microlites from an intermediate silicate melt, resulting in magnetite that is enriched in trace elements such as Ti, V, Al, and Mn, consistent with the chemistry of magnetite cores at Los Colorados. During decompression of a magnetite-saturated, volatile-undersaturated silicate magma, if the melt reaches volatile saturation, owing to the decreasing water solubility as a function of decreasing pressure, aqueous bubbles nucleate preferentially on the surface of magnetite crystals (Hurwitz and Navon 1994; Gualda and Ghiorso 2007). Continued degassing results in the formation of a magnetite-fluid suspension, wherein the magnetite crystal chemistry is dictated by partitioning of elements between magnetite and the magmatic-hydrothermal fluid. This results in progressively lower concentrations of trace elements such as Ti, V, Al, and Mn in magnetite, as recorded in magnetite rims at Los Colorados. The presence of halite-saturated fluid inclusions in magnetite from Los Colorados, which, in conjunction with the progressive core-to-rim depletion of fluid-compatible trace elements, is interpreted as evidence that magnetite rims grew from a cooling magmatic-hydrothermal fluid. The magnetite-fluid suspension has a lower bulk density than the surrounding magma and can ascend from the source magma along pre-existing faults that are opened during regional extension (Edmonds 2015; Knipping et al. 2015a).

Igneous apatite microlites are also preferential nucleation sites for a magmatic-hydrothermal fluid that exsolves from a silicate melt during decompression. Hurwitz and Navon (1994) performed experiments to assess nucleation of aqueous fluid from an apatite- and magnetite-bearing silicate melt during decompression from an initial pressure of 150 MPa. They report that for decompression of <10 MPa, only magnetite microlites are wetted by the exsolving volatile phase. However, for decompression >10 MPa, aqueous bubbles nucleated preferentially on apatite as well as magnetite microlites. Considering that apatite is commonly a near-liquidus

phase in silicate magmas (Watson and Capobianco 1981; Boudreau and Kruger 1990; Piccoli and Candela 2002), we suggest that the F-rich domains in apatite at Los Colorados record crystallization of F-rich apatite from a silicate melt. Considering that apatite (3.17 g/cm^3) is less dense than magnetite (5.1 g/cm^3), and that apatite is a modally minor, albeit ubiquitous, phase in IOA deposits, the addition of a small amount of apatite does not change the results presented by Knipping et al. (2015a). Those authors cited experiments by Matveev and Ballhaus (2002) and Mungall et al. (2015) as evidence for flotation of ore minerals by such a process.

We suggest that igneous apatite microlites were enveloped by magmatic-hydrothermal fluid and became part of the fluid suspension that also contained magnetite, which is comparable to the "sweeping" process described by Edmonds et al. (2014). The magmatic-hydrothermal fluid exsolving from the silicate melt is expected to be Cl-rich owing to the strong partitioning of Cl between the silicate melt and aqueous fluid, and likely had a composition dominated by dissolved $FeCl_2$, NaC, KCl and $CaCl_2$ (Webster and Mandeville 2007). The magmatic-hydrothermal fluid would effectively scavenge P, and other fluid-compatible elements (e.g., Mn, Sr, As, LREEs) from the silicate melt, with reported brine/melt partition coefficients for P ranging from 2 to 6 (Zajacz et al. 2008). As the suspension coalesces, regional extension causes a sudden destabilization of the magma body, which results in rapid transport (5–20 m/s) of the suspension through hydraulic fractures in a ductile crystal-mush regime (Hersum et al. 2005; Hautmann et al. 2014). During ascent of the fluid suspension, apatite continues to grow from the Cl-rich magmatic-hydrothermal fluid owing to decreases in pressure and temperature. This explains the statistically distinct F-rich and Cl-rich domains within apatite from Los Colorados. The monazite and thorite/ huttonite inclusions \likely formed via supersaturation on grain boundaries as the Cl-rich apatite grew from the cooling ore fluid.

2.7 Conclusions

Apatite grains from the Los Colorados IOA deposit contain statistically distinct F-rich and Cl-rich domains that are not the result of crystallization from a single fluid. The F-rich domains have halogen and trace element compositions consistent with apatite that grew from a mafic to intermediate silicate melt, whereas the Cl-rich domains have halogen and trace element compositions consistent with apatite growth in the presence of a magmatic-hydrothermal fluid. Apatite that grew in the hotter part of the mineralizing system is systematically enriched in trace elements compared to apatite from the cooler part of the system. The abundances of Cl and other fluid compatible elements (e.g., Sr, Mn, As) are enriched in apatite rims. Apatite contains inclusions of monazite and $ThSiO_4$, which likely formed by supersaturation on grain boundaries during mineralization. The chemistry of apatite from Los Colorados is consistent with a genetic model wherein the F-rich domains of apatite record growth of apatite microlites from a silicate melt, and the Cl-rich domains record growth of apatite from a magmatic-hydrothermal fluid during ascent of a magnetite-apatite-fluid suspension through the Los Colorados fault.

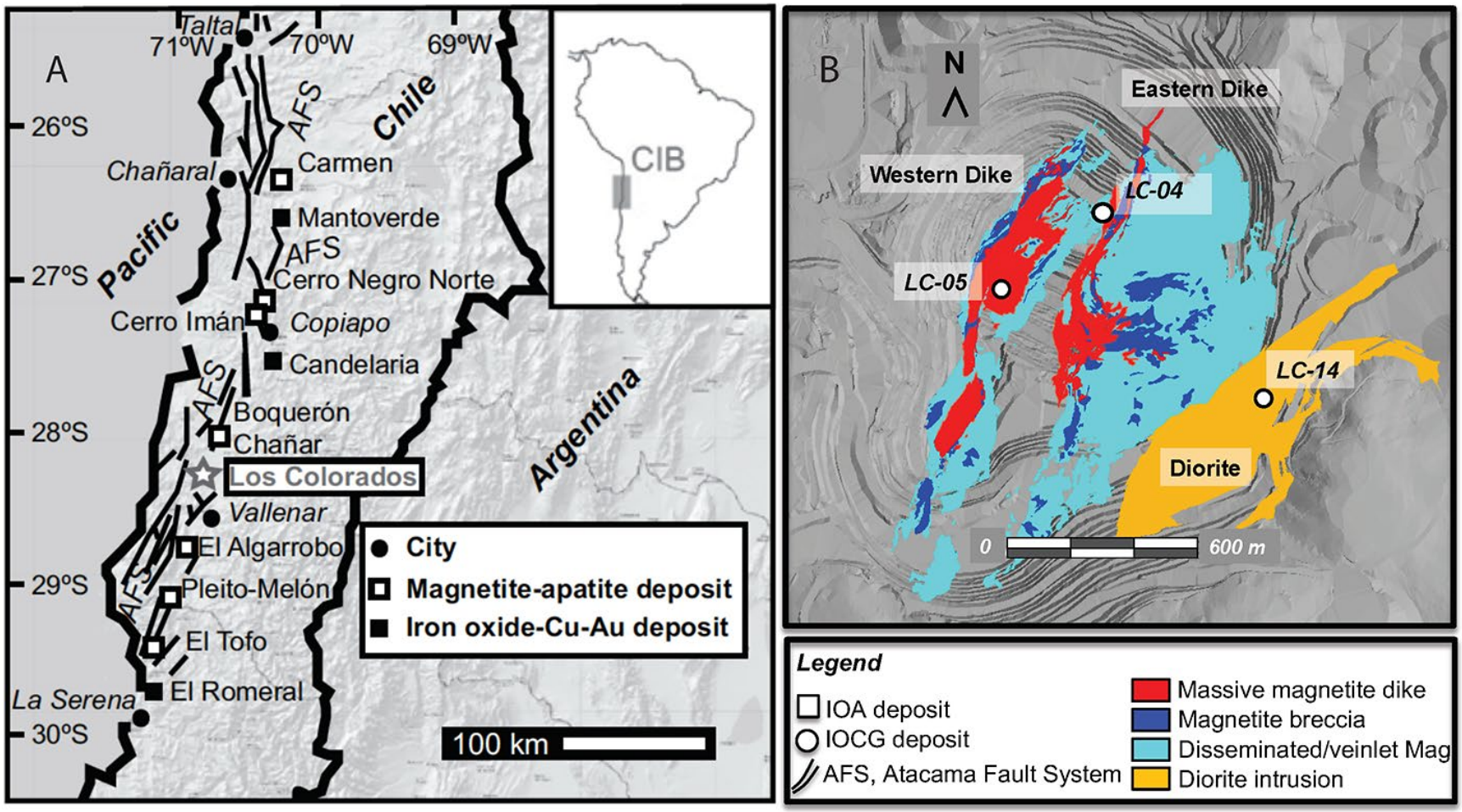

Figure 2.1: (A) Location of the Los Colorados iron oxide – apatite (IOA) deposit and the Chilean Iron Belt (inset). The major structures of the Atacama Fault System are highlighted in the map (modified from Knipping et al. 2015a). (B) Plan view of the Los Colorados IOA deposit (modified from Reich et al. 2016).

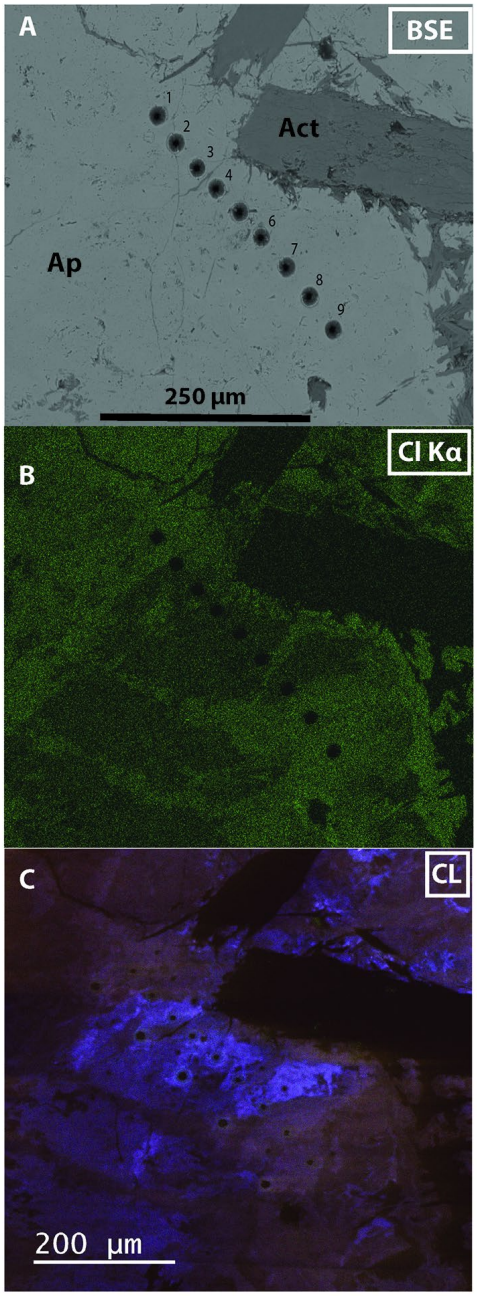

Figure 2.2: (A) Backscattered electron (BSE) image of a representative apatite grain from drill core LC-04 (sample 04-99.5B in Knipping et al., 2015a, b) taken from the western massive magnetite ore body. The spots identified on the grain indicate the electron probe micro-analyzer (EPMA) and laser ablation inductively coupled plasma mass spectrometry (LA-ICP-MS) analysis locations. (B) EDS map of the distribution of Cl in the apatite grain reveals variations in the distribution of Cl. (C) Cathodoluminescence (CL) images of the same apatite grain reveal variations in luminescence in different regions of the grain. (Comparison of (B) and (C) indicates that the areas of bright luminescence correspond to the areas of low Cl concentration. Note that the image in B is a false color image.

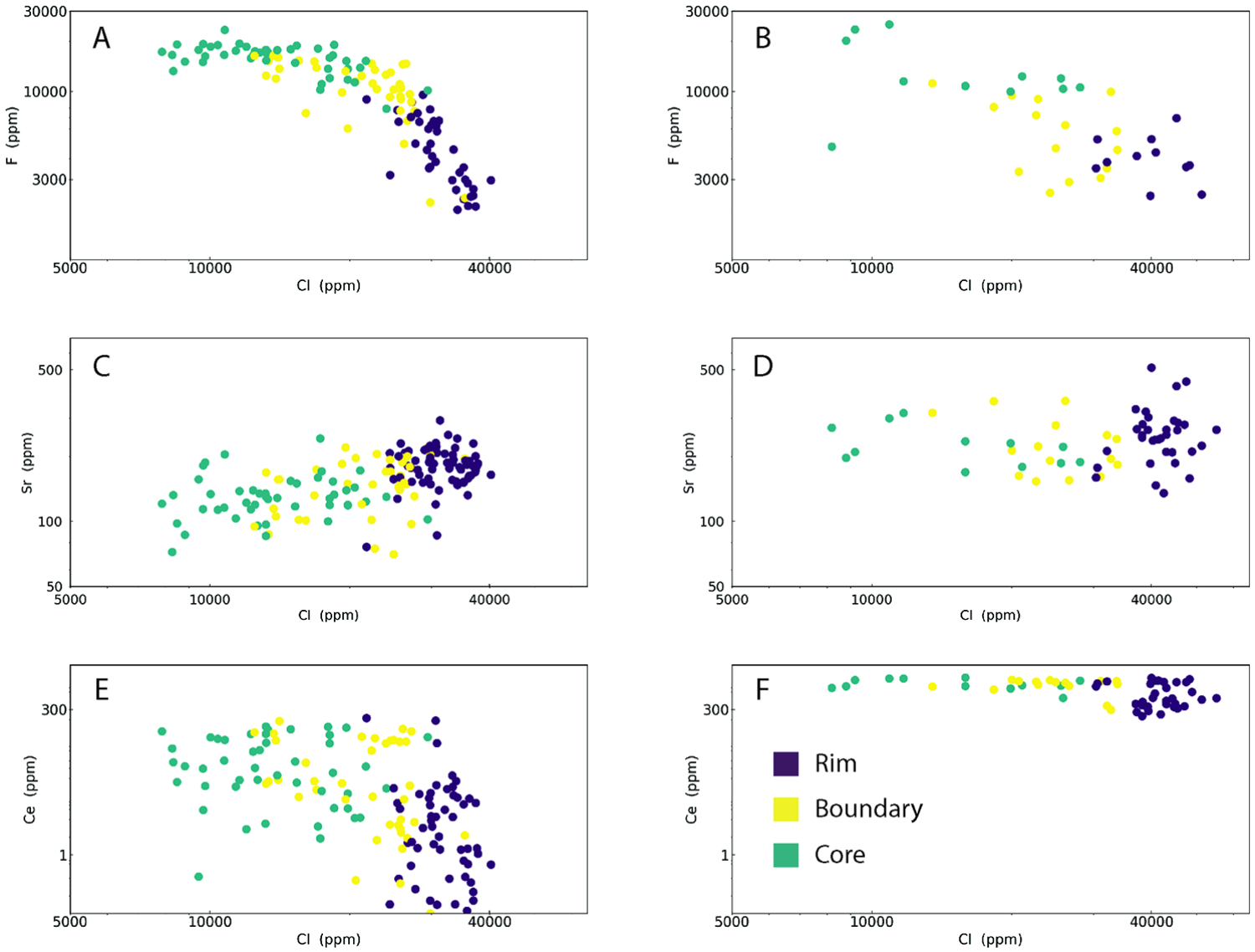

Figure 2.3: The concentrations of F, Sr and Ce versus the concentration of Cl for apatite from the pit (A, C, E) and drill core B (B, D, F) samples, respectively. Each spot represents an individual EPMA and LA-ICP-MS analysis.

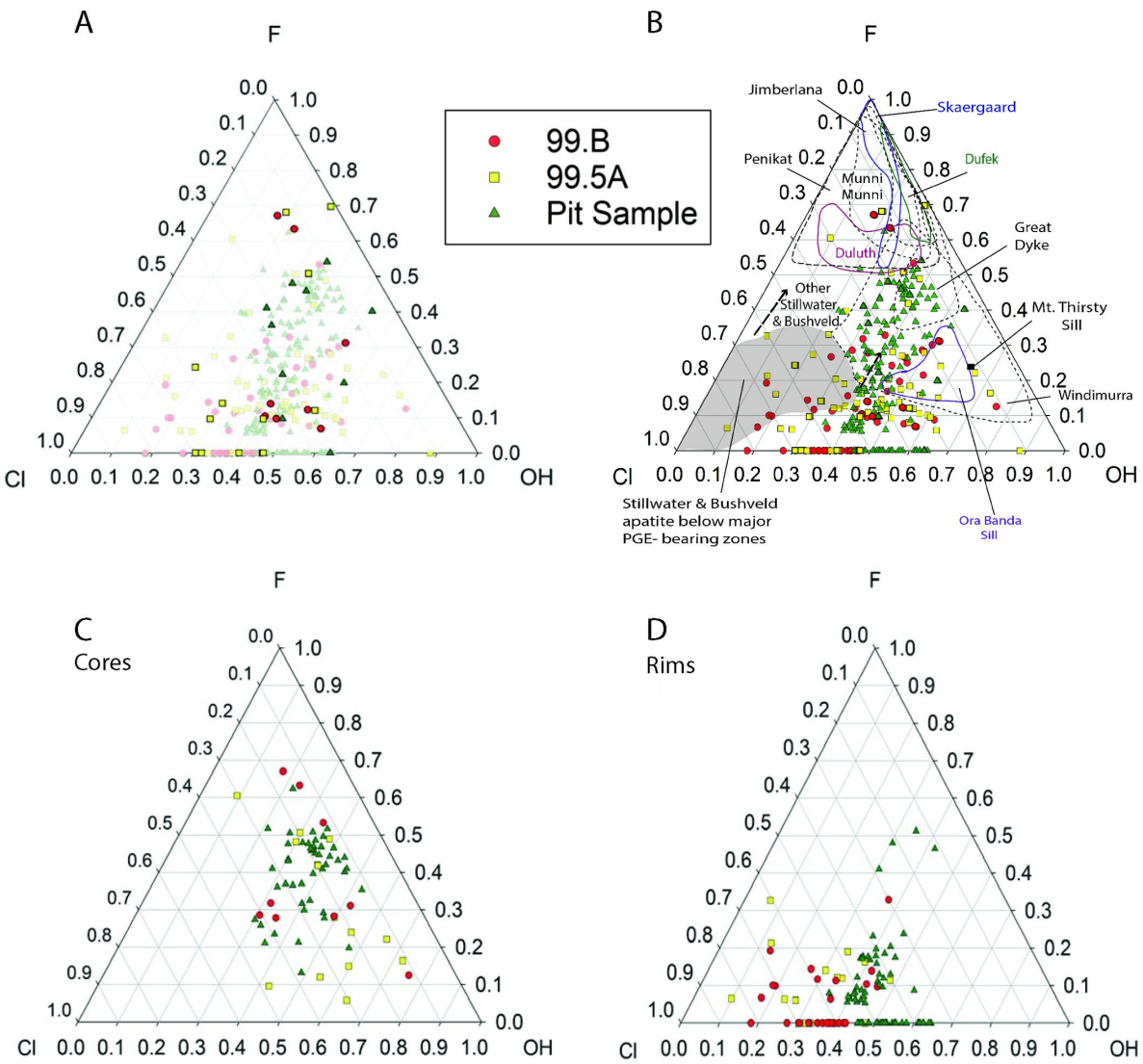

Figure 2.4: (A) Ternary plot showing significant intracrystalline variability of F, Cl, and calculated OH based on individual spot analyses among all apatite grains analyzed from Los Colorados. The figure contains two layers of data. The first layer contains data for all apatite grains analyzed, while the second layer, contains data for representative apatite grains from the three samples (those presented in Figs. 2, and Figs. 2.A1, and 2). (B) Measured concentrations of F, Cl, and calculated OH are compared with the fields representing the range of compositions for apatite grains from mafic layered intrusions worldwide (fields after Boudreau et al. 1995). (C) and (D) are ternary plots comparing the distribution of F, Cl, and OH in the cores and rims, respectively, of all apatite grains from Los Colorados. It is evident from the plots that spot analyses plot in different fields. Further, the composition of the cores and rims of the apatite grains are resolved in F-Cl-OH space. For example, analyses of cores from apatite grains from all three samples plot in regions where $X_{Cl} < 0.5$, such as Munni Munni and Duluth, while analyses from apatite grain rims plot in Cl rich regions such as the 'Stillwater & Bushveld apatite below major PGE - bearing zones' and on the Cl-OH join of the ternaries.

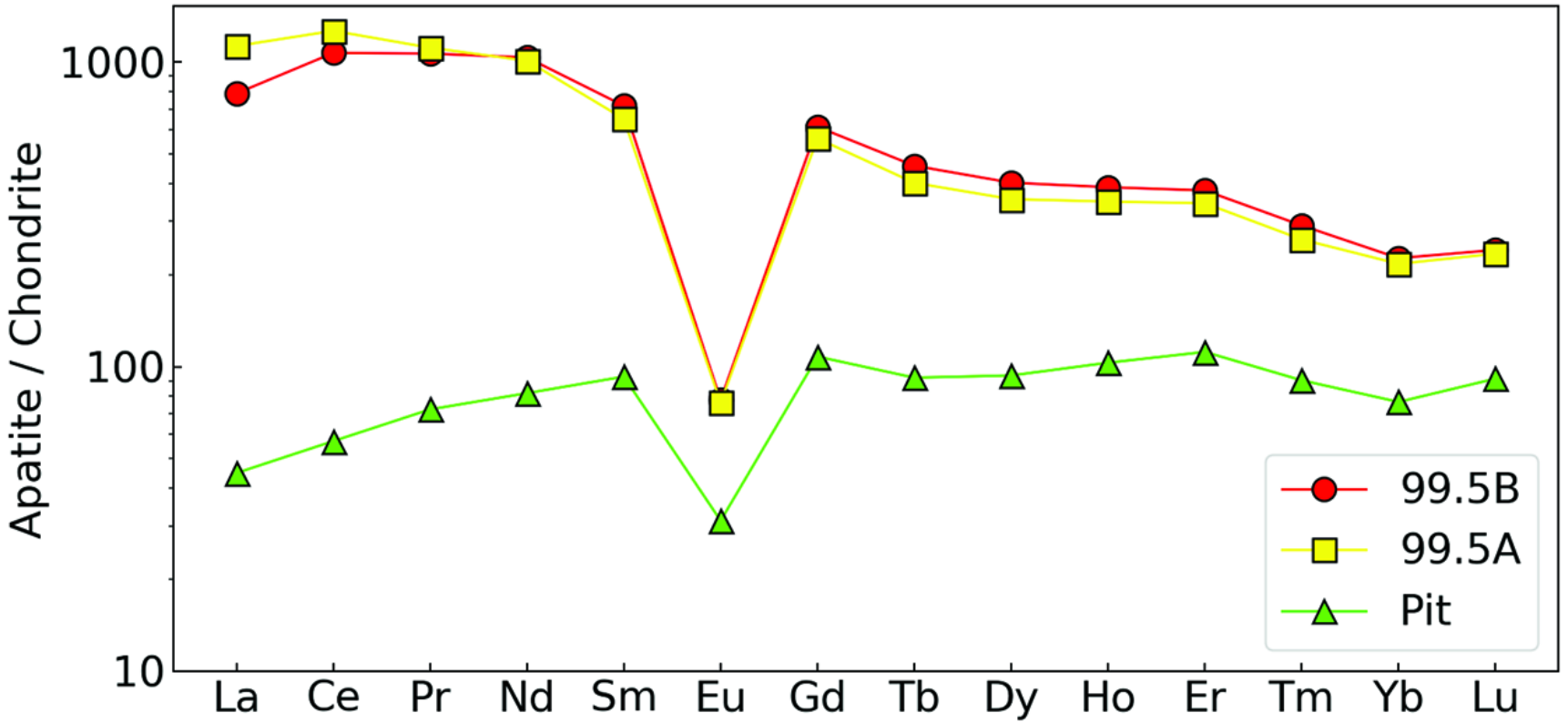

Figure **2.5:** Average chondrite normalized (Sun and McDonough 1989) rare earth element (REE) patterns for all apatite grains from Los Colorados.

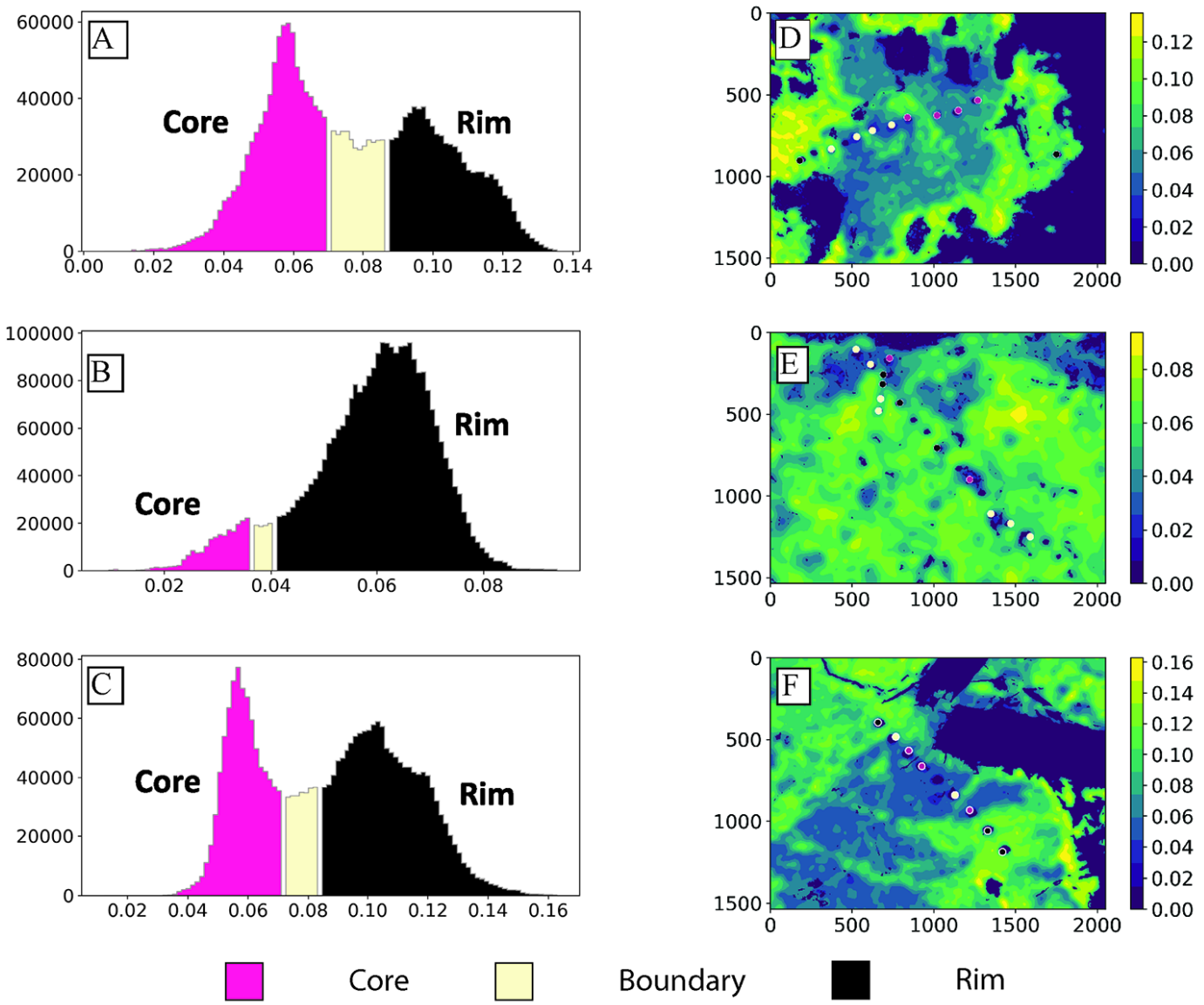

Figure 2.6: (A, B, C) Histograms of measured Cl intensity in representative apatite grains from each sample show two distinct populations. The x-axis represents pixel intensity and the y-axis represents the absolute number of pixels. The histograms depict the

pixel intensity distributions in the corresponding smoothed EDS Cl Kα maps (D, E, F). Color in the maps corresponds to Cl abundance. The bimodal Cl intensity distributions indicate the presence of Cl-rich (rim) and Cl-poor (core) populations, which are seen in the chemical maps to correspond to spatially coherent domains, separated by a boundary zone with intermediate values. The dots on the smoothed Cl Kα maps indicate the location of EPMA and LA-ICP-MS spot analyses. See Appendix 2.1 for details.

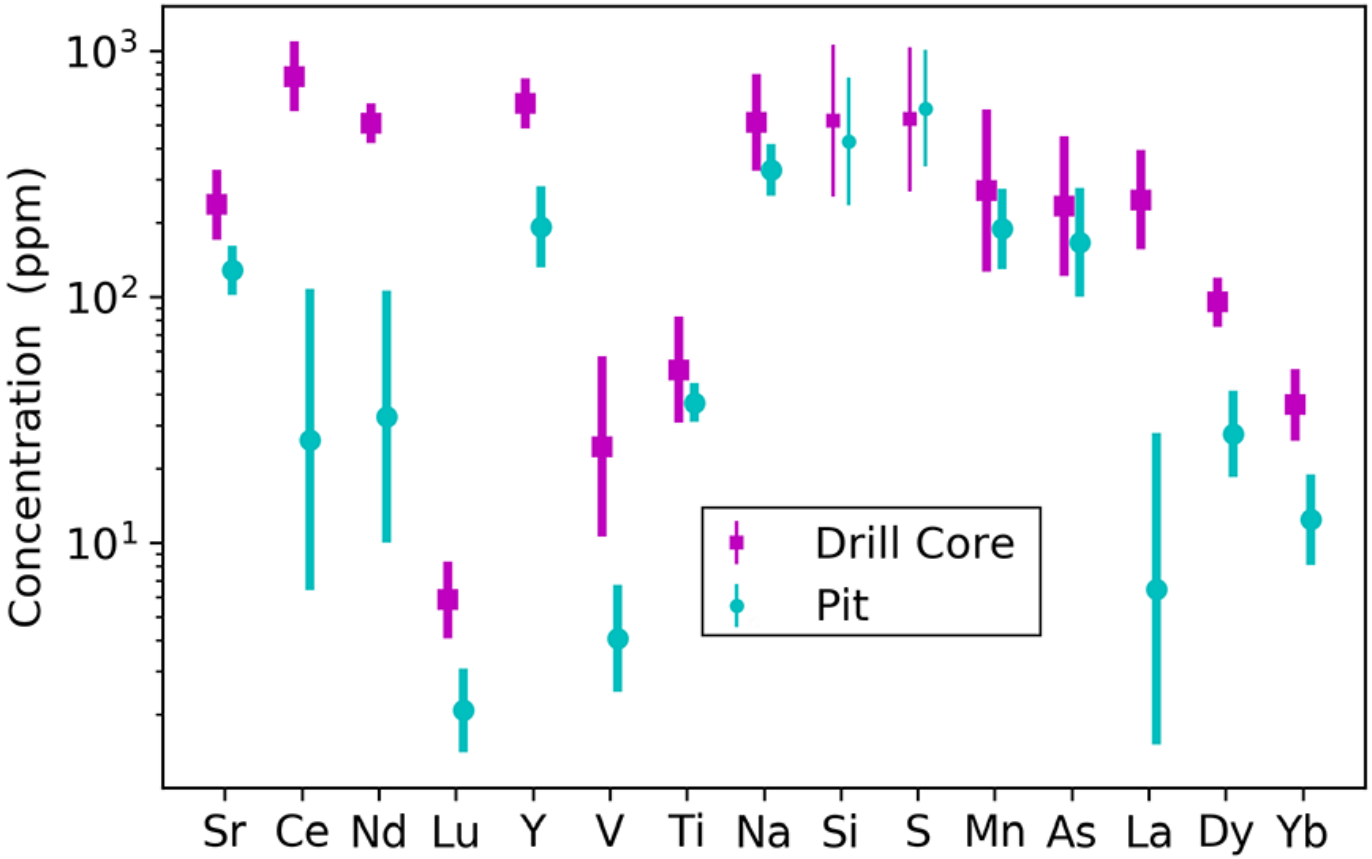

Figure 2.7: Comparison of minor and trace element abundances in the cores of apatite from the drill core and pit samples. The concentration distributions are statistically distinguishable ($p << 0.05$, shown in bold) for nearly every element reported, except for S and Si. The statistically significant difference in elemental concentrations in the cores of apatite from the pit and drill core samples most plausibly reflects differences in the temperature of the fluids from which these apatite grew or reequilibrated. The enrichment of elements in the cores of apatite from the drill core sample obtained from the massive magnetite ore body is consistent with growth of these apatite grains from a higher temperature fluid relative to the (disseminated) apatite grains in the brecciated host rock from which the pit sample was collected.

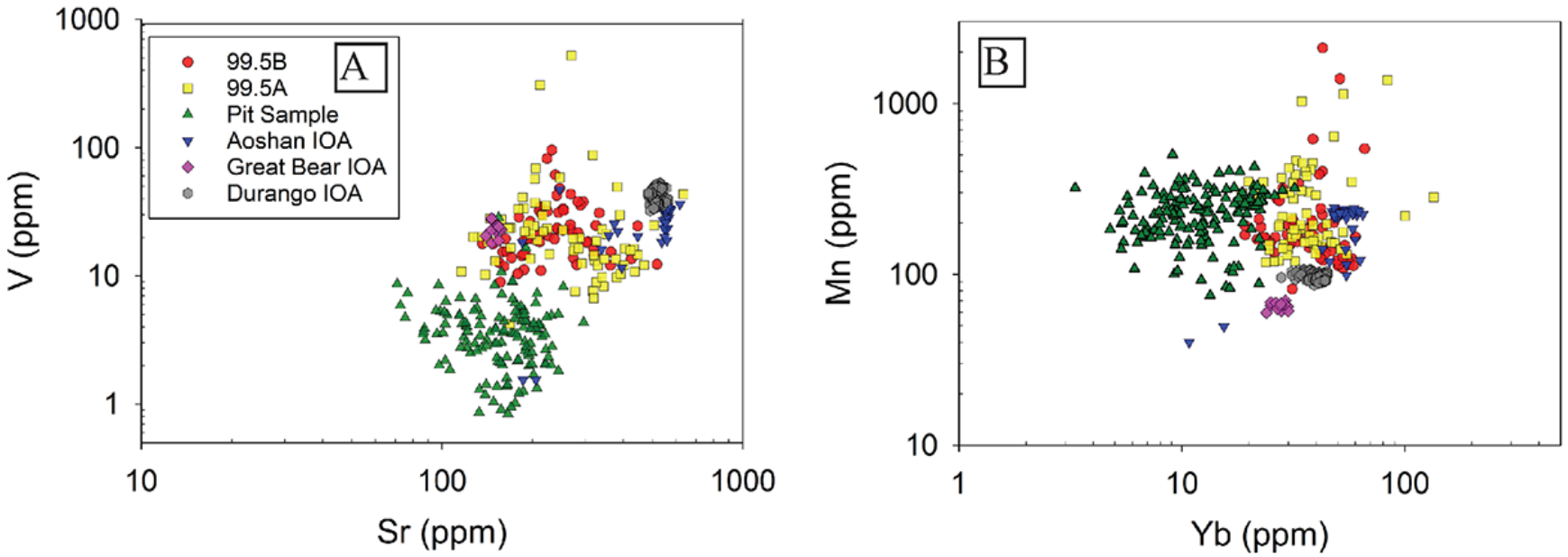

Figure 2.8: The concentrations of (A) V vs. Sr, and (B) Mn vs. Yb in apatite from Los Colorados and other IOA deposits (Aoshan, Great Bear, and Durango). Data for comparison taken from Mao et al. 2016.

2.8 References

Barra F, Reich M, Selby D, Rojas P, Simon AC, Salazar E, Palma G (2017) Unraveling the origin of the Andean IOCG clan: A Re-Os approach. Ore Geol Rev 81:62-78.

Barton MD (2013) Iron Oxide(-Cu-Au-REE-P-Ag-U-Co) Systems. In: Turekian KK, Holland HD (ed) Treatise on Geochemistry, 2nd edn. Elsevier, Amsterdam: 515 - 541.

Barton MD, Johnson DA (1996) Evaporitic-source model for igneous-related Fe oxide–(REE-Cu-Au-U) mineralization. Geology 24(3):259-62.

Barton MD and Johnson DA (2004) Footprints of Fe-oxide(-Cu-Au) systems. SEG 2004: Predictive Mineral Discovery Under Cover. Centre for Global Metallogeny, Spec. Pub. 33, The University of Western Australia: 112-116.

Belousova EA, Griffin WL, O'Reilly SY, Fisher NI (2002) Apatite as an indicator mineral for mineral exploration: Trace-element compositions and their relationship to host rock type. J Geochemical Explor 76:45–69.

Betkowski WB, Harlov D and Rakovan JF (2016) Hydrothermal mineral replacement reactions for an apatite-monazite assemblage in alkali-rich fluids at 300-600 C and 100 MPa. Am Mineral 101:2620-2637.

Bilenker LD, Simon AC, Reich M, Lundstrom CC, Gajos N, Bindeman I, Barra F, Munizaga R (2016) Fe-O stable isotope pairs elucidate a high-temperature origin of Chilean iron oxide-apatite deposits. Geochim Cosmochim Ac 177:94–104.

Bodnar RJ, Vityk MO (1994) Interpretation of microthermometric data for H2O-NaCl fluid inclusions. In De Vivo B and Frezzotti ML (ed) Fluid inclusions in minerals, methods and Applications, Virginia Tech, Virginia: 117-30.

Bonyadi Z, Davidson GJ, Mehrabi B, Meffre S, Ghazban F (2011) Significance of apatite REE depletion and monazite inclusions in the brecciated Se-Chahun iron oxide apatite deposit, Bafq district, Iran: Insights from paragenesis and geochemistry. Chem Geol 281:253–269.

Boudreau AE (1993) Chlorine as an exploration guide for the platinum-group elements in layered intrusions. J Geochem Explor 48:21–37.

Boudreau AE, Kruger FJ (1990) Variation in the composition of apatite through the Merensky cyclic unit in the western Bushveld Complex. Econ Geol 85: 737–745.

Boudreau AE, Love C, Prendergast MD (1995) Halogen geochemistry of the Great Dyke Zimbabwe. Contrib Mineral Petr V:289-300.doi:10.1007/s004100050128

Boudreau AE, Mathez EA, Mccallum IS (1986) Halogen geochemistry of the stillwater and bushveld complexes: Evidence for transport of the platinum-group elements by Cl-rich fluids. J Petrol 27:967–986.

Boudreau AE, Simon AC (2007) Crystallization and degassing in the basement sill, McMurdo Dry Valleys, Antarctica. J Petrol 48(7):1369-1386.

Bouzari F, Hart CJ, Bissig R, Barker S (2016) Hydrothermal alteration revealed by apatite luminescence and chemistry: A potential indicator mineral for exploring covered porphyry copper deposits. Econ Geol 111:1397–1410.

Broughm SG, Hanchar JM, Tornos F, Westhues A, Attersley S (2017) Mineral chemistry of magnetite from magnetite-apatite mineralization and their host rocks: examples from Kiruna, Sweden, and El Laco, Chile. Miner Deposita 52:1223. doi.10.1007/s00126-017-0718-8

Brown GM, Peckett A (1977) Fluorapatites from Skaergaard Intrusion, East Greenland. Mineral Mag 41:227–232.
Compañía Minera del Pacífico (2013) Presentation NEVASA www.cap.cl/wp/content/uploads/2013/09/cap_presentacion_nevasa_septiembre_2013.p Accessed 10 December 2015.
Dare SAS, Barnes SJ, Beaudoin G (2014) Did the massive magnetite "lava flows" of El Laco (Chile) form by magmatic or hydrothermal processes? New constraints from magnetite composition by LA-ICP-MS. Miner Depos 50:607–617. doi: 0.1007/s00126-014-0560-1
Dare SA, Barnes SJ, Beaudoin G, Méric J, Boutroy E, Potvin-Doucet C (2014) Trace elements in magnetite as petrogenetic indicators. Miner Deposita 49:785–796.
Davidson GJ, Large RR (1994) Gold metallogeny and the copper-gold association of the Australian Proterozoic. Miner Deposita 29(3):208-23.
Deditius A, Reich M, Simon AC, Suvorova A, Knipping J, Roberts MP, Rubanov S, Dodd A, Saunders, M. (2018) Nanogeochemistry of hydrothermal magnetite. Contrib Min Petrol 173(6): 46
de Jong G, Rotherham J, Phillips GN, Williams PJ (1998) Mobility of rare-earth elements and copper during shear-zone-related retrograde metamorphism. Geol Mijnbouw 76(4):311-9.
Edmonds M (2015). Flotation of magmatic minerals. Geology, 43(7):655-656.
Edmonds M, Brett A, Herd RA, Humphreys MCS, Woods A (2014) Magnetite-bubble aggregates at mixing interfaces in andesite magma bodies: Geol Soc London, Spc Pub 410(1):95- 121.
Frietsch R (1978) On the magmatic origin of iron ores of the Kiruna type. Econ. Geol 73: 478–485.
Frietsch R, Perdahl JA (1995) Rare earth elements in apatite and magnetite in Kiruna-type iron ores and some other iron ore types. Ore Geol Rev 9:489–510.
Götze J (2012) Application of cathodoluminescence microscopy and spectroscopy in geosciences. Microsc Microanal 18:1270–1284.
Götze J, Plötze M, Habermann D (2001) Origin, spectral characteristics and practical applications of the cathodoluminescence (CL) of quartz - A review. Mineral Petrol 71: 225–250.
Gros K, Słaby E, Förster HJ, Michalak PP, Munnik F, Götze J, Rhede D (2016) Visualization of trace-element zoning in fluorapatite using BSE and CL imaging, and EPMA and μPIXE/μPIGE mapping. Miner Petrol. 110(6):809-821. doi:10.1007/s00710-016-0452-4
Groves DI, Bierlein FP, Meinert LD, Hitzman MW (2010) Iron oxide copper-gold (IOCG) deposits through earth history: Implications for origin, lithospheric setting, and distinction from other epigenetic iron oxide deposits. Econ Geol 105:641–654.
Gualda GAR, Ghiorso MS (2007) Magnetite scavenging and the buoyancy of bubbles in magmas. Part 2: Energetics of crystal-bubble attachment in magmas: Contrib Min Petrol 154:479–490
Guillong M, Meier DL, Allan MM, Heinrich CA, Yardley BWD (2008) Appendix A6: SILLS: A Matlab-based program for the reduction of laser ablation ICP-MS data of homogeneous materials and inclusions. Mineralogical Association of Canada Short Course 40, pp. 328–333.
Harlov DE (2015) Apatite: A Fingerprint for Metasomatic Processes. Elem 11:171–176.
Harlov DE, Andersson UB, Förster HJ, Nyström JO, Dulski P, Broman C (2002a) Apatite – monazite relations in the Kiirunavaara magnetite – apatite ore, northern Sweden. Chem Geol 191:47–72.

Harlov DE, Förster HJ (2003) Fluid-induced nucleation of (Y-REE)-phosphate minerals within apatite: Nature and experiment. Part II. Fluorapatite. Am Mineral 88:1209–1229.
Harlov DE, Meighan CJ, Kerr ID, Samson IM (2016) Mineralogy, chemistry, and fluid-aided evolution of the Pea Ridge Fe oxide-(Y+ REE) deposit, southeast Missouri, USA. Econ Geol 111(8): 1963-1984.
Hautmann S, Witham F, Christopher T, Cole P, Linde AT, Sacks S, Sparks SJ (2014) Strain field analysis on Montserrat (W.I.) as tool for assessing permeable flow paths in the magmatic system of Soufriere Hills Volcano. Geoch. Geophys. Geosys. 15:676–690.
Hersum T, Hilpert M, Marsh B (2005) Permeability and melt flow in simulated and natural partially molten basaltic magmas. Earth Planet Sci Lett 237(3):798-814.
Hitzman MW, Oreskes N, Einaudi MT (1992) Geological characteristics and tectonic setting of proterozoic iron oxide (Cu-U-Au-REE) deposits. Precambrian Res 58: 241–287.
Hofstra AH, Meighan CJ, Song X, Samson I, Marsh EE, Lowers HA, Emsbo P, Hunt AG (2016) Mineral thermometry and fluid inclusion studies of the Pea Ridge iron oxide-apatite–rare earth element deposit, Mesoproterozoic St. Francois Mountains terrane, southeast Missouri, USA. Econ Geol 111:1985–2016.
Hughes, J.M., Rakovan, J.F. (2015) Structurally robust, chemically diverse: apatite and apatite supergroup minerals. Elements 11:165–170.
Hurwitz S, Navon O (1994) Bubble nucleation in rhyolitic melts: Experiments at high pressure, temperature, and water content. Earth Planet Sci Lett 122(3-4):267-80.
Jochum KP, Weis U, Stoll B, Kuzmin D, Yang Q, Raczek I, Jacob DE, Stracke A, Birbaum K, Frick DA, Günther D (2011) Determination of reference values for NIST SRM 610-617 glasses following ISO guidelines. Geostand Geoanal Res 35:397–429.
Jonsson E, Harlov DE, MaJka J, Högdahl K, Persson-Nilsson K (2016) Fluorapatite-monazite allanite relations in the Grängesberg apatite-iron oxide ore district, Bergslagen, Sweden. American Mineralogist, 101(8): 1769-1782.
Jonsson E, Troll VR, Högdahl K, Harris C, Weis F, Nilsson KP, Skelton A (2013) Magmatic origin of giant 'Kiruna-type' apatite-iron-oxide ores in central Sweden. Sci Rep 3:1644.
Kempe U, Götze J (2002) Cathodoluminescence (CL) behaviour and crystal chemistry of apatite from rare-metal deposits. Mineral Mag 66:151–172.
Ketcham RA (2015) Technical Note: Calculation of stoichiometry from EMP data for apatite and other phases with mixing on monovalent anion sites. Am Mineral 100:1620–1623. doi:10.2138/am-2015-5171
Knipping JL, Bilenker LD, Simon AC, Reich M, Barra F, Deditius AP, Lundstrom C, Bindeman I, Munizaga R (2015a) Giant Kiruna-type deposits form by efficient flotation of magmatic magnetite suspensions. Geology 43:591–594.
Knipping JL, Bilenker LD, Simon AC, Reich M, Barra F, Deditius AP, Wälle M, Heinrich CA, Holtz F, Munizaga R. (2015b) Trace elements in magnetite from massive iron oxide-apatite deposits indicate a combined formation by igneous and magmatic-hydrothermal processes. Geochim Cosmochim Acta 171: 15–38.
Konecke BA, Fiege A, Simon AC, Parat F, Stechern A (2017a) Co-variability of S6+, S4+ and S2-in apatite as a function of oxidation state: Implications for a new oxybarometer. Am Mineral 102(3):548-557. doi.10.2138/am-2017-5907
Konecke B, Fiege A, Simon AC, Holtz F (2017b) Cryptic metasomatism during late-stage lunar magmatism implicated by sulfur in apatite. Geology 45:739-742.

Krneta S, Ciobanu CL, Cook NJ, Ehrig K, Kontonikas-Charos A (2016) Apatite at Olympic Dam, South Australia: A petrogenetic tool. Lithos 262:470–485.
Matveev S, Ballhaus C (2002) Role of water in the origin of podiform chromitite deposits. Earth Planet Sci Lett 203: 235–243.
Mao M, Rukhlov AS, Rowins SM, Spence J, Coogan LA (2016) Apatite trace element compositions: A robust new tool for mineral exploration. Econ Geol 111:187–1222.
Mungall JE, Brenan JM, Godel B, Barnes SJ, Gaillard F (2015) Transport of metals and sulphur in magmas by flotation of sulphide melt on vapour bubbles. Nat Geosci 8(3):216-219.
Nadoll P, Angerer T, Mauk J, French D, Walshe J (2014) The chemistry of hydrothermal magnetite: a review. Ore Geol Rev 61:1-32.
Naslund HR, Henríquez F, Nyström JO, Vivallo W, Dobbs FM (2002) Magmatic iron ores and associated mineralization: examples from the Chilean High Andes and Coastal Cordillera. In: Porter TM (ed) Hydrothermal iron oxide copper-gold and related deposits: A global perspective, 2nd edn, PGC Publishing, Adelaide: 207-226.
Nyström JO, Henríquez F (1994) Magmatic features of iron ores of the Kiruna type in Chile and Sweden: ore textures and magnetite geochemistry. Econ Geol 89: 820–839.
Oyarzún J, Frutos J (1984) Tectonic and petrological frame of the Cretaceous iron deposits of North Chile. Mining Geol 34:21-31.
Parat F, Holtz F, Streck MJ (2011) Sulfur-bearing Magmatic Accessory Minerals. Rev Mineral Geochemistry 73:285–314. doi: 10.2138/rmg.2011.73.10
Pettke T, Oberli F, Audetat A, Guillong M, Simon A C, Hanley JJ, Klemm LM (2012) Recent developments in element concentration and isotope ratio analysis of individual fluid inclusions by laser ablation single and multiple collector ICP-MS. Ore Geol Rev 44:10–38.
Piccoli PM, Candela PA (2002) Apatite in Igneous system. Rev Mineral Geochem 48(1):255–292.
Pichon R (1981) Contribution a l'étude de la ceinture du fer du Chili: Les gisements de Bandurrias (Prov. d'Atacama) et Los Colorados norte. (Prov. de Huasco). Dissertation, University of Paris.
Pincheira M, Thiele R, Fontbote L (1990) Tectonic transpression along the southern segment of the Atacama Fault-Zone, Chile. In Proceedings, Symposium International "Géodynamique Andine", Grenoble: 15-17.
Pirajno F, Bagas L (2008) A review of Australia's Proterozoic mineral systems and genetic models. Precambrian Res 166(1):54-80.
Pyle JM, Spear FS, Wark DA (2002) Electron microprobe analysis of REE in apatite, monazite and xenotime: protocols and pitfalls. Rev Mineral Geochem 48(1):337-362.
Reed MJ, Candela PA, Piccoli PM (2000) The distribution of rare earth elements between monzogranitic melt and the aqueous volatile phase in experimental investigations at 200 MPa and 800 °C. Contrib Min Petr 140:251-262.
Reich M, Simon AC, Deditius A, Barra F, Chryssoulis S, Lagas G, Tardani D, Knipping J, Bilenker L, Sánchez-Alfaro P, Roberts MP (2016) Trace element signature of pyrite from the Los Colorados iron oxide-apatite (IOA) deposit, Chile: A missing link between Andean IOA and iron oxide copper-gold systems? Econ Geol 111:743–761.
Rhodes AL, Oreskes N (1999) Oxygen isotope composition of magnetite deposits at El Laco, Chile: evidence of formation from isotopically heavy fluids. Soc Econ Geol Spc Pub 7:333-351.

Rhodes AL, Oreskes N, Sheets S (1999) Geology and rare earth element geochemistry of magnetite deposits at El Laco, Chile. Soc Econ Geol Spc Pub 7:299-332.
Schettler G, Gottschalk M, Harlov DE (2011) A new semi-micro wet chemical method for apatite analysis and its application to the crystal chemistry of fluorapatite-chlorapatite solid solutions. Am Mineral 96:138–152.
Sillitoe RH (2003) Iron oxide-copper-gold deposits: An Andean view. Miner Deposita 38:787–812.
Sillitoe RH, Burrows DR (2002) New field evidence bearing on the origin of the El Laco magnetite deposit, northern Chile. Econ Geol 97(5):1101-1109.
Simon AC, Pettke T, Candela PA, Piccoli PM, Heinrich C (2007) The partitioning behavior of As and Au in a S-free and S-bearing magmatic systems. Geochim Cosmochim Ac 71:1764-1782.
Simon AC, Knipping J, Reich M, Barra F, Deditius A, Bilenker L, Childress T (2018) Kiruna - Type Iron Oxide-Apatite (IOA) and Iron Oxide Copper-Gold (IOCG) Deposits Form by a Combination of Igneous and Magmatic-Hydrothermal Processes: Evidence from the Chilean Iron Belt. SEG Special Publications No. 21. pp. 89-114.
Streck MJ, Dilles JH (1998) Sulfur evolution of oxidized arc magmas as recorded in apatite from a porphyry copper batholith. Geology 26:523–526. doi: .1130/0091-7613(1998)026<0523:SEOOAM>2.3.CO
Sun S, McDonough WF (1989) Chemical and isotopic systematics of oceanic basalts: implications for mantle composition and processes. Geol Soc London, Spc Pub 42: 313–345.
Tornos F, Velasco F, Hanchar JM (2016) Iron-rich melts, magmatic magnetite, and superheated hydrothermal systems: The El Laco deposit, Chile. Geology 44:427–430.
Torab FM, Lehmann B (2007) Magnetite-apatite deposits of the Bafq district, Central Iran: apatite geochemistry and monazite geochronology. Mineral Mag 71:347–363.
Treloar PJ, Colley H (1996) Variation in F and Cl contents in apatites from magnetite-apatite ores in northern Chile, and their ore-genetic implications. Mineral Mag 60:285–301.
Velasco F, Tornos F, Hanchar JM (2016) Immiscible iron-and silica-rich melts and magnetite geochemistry at the El Laco volcano (northern Chile): Evidence for a magmatic origin for the magnetite deposits. Ore Geol Rev 79:346-366.
Watson EB, Capobianco CJ (1981) Phosphorus and the rare earth elements in felsic magmas: an assessment of the role of apatite. Geochim Cosmochim Ac 45:2349-2358.
Waychunas GA (2002) Apatite Luminescence. Rev Mineral Geochem 48:701–742.
Webster JD, Goldoff BA, Flesch RN, Nadeau PA, Silbert ZW (2017) Hydroxyl, Cl, and F partitioning between high-silica rhyolitic melts-apatite-fluid (s) at 50–200 MPa and 700–1000 C. Am Mineral 102(1): 61-74.
Webster JD, Piccoli PM (2015) Magmatic Apatite: A Powerful, Yet Deceptive, Mineral. Elements 11:177–182.
Webster JD, Mandeville CD (2007) Fluid immiscibility in volcanic environments. Rev. Min. Geochem 65:313-362.
Weis F (2013) Oxygen and Iron Isotope Systematics of the Grängesberg Mining District (GMD), Central Sweden. Master's thesis, Uppsala universitet.
Westhues A, Hanchar JM, Whitehouse MJ, Martinsson O (2016) New constraints on the timing of host-rock emplacement, hydrothermal alteration, and iron oxide-apatite mineralization in the Kiruna District, Norrbotten, Sweden. Econ Geol 111(7):1595-618.

Westhues A, Hanchar JM, LeMessurier MJ, Whitehouse MJ (2017a) Evidence for hydrothermal alteration and source regions for the Kiruna iron oxide – apatite ore (northern Sweden) from zircon Hf and O isotopes. Geology 45:571-574.

Westhues A, Hanchar JM, Voisey CR, Whitehouse MJ, Rossman GR, Wirth R (2017b) Tracing the fluid evolution of the Kiruna iron oxide apatite deposits using zircon, monazite, and whole rock trace elements and isotopic studies. Chem Geol 466:303-322.

Williams PJ (1994) Iron mobility during synmetamorphic alteration in the Selwyn Range area, NW Queensland: implications for the origin of ironstone-hosted Au-Cu deposits. Miner Deposita 29(3):250-60.

Williams-Jones AE, Heinrich CA (2005) Vapor transport of metals and the formation of magmatic-hydrothermal ore deposits. Econ Geol 100(7):1287-312.

Young EJ, Myers AT, Munson EL, Conklin NM. Mineralogy and geochemistry of fluorapatite from Cerro de Mercado, Durango, Mexico. US Geological Survey Professional Paper. 650 (D):D84-93 (1969)

Zajacz Z, Halter WE, Pettke T, Guillong M (2008) Determination of fluid/melt partition coefficients by LA-ICPMS analysis of co-existing fluid and silicate melt inclusions: Controls on element partitioning: Geochim Cosmochim Ac 72: 2169–2197.

Chapter 3

The Geochemistry of Magnetite and Apatite From the El Laco Iron Oxide – Apatite Deposit, Chile: Implications for Ore Genesis

Co-authors: J. Tomás Ovalle, Adam C. Simon, Brian A. Konecke,
Fernando Barra, Martin Reich, Mathieu Leisen, Tristan M. Childress

Accepted for publication in *Economic Geology* (2020)

3.1 Abstract

The textures of outcrop and near-surface exposures of the massive magnetite ore bodies (> 90 vol% magnetite) at the Plio-Pleistocene El Laco iron oxide - apatite (IOA) deposit in northern Chile are similar to basaltic lava flows and have compositions that overlap high-temperature and low-temperature hydrothermal magnetite. Existing models — liquid immiscibility and complete metasomatic replacement of andesitic lava flows — attempt to explain the genesis of the ore bodies by entirely igneous or entirely hydrothermal processes. Importantly, those models were developed by studying only near-surface and outcrop samples. Here, we present the results of a comprehensive study of samples from outcrop and drill core that require a new model for the evolution of the El Laco ore deposit. Backscattered electron (BSE) imaging, electron probe microanalysis (EPMA) and laser ablation inductively coupled plasma mass spectrometry (LA-ICP-MS) were used to investigate the textural and compositional variability of magnetite and

apatite from surface and drill core samples in order to obtain a holistic understanding of textures and compositions laterally and vertically through the ore bodies. Magnetite was analyzed from 39 surface samples from five ore bodies (Cristales Grandes, Rodados Negros, San Vicente Alto, Laco Norte, and Laco Sur) and 47 drill core samples from three ore bodies (Laco Norte, Laco Sur, and Extensión Laco Sur). The geochemistry of apatite from 8 surface samples from three ore bodies (Cristales Grandes, Rodados Negros, and Laco Sur) was investigated. Minor and trace element compositions of magnetite in these samples are similar to magnetite from igneous rocks and magmatic-hydrothermal systems. Magnetite grains from deeper zones of the ore bodies contain >1 wt% titanium, as well as ilmenite exsolution lamellae and interstitial ilmenite. The concentrations of trace elements (e.g., Mn, Al, Ti, V) in magnetite from surface outcrops and intermediate to shallow depths, e.g. 0 - 100 m, are consistent with growth from a cooling magmatic-hydrothermal fluid. The ilmenite exsolution lamellae, interstitial ilmenite, and igneous-like trace element concentrations in magnetite from the deeper parts of the ore bodies are consistent with primary crystallization of magnetite–ulvöspinel$_{ss}$ from a silicate melt. The systematic decrease of trace element concentrations in magnetite from intermediate to shallow depths are consistent with progressive growth of magnetite from a cooling magmatic-hydrothermal fluid. Apatite grains from surface outcrops are F-rich (typically >3 wt%) and have compositions that overlap igneous and magmatic-hydrothermal apatite. Magnetite and apatite grains contain mineral inclusions (e.g., monazite and thorite). Magnetite grains commonly meet at triple junctions, which preserves evidence for reequilibration of the ore minerals with hydrothermal fluid during or after mineralization. The data presented here are consistent with genesis of the El Laco ore bodies via shallow emplacement and eruption of magnetite-bearing magmatic-hydrothermal fluid suspensions that were mobilized by decompression-induced collapse of the volcanic edifice.

3.2 Introduction

Kiruna-type iron oxide - apatite (IOA) deposits are an important source of iron, and a potentially important source of rare earth elements (REE). IOA deposits are found in districts globally and are commonly hosted in volcanic and plutonic rocks in convergent margins and rift-related environments (Williams et al., 2005; Groves et al., 2010; Barton, 2014; Simon et al., 2018). El Laco, the youngest known and best-preserved IOA deposit, is one of the most enigmatic ore deposits on Earth. It has perplexed geologists since Park (1961) first described textures of the ore bodies as resembling a magnetite "flow".

Currently, there are three hypotheses for the formation of the El Laco ore bodies. One hypothesis invokes crystallization of magnetite from erupted H_2O-saturated, Cl-, S-, F-rich iron oxide magma that formed as a result of liquid immiscibility (Nyström and Henríquez, 1994; Naslund et al., 2002; Naranjo et al., 2010; Tornos et al., 2016; Velasco et al., 2016; Broughm et al., 2017; Xie et al., 2019). A second hypothesis invokes complete, texture-preserving replacement of andesitic volcanic and hypabyssal rocks by magnetite that precipitated from a hydrothermal fluid (Rhodes and Oreskes, 1995; Rhodes and Oreskes, 1999; Rhodes et al., 1999; Sillitoe and Burrows, 2002; Dare et al., 2015). A third, hybrid hypothesis invokes early crystallization of magnetite microlites from a silicate melt followed by exsolution of a magmatic volatile phase that attaches to the microlites forming a magnetite-rich suspension. This suspension ascends and is later injected into the crust and vented to the surface owing to collapse of the volcanic edifice (Ovalle et al., 2018). This third hypothesized process results in the formation of large breccia bodies at depth and massive magnetite bodies at shallow levels that exhibit igneous and hydrothermal textural and geochemical features, respectively.

In this study, we have attempted to distinguish among these alternative models by evaluating textural and chemical characteristics of magnetite — the primary ore mineral — and apatite — a common gangue mineral — at El Laco. Magnetite samples investigated in the study came from surface outcrops at Cristales Grandes (CG), Rodados Negros (RN), San Vicente Alto (SVA), Laco Norte (LN), and Laco Sur (LS), and from drill cores from the Laco Norte (LN), Laco Sur (LS), and Extensión Laco Sur ore bodies. This study is the second one to incorporate samples from depth at El Laco (Ovalle et al., 2018). Apatite samples used in this study came from outcrop samples at Cristales Grandes (CG), Rodados Negros (RN), and Laco Sur (LS). The geochemistry and textures of magnetite and apatite reveal that the ore bodies formed by a combination of magmatic and magmatic-hydrothermal processes that is consistent with the hybrid magmatic/magmatic-hydrothermal model proposed by Ovalle et al. (2018).

3.3 Geological Background

The El Laco volcanic complex (ELVC) and associated IOA deposit are located east of the active volcanic arc in the Central Andes along the western South American continental margin (Fig. 3.1A; Nyström and Henríquez, 1994; Rhodes and Oreskes, 1995; Naslund et al., 2002; Sillitoe and Burrows, 2002; Tornos et al., 2016; 2017; Ovalle et al., 2018). The volcanic host rocks and the ore bodies of the ELVC have yielded ages ranging from 5.3 ± 1.9 Ma to 1.6 ± 0.5 Ma (K-Ar), and 2.1 ± 0.1 Ma (apatite fission track), respectively (Maksaev et al., 1988; Naranjo et al., 2010). The volcanic rocks in the ELVC are andesitic to dacitic in composition with the ore bodies distributed around the Pico Laco volcanic edifice (Fig. 3.1B; Naslund et al., 2002; Tornos et al., 2016; Ovalle et al., 2018). The El Laco ore deposit consists of seven individual ore bodies with a total estimated resource endowment of ~734 million tons (Mt) at an average grade of ~49% Fe (CAP Mineria, 2016).

Magnetite is the dominant iron oxide in the El Laco deposit, with modal abundances >90 vol%, and apatite, scapolite, and diopside are modally minor phases (Nyström and Henriquez, 1994; Rhodes and Oreskes, 1995; Rhodes and Oreskes, 1999; Rhodes et al., 1999; Naslund et al., 2002; Ovalle et al., 2018). Magnetite is locally altered to hematite and goethite in the upper 40 to 50 m of the ore bodies (Ovalle et al., 2018). The ore bodies have distinct morphologies and have been classified as: (1) flows with feeder dikes (Laco Norte, Laco Sur, San Vicente Alto), (2) dome-like intrusions (San Vicente Bajo), and (3) dikes (Cristales Grandes, Rodados Negros) (Nyström and Henriquez, 1994). The massive magnetite ore bodies with flow morphology in outcrops contain what appear to be gas escape tubes, and the magnetite contains unfilled vesicles, are coarse grained, and have spherulitic and dendritic textures. Logging of drill cores from Laco Sur and Laco Norte indicate that the outcropping massive magnetite ore bodies transition to breccia bodies at depths greater than 40 m (Ovalle et al., 2018). Razor-sharp chilled contacts are observed between the massive magnetite and the host andesite and friable pyroclastic ore material, including iron oxide ash, is observed near the ore bodies (Henriquez and Martin, 1978; Nyström and Henriquez, 1994; Naslund et al., 1997; 1998; 2002; Mungall et al., 2018; Ovalle et al., 2018; Xie et al., 2019). The host andesite along the margins of the massive magnetite ore bodies contains metasomatic aureoles, which are characterized by an alteration assemblage containing pyroxene, magnetite, quartz, and scapolite (Vivallo et al., 1994; Naslund et al., 2002; Velasco et al., 2016). The alteration assemblages observed in the host rocks below the flow-like ore bodies include clays (illite, smectite), pyrophyllite, quartz, feldspar, and magnetite veinlets without pyroxene fringes (Broman et al., 1999; Naslund et al. 2002). The open spaces in the extrusive ore bodies contain alteration assemblages of quartz, tridymite, amorphous silica, hematite, Na-rich alunite, iron phosphates, labradorite, sanidine, and rutile (Naslund et al., 2002). The host rocks are also overprinted by post-

mineralization low temperature hydrothermal alteration that is manifested as silicification (characterized by quartz, tridymite, cristobalite, alunite, jarosite, K-feldspar, anatase, iron phosphates, iron sulphates), advanced argillic alteration (characterized by quartz, alunite, kaolinite, gypsum, cristobalite, smectite, bassanite, pyrite, pyrophyllite), and the formation of fumarolic deposits (characterized by gypsum, alunite, jarosite, native sulfur, cristobalite, tridymite, calcite) (Vivallo et al., 1994; Broman et al., 1999; Naslund et al., 2002; Sillitoe and Burrows, 2002).

3.4 Sample Selection and Methodology

We collected magnetite-rich ore samples from outcrops at the Cristales Grandes (CG), Rodados Negros (RN), San Vicente Alto (SVA), Laco Norte (LN), and Laco Sur (LS) ore bodies, and drill core samples at Laco Norte, Laco Sur, and Extensión Laco Sur (Fig. 3.1B). We analysed magnetite grains from outcrop samples and representative drill core samples. We studied apatite grains collected from outcrop at Cristales Grandes, Rodados Negros, and Laco Sur. Outcrop magnetite samples were examined by using an optical microscope and then crushed and separated into two aliquots: one aliquot was used in this study, and the second in a separate study that measured Fe, H, and O stable isotope concentrations (Childress, 2019). For this study, a combination of thin and thick sections and grain mounts were prepared for detailed petrographic inspection and micro-textural observations of magnetite and apatite grains.

3.4.1 Imaging and Electron Probe Micro-Analyses

3.4.1.1 Magnetite

Magnetite grains from outcrop samples at the five ore bodies (Cristales Grandes, Rodados Negros, San Vicente Alto, Laco Norte, Laco Sur) were characterized by back-scattered electron (BSE) imaging and energy-dispersive X-ray spectrometry (EDS) elemental mapping by using the

JEOL JSM – 7800FLV Field-Emission Scanning Electron Microscope (FE-SEM) at the University of Michigan Electron Microbeam Analysis Laboratory (EMAL) with an accelerating voltage of 15kV and a medium beam current. Drill core samples were characterized by using a Model FEI Quanta 250 SEM at Universidad de Chile with an accelerating voltage of 12.5 kV. Quantitative compositional analyses of all magnetite grains were performed by using the EMAL Cameca SX100 electron probe micro-analyzer (EPMA) in wavelength-dispersive X-ray spectrometry (WDS) mode. The concentrations of Fe, Ti, V, Mn, Ca, P, Mg, Cr, Al, and Si were measured by using an accelerating voltage of 20 keV, a beam current of 30 nA, and a focused electron beam. The counting times and standards used are presented in Table 3.A1. Vanadium measurements were corrected for the spectral overlap of the V Kα X-ray line by the Ti Kβ. A total of 1917 individual EPMA spot analyses were conducted on representative iron oxide grains from the outcrop and drill core samples collected at the 5 ore bodies. These EPMA data are presented in the electronic supplementary materials of Ovalle et al. (2018).

3.4.1.2 Apatite

The apatite grains from the three ore bodies (Cristales Grandes, Rodados Negros, Laco Sur) were investigated by using a combination of BSE and cathodoluminescence (CL) imaging, and EDS element mapping, by using an accelerating voltage of 20 kV on the FE-SEM in EMAL. Quantitative compositional analyses were made by using the EMAL EPMA and the Cameca SX100 EPMA at the American Museum of Natural History in New York. Line transects and spot analyses were performed on apatite grains in thin section (Laco Sur) and epoxy mounts (Cristales Grandes and Rodados Negros), and the measurements were made by using an excitation voltage of 15 keV, a beam current of 10 nA, and a spot size of 2-10 μm. The standards, counting times, and analytical conditions are presented in Table 3.A2. Calcium, P, Cl, and F were analyzed first in

the analytical sequence as suggested by Goldoff et al. (2012) to mitigate elemental migration during the analyses. The hydroxide (OH) content of apatite for individual spot analyses was calculated using the mass balance method of Ketcham et al. (2015), which uses the measured Cl and F concentrations and the assumption that the halogen site in apatite is occupied by $X_F + X_{Cl} + X_{OH} = 1$.

3.4.2 LA-ICP-MS ANALYSES

Laser ablation inductively coupled plasma mass spectrometry (LA-ICP-MS) analyses of magnetite and apatite were performed by using a Thermo Scientific iCapQ quadrupole inductively coupled plasma mass spectrometer (ICP-MS), coupled with a 193 nm ArF excimer laser at the Andean Geothermal Center of Excellence (CEGA) laboratory at Universidad de Chile. The LA-ICP-MS analyses were performed along the same transects that were previously analyzed by EPMA in order to obtain trace element chemistry to complement the major and minor element chemistry obtained via EPMA. The concentrations of the elements analyzed, and their associated limits of detection were determined by using the Iolite software package (Paton et al., 2011) based on Longerich et al. (1996). Each LA-ICP-MS transient signal was evaluated for the presence of inclusions, and only inclusion-free signals were considered.

3.4.2.1 Magnetite

The concentrations of Na, Mg, Al, Si, P, S, K, Ca, Sc, Ti, V, Cr, Mn, Co, Ni, Cu, Zn, Ga, Ge, As, Se, Kr, Rb, Sr, Y, Zr, Nb, Mo, Ag, Cd, Sn, Sb, Te, Ba, Hf, Ta, Au, Pb, Th, U, and rare earth elements (REEs; La, Ce, Pr, Nd, Sm, Eu, Gd, Tb, Dy, Ho, Er, Tm, Yb, Lu) were measured in magnetite from outcrop and drill core samples from the five ore bodies. Additionally, tungsten was measured in magnetite grains from the drill core samples. A beam diameter of 40 μm was used to conduct spot analyses. The iron concentrations previously quantified by using EPMA were

used as the internal standard for LA-ICP-MS calibration, and the analyses of the samples were bracketed at the start and end of each run by pairs of analyses of the GSE-1G (Jochum et al., 2005) reference glass. A pair of analyses on the NIST-610 or GSE-1D reference glasses were done prior to the spot analyses, and after the initial pair of analyses of the GSE-1G reference glass, to evaluate the accuracy of the analyses (Jochum et al., 2005, 2011). Details of the analytical protocol are presented in Appendix – 3.1.

3.4.2.2 Apatite

The concentrations of Na, Mg, Al, Si, P, S, Cl, Sc, Ti, V, Cr, Mn, Fe, Co, Ni, Cu, Zn, Ge, As, Rb, Sr, Y, Zr, Nb, Mo, Xe, Ba, Hf, Ta, W, Os, Pb, Th, U, and REEs (La, Ce, Pr, Nd, Sm, Eu, Gd, Tb, Dy, Ho, Er, Tm, Yb, Lu) were measured in apatite from Cristales Grandes and Rodados Negros. No LA-ICP-MS analyses were performed on apatite from Laco Sur because the grains were too small to analyze. A beam diameter of 30 μm was utilized for the analyses. Calcium concentrations previously quantified by using EPMA were used as the internal standard for LA-ICP-MS calibration. The NIST-610 reference glass was used as the bracketing external calibration standard, and the Durango apatite (Chew et al., 2016) was measured twice prior to the analysis of the samples and after the initial analyses of the NIST-610 (Jochum et al., 2011) glass during each run to evaluate the accuracy of the analyses. Details of the analytical conditions are presented in Appendix – 3.1.

3.5 Results

3.5.1 Magnetite textures and associated minerals

BSE imaging of surface samples revealed the presence of magnetite with differing minor and trace element compositions and the presence of martite/hematite and goethite in some samples (Fig. 3.2). Light gray magnetite in the BSE images in samples from Cristales Grandes (magnetite

S1) contains nano-inclusions, whereas nano-inclusions were not observed in light gray magnetite (magnetite S2) from other ore bodies (Fig. 3.2B, C, D, E, F, G, H). In BSE images from all ore bodies, we observe magnetite A, which is a darker shade of gray compared to magnetite S1 and S2 (Fig. 3.2F, H). Hematite was observed in samples from Cristales Grandes, San Vicente Alto, Laco Sur, and Laco Norte (Fig. 3.2A, C, G), but not in samples from Rodados Negros. Goethite was identified in surface samples from all ore bodies except Cristales Grandes and Rodados Negros (Fig. 3.2C, G, H). Magnetite grains in surface samples from all ore bodies commonly meet at triple junctions and contain mineral inclusions (Fig. 3.2H). Apatite occurs as inclusions and/or within fractures in magnetite from Cristales Grandes, Rodados Negros, Laco Sur, and Laco Norte (Fig. 3.2D). Pyroxene is present as intergrowths in magnetite grains from Cristales Grandes, Rodados Negros, and San Vicente Alto (Fig. 3.2A). Monazite is present as inclusions and/or within fractures in magnetite grains from San Vicente Alto, Laco Norte, and Laco Sur (Fig. 3.2B, D). Quartz and an iron phosphate phase, which appear to be the result of the alteration of apatite, are present as inclusions in some magnetite grains from San Vicente Alto and Laco Norte (Fig. 3.2B). Thorite is present as inclusions in some magnetite grains from Laco Norte (Fig. 3.2C). A Nb-rich oxide phase with a composition similar to columbite is present as inclusions within one magnetite sample from Laco Sur (Fig. 3.2F). Magnetite in surface samples contain visible microporosity.

Textures observed by BSE imaging of samples from drill core at Laco Norte and Laco Sur are described in detail by Ovalle et al. (2018) and shown here in Fig. 3.2. In ore samples from the deepest zones (>152 m) at Laco Sur, Extensión Laco Sur, and Laco Norte, we observe agglomerates of titanomagnetite grains that range in size from 100 - 300 μm and contain well-developed trellis- and sandwich-textured ilmenite exsolution lamellae (magnetite-α) (Fig. 3.2I), and euhedral magnetite grains with inclusion-rich cores, surrounded by inclusion-free rims

(magnetite-β) (Fig. 3.2M). Magnetite grains from the deepest samples at Laco Sur contain more ilmenite exsolution lamellae than samples from Laco Norte (Fig. 3.2P). In samples from intermediate depths (66 m - 144 m), we observe magnetite grains up to 500 μm in size that each have an inclusion-free microcrystalline core (magnetite-X) surrounded by alternating layers of inclusion-rich and inclusion-poor magnetite (magnetite-Y) (Fig. 3.2J). In the upper 65 m of the deposit we observe agglomerates of euhedral magnetite grains (magnetite-Z) that are weakly to moderately oxidized to hematite/martite along rims and in fractures (Fig. 3.2N). Magnetite grains from the upper 65 m of drill core also contain visibly abundant microporosity. Magnetite in surface samples from Laco Sur and Laco Norte are replaced by hematite and minor goethite, whereas samples at depth show little or no alteration. Rare scapolite inclusions are observed in magnetite from the deep zones at Laco Sur and Laco Norte. Thorite inclusions are observed in magnetite at intermediate depths at Laco Sur and Laco Norte (Fig. 3.2K), and clinopyroxene inclusions are observed in magnetite at all depths in the drill cores from Laco Sur and Laco Norte.

3.5.2 Magnetite chemistry

Major, minor, and trace element compositions for magnetite from all samples are presented in Table 3.A2 and average, minimum and maximum values in Table 3.1. The concentrations of Au, Ag, Cu, As, Rb, Cd, Sb, Pb, W, Se, Kr, Te, and S were below the limit of detection for many analyses. The light gray magnetite (magnetite S1 and S2) observed in BSE images of outcrop samples from all ore bodies has average measured Fe concentrations ranging from 69 to 71 wt%, and notably have higher concentrations of minor and trace elements compared to hematite and goethite. The gray magnetite phase (magnetite A) in samples from Cristales Grandes, Rodados Negros, and Laco Sur has average measured Fe concentrations ranging from 69.0 wt% to 69.5 wt%, and generally has higher silica content than magnetite S1 or S2. The average major and minor

element compositions for magnetite from the drill core and surface samples at Laco Sur and Laco Norte were previously reported by Ovalle et al. (2018). The measured concentrations of minor and trace elements in magnetite from outcrops and drill cores are presented in Table 3.1, and Ti, V, Al, Mn, Sn, and Ga concentrations are plotted in Fig. 3.3. The concentrations of Ti, V, Al, Mn, Ga, and Sn decrease progressively in magnetite from Cristales Grandes to Rodados Negros to San Vicente Alto, whereas the concentration of Ni increases (Fig. 3.3 and Fig. 3.A1). The concentrations of Ni, Ti, V, Mn, Co, Ga, and Al in magnetite from Laco Norte generally increase with increasing depth in the deposit, whereas the concentration of Sn moderately increases with increasing depth. At Laco Sur, the concentrations of Ti, Zn, Al, Cr, Ga, Ni, and V increase from surface to depth.

In Figs. 3.4, 3.5, and 3.A2, we present comparisons of the average concentrations of minor and trace elements normalized to bulk continental crust (cf. Rudnick and Gao, 2003) for magnetite sampled from outcrop and drill core along with compositional data from Dare et al. (2014) for magnetite from Kiruna-type deposits, including El Laco, and magmatic (i.e., intermediate to felsic igneous rocks), magmatic-hydrothermal (i.e., porphyry), and low-temperature hydrothermal (i.e., banded iron formations and skarns) environments. Magnetite from magmatic, magmatic-hydrothermal, and low-temperature hydrothermal environments form from fluids with temperatures >500 °C, between 300 – 500 °C, and between 200 – 300 °C, respectively (Nadoll et al., 2014). The compositions of magnetite from outcrop and drill core samples overlap the fields for magnetite from igneous rocks, magmatic-hydrothermal temperature environments, and Kiruna-type ore deposits. There is minimal overlap between the El Laco samples and low temperature hydrothermal magnetite. We highlight that the Ti concentrations of magnetite that contain ilmenite

exsolution lamellae (Fig. 3.2I, P) are lower than the original Ti content of magnetite owing to the partitioning of Ti into exsolved ilmenite lamellae, which is discussed below.

In Fig. 3.6, the concentrations of [Al+Mn] and [Ti+V] in magnetite from the surface (A) and drill core samples (B) are plotted on the magnetite discriminant diagram of Nadoll et al. (2014). Also plotted on Fig. 3.6 are the [Al+Mn] and [Ti+V] concentrations of magnetite from the El Laco andesite host (cf. Dare et al., 2015). Colored contours represent the temperatures of crystallization of magnetite reported by Nadoll et al. (2014). The concentrations of Al, Mn, Ti, and V are highest in magnetite from the host andesite and decrease progressively among the surface samples from Cristales Grandes to Rodados Negros to San Vicente Alto (Fig. 3.6A). The [Ti+V] content of magnetite from the deepest drill core samples from Laco Sur is similar to igneous magnetite from iron-titanium-vanadium (Fe-Ti,V) deposits and trends toward the composition of magnetite from the El Laco andesite host, although the drill core samples have lower [Al+Mn] contents (Fig.3. 6B). Importantly, the original concentrations of Al, Mn, Ti, and V in magnetite would have been higher prior to the unmixing of the original magnetite-ulvöspinel$_{ss}$ during post-mineralization cooling that resulted in the oxy-exsolution of ilmenite lamellae (Buddington and Lindsley, 1964). For all magnetite samples from the drill core, [Al+Mn] and [Ti+V] contents decrease from depth to surface (Fig. 3.6D).

3.5.3 Apatite textures and associated minerals

The apatite grains from Cristales Grandes, Rodados Negros, and Laco Sur are almost homogeneous in color in BSE images, except for a few grains from Cristales Grandes which exhibit growth zones of lighter color (Fig. 3.7A, C, E). Generally, the apatite in samples from all three ore bodies contains varying amounts of microporosity, fractures, and inclusions (Fig. 3.7A, C, E). The EDS element maps of the apatite grains indicate homogeneous distribution of Ca and

P. The EDS maps indicate a heterogeneous distribution of sulfur in apatite from Laco Sur where the concentrations of sulfur are higher near grain boundaries and proximal to cracks within grains (Fig. 3.7G). Variations in cathodoluminescence intensity were observed in apatite grains from all samples. At Cristales Grandes, most of the apatite grains display purple luminescence, while the areas with lighter color in BSE display dark blue luminescence; oscillatory growth zoning is observed in CL images in some grains from this ore body (Fig. 3.7B). Apatite grains from Rodados Negros display mauve luminescence, while the highly porous regions of the grains display orange luminescence (Fig. 3.7D). The apatite from Laco Sur displays purple or blue luminescence in the inner portions of the grains, whereas the grain boundaries and areas proximal to cracks, which have higher S contents, display dark or minimal luminescence (Fig. 3.7F). Growth zoning is not observed in the apatite grains from Rodados Negros and Laco Sur. Monazite is present as inclusions and in cracks and on grain boundaries in apatite grains from Cristales Grandes and Rodados Negros; these inclusions are more common in the mottled/porous regions of apatite grains from Rodados Negros (Fig. 3.7A, C). Small euhedral magnetite grains are observed within agglomerates of apatite from Laco Sur (Fig. 3.7E).

3.5.4 Apatite chemistry

The major, minor, and trace element compositions for apatite from all samples are presented in Table 3A2 and the minimum, maximum, and average compositions are presented in Table 3.2. The concentrations of Ti, Sc, Cr, Co, Cu, Zn, Nb, Mo, Xe, W, and Os were below the limit of detection for the majority of the analyses. Apatite from Cristales Grandes and Laco Sur is fluorapatite (Fig. 3.8). Apatite from Rodados Negros exhibits a larger range of F and Cl concentrations, with the porous/mottled regions in apatite grains containing higher concentrations of Cl (up to ~2.1 wt%) compared to visually homogeneous portions of the apatite grains that

contain lower Cl concentrations (~1.1 wt%). For apatite from Cristales Grandes, regions with purple luminescence have higher concentrations of Na, V, Fe, Th, and total REEs, while the regions with blue luminescence have higher concentrations of Si. The regions of mauve luminescence in apatite at Rodados Negros have higher concentrations of F, calculated OH, Th, and total REEs, while the regions of orange luminescence have higher Fe and Cl contents. For the apatite from Laco Sur, the regions with dark luminescence have higher average sulfur (8089 ppm) and iron contents than the regions with purple/blue luminescence.

3.6 Discussion

3.6.1 Magnetite minor and trace element compositions

Magnetite has inverse spinel structure with tetrahedral and octahedral sites that accommodate ferric iron, and ferric and ferrous iron, respectively. The two cation sites in magnetite allow it to incorporate a wide range of cations that substitute for ferric and ferrous iron based on charge and size considerations (Dupuis and Beaudoin, 2011; Nadoll et al., 2014). Comprehensive investigations of the minor and trace element composition of magnetite from mineral systems in which the temperature of magnetite crystallization is inferred from the homogenization temperatures of fluid inclusions hosted in paragenetically equivalent phases, such as quartz and calcite, were used by Nadoll et al. (2014) to propose a discriminant diagram that distinguishes magnetite from different ore deposits based on minor and trace element chemistry. This discriminant diagram allows the chemical composition of magnetite to be used to approximate its temperature of crystallization. Generally, the minor and trace element contents of magnetite decrease as the temperature of the parent fluid (i.e., silicate melts and hydrothermal fluids) decrease (Nadoll et al., 2014). The use of the discriminant diagram of Nadoll et al. (2014) and comparisons of our data to that from other studies that investigate magnetite chemistry from

different environments (e.g., Dupuis and Beaudoin, 2011; Dare et al., 2014; Knipping et al., 2015b; Wen et al., 2017) allow us to gain insights about the evolution of the temperatures of the ore fluids that can then be linked to genetic processes for understanding ore genesis.

3.6.2 Surface to depth chemical variability of magnetite

The concentrations of minor and trace elements in magnetite decrease systematically from depth to surface for drill core samples from Laco Norte and Laco Sur (Fig. 3.6D). In surface samples, Ti concentrations are highest at Cristales Grandes and progressively decrease in samples from Rodados Negros to San Vicente Alto (Figs. 3.3A and 3.6). The average Ti concentrations in surface samples at Laco Sur and Laco Norte are 200 - 300 ppm and are generally consistent with published studies that focused on surface samples from El Laco (e.g., Nyström and Henriquez, 1994; Dare et al., 2015; Velasco et al., 2016; Broughm et al., 2017; Ovalle et al., 2018). However, the data reported here indicate that magnetite A and S1 from Cristales Grandes have average Ti concentrations of ~1000 ppm and ~4000 ppm, and range up to ~7300 ppm; these values are much higher than those found in previous studies. The Ti concentrations reported here for magnetite from Cristales Grandes are consistent with Ovalle et al. (2018) who reported Ti concentrations >0.5 wt% in magnetite samples from deeper levels of Laco Sur and Laco Norte. Those authors report that the Ti concentrations in surface samples from Laco Sur and Laco Norte are low, i.e., <0.1 wt%, but that magnetite at depths >100 m in those ore bodies contains as much as >1 wt% Ti and also contain ilmenite exsolution lamellae. The presence of exsolved ilmenite, which can result from oxy-exsolution during cooling (Buddington and Lindsley, 1964), indicates that the original concentration of Ti in magnetite was higher than the values reported by Ovalle et al. (2018). We highlight that the Ti concentrations measured by LA-ICP-MS in the current study are in good agreement with the Ti concentrations determined by EPMA (Ovalle et al., 2018) (Fig. 3.A3).

Generally, the concentrations of V, Mg Al, Mn, Cr, and Ga in magnetite from surface samples are highest at Cristales Grandes and decrease progressively in samples from Rodados Negros and San Vicente Alto, following the same trend described above for Ti (Fig. 3.3; Fig. 3.A1). The concentrations of Mn and Zn in magnetite are highest at Rodados Negros and are progressively lower in samples from Cristales Grandes and San Vicente Alto (Fig. 3.3; Fig. 3.A1). For the drill core samples, the concentrations of Ti, V, Al, Mn, Ga, and Cr at Laco Sur and Laco Norte decrease systematically from depth to surface (Fig. 3.3; Fig. 3.A1). The Ti and Al concentrations of magnetite from Cristales Grandes and the drill core samples from deep (150 - 200 m) and intermediate (65 - 145 m) depths are consistent with concentrations reported by Nadoll et al. (2014) for magnetite from igneous and high temperature magmatic-hydrothermal environments (Fig. 3.6). The V, Mn, and Cr concentrations of magnetite from all El Laco ore bodies at all depths are similar to concentrations reported by Nadoll et al. (2014) for igneous and magmatic-hydrothermal magnetite, although the Cr content in magnetite from El Laco is generally low (Figs. 3.3, 3.A1). The presence of Ti-enriched magnetite in the deeper parts of the ore bodies (Fig. 3.2) and the systematic decrease of minor and trace element concentrations in magnetite from the ore bodies (Fig. 3.6) suggest that both igneous and magmatic-hydrothermal processes played a role in forming the El Laco ore deposit.

3.6.3 Comparisons of El Laco magnetite geochemistry to magnetite from other environments

The compositions of magnetite at El Laco are compared in Figures 3.4, 3.5, and 3.A2 with magnetite compositions from other Kiruna-type deposits, igneous rocks, and magnetite that grew from high-temperature and low-temperature hydrothermal fluids on the multi-element plots proposed by Dare et al. (2014). The compositional field for magmatic magnetite comprises data for magnetite that crystallized from silicate melts of intermediate and felsic compositions (Dare et

al., 2014). The field for low-temperature hydrothermal magnetite comprises data for magnetite from banded iron formations (BIFs), and Fe-rich skarns, whereas the field for high-temperature hydrothermal magnetite comprises data for magnetite from iron oxide copper gold (IOCG) and porphyry Cu deposits (Dare et al., 2014). The compositional field for Kiruna-type magnetite comprises data for magnetite from the El Laco, El Romeral, and Kiirunavaara IOA deposits. The magnetite compositions reported here are most consistent with magnetite formed in magmatic-hydrothermal environments. There is also considerable overlap with the data for igneous magnetite (Figs. 3.4 and 3.5, Fig. 3.A2). The continental-crust normalized concentrations of all plotted elements overlap the field for high-temperature hydrothermal environments, except for Si, Ca, Y, Mg, P, Zr, Hf, and Ge that are slightly elevated, and Ga and Ti that are slightly depleted, relative to the published data. The crust-normalized concentrations of all plotted elements overlap the field for igneous magnetite except for Si, Ca, Y, P, and Ge that are elevated in some samples, and Al, Ga, Mn, Ti, and Zn that are slightly depleted in some samples relative to published data. As expected, the geochemical data for surface samples from Cristales Grandes, Rodados Negros, and San Vicente Alto, and surface and drill core samples from Laco Sur and Laco Norte overlap the signature for magnetite from Kiruna-type deposits. The continental-crust-normalized concentrations of Zr, Hf, and Ge determined in the present study are elevated relative to data reported by Dare et al. (2014), whereas the concentration of Ga in samples from San Vicente Alto is slightly lower than that reported by those authors. We note that the overlap between the trace element signature for magnetite from outcrop and drill core samples reported in this study, and that for magmatic-hydrothermal and magmatic magnetite is consistent with magmatic and high-temperature hydrothermal fluids having played a role in IOA ore genesis.

The [Al+Mn] and [Ti+V] data for magnetite from the five ore bodies investigated are compared in Fig. 3.6 with data for magnetite from the andesite host rocks (cf. Dare et al., 2015) and magnetite from a variety of different ore forming environments (Nadoll et al., 2014). Magnetite data for Cristales Grandes, Rodados Negros, and the shallow massive magnetite body at Laco Sur plot in the Kiruna field (Fig. 3.6A). Magnetite data from surface samples of all ore bodies plot in the IOCG field (Fig. 3.6A). Data for surface samples at Rodados Negros, Laco Sur, and Laco Norte plot in the BIF field, and a few data for magnetite from Cristales Grandes, Rodados Negros, and the deep samples at Laco Sur and Laco Norte plot in the Skarn field. Magnetite from the deep levels of Laco Norte and the deep- and intermediate-levels of Laco Sur (Fig. 3.6B) plot in the igneous Fe-Ti/V field, and some samples from Laco Sur have [Ti+V] contents that overlap magnetite from the El Laco andesite host rocks (Fig. 3.6B). Data for magnetite from Cristales Grandes, Rodados Negros, intermediate depths of Laco Norte, and all depths of Laco Sur plot in the porphyry field. Our data for magnetite from the same ore bodies plot in fields for different ore deposit types. This result highlights that this discriminant diagram does not successfully identify magnetite from these ore deposits. Rather, the comparisons in Fig. 3.6 reveal differences of [Al+Mn] and [Ti+V] among different ore bodies at El Laco as well as systematic decreases of these elements among samples within individual ore bodies that can be used to infer differences in temperature within and among the ore bodies. The compositions of magnetite from the dike-like ore bodies at Cristales Grandes and Rodados Negros and from the flow-like ore bodies (San Vicente Alto, Laco Sur, and Laco Norte) record crystallization at temperatures >500 °C, 300 - 500 °C, and 200 - 300 °C , respectively (Fig. 3.6C, D; Nadoll et al., 2014). The temperatures inferred from magnetite chemistry for Rodados Negros are consistent with homogenization temperatures of fluid inclusions hosted in apatite from that ore body (cf. Broman et al., 1999). Overall, the

considerable overlap for all samples in [Al+Mn] and [Ti+V] space is consistent with magnetite that grew from a cooling magmatic-hydrothermal fluid.

In Fig. 3.9, the V and Ti contents of magnetite grains from the ore bodies and andesite host (cf. Broughm et al., 2017) at El Laco and the Láscar dacite (cf. Broughm et al., 2017) are plotted along with fields that define the range of V and Ti in magnetite from magmatic and hydrothermal environments (cf. Knipping et al., 2015b). The Ti content of magnetite is strongly controlled by temperature, while the V content is controlled by oxygen fugacity (Lindsley, 1991; Nielsen et al., 1994; Toplis and Carroll, 1995; Balan et al., 2006; Bordage et al., 2011). Nadoll et al. (2014) showed that the concentrations of both Ti and V in magnetite decrease with decreasing magnetite crystallization temperature. The V and Ti contents of magnetite from deep and intermediate depths at Laco Sur and Laco Norte, in addition to data for some surface samples from Cristales Grandes and Rodados Negros plot in the field for igneous magnetite (Fig. 3.9). The V and Ti contents of surface samples from Cristales Grandes, Rodados Negros, San Vicente Alto, Laco Norte, and Laco Sur, in addition to data for massive magnetite collected 35 m below surface at Laco Sur, plot in the area where the igneous and hydrothermal fields overlap (Fig. 3.9). A few data points for magnetite from San Vicente Alto plot in the field for hydrothermal magnetite, and some data from surface samples from all ore bodies plot outside the fields in the low Ti region of the plot (Fig. 3.9). The distribution of data for samples from the five ore bodies is similar to that reported by Broughm et al. (2017) who found an almost identical spread of V and Ti concentrations at El Laco. Notably, the data reported here demonstrate that magnetite in the deeper levels of Laco Sur, Extensión Laco Sur, and Laco Norte has Ti concentrations that overlap those for igneous magnetite from the El Laco andesite host and nearby Láscar dacite (Fig. 3.9B; Broughm et al., 2017).

Nadoll et al. (2014) reported that Ti, V, Al, Sn, and Ga concentrations are highest in igneous magnetite and decrease systematically in magnetite that forms in hydrothermal systems as a function of decreasing temperature. Salazar et al. (2019) also report that the V and Ga concentrations in magnetite from the Cerro Negro Norte IOA deposit in the Chilean Iron Belt display a cooling trend from magmatic to hydrothermal conditions. In Fig. 3.10, the concentrations of Ti, V, Al, and Sn are each plotted against Ga. The data for the El Laco ore bodies indicate decreasing Ti, V, Al, and Ga concentrations in surface samples from Cristales Grandes, to Rodados Negros to San Vicente Alto (Fig. 3.10). The concentrations of Ga in drill core samples from Laco Sur and Laco Norte decrease from depth to surface, while the Sn concentrations have an average value of ~10 ppm (Fig. 3.10D). However, a subset of the data for the surface samples from Laco Norte and Laco Sur, and deep drill core samples from Laco Sur has increased Sn content similar to that observed in hydrothermal magnetite from the Mg-Skarn ore at the Santa Rita deposit and in igneous magnetite from the Henderson Climax-type Mo deposit as reported by Nadoll et al. (2014). Those authors suggested that the high Sn contents of magnetite from Santa Rita and Henderson are controlled by fluid composition during fluid-host rock interactions. The high Sn content in the magnetite at Laco Sur and Laco Norte is, therefore, either the result of ore fluid composition or fluid-rock interactions. Further, the magnetite with the high Sn content (~100 ppm) at Laco Sur also contains the highest concentrations of Nb (average value of ~580 ppm), Th (455 ppm), and U (~253 ppm), as well as Nb-rich oxide inclusions in the magnetite grains. We hypothesize that the high Sn (and Nb) concentrations with corresponding low Ga concentrations reflect metasomatic alteration after ore emplacement, since these magnetite grains also contain elevated levels of Th, U, and REEs, which can be liberated during metasomatic reactions with apatite and hydrothermal fluids (Harlov et al., 2002). The trace element concentrations in

magnetite from the El Laco ore bodies are consistent with growth of magnetite from a cooling magmatic-hydrothermal fluid as it ascended through the crust.

Wen et al. (2017) proposed a new plot for discriminating between magmatic and hydrothermal magnetite that considers the hydrothermal re-equilibration of igneous magnetite. Those authors found that plotting the V/Ti ratio versus the Fe content of magnetite allows for the discrimination of magmatic magnetite, magmatic magnetite that has re-equilibrated with a hydrothermal fluid, and purely hydrothermal magnetite. In Fig. 3.11, we compare our data for magnetite from the five ore bodies and host andesite (Dare et al., 2015) at El Laco, the discriminant fields of Wen et al. (2017) (lines), and (colored) fields representing igneous, magmatic-hydrothermal, and low-temperature hydrothermal magnetite based on data from Nadoll et al. (2014). Data for magnetite from surface samples from all ore bodies, and from the deep, intermediate, and shallow zones of the drill cores plot in the field for re-equilibrated magnetite. Data from all surface samples and all levels of the drill cores plot in the field for hydrothermal magnetite defined by Wen et al. (2017). The vast majority of the data from the El Laco ore bodies plot in the overlapping region of the fields for igneous and magmatic-hydrothermal magnetite from Nadoll et al. (2014) that we superposed on the Wen et al. (2017) plot. The deepest samples from the drill cores plot in the field for igneous magnetite from Nadoll et al. (2014), and no data plot in the field for low temperature hydrothermal magnetite. Similar to Wen et al. (2017), we observe textural and chemical evidence for re-equilibration of igneous magnetite with magmatic-hydrothermal fluid, and growth of magnetite from magmatic-hydrothermal fluids. Magnetite at depth in drill core contains ilmenite exsolution lamellae surrounded by magnetite with no exsolution lamellae (Fig. 3.2I) or inclusion-rich magnetite cores surrounded by inclusion-poor rims (Fig. 3.2J). Magnetite grains from surface samples terminate at triple junctions (Figs. 3.2H, I),

consistent with re-equilibration of magnetite with magmatic-hydrothermal fluid. Overall, the compositions of magnetite from El Laco plotted on the V/Ti vs. Fe diagram of Wen et al. (2017), with the fields for data from Nadoll et al. (2014), are consistent with magmatic-hydrothermal fluids being responsible for formation of the ore bodies.

3.6.4 Insights for ore-forming processes from El Laco apatite chemistry

Apatite —$Ca_{10}(PO_4)_6(F,Cl,OH)_2$ — is a common accessory mineral in many terrestrial and extraterrestrial geologic environments. Apatite is able to incorporate nearly one-third of the elements in the periodic table into its structure, including the essential structural constituents F, OH, and Cl, as well as trace elements such as S, REEs, and Fe (Hughes and Rakovan, 2015). Trace element abundances in apatite have been used as petrogenetic indicators to gain insights into the evolution of geologic systems (Streck and Dilles, 1998; Belousova et al., 2002; Piccoli and Candela, 2002; Parat et al., 2011; Harlov, 2015; Hughes and Rakovan, 2015; Webster and Piccoli, 2015; Bouzari et al., 2016; Mao et al., 2016; Konecke et al., 2017a, b). Prior to this study, there was a scarcity of published geochemical data for apatite from the El Laco ore bodies.

Generally, the apatite grains from Laco Sur, Cristales Grandes, and Rodados Negros are fluorapatite with lesser amounts of Cl and OH (Fig. 3.8). Our data are consistent with Dare et al. (2015) who report that apatite contains, on average, ~2 wt% F. The analyses of some apatite grains from Laco Sur yielded fluorine concentrations greater than the pure, end-member stoichiometric concentration for end-member fluorapatite (3.77 wt%). This is not an analytical artifact considering the reproducibility of the standards and strict adherence to the analytical protocol of Stromer et al. (1993) and Goldoff et al. (2012). We highlight that high F concentrations (> 3.77 wt%) have also been reported for apatite from Kiruna-type deposits in the Kiruna and Grängesberg districts in Sweden and the Pea Ridge IOA deposit, USA (Harlov et al., 2002a; Jonsson et al.,

2013; Harlov et al., 2016) (Fig. 3.8). Apatite from Laco Sur, Cristales Grandes, and Rodados Negros cluster near the fluorine end of the F-Cl join and overlap with apatite compositions from mafic igneous rocks and their evolved ore deposits (Marks et al., 2012; Rojas et al., 2018).

The El Laco apatite data overlap data for apatite from other IOA deposits, including Kiirunavaara (Sweden), Pea Ridge (USA), Cerro de Mercado (Durango, Mexico), deposits in the Bafq district (Iran), the Carmen deposit in the Chilean Iron Belt, and hydrothermal apatite (Harlov et al., 2002; Torab and Lehman, 2007; Marks et al., 2012; Harlov et al., 2016; Mao et al., 2016; Palma et al. 2019). Some apatite grains from Rodados Negros (highlighted by the orange ellipse in Fig. 3.8) contain Cl-enriched domains that are shifted towards the chlorine end of the F-Cl join, consistent with halogen chemistry reported for apatite from the Los Colorados (La Cruz et al., 2019) and Fresia IOA deposits (Palma et al., 2019) in the Chilean Iron Belt. Broman et al. (1999) report that apatite-hosted fluid inclusions from Rodados Negros contain up to 60 wt% NaCl equivalent, thus the Cl-enrichment in grains from Rodados Negros, likely reflect growth from, or re-equilibration with this Cl-rich, F-poor fluid. The composition of apatite from hydrothermal environments exhibits a wide range of F, Cl, and OH concentrations that reflect the composition of the hydrothermal fluid from which apatite precipitates, the temperature of mineralization, and the preference for the anions ($F >> Cl > OH$) in the apatite structure (cf. Boudreau et al., 1995; Barth and Dorais, 2000; Belousova et al., 2002; Patiño Douce et al., 2011; Marks et al., 2012; Hughes and Rakovan, 2015; Webster and Piccoli, 2015; Bao et al., 2016; Krneta et al., 2016). The majority of analyzed apatite grains from El Laco are compositionally similar to fluorapatite from mafic igneous rocks and hydrothermal fluids evolved from mafic silicate melts and are consistent with growth from a silicate melt or magmatic- hydrothermal fluid.

The Cl-enriched domains in some apatite grains from Rodados Negros are consistent with the variability of cathodoluminescence (CL) in those apatite grains and variations in the concentrations of CL activators such as Ce^{3+}, Eu^{2+}, and Mn^{2+}, and quenchers such as $Fe^{2+}$and La^{3+} (cf. Kempe and Götze, 2002). The areas of bright luminescence in apatite grains from Rodados Negros have the highest chlorine content of all apatite grains from the El Laco ore bodies and correspond spatially to the porous/mottled regions of those apatite grains. The areas of dark luminescence in apatite from Laco Sur have the highest sulfur content (up to ~1 wt% S) among all apatite grains from the El Laco ore bodies. Sulfur, Cl, Mn, REEs, and Fe are highly mobile in magmatic-hydrothermal fluids (Hedenquist and Lowenstern, 1994; Reed et al., 2000; Williams-Jones and Heinrich, 2005; Simon et al., 2007; Simon and Ripley, 2011). The enrichment of these elements within the apatite grains, in addition to the presence of monazite inclusions within and between grains, is consistent with late-stage re-equilibration of the apatite with mineralizing magmatic-hydrothermal fluids.

3.6.5 Magnetite and apatite hosted mineral inclusions

The presence of mineral inclusions in magnetite (e.g., monazite, apatite, thorite, and Nb-rich oxide; Fig. 3.2) and apatite (e.g., monazite; Fig. 3.7B) from the El Laco ore bodies has not, to our knowledge, been reported in previous studies for this deposit. Monazite and thorite inclusions in apatite have been reported from IOA deposits in the Cretaceous Iron Belt (CIB) in northern Chile (La Cruz et al. 2019; Palma et al., 2019), the Kiruna and Bafq districts (Harlov et al., 2002; Bonyadi et al., 2011), and at the Olympic Dam IOCG deposit in Australia (Krneta et al., 2016). Inclusions of monazite have been identified in the banded iron ore at Kiirunavaara, and intergrown with the iron oxides and apatite in the magnetite and hematite zones in the Pea Ridge deposit (Harlov et al., 2002; 2016). Many authors explain the presence of these inclusions in apatite as the

result of metasomatic alteration of apatite (Harlov et al., 2002; 2016; Bonyadi et al., 2011; Krneta et al., 2016; Palma et al., 2019; Sadove et al., 2019). For instance, Palma et al. (2019) report that altered Cl-OH apatite from the Carmen and Fresia IOA deposits in the CIB contains inclusions of monazite and xenotime and proposed that the inclusions record fluid-induced dissolution-reprecipitation of apatite during metasomatism. Alternatively, monazite and thorite inclusions in magnetite samples may reflect growth of those phases as a result of local supersaturation of REE, Th, Si, and P in the fluid in contact with the magnetite grains (La Cruz et al., 2019).

The presence of the Nb-rich oxides, which were observed along cracks between magnetite S2 and high-Si and Mg-magnetite A (Fig. 3.2F), and monazite inclusions in magnetite from Laco Sur (Fig. 3.2D), although not reported by Dare et al. (2015) and Broughm (2017), is consistent with the high field strength elements (HFSE) and light rare earth element (LREE) magnetite signatures reported by those authors. Magnetite grains that host Nb-rich oxides are depleted in Nb as well as Ti, Al, V, and Mn. This observation is consistent with the growth of Nb-oxide during hydrothermal alteration of originally Nb-enriched magnetite by meteoric fluids (Giovannini et al., 2017), which is supported by H and O stable isotope signatures of these magnetite grains (Childress, 2019).

3.6.6 Post-mineralization alteration of the ore bodies

Goethite and hematite in surface samples from San Vicente Alto, Laco Sur, and Laco Norte indicate oxidation and hydration of magnetite, which Alva-Valdivia et al. (2003) report can occur by supergene alteration. Those authors report that the greater degree of oxidation observed in samples from Laco Norte reflects greater degrees of alteration by meteoric waters relative to samples from Laco Sur that exhibit less oxidation. It is well established that goethite is a product of the oxidation and low-temperature hydrothermal alteration of titanomagnetite (Alt et al., 1984;

Xu et al. 1997). Childress (2019) present O (^{16}O, ^{17}O, and ^{18}O) and H stable isotope data and H_2O contents of aliquots of the same surface samples investigated in this study. Values of δ^2H reported by those authors become increasingly negative with increasing H_2O contents, and $\Delta^{17}O$ and $\delta^{18}O$ values fingerprint low-latitude, high altitude meteoric water in samples with increasing goethite contents. Thus, we conclude that goethite, and possibly hematite, formed by secondary processes after emplacement of the ore body.

3.6.7 Formation of the El Laco ore bodies

The body of data presented here for magnetite and apatite geochemistry is most consistent with formation of the El Laco ore bodies by a combination of igneous and magmatic-hydrothermal processes. Titanium-enriched magnetite at depths greater than 150 m in the ore bodies indicates that some proportion of magnetite grew from a silicate melt. In contrast, the systematic decrease of trace element concentrations in magnetite from deep to shallow levels, with a corresponding cooling trend, is consistent with the growth of the remaining volume of magnetite from an ascending magmatic-hydrothermal fluid. We highlight that our data for surface samples are consistent with the findings of Dare et al. (2015) who concluded that a magmatic-hydrothermal fluid was responsible for mineralization at El Laco. Those authors invoked hydrothermal replacement originally proposed by Rhodes and Oreskes (1995) and modified by Sillitoe and Burrows (2002) to explain mineralization at El Laco. In that model, mineralization at El Laco is proposed to have occurred by complete replacement of andesitic lava flows by magnetite that precipitated from a magmatic-hydrothermal fluid percolating through the andesite host. This hydrothermal replacement model was developed by only considering the chemistry of surface samples. The data reported here and in Ovalle et al. (2018) reveal the presence of igneous Ti-rich magnetite in the deepest portions of the ore bodies. The Ti-enriched magnetite can only be

explained by crystallization from a silicate melt owing to the fact that titanium is insoluble in hydrothermal fluids even at magmatic conditions (Audetat and Keppler, 2005). Thus, it is not plausible that the Ti-rich magnetite precipitated from a magmatic-hydrothermal fluid. It also seems implausible that a magmatic hydrothermal fluid would percolate through andesite and replace – atom by atom – silicate minerals in andesite and perfectly preserve the original textures of the lavas, including the vesicles. This is also difficult to reconcile with the sharp chilled contacts between the ore bodies and the andesite host, and the presence of andesite clasts in magnetite ore on the margins of the ore body. Gradational contacts are expected if the ore bodies resulted from replacement.

The data presented here are consistent with those reported by Dare et al. (2015) and support the new genetic model for El Laco proposed by Ovalle et al. (2018). Here, we briefly summarize the model of Ovalle et al. (2018), which is based on the model of Knipping et al. (2015a). The Ti-rich magnetite in the ore bodies crystallized from silicate melt, wherein magnetite is commonly the liquidus phase (Martel et al., 1999). After crystallization of magnetite, the silicate melt reached volatile saturation and exsolved a magmatic-hydrothermal fluid. Magnetite nanolites and microlites have been experimentally and numerically demonstrated to serve as nucleation surfaces for magmatic-hydrothermal fluid bubbles exsolving from silicate melts (Hurwitz and Navon, 1994; Edmonds et al., 2014; Knipping et al., 2019; Pleše et al., 2019). Continued degassing of the silicate melt during magma decompression and crystallization results in the formation of a magnetite-bearing bubble-rich suspension (Edmonds et al., 2014; Ovalle et al., 2018; Knipping et al., 2019). The magmatic-hydrothermal fluid component of the suspension would be Cl and Fe rich, based on experiments that demonstrate the efficient partitioning of these elements from silicate melt to exsolved aqueous fluid (Bell and Simon, 2011). This is consistent with fluid inclusion studies of

samples from El Laco that document the high-temperature Cl-rich nature of the mineralizing fluid at El Laco (Broman et al., 1999). The magmatic-hydrothermal fluid also scavenges elements such as F, P, and Ca that allow the precipitation of fluorapatite in the ore bodies.

During the collapse of the volcanic edifice at El Laco, as evidenced by the observation of fissures and ring structures (Ovalle et al., 2018), the magnetite-bearing bubble-rich suspension was forcibly injected into the upper crust where it formed the hydrothermal breccia bodies observed in drill core from the deeper levels of the deposit. The observation that Ti-rich magnetite (Fig. 3.2) is only found at intermediate to deeper levels of the ore body likely reflects gravitational settling of these igneous Ti-rich magnetite grains during ascent of the mineralizing fluid. Continued ascent, shallow level emplacement, and surface venting of the hydrothermal magnetite suspended in the magmatic-hydrothermal fluids gave rise to the formation of the massive magnetite flows and dike-like bodies that outcrop around the Pico Laco resurgent dome. As discussed by Ovalle et al. (2018), numerical modeling (Edmonds et al., 2014), experimental studies (Knipping et al., 2019), and empirical studies of industrial froth flotation processes indicate that mineral-fluid-bubble aggregates have rheological properties similar to basaltic lava flows, which explains the presence of cavities and gas escape tubes in surface outcrops originally described by Park (1961). The presence of triple junctions among magnetite grains likely reflects local reequilibration of magnetite with interstitial high-temperature ore fluid after emplacement, which also explains the presence of monazite, thorite, and Nb-oxide inclusions in magnetite, monazite inclusions in apatite, and magnetite octahedra observed growing from the walls of cavities and gas escape tubes. Circulation and cooling of the interstitial magmatic-hydrothermal fluid also explains the presence of sulfide-bearing magnetite-diopside-scapolite veins and late veinlets of gypsum-magnetite-pyrite

that crosscut the main breccia bodies at depth (Ovalle et al., 2018), as well as the advanced argillic alteration at the surface (Sillitoe and Burrows, 2002).

The El Laco ore bodies contain ~367 million tons (Mt) of iron based on the reported resources of ~734 Mt at an average grade of ~49 % iron (CAP Mineria, 2016). Following the methodology of Knipping et al. (2015a), if the magnetite-fluid suspension evolved from a hydrous magma that contained 6 wt% H_2O, and the suspension contained 20 wt% primary Ti-rich magnetite, a parent magma on the order of 50 km^3 is required to account for the Fe in the El Laco ore bodies if 50% of the Fe in the fluid phase precipitated during emplacement. This magma volume is consistent with typical arc volcano magma chambers (4–60 km^3; Marsh, 1989) and seems plausible considering the ~30 km^2 diameter volcanic edifice at El Laco (Oyarzún and Frutos, 1984; Nyström and Henríquez, 1994).

Finally, we highlight that the $\delta^{18}O$, $\Delta^{17}O$, $\delta^{2}H$, and $\delta^{56}Fe$ data reported by Childress et al. (in review) and Bilenker et al. (2016) are consistent with the model presented here for the formation of the El Laco ore bodies. Childress et al. (in review) report $\delta^{56}Fe$ and $\delta^{18}O$ values for magnetite from outcrop samples collected from Cristales Grandes, Laco Norte, Laco Sur, Rodados Negros, and San Vicente Alto, which in addition to the magnetite geochemistry presented here for the same samples, are consistent with magnetite crystallization from silicate melt and magmatic-hydrothermal fluid. They report that values of $\delta^{2}H$ become increasingly negative with increasing goethite modal abundance and H_2O content of the samples. The $\Delta^{17}O$, which is defined as $(\delta^{17}O_{sample} - \delta^{18}O_{sample})* 5.302$, and $\delta^{18}O$ data for goethite-bearing samples indicate alteration of primary magmatic and magmatic-hydrothermal magnetite by meteoric water. Importantly, the O-isotope data for samples of the El Laco ore bodies disallow formation by liquid immiscibility based on the experimental data of Lester et al. (2013a) that constrain the partitioning of O isotopes

between conjugate Fe-rich and Si-rich melts. Lester et al. (2013a) report values of $\Delta^{18}O$, which is defined as $\delta^{18}O_{Si\text{-}rich\text{-}melt} - \delta^{18}O_{Fe\text{-}rich\text{-}melt}$, of 0.5 to 0.6 ‰, requiring that the Fe-oxide ore bodies at El Laco should yield $\delta^{18}O$ values of ~7 to 9 ‰ if the ore bodies crystallized from an iron-rich liquid that had been in equilibrium with andesite host rocks. Rather, the El Laco ore bodies yield $\delta^{18}O$ values of ~3.5 to 5 ‰ and the andesite host rock yield $\delta^{18}O$ values of ~8 to 9 ‰, eliminating the possibility that silicate magmas in the El Laco plumbing system could be related to magnetite in the ore bodies by liquid immiscibility. The $\delta^{18}O$ values of ore samples from El Laco match exactly the values expected for magnetite precipitated from a magmatic-hydrothermal fluid. The constraints from O-isotope data are also consistent with experimental data from Lester et al. (2013b) that demonstrate that liquid immiscibility does not occur in H_2O + Cl-bearing silicate melts because the presence of chlorine increases the activity of silica in the melt, resulting in increased temperatures for the silicate mineral saturation surface, and eliminates unmixing of the silicate liquid. The Cl-rich nature of the ore fluids at El Laco as demonstrated by Broman et al. (1999), coupled with the experimental and O-isotope partitioning results of Lester et al. (2013a, b) falsify the liquid immiscibility hypothesis.

3.7 Conclusions

Magnetite from five ore bodies and apatite from three ore bodies at the El Laco iron oxide - apatite deposit in Chile have major, minor, and trace element chemistry consistent with growth from both a silicate melt and a magmatic-hydrothermal fluid. The magnetite grains contain mineral inclusions that preserve evidence of reequilibration of ore minerals with hydrothermal fluids during or after emplacement of the ore bodies. These observations are consistent with ore genesis at El Laco via shallow-level emplacement and surface venting of magnetite-bearing magmatic-hydrothermal fluid suspensions according to the model described in Ovalle et al. (2018). The

current study adds to a growing body of geochemical and petrologic data for ore minerals from IOA deposits that indicate formation of Kiruna-type IOA deposits via the ascent of a cooling, decompressing Fe-bearing magmatic-hydrothermal fluid that contains and transports igneous magnetite nanolites and microlites.

Table 3.1: Summary of compositions of magnetite from outcrops at Cristales Grandes, Rodados Negros, San Vicente Alto, and outcrops and drill core at Laco Norte.

		Cristales Grandes							
		Magnetite S1				Magnetite A			
EPMA	D. L.	N= 49				N= 69			
		Min.	Mean	Max.	Std. Dev	Min.	Mean	Max.	Std. Dev
Fe (wt%)	0.02	67.0	69.2	71.4	1.1	65.5	69.0	70.9	1.2
Ti (ppm)	89.46	104.0	3981.6	7346.0	2155.2	B.D.L.	1039.2	6554.0	1605.7
V (ppm)	66.39	848.0	1677.3	1983.0	200.4	1151.0	1653.6	1875.0	170.3
Al (ppm)	81.24	674.0	3420.6	8103.0	1468.8	532.0	1459.8	5162.0	1101.4
Mn (ppm)	80.45	439.0	821.5	1459.0	179.2	B.D.L.	716.3	1009.0	211.6
Mg (ppm)	128.04	2067.0	6854.4	12313.0	2268.7	1284.0	10735.8	22613.0	3553.1
Si (ppm)	68.07	597.0	4736.6	15724.0	3007.6	174.0	5430.6	14983.0	3017.8
P (ppm)	83.51	B.D.L.	B.D.L.	B.D.L.	B.D.L.	B.D.L.	B.D.L.	211.0	20.4
Ca (ppm)	83.73	B.D.L.	1411.6	3423.0	871.2	B.D.L.	1881.0	4904.0	1239.7
Cr (ppm)	62.61	B.D.L.	54.6	100.0	27.2	B.D.L.	B.D.L.	122.0	21.8
LA-ICP-MS (ppm)	D. L. (ppm)								
Na	56.67	B.D.L.	404.9	1110.0	260.6	B.D.L	376.3	956.0	209.9
Mg	43.53	4120.0	7281.6	13110.0	2034.6	4840.0	10461.3	14600.0	2821.4
Al	36.52	712.0	3483.0	6140.0	1706.0	604.0	1663.9	4860.0	1120.3
Si	2989.50	100.0	5342.3	11900.0	2940.9	200.0	6856.9	20700.0	3867.3
P	9.57	B.D.L.	40.2	134.0	43.2	B.D.L	229.7	13110.0	1573.9
K	35.84	B.D.L.	193.8	1570.0	258.9	B.D.L	125.9	1890.0	244.9
Ca	738.79	B.D.L.	1417.9	5290.0	1294.7	B.D.L	2285.2	22800.0	2795.2
Sc	4.90	B.D.L.	2.9	12.9	1.8	B.D.L	3.0	10.4	1.5
Ti	37.26	99.0	4292.8	7650.0	2749.6	277.0	1270.7	7290.0	1594.3
V	14.33	1415.0	1759.2	2050.0	192.5	1397.0	1795.7	2100.0	182.2
Cr	3.40	B.D.L.	11.1	57.9	13.9	B.D.L	B.D.L	25.4	2.9
Mn	5.59	578.0	926.2	1420.0	147.5	411.0	807.0	1162.0	210.7
Co	2.13	65.8	117.9	140.7	14.3	61.7	95.4	153.7	26.1
Ni	4.44	42.0	89.4	116.2	17.0	39.9	78.0	146.7	32.9

Cu	1.76	B.D.L.	8.5	44.5	10.2	B.D.L	4.6	48.2	9.5
Zn	5.57	89.0	148.6	201.0	26.0	51.9	116.9	195.0	32.8
Ga	0.94	13.9	36.2	47.5	12.4	9.2	24.3	46.0	10.5
Ge	2.19	22.4	26.6	31.9	2.1	22.5	26.5	32.7	1.8
As	5.51	B.D.L	B.D.L	9.5	1.5	B.D.L	B.D.L	11.7	2.8
Rb	1.09	B.D.L.	B.D.L.	24.5	3.4	B.D.L	1.4	38.4	4.7
Sr	0.08	0.3	5.9	19.5	4.6	0.3	4.8	59.6	7.7
Y	0.99	B.D.L	9.8	214.0	30.3	B.D.L	14.0	94.8	14.4
Zr	0.08	0.5	3.5	77.0	10.8	B.D.L	2.6	9.1	1.4
Nb	0.27	1.1	3.5	40.6	7.9	0.8	16.6	44.1	16.2
Mo	1.42	B.D.L	B.D.L	B.D.L.	B.D.L.	B.D.L	B.D.L	1.8	0.1
Ag	1.73	B.D.L	B.D.L	B.D.L	B.D.L.	B.D.L	B.D.L.	B.D.L.	B.D.L.
Cd	0.36	B.D.L.	0.4	1.8	0.2	B.D.L	B.D.L.	B.D.L.	B.D.L.
Sn	0.95	4.0	6.9	27.7	5.2	3.6	13.4	29.4	9.0
Sb	1.28	B.D.L.	0.9	3.5	0.7	B.D.L.	B.D.L.	2.0	0.3
Ba	0.15	B.D.L.	7.2	114.0	16.1	B.D.L.	3.9	44.3	6.7
La	0.21	0.4	9.3	76.7	14.5	0.9	33.8	168.0	32.9
Ce	0.46	0.6	22.4	199.0	37.5	1.3	82.5	342.0	79.8
Pr	0.07	B.D.L.	2.6	21.8	4.0	B.D.L.	9.2	42.7	9.0
Nd	0.27	B.D.L.	9.7	61.4	12.4	B.D.L.	29.8	167.0	29.8
Sm	0.25	B.D.L.	1.5	7.7	1.7	B.D.L.	4.0	30.9	4.5
Eu	0.05	B.D.L.	0.1	0.7	0.2	B.D.L.	0.4	1.7	0.4
Gd	0.18	B.D.L.	1.7	13.3	2.4	B.D.L.	4.1	31.2	4.5
Tb	0.06	B.D.L.	0.2	2.9	0.4	B.D.L.	0.4	3.2	0.5
Dy	0.20	B.D.L.	1.4	21.8	3.2	B.D.L.	2.6	19.4	2.8
Ho	0.08	B.D.L.	0.3	5.3	0.8	B.D.L.	0.5	3.5	0.5
Er	0.15	B.D.L.	1.0	18.6	2.7	B.D.L.	1.7	11.7	1.8
Tm	0.09	B.D.L.	0.1	2.7	0.4	B.D.L.	0.3	1.3	0.2
Yb	0.19	B.D.L.	1.0	13.6	2.0	B.D.L.	2.0	8.8	1.7
Lu	0.08	B.D.L.	0.2	2.7	0.4	B.D.L.	0.3	1.5	0.3
Hf	0.07	B.D.L.	0.1	0.9	0.1	B.D.L.	B.D.L.	B.D.L.	B.D.L.
Ta	0.07	B.D.L.	0.1	0.3	0.1	B.D.L.	0.2	0.6	0.2
Au	0.03	B.D.L.	B.D.L.	B.D.L.	B.D.L.	B.D.L.	B.D.L.	0.0	0.0

Pb	0.44	B.D.L.	0.4	3.3	0.5	B.D.L.	B.D.L.	2.0	0.3
Th	0.31	B.D.L.	5.6	65.0	13.4	B.D.L.	30.0	101.0	29.8
U	0.11	B.D.L.	0.9	10.0	2.2	0.2	3.9	12.7	3.8

		Rodados Negros				
		Magnetite S2				Magnetite A
EPMA	D. L.	N= 104				N= 1
		Min.	Mean	Max.	Std. Dev	
Fe (wt%)	0.02	68.2	70.5	71.5	0.6	69.8
Ti (ppm)	89.46	B.D.L.	364.4	1662.0	375.7	103.0
V (ppm)	66.39	259.0	1050.3	1447.0	284.2	274.0
Al (ppm)	81.24	126.0	917.7	3327.0	721.0	884.0
Mn (ppm)	80.45	642.0	968.0	1404.0	215.0	927.0
Mg (ppm)	128.04	5881.0	7739.0	19610.0	1705.4	7406.0
Si (ppm)	68.07	107.0	1809.5	12190.0	2196.5	609.0
P (ppm)	83.51	B.D.L.	B.D.L.	B.D.L.	B.D.L.	B.D.L.
Ca (ppm)	83.73	B.D.L.	481.0	2782.0	726.2	B.D.L.
Cr (ppm)	62.61	B.D.L.	B.D.L.	81.0	10.6	B.D.L.
LA-ICP-MS (ppm)	D. L. (ppm)					
Na	56.67	B.D.L.	122.7	761.0	160.0	78.0
Mg	43.53	6100.0	7710.1	11490.0	1166.7	7280.0
Al	36.52	155.3	1074.4	3620.0	882.1	345.0
Si	2989.50	B.D.L.	4378.3	13700.0	3244.5	8300.0
P	9.57	B.D.L.	58.0	1600.0	169.1	58.0
K	35.84	B.D.L.	37.9	224.0	46.9	B.D.L.
Ca	738.79	B.D.L.	934.2	3780.0	889.2	B.D.L.
Sc	4.90	B.D.L.	B.D.L.	11.8	1.2	B.D.L.
Ti	37.26	60.0	454.9	1840.0	450.6	103.0
V	14.33	311.0	1112.5	1499.0	289.8	266.0
Cr	3.40	B.D.L.	B.D.L.	30.7	3.6	B.D.L.
Mn	5.59	723.0	1055.4	1520.0	223.2	1017.0
Co	2.13	100.4	132.3	165.5	16.2	147.1
Ni	4.44	96.8	123.2	150.0	14.2	106.0
Cu	1.76	B.D.L.	B.D.L.	20.8	2.6	1.9
Zn	5.57	89.7	153.3	266.0	43.4	188.0
Ga	0.94	6.5	11.2	19.4	3.2	7.7
Ge	2.19	23.7	27.1	31.6	1.4	24.8
As	5.51	B.D.L.	B.D.L.	12.0	1.1	B.D.L.
Rb	1.09	B.D.L.	B.D.L.	1.1	0.1	B.D.L.
Sr	0.08	B.D.L.	1.0	7.1	1.8	B.D.L.
Y	0.99	B.D.L.	3.9	103.0	13.5	1.8
Zr	0.08	0.3	1.1	4.8	0.9	0.7
Nb	0.27	B.D.L.	1.6	7.5	1.7	1.1
Mo	1.42	B.D.L.	B.D.L.	1.6	0.1	B.D.L.
Ag	1.73	B.D.L.	B.D.L.	B.D.L.	B.D.L.	B.D.L.
Cd	0.36	B.D.L.	B.D.L.	B.D.L.	B.D.L.	B.D.L.
Sn	0.95	3.9	5.4	8.0	0.9	8.5
Sb	1.28	B.D.L.	B.D.L.	B.D.L.	B.D.L.	B.D.L.
Ba	0.15	B.D.L.	B.D.L.	8.7	1.7	B.D.L.
La	0.21	B.D.L.	4.2	20.4	5.9	B.D.L.

Ce	0.46	B.D.L.	8.2	48.7	12.3	0.8
Pr	0.07	B.D.L.	0.8	4.5	1.2	0.1
Nd	0.27	B.D.L.	2.8	12.2	3.7	B.D.L.
Sm	0.25	B.D.L.	0.5	3.0	0.6	B.D.L.
Eu	0.05	B.D.L.	0.1	1.4	0.2	B.D.L.
Gd	0.18	B.D.L.	0.7	11.3	1.4	B.D.L.
Tb	0.06	B.D.L.	0.1	0.9	0.1	B.D.L.
Dy	0.20	B.D.L.	0.6	11.9	1.6	0.3
Ho	0.08	B.D.L.	0.1	2.2	0.3	B.D.L.
Er	0.15	B.D.L.	0.4	11.9	1.3	0.3
Tm	0.09	B.D.L.	B.D.L.	0.9	0.1	B.D.L.
Yb	0.19	B.D.L.	0.4	6.9	1.0	B.D.L.
Lu	0.08	B.D.L.	B.D.L.	0.9	0.1	B.D.L.
Hf	0.07	B.D.L.	B.D.L.	0.3	0.0	B.D.L.
Ta	0.07	B.D.L.	B.D.L.	0.1	0.0	B.D.L.
Au	0.03	B.D.L.	B.D.L.	B.D.L.	B.D.L.	B.D.L.
Pb	0.44	B.D.L.	B.D.L.	B.D.L.	B.D.L.	B.D.L.
Th	0.31	B.D.L.	3.6	24.9	6.4	B.D.L.
U	0.11	B.D.L.	0.3	2.3	0.5	B.D.L.

		San Vicente Alto							
		Magnetite S2				Magnetite A			
EPMA	D. L.	N= 23				N= 44			
		Min.	Mean	Max.	Std. Dev	Min.	Mean	Max.	Std. Dev
Fe (wt%)	0.02	67.5	69.2	71.2	1.2	66.4	67.9	69.9	0.5
Ti (ppm)	89.46	B.D.L.	123.3	243.0	60.8	B.D.L.	156.4	345.0	90.6
V (ppm)	66.39	620.0	873.8	979.0	95.3	668.0	902.3	1091.0	83.6
Al (ppm)	81.24	B.D.L.	737.3	2311.0	629.6	282.0	922.8	4500.0	708.6
Mn (ppm)	80.45	B.D.L.	473.8	684.0	173.7	B.D.L.	292.8	629.0	203.6
Mg (ppm)	128.04	417.0	6668.2	10600.0	2335.5	B.D.L.	4324.1	39018.0	6281.4
Si (ppm)	68.07	64.4	411.3	688.0	200.2	306.0	3750.4	11907.0	2881.6
P (ppm)	83.51	B.D.L.	205.3	1109.0	313.9	B.D.L.	256.0	2194.0	461.1
Ca (ppm)	83.73	B.D.L.	738.2	1879.0	626.9	B.D.L.	377.9	2063.0	554.0
Cr (ppm)	62.61	B.D.L.	B.D.L.	B.D.L.	0.0	B.D.L.	B.D.L.	73.0	9.9
LA-ICP-MS (ppm)	D. L. (ppm)								
Na	56.67	B.D.L.	168.3	451.0	162.3	B.D.L.	142.9	584.0	209.0
Mg	43.53	635.0	4533.3	7980.0	2440.8	180.0	3147.4	8580.0	2938.0
Al	36.52	64.4	411.3	688.0	200.2	196.0	527.7	974.0	237.5
Si	2989.50	B.D.L.	4677.6	17600.0	4139.0	B.D.L.	4163.5	14000.0	2756.3
P	9.57	12.0	111.9	449.0	120.1	B.D.L.	102.7	344.0	106.2

K	35.84	B.D.L.	47.5	113.3	34.1	B.D.L.	41.1	150.0	45.7
Ca	738.79	B.D.L.	852.7	2470.0	700.3	B.D.L.	B.D.L.	1960.0	461.3
Sc	4.90	B.D.L	B.D.L	B.D.L.	0.0	B.D.L.	B.D.L.	B.D.L.	0.0
Ti	37.26	17.7	149.4	250.0	76.5	49.4	185.5	350.0	90.7
V	14.33	532.0	906.5	1082.0	130.5	725.0	916.1	1095.0	87.2
Cr	3.40	B.D.L.	B.D.L.	B.D.L.	0.0	B.D.L.	B.D.L.	B.D.L.	0.0
Mn	5.59	77.0	391.3	746.0	221.1	38.7	307.5	646.0	191.5
Co	2.13	88.6	129.7	156.4	19.3	78.6	119.5	154.0	22.8
Ni	4.44	175.4	245.2	287.0	29.5	182.6	242.6	293.0	27.0
Cu	1.76	B.D.L.	10.6	61.1	18.1	B.D.L.	10.2	93.4	21.1
Zn	5.57	20.3	61.6	95.4	23.1	18.5	57.3	90.9	21.5
Ga	0.94	B.D.L.	2.2	3.8	1.0	B.D.L.	2.4	4.1	0.8
Ge	2.19	21.0	22.9	26.2	1.3	21.2	23.8	26.9	1.3
As	5.51	B.D.L.	B.D.L.	7.1	0.9	B.D.L.	B.D.L.	B.D.L.	0.0
Rb	1.09	B.D.L.	B.D.L.	B.D.L.	0.0	B.D.L.	B.D.L.	B.D.L.	0.0
Sr	0.08	0.4	1.9	4.0	1.0	0.2	1.7	5.5	1.2
Y	0.99	B.D.L.	2.4	7.5	2.1	B.D.L.	1.8	4.2	0.9
Zr	0.08	B.D.L.	4.7	98.0	20.3	0.3	0.6	1.6	0.3
Nb	0.27	0.8	5.0	14.5	3.8	0.8	4.1	11.1	2.7
Mo	1.42	B.D.L.	B.D.L.	4.3	0.9	B.D.L.	B.D.L.	1.9	0.3
Ag	1.73	B.D.L.	B.D.L.	B.D.L.	0.0	B.D.L.	B.D.L.	B.D.L.	0.0
Cd	0.36	B.D.L.	B.D.L.	B.D.L.	0.0	B.D.L.	B.D.L.	B.D.L.	0.0
Sn	0.95	3.2	4.0	5.6	0.7	2.9	3.8	4.4	0.4
Sb	1.28	B.D.L.	B.D.L.	B.D.L.	0.0	B.D.L.	B.D.L.	B.D.L.	0.0
Ba	0.15	0.2	7.4	47.2	13.0	B.D.L	9.0	118.1	19.8
La	0.21	1.0	5.3	18.7	5.3	0.8	3.3	7.9	1.9
Ce	0.46	1.8	9.8	31.6	9.2	1.9	6.5	15.5	3.4
Pr	0.07	0.2	1.0	3.3	0.9	0.2	0.7	1.6	0.4
Nd	0.27	0.6	3.5	11.1	3.2	0.7	2.4	5.3	1.2
Sm	0.25	B.D.L.	0.5	1.5	0.5	B.D.L.	0.4	0.9	0.2
Eu	0.05	B.D.L.	0.1	0.2	0.1	B.D.L.	B.D.L.	0.1	0.0
Gd	0.18	B.D.L.	0.5	1.4	0.4	B.D.L.	0.4	0.9	0.2
Tb	0.06	B.D.L.	0.1	0.2	0.1	B.D.L.	B.D.L.	0.1	0.0
Dy	0.20	B.D.L.	0.4	1.1	0.3	B.D.L.	0.3	0.7	0.2

Ho	0.08	B.D.L.	0.1	0.4	0.1	B.D.L.	B.D.L.	0.2	0.0
Er	0.15	B.D.L.	0.2	0.9	0.2	B.D.L.	0.2	0.4	0.1
Tm	0.09	B.D.L.	B.D.L.	0.1	0.0	B.D.L.	B.D.L.	B.D.L.	0.0
Yb	0.19	B.D.L.	0.3	0.8	0.2	B.D.L.	0.2	0.6	0.2
Lu	0.08	B.D.L.	B.D.L.	0.2	0.0	B.D.L.	B.D.L.	0.1	0.0
Hf	0.07	B.D.L.	0.1	1.2	0.2	B.D.L.	B.D.L.	B.D.L.	0.0
Ta	0.07	B.D.L.	0.3	1.1	0.2	B.D.L.	B.D.L.	0.7	0.2
Au	0.03	B.D.L.	B.D.L.	B.D.L.	0.0	B.D.L.	B.D.L.	B.D.L.	0.0
Pb	0.44	B.D.L.	B.D.L.	0.7	0.1	B.D.L.	B.D.L.	0.5	0.0
Th	0.31	0.6	6.8	23.4	7.3	0.4	3.5	10.7	2.7
U	0.11	B.D.L.	0.5	2.5	0.6	B.D.L.	B.D.L.	1.8	0.6

		Laco Norte: Surface/ Outcrop							
		Magnetite S2				Magnetite A			
EPMA	D. L.	N= 14				N= 15			
		Min.	Mean	Max.	Std. Dev	Min.	Mean	Max.	Std. Dev
Fe (wt%)	0.02	67.30	69.55	70.98	1.16	64.73	66.88	69.35	1.52
Ti (ppm)	89.46	B.D.L.	B.D.L.	170.00	42.66	B.D.L.	101.61	212.00	58.55
V (ppm)	66.39	359.00	817.57	1208.00	359.81	401.00	532.80	629.00	74.39
Al (ppm)	81.24	115.00	3923.64	39767.00	10549.22	85.00	1108.47	7764.00	1870.72
Mn (ppm)	80.45	B.D.L.	152.72	387.00	110.25	B.D.L.	290.66	504.00	185.19
Mg (ppm)	128.04	2618.00	8795.86	15627.00	3233.57	5956.00	13375.47	20437.00	4745.11
Si (ppm)	68.07	454.00	3642.29	10293.00	3122.77	318.00	11239.27	18839.00	7011.18
P (ppm)	83.51	B.D.L.	110.81	559.00	153.97	B.D.L.	177.47	960.00	227.30
Ca (ppm)	83.73	124.00	1262.29	3261.00	1100.96	B.D.L.	3421.12	5509.00	2036.13
Cr (ppm)	62.61	B.D.L.	B.D.L.	151.00	31.99	B.D.L.	B.D.L.	B.D.L.	0.00
LA-ICP-MS (ppm)	D. L. (ppm)								
Na	56.67	60.00	463.14	856.00	275.85	76.00	832.93	1205.00	385.76
Mg	43.53	503.00	8311.64	11320.00	2744.30	6480.00	11180.00	14800.00	3017.02
Al	36.52	B.D.L.	39.12	110.00	34.36	B.D.L.	377.25	717.00	309.58
Si	2989.50	B.D.L.	7163.91	11500.00	3424.70	B.D.L.	15966.32	33900.00	10620.55
P	9.57	43.00	157.07	371.00	96.54	B.D.L.	187.25	343.00	79.60
K	35.84	B.D.L.	150.57	252.00	80.46	65.00	360.40	594.00	181.36
Ca	738.79	B.D.L.	1763.36	3830.00	1323.37	B.D.L.	3231.92	6500.00	2005.61

Sc	4.90	B.D.L.	B.D.L.	B.D.L.	0.00	B.D.L.	3.12	8.70	1.82
Ti	37.26	B.D.L.	B.D.L.	B.D.L.	0.00	B.D.L.	91.23	191.00	83.25
V	14.33	370.00	638.36	842.00	157.40	404.00	521.53	606.00	66.08
Cr	3.40	B.D.L.	B.D.L.	B.D.L.	0.00	B.D.L.	B.D.L.	3.80	0.54
Mn	5.59	57.10	247.92	374.00	134.16	55.30	305.33	496.00	183.88
Co	2.13	60.50	115.23	153.00	22.39	106.00	128.68	168.00	21.07
Ni	4.44	175.00	227.03	253.00	22.59	188.00	212.60	246.00	17.22
Cu	1.76	B.D.L.	6.21	34.30	10.65	B.D.L.	6.36	29.20	9.95
Zn	5.57	15.60	39.54	56.90	14.24	20.20	55.26	118.00	22.41
Ga	0.94	B.D.L.	B.D.L.	1.54	0.37	B.D.L.	3.14	5.90	2.40
Ge	2.19	21.50	24.35	26.20	1.61	21.50	24.05	27.80	1.80
As	5.51	B.D.L.	22.25	33.40	11.46	B.D.L.	20.37	35.00	9.62
Rb	1.09	B.D.L.	B.D.L.	2.40	0.50	B.D.L.	B.D.L.	1.56	0.34
Sr	0.08	0.79	5.45	13.40	2.94	0.90	6.48	9.70	2.83
Y	0.99	1.68	14.80	24.50	7.25	1.74	30.03	57.60	19.27
Zr	0.08	B.D.L.	0.18	0.64	0.18	B.D.L.	1.76	3.70	1.52
Nb	0.27	1.00	31.23	63.30	22.29	1.25	38.37	74.00	28.00
Mo	1.42	B.D.L.	B.D.L.	3.40	0.86	B.D.L.	1.67	7.50	1.93
Ag	1.73	B.D.L.	B.D.L.	B.D.L.	0.00	B.D.L.	B.D.L.	B.D.L.	0.00
Cd	0.36	B.D.L.	0.48	2.00	0.44	B.D.L.	B.D.L.	B.D.L.	0.00
Sn	0.95	6.20	11.53	15.92	3.65	5.72	14.64	24.30	6.85
Sb	1.28	B.D.L.	2.83	5.11	1.79	B.D.L.	3.34	6.80	2.43
Ba	0.15	0.44	4.14	6.53	1.80	0.73	3.50	6.90	2.41
La	0.21	3.38	31.70	58.20	16.68	1.78	7.23	11.40	2.67
Ce	0.46	12.80	77.81	133.70	37.72	3.26	53.28	86.10	28.73
Pr	0.07	1.02	8.22	14.87	4.31	9.48	119.87	193.00	62.12
Nd	0.27	3.60	29.33	53.50	14.61	0.85	12.81	20.50	6.66
Sm	0.25	B.D.L.	4.27	7.70	2.33	2.66	44.20	80.80	25.04
Eu	0.05	B.D.L.	0.54	0.97	0.29	0.67	6.50	11.50	3.59
Gd	0.18	B.D.L.	3.56	7.40	1.97	B.D.L.	0.69	1.33	0.39
Tb	0.06	B.D.L.	0.44	0.75	0.23	B.D.L.	0.87	1.59	0.51
Dy	0.20	B.D.L.	2.97	4.88	1.53	0.25	5.27	9.80	3.54
Ho	0.08	B.D.L.	0.54	0.87	0.29	B.D.L.	1.16	2.40	0.77
Er	0.15	B.D.L.	1.63	3.00	0.90	0.08	3.67	7.60	2.64
Tm	0.09	B.D.L.	0.25	0.41	0.13	B.D.L.	0.60	1.29	0.49
Yb	0.19	B.D.L.	B.D.L.	2.81	0.89	B.D.L.	4.72	8.80	3.45
Lu	0.08	B.D.L.	0.32	0.52	0.17	B.D.L.	0.76	1.61	0.63
Hf	0.07	B.D.L.	B.D.L.	B.D.L.	0.00	B.D.L.	B.D.L.	0.04	0.00
Ta	0.07		0.19	0.37	0.10	B.D.L.	1.46	2.88	1.17
W	0.49	N.M.	N.M.	N.M.	N.M.	N.M.	N.M.	N.M.	N.M.
Au	0.03	B.D.L.	B.D.L.	B.D.L.	0.00	B.D.L.	B.D.L.	B.D.L.	0.00
Pb	0.44	B.D.L.	B.D.L.	B.D.L.	0.00	B.D.L.	B.D.L.	B.D.L.	0.00
Th	0.31	3.83	40.52	65.10	20.80	3.08	89.72	157.00	56.72
U	0.11	0.37	4.03	6.67	2.11	0.68	7.46	14.30	5.28

Laco Norte		Drill core: Intermediate depths				Drill core: Shallow			
		Magnetite X and Y				Magnetite Z			
EPMA	D. L.	N= 21				N= 14			
		Min.	Mean	Max.	Std. Dev	Min.	Mean	Max.	Std. Dev
Fe (wt%)	0.02	66.47	69.44	70.91	1.36	67.82	70.02	70.93	1.00
Ti (ppm)	89.46	1672.83	2782.03	6271.75	1245.11	900.00	1264.29	1800.00	264.89

V (ppm)	66.39	793.81	894.98	1090.07	85.19	800.00	957.14	1000.00	64.62
Al (ppm)	81.24	1575.32	2722.70	4287.65	773.80	1562.00	2069.14	2670.00	302.57
Mn (ppm)	80.45	B.D.L.	372.04	933.76	263.33	B.D.L	228.57	500.00	216.36
Mg (ppm)	128.04	5021.56	8564.88	13962.82	2825.28	1000.00	7121.43	8900.00	2393.00
Si (ppm)	68.07	76.68	3825.26	11895.99	4221.33	100.00	235.71	900.00	227.38
P (ppm)	83.51	B.D.L.	B.D.L.	B.D.L.	0.00	B.D.L	B.D.L	200.00	53.45
Ca (ppm)	83.73	B.D.L.	1271.86	3789.22	1454.62	B.D.L	B.D.L	B.D.L	0.00
Cr (ppm)	62.61	B.D.L.	B.D.L.	B.D.L.	0.00	B.D.L	B.D.L	B.D.L	0.00
LA-ICP-MS (ppm)	D. L. (ppm)								
Na	56.67	B.D.L.	553.39	2130.00	661.98	B.D.L.	B.D.L.	207.00	48.30
Mg	43.53	5750.00	9442.38	14240.00	2605.09	5520.00	7422.14	9740.00	1610.30
Al	36.52	3660.00	6492.38	9100.00	1387.52	1562.00	2069.14	2670.00	302.57
Si	2989.50	B.D.L.	8861.29	28400.00	7953.87	B.D.L.	10167.09	69000.00	18120.91
P	9.57	10.00	48.44	134.00	37.56	10.16	953.61	9100.00	2399.61
K	35.84	B.D.L.	627.05	3130.00	836.92	B.D.L.	B.D.L.	165.00	47.39
Ca	738.79	B.D.L.	2288.56	9020.00	2491.09	B.D.L.	1630.15	9900.00	2640.57
Sc	4.90	B.D.L.	B.D.L.	8.80	1.99	B.D.L.	3.76	11.20	2.16
Ti	37.26	2040.00	3363.38	5240.00	878.31	B.D.L.	1410.93	2040.00	277.74
V	14.33	1688.00	2027.52	2590.00	248.24	1830.00	2158.71	2410.00	149.93
Cr	3.40	B.D.L.	B.D.L.	6.80	1.04	B.D.L.	B.D.L.	5.20	0.80
Mn	5.59	313.00	561.95	829.00	120.04	122.30	428.16	677.00	152.55
Co	2.13	143.90	155.07	170.00	6.91	89.00	137.79	162.00	20.01
Ni	4.44	272.00	306.38	338.00	18.55	278.00	305.07	350.00	16.96
Cu	1.76	B.D.L.	B.D.L.	B.D.L.	0.00	B.D.L.	B.D.L.	B.D.L.	0.00
Zn	5.57	21.10	47.79	112.00	19.80	41.50	70.38	107.00	17.95
Ga	0.94	34.20	46.26	57.50	6.68	25.00	27.33	30.20	1.68
Ge	2.19	B.D.L.	2.91	4.50	0.86	B.D.L.	2.37	3.90	0.72
As	5.51	B.D.L.	B.D.L.	5.60	2.04	B.D.L.	B.D.L.	38.00	10.03
Rb	1.09	B.D.L.	2.09	22.50	4.90	B.D.L.	B.D.L.	B.D.L.	0.00
Sr	0.08	B.D.L.	3.40	13.80	4.47	B.D.L.	2.00	14.20	3.70
Y	0.99	B.D.L.	2.99	13.70	3.92	B.D.L.	B.D.L.	2.54	0.62
Zr	0.08	0.44	7.80	22.30	7.73	0.44	0.55	1.18	0.22
Nb	0.27	B.D.L.	1.48	4.63	1.52	B.D.L.	B.D.L.	0.45	0.10
Mo	1.42	0.45	1.51	4.50	0.75	B.D.L.	1.70	2.60	0.41
Ag	1.73	B.D.L.	B.D.L.	1.76	0.37	B.D.L.	B.D.L.	B.D.L.	0.00
Cd	0.36	B.D.L.	B.D.L.	B.D.L.	0.00	B.D.L.	B.D.L.	B.D.L.	0.00
Sn	0.95	4.58	6.00	8.10	1.20	4.03	5.44	7.20	0.82
Sb	1.28	B.D.L.	B.D.L.	B.D.L.	0.00	B.D.L.	B.D.L.	B.D.L.	0.00
Ba	0.15	B.D.L.	6.92	26.70	8.88	B.D.L.	4.48	34.00	9.66
La	0.21	B.D.L.	4.57	29.10	7.75	B.D.L.	3.92	29.00	7.53
Ce	0.46	B.D.L.	10.19	53.90	15.28	B.D.L.	9.56	73.00	18.98
Pr	0.07	B.D.L.	0.96	3.84	1.24	B.D.L.	0.90	7.80	2.04
Nd	0.27	B.D.L.	3.32	13.30	4.26	B.D.L.	2.71	24.10	6.31

Sm	0.25	B.D.L.	0.42	2.03	0.63	B.D.L.	B.D.L.	3.10	0.82
Eu	0.05	B.D.L.	B.D.L.	0.27	0.08	B.D.L.	B.D.L.	0.27	0.07
Gd	0.18	B.D.L.	0.34	1.38	0.48	B.D.L.	0.19	2.26	0.60
Tb	0.06	B.D.L.	B.D.L.	0.23	0.07	B.D.L.	B.D.L.	0.30	0.08
Dy	0.20	B.D.L.	0.41	2.05	0.63	B.D.L.	B.D.L.	1.42	0.38
Ho	0.08	B.D.L.	0.08	0.34	0.12	B.D.L.	B.D.L.	0.22	0.06
Er	0.15	B.D.L.	0.22	1.52	0.43	B.D.L.	B.D.L.	0.23	0.06
Tm	0.09	B.D.L.	B.D.L.	0.20	0.05	B.D.L.	B.D.L.	B.D.L.	0.00
Yb	0.19	B.D.L.	0.35	2.00	0.53	B.D.L.	B.D.L.	B.D.L.	0.00
Lu	0.08	B.D.L.	B.D.L.	0.19	0.05	B.D.L.	B.D.L.	B.D.L.	0.00
Hf	0.07	0.11	0.11	0.12	0.00	0.11	0.11	0.11	0.00
Ta	0.07	0.05	0.15	0.43	0.11	B.D.L.	B.D.L.	B.D.L.	0.00
W	0.49	B.D.L.	0.78	5.90	1.54	B.D.L.	0.53	2.06	0.56
Au	0.03	B.D.L.	B.D.L.	B.D.L.	0.00	B.D.L.	B.D.L.	B.D.L.	0.00
Pb	0.44	B.D.L.	B.D.L.	0.49	0.07	B.D.L.	B.D.L.	B.D.L.	0.00
Th	0.31	B.D.L.	1.44	7.01	1.95	B.D.L.	1.31	6.40	1.58
U	0.11	B.D.L.	0.46	1.87	0.68	B.D.L.	0.22	1.16	0.37

		Laco Norte: Deep Drill core							
		Magnetite Alpha				Magnetite Beta			
EPMA	D. L.	N= 9				N= 20			
		Min.	Mean	Max.	Std. Dev	Min.	Mean	Max.	Std. Dev
Fe (wt%)	0.02	68.72	69.96	71.18	0.84	67.91	69.50	70.41	0.77
Ti (ppm)	89.46	3826.61	8389.02	16586.21	4205.36	755.45	5860.43	15432.87	3012.86
V (ppm)	66.39	1170.52	1330.50	1589.70	151.37	1059.68	1288.89	1439.84	75.62
Al (ppm)	81.24	4870.00	6127.78	6960.00	728.11	1315.25	2111.78	2921.76	393.52
Mn (ppm)	80.45	B.D.L.	B.D.L.	274.64	91.55	B.D.L.	294.25	967.80	282.76
Mg (ppm)	128.04	712.78	2484.46	4351.13	1071.58	1636.74	5997.97	9638.92	1939.45
Si (ppm)	68.07	100.67	130.25	184.40	25.20	111.49	760.12	6052.66	1422.92
P (ppm)	83.51	B.D.L.	B.D.L.	B.D.L.	B.D.L.	B.D.L.	B.D.L.	B.D.L.	0.00
Ca (ppm)	83.73	B.D.L.	B.D.L.	124.90	41.63	B.D.L.	679.10	4258.66	1255.68
Cr (ppm)	62.61	B.D.L.	B.D.L.	B.D.L.	0.00	B.D.L.	B.D.L.	B.D.L.	0.00
LA-ICP-MS (ppm)	D. L. (ppm)								
Na	56.67	B.D.L.	B.D.L.	103.00	27.88	B.D.L.	448.65	4310.00	930.72
Mg	43.53	881.00	2534.33	4490.00	1110.76	5610.00	8124.50	10130.00	1363.01
Al	36.52	4870.00	6127.78	6960.00	728.11	5086.00	5863.80	6350.00	379.85
Si	2989.50	B.D.L.	B.D.L.	9100.00	2383.40	B.D.L.	3522.83	9900.00	2119.59
P	9.57	10.16	29.74	117.00	35.60	10.16	41.98	107.00	32.06
K	35.84	B.D.L.	B.D.L.	45.00	17.65	B.D.L.	130.36	351.00	117.26
Ca	738.79	B.D.L.	794.15	3700.00	1098.80	B.D.L.	B.D.L.	1880.00	485.98
Sc	4.90	B.D.L.	5.29	11.10	2.47	B.D.L.	7.30	11.60	2.55

Ti	37.26	6540.00	11537.78	20200.00	5365.23	7680.00	8654.00	9870.00	547.66
V	14.33	2580.00	2978.00	3690.00	423.21	2690.00	2957.40	3400.00	207.25
Cr	3.40	B.D.L.	8.13	42.70	13.07	B.D.L.	4.69	10.00	2.60
Mn	5.59	55.60	115.31	186.00	46.41	441.00	606.75	872.00	130.72
Co	2.13	141.20	159.74	174.40	11.10	120.80	148.88	171.30	13.68
Ni	4.44	402.00	440.00	476.00	29.64	344.00	391.67	428.00	24.13
Cu	1.76	B.D.L.	1.93	9.40	2.82	B.D.L.	B.D.L.	2.68	0.66
Zn	5.57	64.20	74.14	90.60	11.21	65.40	93.64	127.00	14.43
Ga	0.94	29.20	34.51	38.50	2.47	39.70	45.51	50.50	2.66
Ge	2.19	2.30	3.00	4.30	0.64	B.D.L.	2.36	3.11	0.51
As	5.51	B.D.L.	B.D.L.	B.D.L.	0.00	B.D.L.	B.D.L.	11.40	2.63
Rb	1.09	B.D.L.	B.D.L.	B.D.L.	0.00	B.D.L.	B.D.L.	2.83	0.79
Sr	0.08	B.D.L.	0.46	4.10	1.37	0.00	1.57	8.40	2.31
Y	0.99	B.D.L.	B.D.L.	4.41	1.41	B.D.L.	1.07	4.47	1.21
Zr	0.08	B.D.L.	2.64	6.80	1.87	0.90	4.53	12.20	3.48
Nb	0.27	B.D.L.	0.54	1.29	0.41	B.D.L.	0.68	1.97	0.52
Mo	1.42	B.D.L.	1.47	2.00	0.20	1.40	1.41	1.51	0.02
Ag	1.73	B.D.L.	B.D.L.	B.D.L.	0.00	B.D.L.	B.D.L.	B.D.L.	0.00
Cd	0.36	B.D.L.	B.D.L.	B.D.L.	0.00	B.D.L.	B.D.L.	B.D.L.	1.00
Sn	0.95	3.26	4.93	6.28	0.87	3.49	4.56	5.80	0.60
Sb	1.28	B.D.L.	B.D.L.	B.D.L.	0.00	B.D.L.	B.D.L.	1.37	0.35
Ba	0.15	B.D.L.	B.D.L.	0.36	0.12	B.D.L.	2.97	36.00	7.89
La	0.21	B.D.L.	B.D.L.	0.94	0.31	B.D.L.	1.07	3.67	1.18
Ce	0.46	B.D.L.	B.D.L.	2.31	0.76	B.D.L.	2.62	10.23	3.05
Pr	0.07	B.D.L.	B.D.L.	0.38	0.13	B.D.L.	0.36	1.88	0.51
Nd	0.27	B.D.L.	B.D.L.	1.08	0.36	B.D.L.	1.50	7.20	2.08
Sm	0.25	B.D.L.	B.D.L.	0.94	0.31	B.D.L.	B.D.L.	1.45	0.36
Eu	0.05	B.D.L.	B.D.L.	0.07	0.02	B.D.L.	B.D.L.	0.10	0.02
Gd	0.18	B.D.L.	0.19	1.74	0.58	B.D.L.	B.D.L.	1.21	0.32
Tb	0.06	B.D.L.	B.D.L.	0.12	0.04	B.D.L.	B.D.L.	0.09	0.03
Dy	0.20	B.D.L.	B.D.L.	1.45	0.48	B.D.L.	B.D.L.	1.02	0.26
Ho	0.08	B.D.L.	B.D.L.	0.20	0.07	B.D.L.	B.D.L.	0.14	0.04
Er	0.15	B.D.L.	B.D.L.	0.46	0.15	B.D.L.	B.D.L.	0.48	0.13
Tm	0.09	B.D.L.	B.D.L.	0.14	0.05	B.D.L.	B.D.L.	B.D.L.	0.00
Yb	0.19	B.D.L.	B.D.L.	1.01	0.34	B.D.L.	B.D.L.	0.20	0.06
Lu	0.08	B.D.L.	B.D.L.	0.14	0.05	B.D.L.	B.D.L.	B.D.L.	0.00
Hf	0.07	0.11	0.11	0.11	0.00	0.11	0.11	0.18	0.02
Ta	0.07	0.05	0.31	0.81	0.29	B.D.L.	0.15	0.32	0.08
W	0.49	B.D.L.	B.D.L.	B.D.L.	0.00	B.D.L.	B.D.L.	B.D.L.	0.00
Au	0.03	B.D.L.	B.D.L.	B.D.L.	0.00	B.D.L.	B.D.L.	B.D.L.	0.00
Pb	0.44	B.D.L.	B.D.L.	0.71	0.15	B.D.L.	B.D.L.	0.84	0.15
Th	0.31	B.D.L.	B.D.L.	2.03	0.67	B.D.L.	1.06	3.30	1.06
U	0.11	B.D.L.	B.D.L.	0.29	0.10	B.D.L.	0.26	0.90	0.27

Table 3.2. Summary of compositions of apatite from outcrop samples at Cristales Grandes, Rodados Negros, and Laco Sur.

		Cristales Grandes							
		Purple luminescence/				Blue luminescence/			
		Gray in BSE				Light gray in BSE			
EPMA	D. L.	N= 145				N= 12			
		Min.	Mean	Max.	Std. Dev	Min.	Mean	Max.	Std. Dev
CaO (wt%)	0.09	49.87	53.43	54.68	0.88	52.33	53.12	53.64	0.37
P_2O_5 (wt%)	0.17	36.75	39.81	41.51	0.91	38.56	39.25	40.37	0.45
F (wt%)	0.27	2.06	3.16	3.98	0.22	2.89	3.10	3.44	0.18
Cl (wt%)	0.02	0.65	0.80	1.16	0.08	0.65	0.69	0.73	0.03
Calc. OH (wt%)	N/A	0.00	0.17	2.04	0.18	0.00	1.70	0.50	0.14
S (ppm)	155.50	B.D.L.	2383.70	4791.05	917.53	1104.55	1821.68	2456.95	416.68
Si (ppm)	245.50	B.D.L.	2923.29	4781.43	1078.02	3183.10	4876.86	5487.07	628.34
Na (ppm)	369.50	B.D.L.	2159.64	4420.76	1126.91	644.24	952.94	1573.49	237.03
Al (ppm)	236.10	B.D.L.	B.D.L.	3845.97	335.94	B.D.L.	B.D.L.	B.D.L.	B.D.L.
Mg (ppm)	250.30	B.D.L.	B.D.L.	368.63	106.71	B.D.L.	B.D.L.	B.D.L.	B.D.L.
Fe (ppm)	828.30	B.D.L.	B.D.L.	1374.48	274.92	B.D.L.	B.D.L.	833.40	240.58
LA-ICP-MS (ppm)	D. L. (ppm)								
Na	29.91	1063.00	1924.60	4540.00	579.28	919.00	1238.83	1600.00	204.67
Mg	0.87	141.30	206.33	310.00	24.67	88.30	159.75	214.30	41.52
Al	5.24	B.D.L.	10.78	555.00	59.14	B.D.L.	3.00	7.10	1.29
Si	2616.06	B.D.L.	6453.76	66200.00	7012.24	B.D.L.	8786.01	52600.00	14110.85
K	9.06	B.D.L.	11.82	300.00	28.45	B.D.L.	18.44	140.00	39.34
V	0.90	7.83	46.44	103.60	27.37	9.30	19.12	42.10	10.94
Mn	2.55	75.60	94.39	171.00	11.27	83.60	91.32	103.60	5.76
Fe	34.20	667.00	922.97	14100.00	1111.14	675.00	761.00	825.00	46.37
Ni	0.97	B.D.L.	2.07	6.00	0.81	B.D.L.	2.30	5.00	1.13
Ge	2.22	7.50	18.00	32.50	6.16	10.60	19.85	32.30	7.47
As	4.77	66.60	120.77	321.00	38.99	87.60	294.63	1155.00	375.17
Sr	0.07	402.00	485.00	774.00	78.59	429.00	447.67	463.00	11.43
Y	0.05	280.00	759.95	1270.00	280.99	474.00	793.08	1132.00	232.25
Zr	0.05	B.D.L.	0.61	7.00	0.67	B.D.L.	0.49	1.24	0.43
Ba	0.10	0.32	1.13	3.70	0.50	0.57	0.93	1.59	0.34
La	0.10	2673.00	4279.85	8670.00	1189.10	3030.00	4297.58	6240.00	1210.80
Ce	0.06	2456.97	4004.35	6265.04	879.70	4210.00	6355.00	9840.00	2109.12
Pr	0.02	256.00	570.53	1352.00	213.13	342.00	571.75	984.00	218.25
Nd	0.08	767.00	1901.03	4200.00	686.57	1172.00	1904.50	3190.00	722.88
Sm	0.06	91.80	299.53	1066.00	160.70	168.00	267.20	466.00	103.73
Eu	0.04	10.12	20.81	53.00	7.93	14.30	19.34	29.10	4.92
Gd	0.05	74.90	230.68	509.00	90.38	127.60	221.48	377.00	81.84
Tb	0.02	8.11	30.80	117.00	18.45	15.20	26.21	44.70	9.80
Dy	0.04	42.80	158.80	400.00	78.74	82.40	137.27	236.00	49.16

Ho	0.01	8.37	31.95	123.70	19.91	15.60	26.70	46.00	9.60
Er	0.03	20.80	81.61	335.00	52.01	37.50	67.56	110.40	23.29
Tm	0.02	2.45	11.41	54.40	8.20	4.80	8.49	14.80	3.00
Yb	0.05	14.40	65.68	337.00	49.27	32.40	50.26	85.40	16.25
Lu	0.01	2.05	11.51	135.70	18.81	4.38	6.22	11.42	2.10
Hf	0.03	B.D.L.	0.26	3.10	0.39	B.D.L.	0.17	0.33	0.10
Ta	0.01	B.D.L.	0.05	0.26	0.04	B.D.L.	0.06	0.19	0.05
Th	0.03	B.D.L.	561.10	17100.00	1458.91	174.90	323.06	625.00	132.66
U	0.01	B.D.L.	33.73	667.00	74.40	9.29	28.62	61.40	17.13
Total REEs	N/A	7699.18	14121.19	31676.80	4608.33	9705.38	13959.55	21674.82	4525.57

		Rodados Negros							
		Purple/ mauve luminescence/				Orange luminescence/			
		Non-porous apatite				Mottled/ porous apatite			
EPMA	D. L.	N= 59				N=11			
		Min.	Mean	Max.	Std. Dev	Min.	Mean	Max.	Std. Dev
CaO (wt%)	0.09	47.48	53.01	53.85	1.16	44.54	51.86	53.66	2.64
P_2O_5 (wt%)	0.17	34.51	39.05	40.13	0.88	34.37	39.62	40.71	1.84
F (wt%)	0.27	2.33	3.10	3.64	0.27	2.07	2.51	2.86	0.23
Cl (wt%)	0.02	0.82	1.00	2.05	0.24	1.76	2.10	2.66	0.26
Calc. OH (wt%)	N/A	0.00	0.04	0.36	0.09	0.00	0.03	0.19	0.06
S (ppm)	155.50	0.00	2080.64	3806.84	1207.70	0.00	1922.42	3777.30	1396.56
Si (ppm)	245.50	0.00	2674.70	8304.48	1530.96	0.00	2749.31	7105.50	2037.85
Na (ppm)	369.50	0.00	1502.46	2518.32	670.31	0.00	1222.62	2052.96	720.53
Al (ppm)	236.10	0.00	573.00	10129.21	1884.19	0.00	4669.78	49579.36	14898.38
Mg (ppm)	250.30	0.00	122.07	671.99	194.84	0.00	178.45	928.36	299.37
Fe (ppm)	828.30	0.00	940.65	6650.07	1638.36	0.00	3139.44	26934.56	8137.43
LA-ICP-MS (ppm)	D. L. (ppm)								
Na	29.91	1126.00	1582.10	2282.00	307.55	847.00	1459.82	2100.00	420.96
Mg	0.87	130.50	186.49	292.00	41.06	135.40	314.04	650.00	130.96
Al	5.24	B.D.L.	270.99	2680.00	586.73	B	1229.15	2420.00	813.01
Si	2616.06	B.D.L.	5123.54	27700.00	3755.01	B	3720.37	5800.00	1762.39
K	9.06	B.D.L.	91.66	2200.00	319.27	4.53	10.87	29.00	9.02
V	0.90	33.20	60.95	96.70	13.93	16.40	38.50	59.20	14.36
Mn	2.55	58.70	118.79	343.00	69.97	80.70	186.56	291.80	63.77
Fe	34.20	722.00	1170.42	6380.00	889.68	722.00	2040.45	4330.00	1126.71
Ni	0.97	B.D.L.	2.91	10.20	1.82	B.D.L.	7.01	13.10	4.32
Ge	2.22	8.40	15.92	22.50	2.63	8.40	14.43	25.40	4.64
As	4.77	68.70	110.11	206.00	29.62	90.80	122.79	222.00	47.02
Sr	0.07	347.00	480.94	858.00	105.46	356.00	491.91	845.00	164.34
Y	0.05	420.00	582.23	1057.00	122.51	402.00	527.82	800.00	144.16
Zr	0.05	B.D.L.	0.21	0.90	0.14	B.D.L.	0.14	0.33	0.10
Ba	0.10	0.35	6.51	101.00	15.45	0.98	17.95	87.00	24.17

La	0.10	2160.00	3852.32	7540.00	1502.55	1250.00	3235.27	6530.00	1845.79
Ce	0.06	3520.00	5725.33	11010.00	2136.71	2330.00	4905.45	9480.00	2499.70
Pr	0.02	297.00	485.97	1097.00	217.11	240.00	448.64	935.00	237.87
Nd	0.08	888.00	1324.58	2490.00	406.99	701.00	1208.36	2070.00	464.03
Sm	0.06	117.20	170.11	298.00	43.00	110.80	165.80	282.00	55.18
Eu	0.04	11.15	18.33	36.00	7.02	11.74	20.82	32.60	7.43
Gd	0.05	95.20	156.68	306.00	55.55	95.20	163.97	270.00	54.83
Tb	0.02	10.08	16.82	37.00	6.35	10.51	18.04	30.70	6.68
Dy	0.04	47.80	81.15	184.00	29.96	52.00	88.35	138.20	30.36
Ho	0.01	10.17	16.14	34.60	5.21	10.76	17.06	27.10	5.57
Er	0.03	25.10	41.34	88.90	14.25	26.50	43.68	69.50	14.91
Tm	0.02	3.23	6.26	15.80	3.19	3.61	7.16	12.90	3.15
Yb	0.05	20.40	36.11	90.50	16.98	20.80	40.18	77.80	18.04
Lu	0.01	2.35	4.32	10.78	2.08	2.66	4.87	9.74	2.16
Hf	0.03	B.D.L.	0.09	0.33	0.07	B.D.L.	0.12	0.27	0.09
Ta	0.01	B.D.L.	0.02	0.07	0.01	B.D.L.	0.02	0.07	0.02
Th	0.03	128.90	395.33	1690.00	383.04	43.50	421.50	1430.00	488.42
U	0.01	8.68	23.18	80.30	17.82	5.75	23.62	64.50	20.03
Total REEs	N/A	7390.27	11935.48	22604.39	4419.18	4961.99	10367.67	19911.34	5204.54

		Laco Sur							
		Bright luminescence/				Dark luminescence/			
		Low S				High S			
EPMA	D. L.	N=62				N=23			
		Min.	Mean	Max.	Std. Dev	Min.	Mean	Max.	Std. Dev
CaO (wt%)	0.09	51.67	54.47	55.51	0.58	50.46	53.27	55.06	1.09
P_2O_5 (wt%)	0.17	39.11	41.16	42.80	0.72	37.64	39.40	40.53	0.82
F (wt%)	0.27	3.08	3.85	5.31	0.38	3.38	4.42	5.40	0.53
Cl (wt%)	0.02	0.26	0.55	0.74	0.12	B.D.L.	0.12	0.54	0.13
Calc. OH (wt%)	N/A	0.00	0.01	0.24	0.05	B.D.L.	0.01	0.10	0.02
S (ppm)	155.50	933.37	2221.27	4860.17	1133.32	4537.44	7997.11	11341.79	1655.10
Si (ppm)	245.50	382.37	731.29	1472.90	168.89	B.D.L.	378.93	1005.46	283.66
Na (ppm)	369.50	873.17	2425.37	6265.75	1114.42	3910.34	5831.25	8479.46	1185.61
Al (ppm)	236.10	B.D.L.	B.D.L.	B.D.L.	B.D.L.	B.D.L.	B.D.L.	B.D.L.	B.D.L.
Mg (ppm)	250.30	B.D.L.	B.D.L.	B.D.L.	B.D.L.	B.D.L.	B.D.L.	B.D.L.	B.D.L.
Fe (ppm)	828.30	4733.82	7626.55	13312.21	1955.31	6553.50	11379.85	41628.06	6967.74
Ce (ppm)	1201.80	0.00	2562.67	3786.47	668.44	B.D.L.	B.D.L.	2037.10	735.68

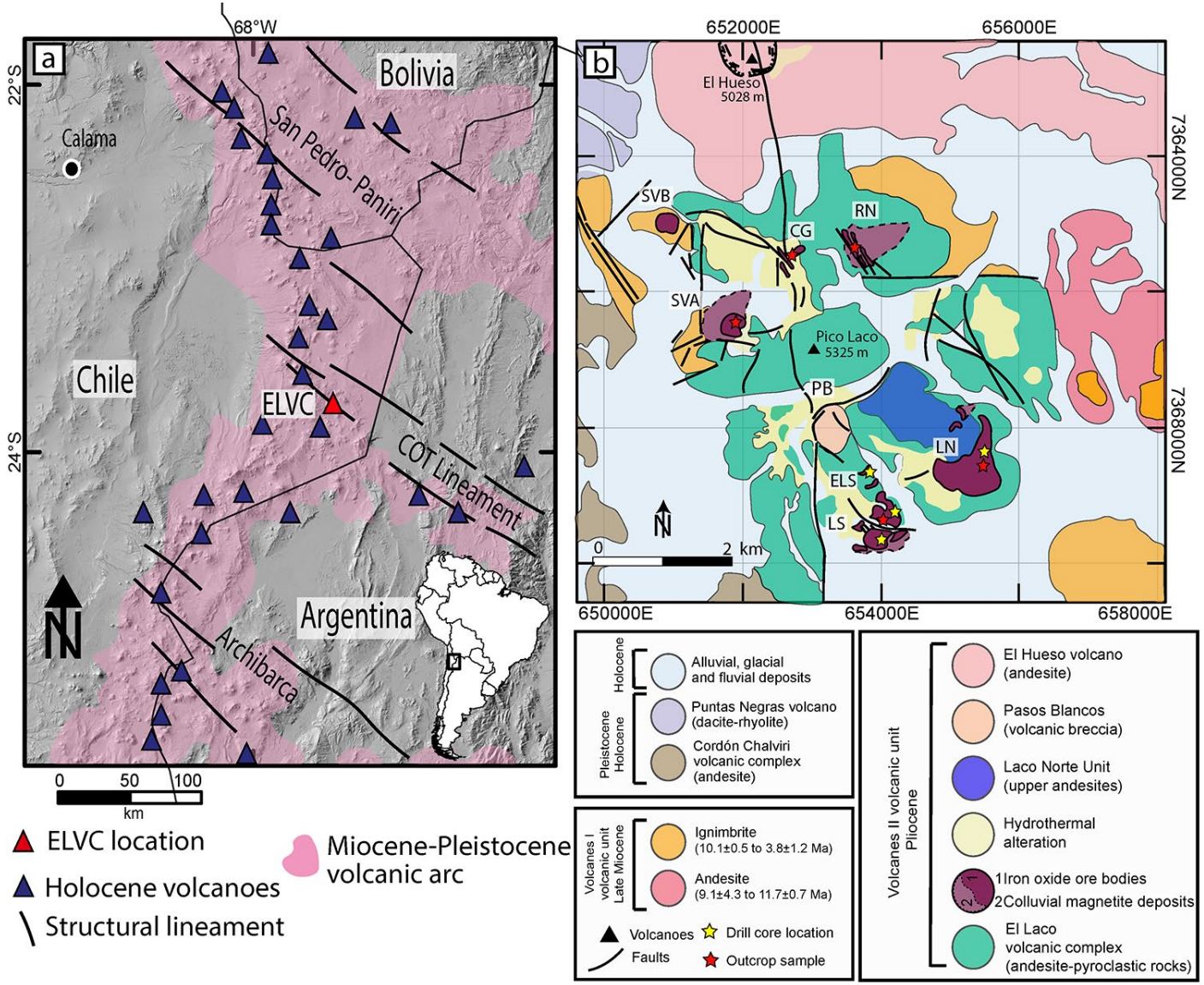

Figure 3.1. Maps showing (A) the location of the El Laco Volcanic Complex in the Miocene-Pleistocene volcanic arc on the western coast of South America, and (B) the locations of ore bodies, and drill core and outcrop samples analyzed in this study.

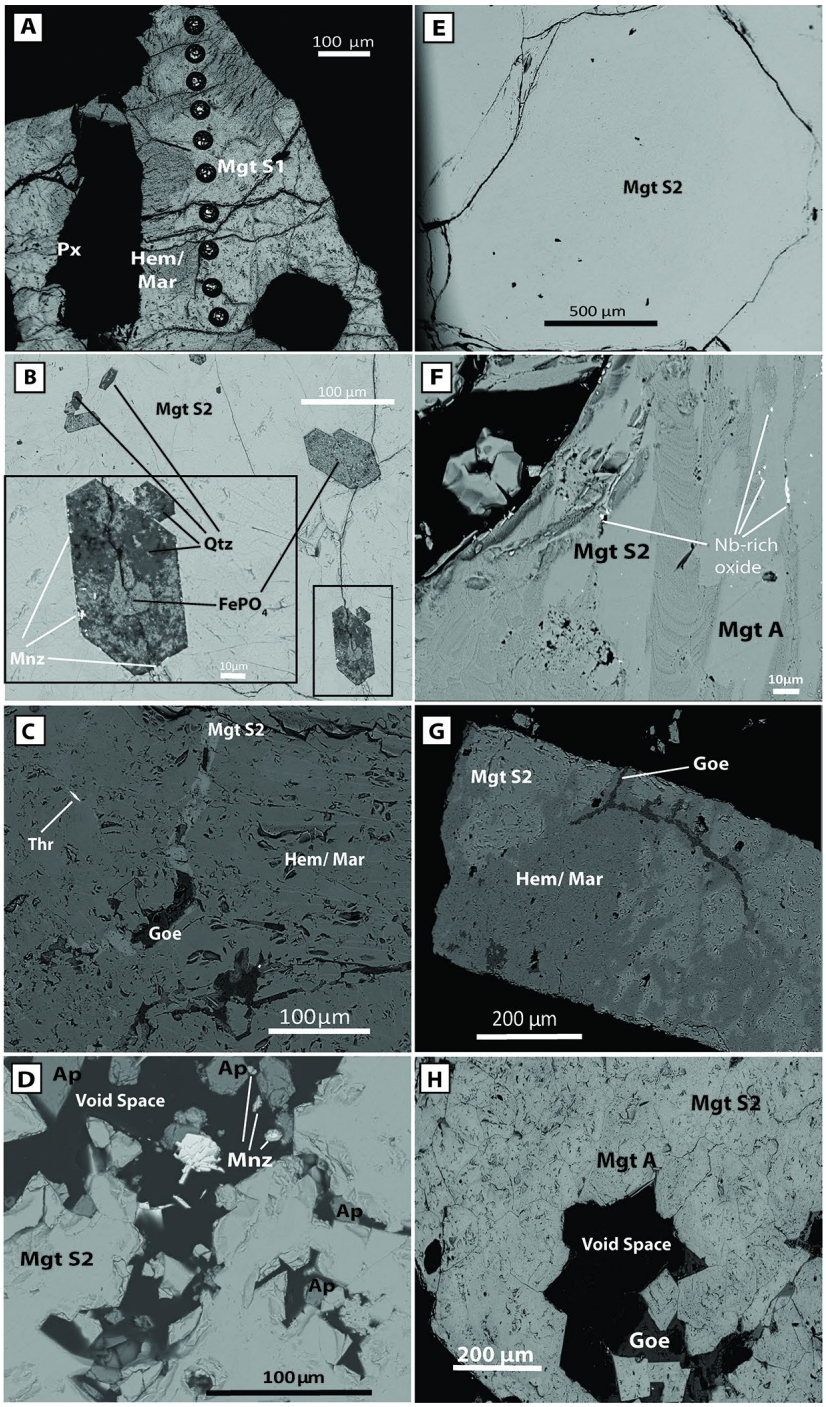

Figure 3.2. Representative backscattered electron (BSE) images of surface and drill core samples from ore bodies at El Laco. (A) Sample from Cristales Grandes containing magnetite (Mgt S1), which is altered to hematite (Hem)/martite (mar), and pyroxene (px). Craters from the LA-ICP-MS transect are visible in image. (B) Sample from San Vicente Alto showing magnetite (Mgt S2) with euhedral hexagonal iron phosphate ($FePO_4$) intergrowths, which are paragentically early and formed pre- or syn-magnetite. The $FePO_4$ intergrowths also contain monazite (Mnz) grains at the $FePO_4$ grain boundaries between the magnetite and and interspersed within the grain. Finally, some $FePO_4$ grains contain quartz (Qtz), which is paragenetically later than the $FePO_4$ (because the

$FePO_4$ is enveloped by the quartz, as highlighted in the inset). (C) Sample from Laco Norte containing magnetite, hematite, goethite (Goe) and thorite inclusions (Thr). (D) Sample from Laco Sur containing apatite (Ap) and monazite inclusions. (E) Massive magnetite grains from Rodados Negros that are subhedral and inclusion free. (F) Sample from Laco Sur containing magnetite, patches of magnetite with high Si and Mg content, and Nb-rich oxide inclusions in cracks and at the boundary of the two generations of magnetite. (G) Sample from Laco Sur containing magnetite, hematite, and goethite (Goe). (H) Sample from Laco Norte containing magnetite Mgt A and Mgt S2, and goethite (Goe).

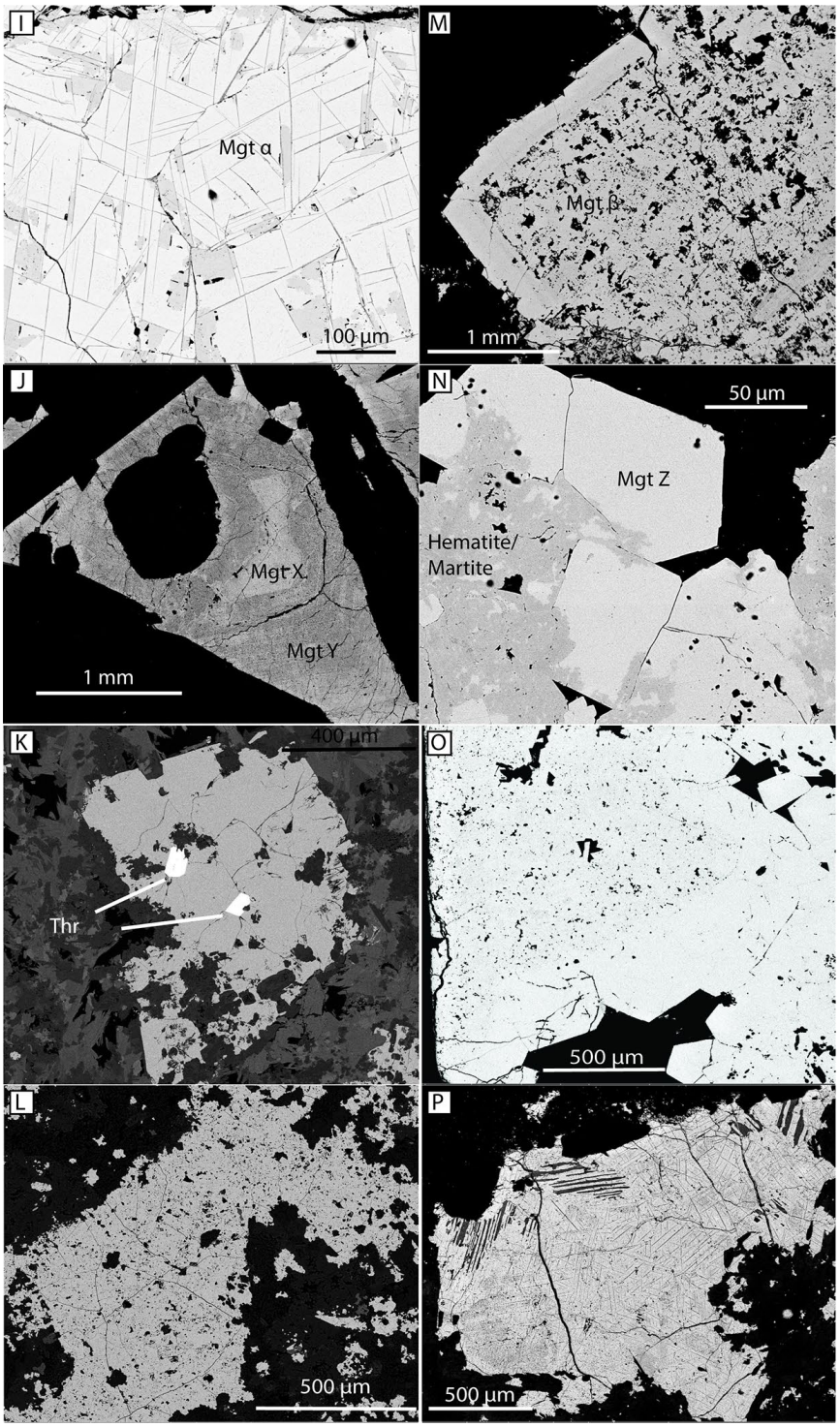

Figure 3.2. (I) Sample from deep zone of Laco Norte showing an aggregate of titanomagnetite crystals (Mgt-α) displaying trellis-textured ilmenite exsolution lamellae. (J) Sample from intermediate zone of Laco Norte showing a partially-dissolved magnetite (Mgt-X) core, which is overgrown by a later magnetite (Mgt-Y) defined by containing oscillatory textures of inclusion-rich and inclusion-poor alternating growth zones. (K-L) Samples from intermediate zones of Laco Sur that correspond to a magnetite-scapolite-pyroxene-rich zone. Thorite inclusions are common in this zone (K). (M) Sample from the deep zone of Laco Norte showing a euhedral core of

inclusion-rich Magnetite-β surrounded by a rim of inclusion-poor magnetite. (N) Sample from the shallow zone of Laco Norte containing an aggregate of inclusion-poor Magnetite-Z grains, partially oxidized to martite/ hematite. (O) Sample from shallow depths of Laco Sur showing a coarse magnetite grain containing an inclusion-rich core surrounded by a rim of inclusion-poor magnetite. (P) Sample from the deep zone of Laco Sur displaying titanomagnetite (Mgt-α) grains from the breccia matrix, which contain well-developed ilmenite exsolution lamellae that exhibit both trellis and sandwich textures.

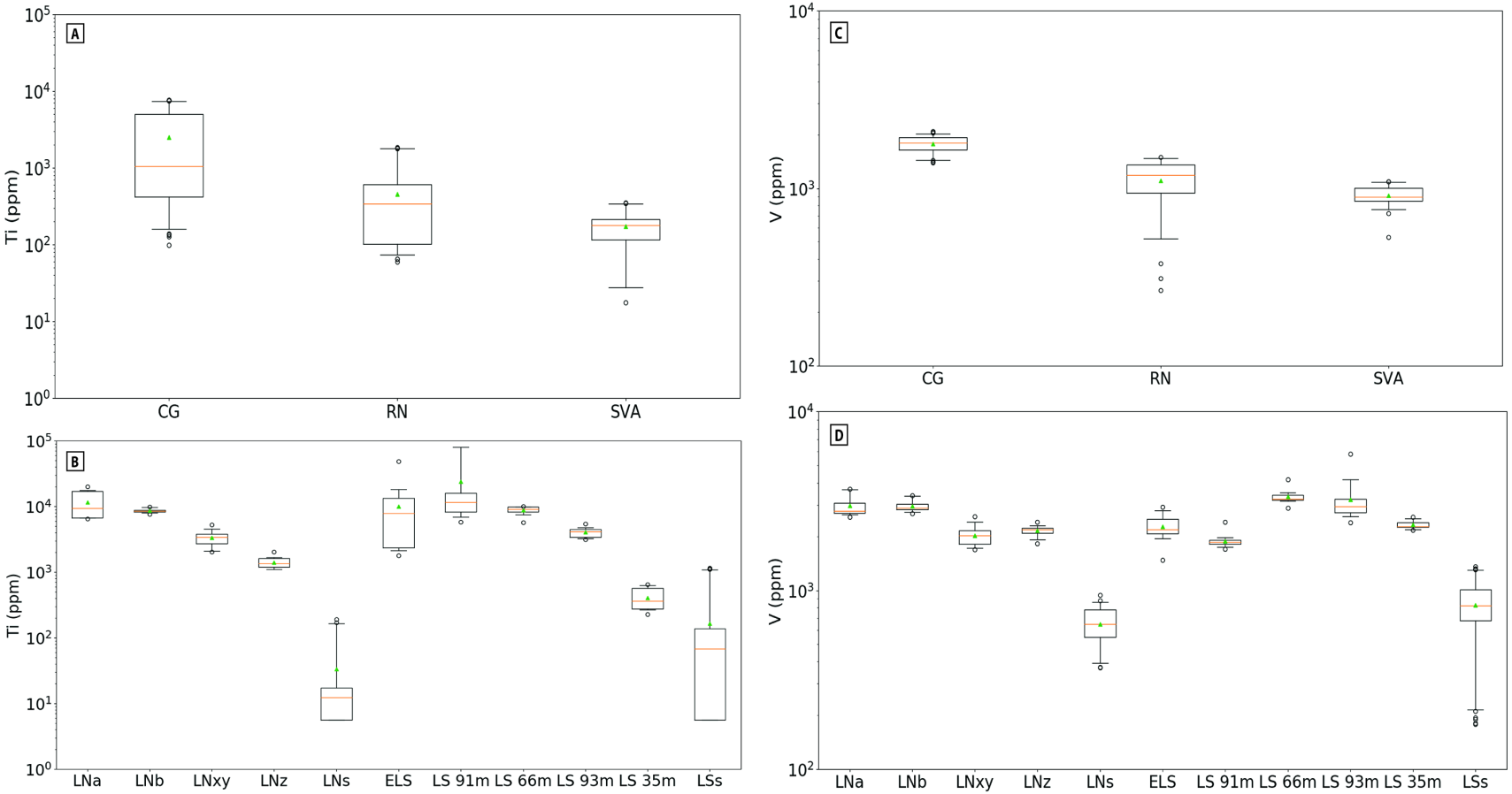

Figure 3.3. Minor and trace element geochemistry of magnetite from surface samples from the Cristales Grandes (CG), Rodados Negros (RN), and San Vicente Alto (SVA) ore bodies from the El Laco deposit (A, C, E, G, I).. Data for magnetite from surface outcrops and drill core samples from the Laco Norte (LN), Extension Laco Sur (ELS), and Laco Sur (LS) ore bodies are displayed in B, D, F, H, J Textural varieties of magnetite from LN are denoted by the same symbols as in Fig. 3.2 (α, β, X, Y, Z, S). Additionally, the drill core depths for the samples from LS are indicated, e.g., 91m. The orange line in the boxes represent the median concentrations and the green triangles represent the mean values. The upper and lower margins of the box identify the upper and lower fifty percent of the data, while the whiskers show the range of concentrations for ninety-five percent of the data.

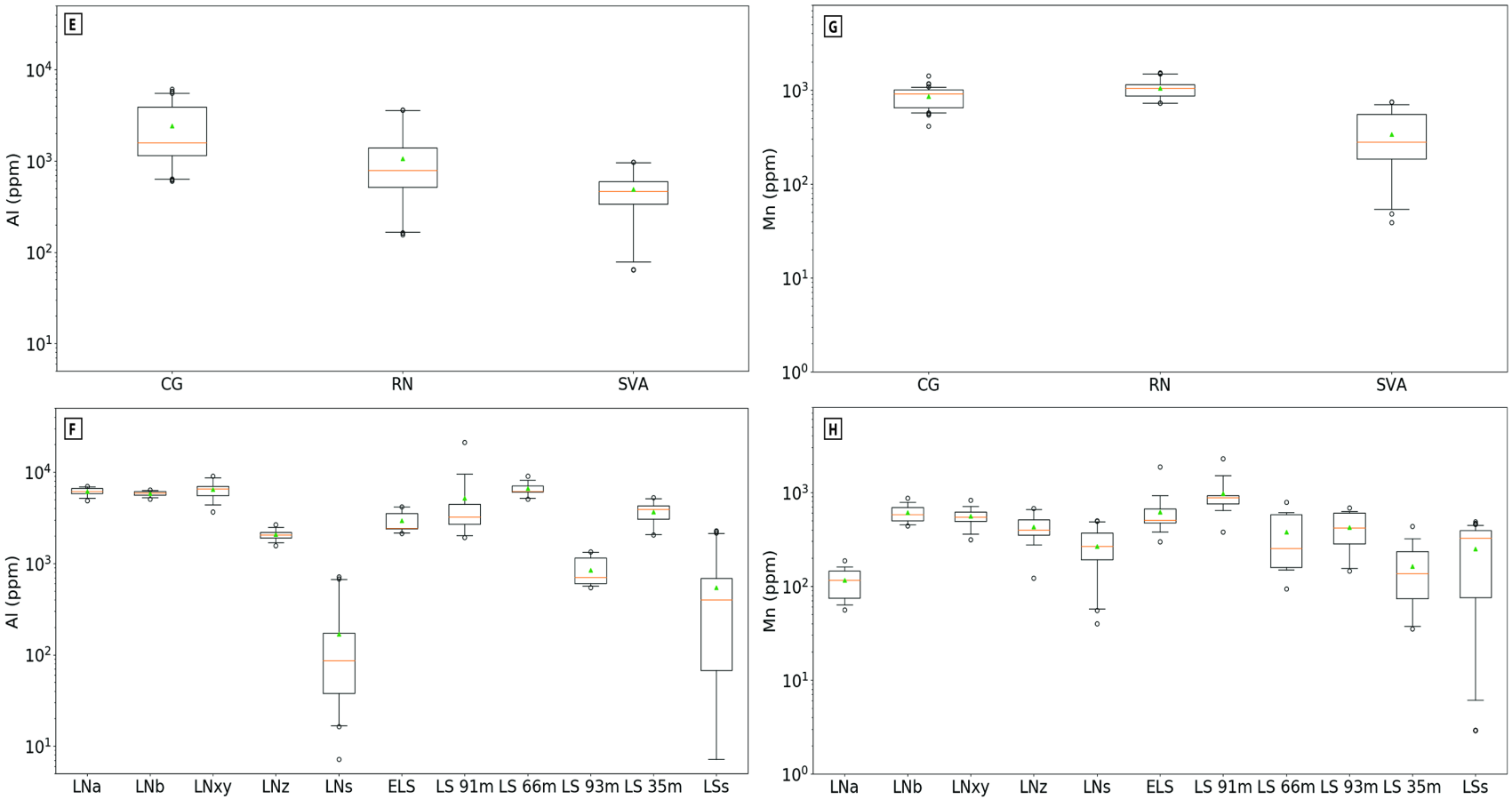
E
Al (ppm)
10^4
10^3
10^2
10^1
CG
RN
SVA
G
Mn (ppm)
10^3
10^2
10^1
10^0
CG
RN
SVA
F
Al (ppm)
10^4
10^3
10^2
10^1
LNa
LNb
LNxy
LNz
LNs
ELS
LS 91m
LS 66m
LS 93m
LS 35m
LSs
H
Mn (ppm)
10^3
10^2
10^1
10^0
LNa
LNb
LNxy
LNz
LNs
ELS
LS 91m
LS 66m
LS 93m
LS 35m
LSs

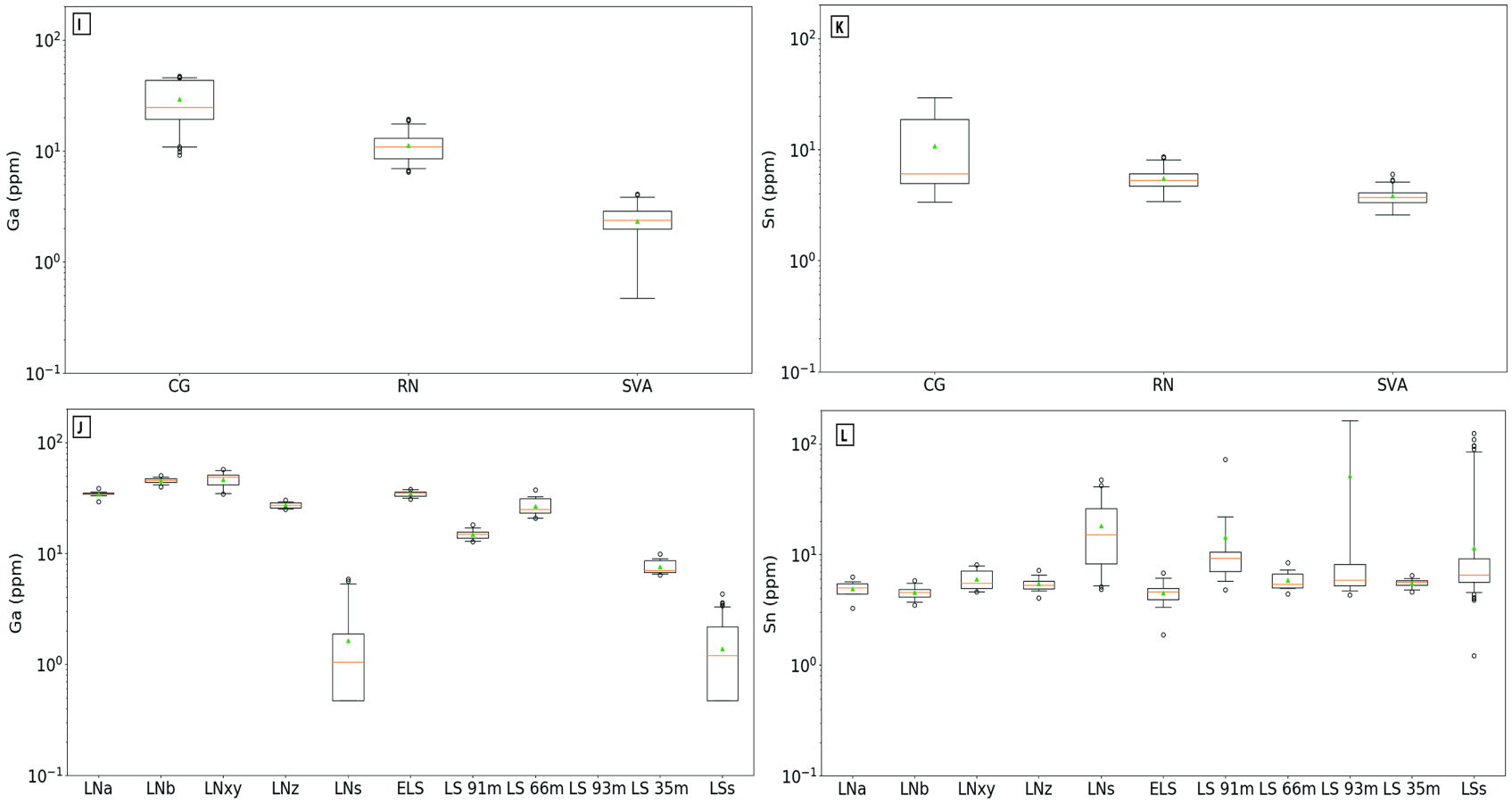
I
Ga (ppm)
10^2
10^1
10^0
10^{-1}
CG
RN
SVA
K
Sn (ppm)
10^2
10^1
10^0
10^{-1}
CG
RN
SVA
J
Ga (ppm)
10^2
10^1
10^0
10^{-1}
LNa
LNb
LNxy
LNz
LNs
ELS
LS 91m
LS 66m
LS 93m
LS 35m
LSs
L
Sn (ppm)
10^2
10^1
10^0
10^{-1}
LNa
LNb
LNxy
LNz
LNs
ELS
LS 91m
LS 66m
LS 93m
LS 35m
LSs

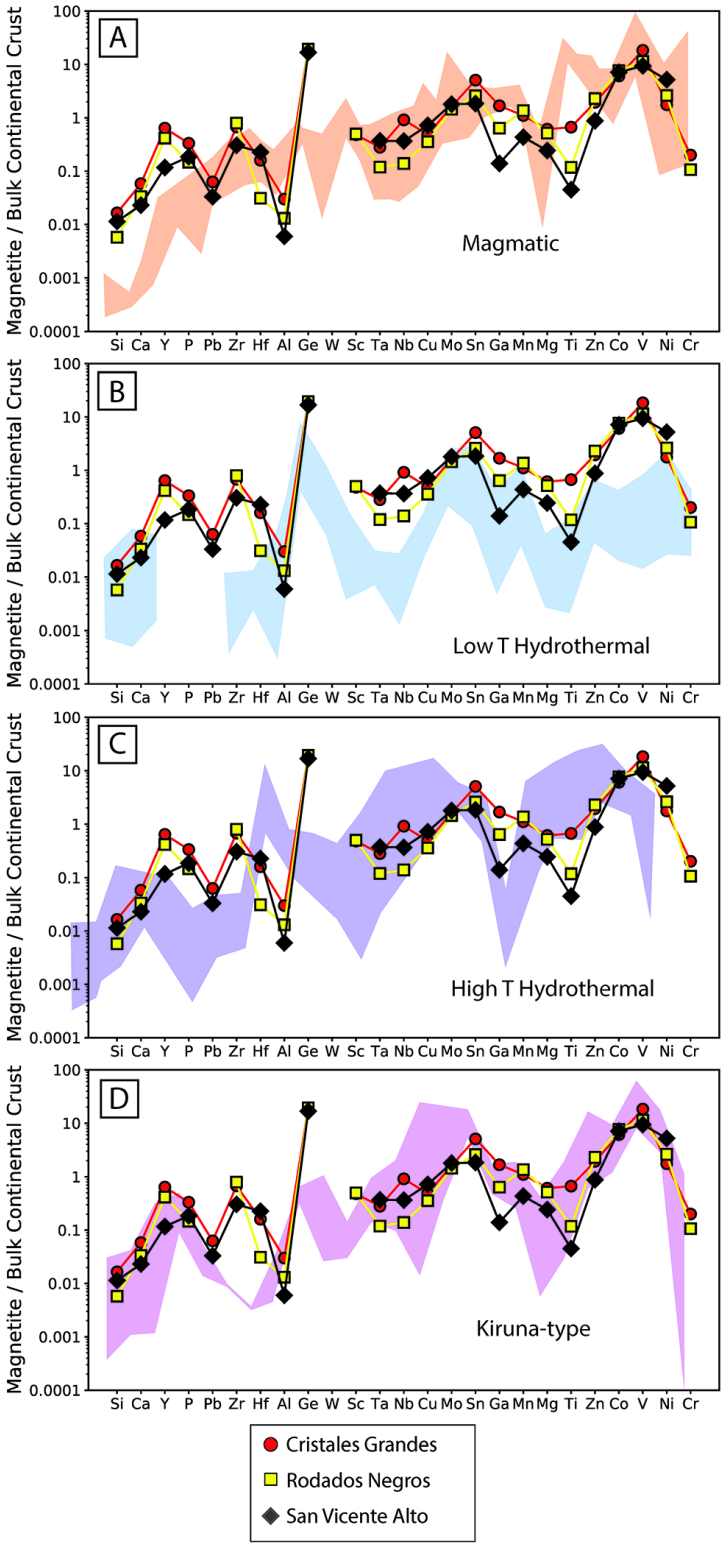

Figure 3.4. The compositions of magnetite from Cristales Grandes, Rodados Negros and San Vicente Alto (lines) compared to the range of magnetite compositions (fields) from (A) igneous rocks, (B) low-temperature hydrothermal environments, (C) magmatic-hydrothermal environments and (D) Kiruna-type IOA deposits. All compositions are normalized to average bulk

continental crust using values in Rudnick and Gao (2003). Fields are taken from Dare et al. (2014) and Knipping et al. (2015b).

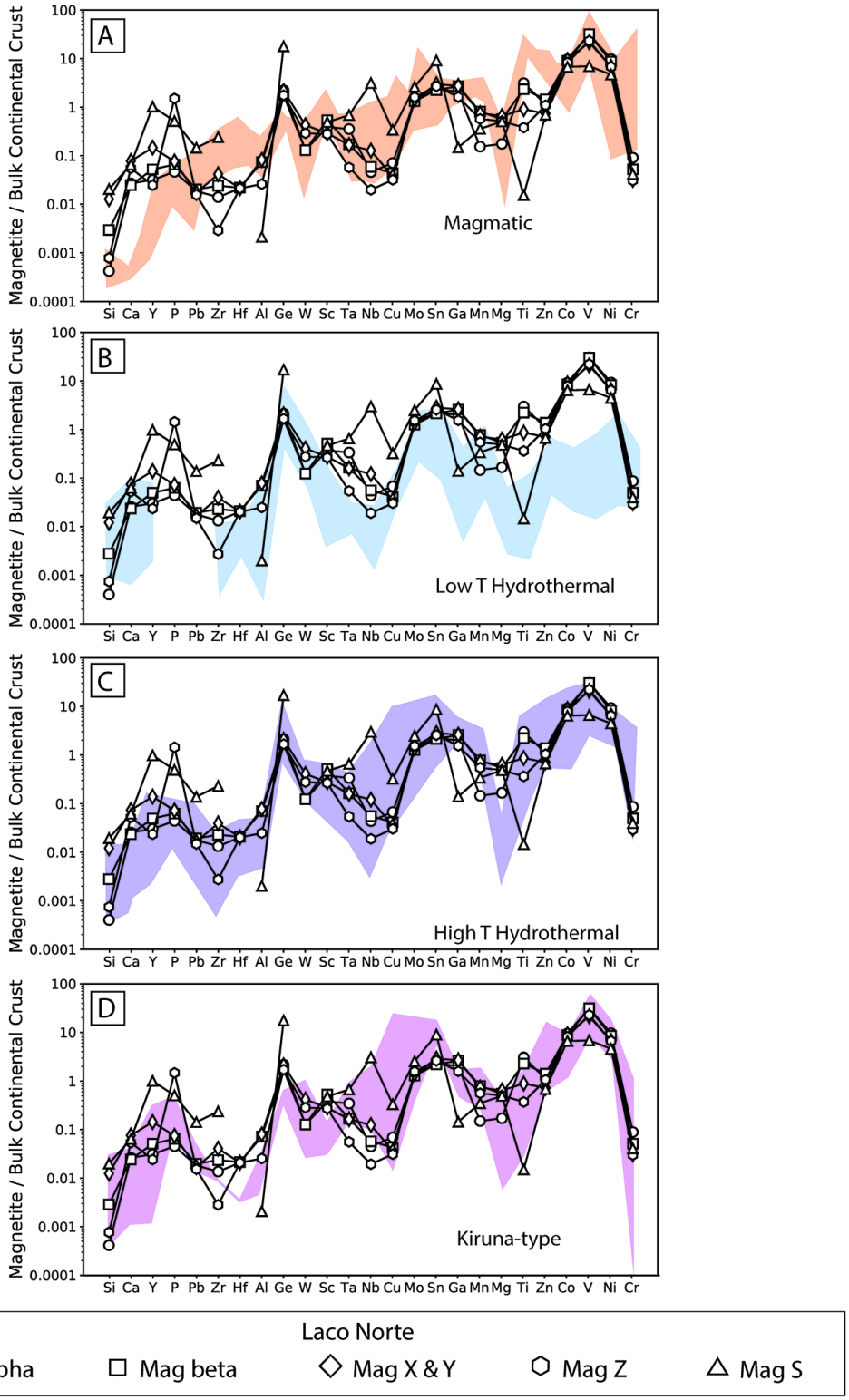

Figure 3.5. Compositions of magnetite from outcrop and drill core samples from Laco Norte compared to the same fields shown in Fig. 3.4. Magnetite alpha and beta represent magnetite from the deep zone of the drill core, magnetite X and Y represent magnetite from intermediate depths in the deposit, magnetite Z represents magnetite from shallow depths below surface, and magnetite

S represents magnetite from outcrop samples.

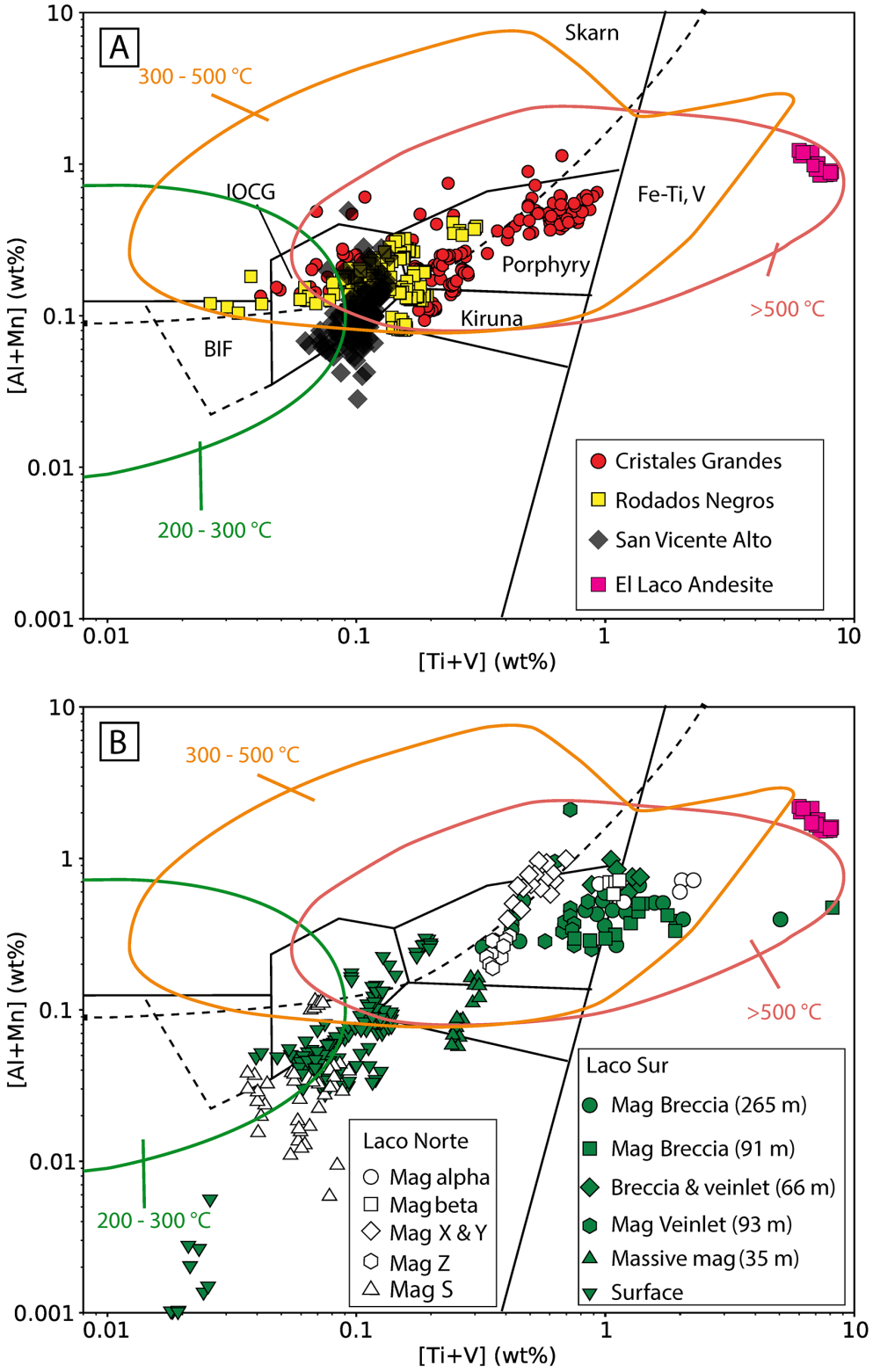

Figure 3.6. [Al + Mn] and [Ti + V] for magnetite from El Laco ore bodies and andesite (cf. Dare et al., 2015) plotted on the chemical discriminant diagram of Nadoll et al. (2014), with colored contours that represent magnetite formed at different temperatures (Nadoll et al., 2014). (A)

contains data for outcrop samples from Cristales Grandes, Rodados Negros, and San Vicente Alto analyzed in this study, and (B) contains data for outcrop and drill core samples form Laco Norte and Laco Sur (depth in meters from surface given in parentheses).

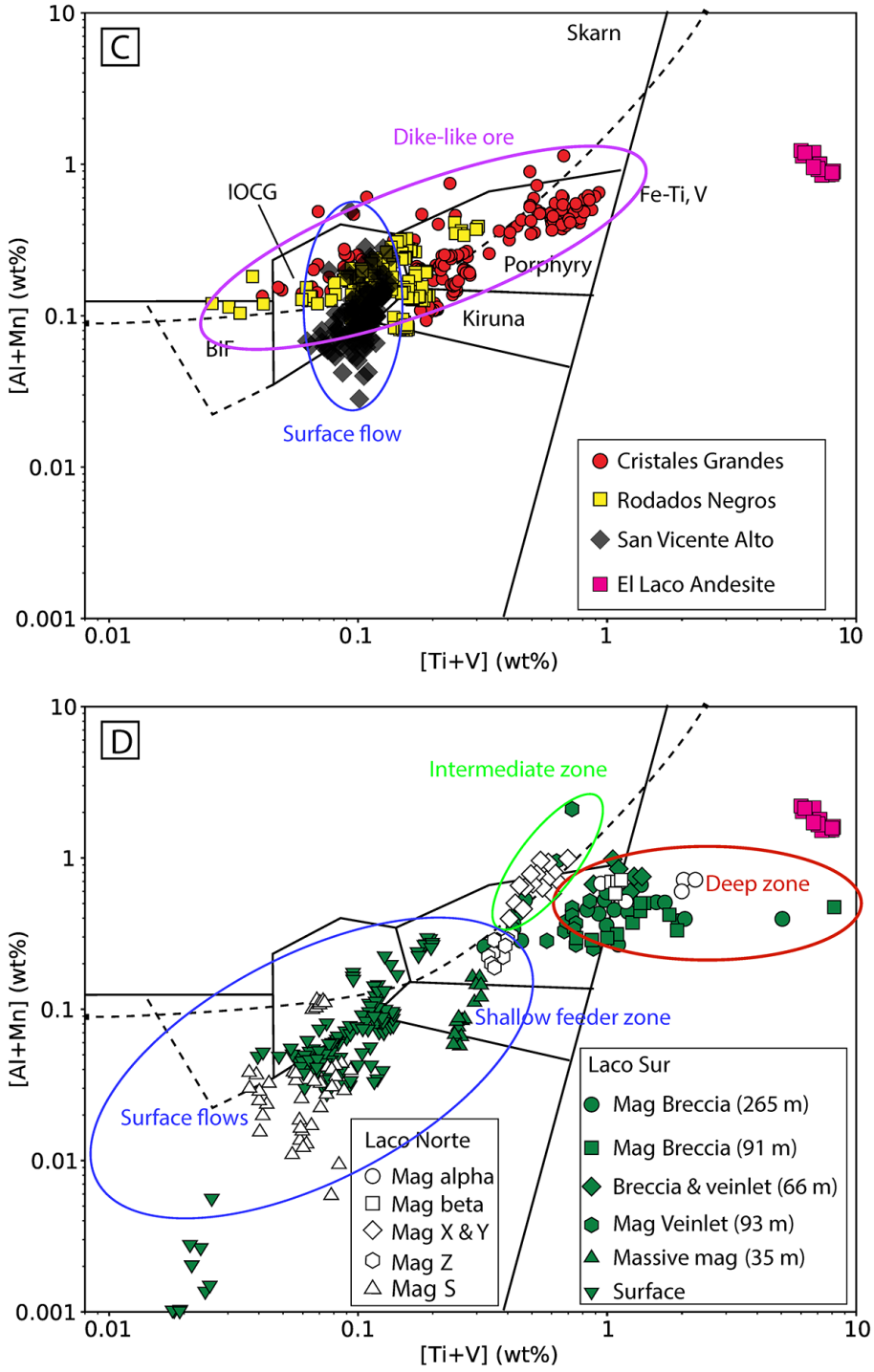

Figure 3.6. In Fig. 3.6C, we use ellipses to identify data from the dike-like ore bodies at Cristales Grandes and Rodados Negros (purple ellipse; red circles and yellow squares) and the flow-like ore body at San Vicente Alto (blue ellipse; black diamonds). Finally, in Fig. 3.6D, we identify magnetite from the deep breccia (red ellipse), the intermediate breccia (green ellipse) and the

shallow feeder zone and the surface flows (blue ellipse) from the Laco Sur and Laco Norte ore bodies.

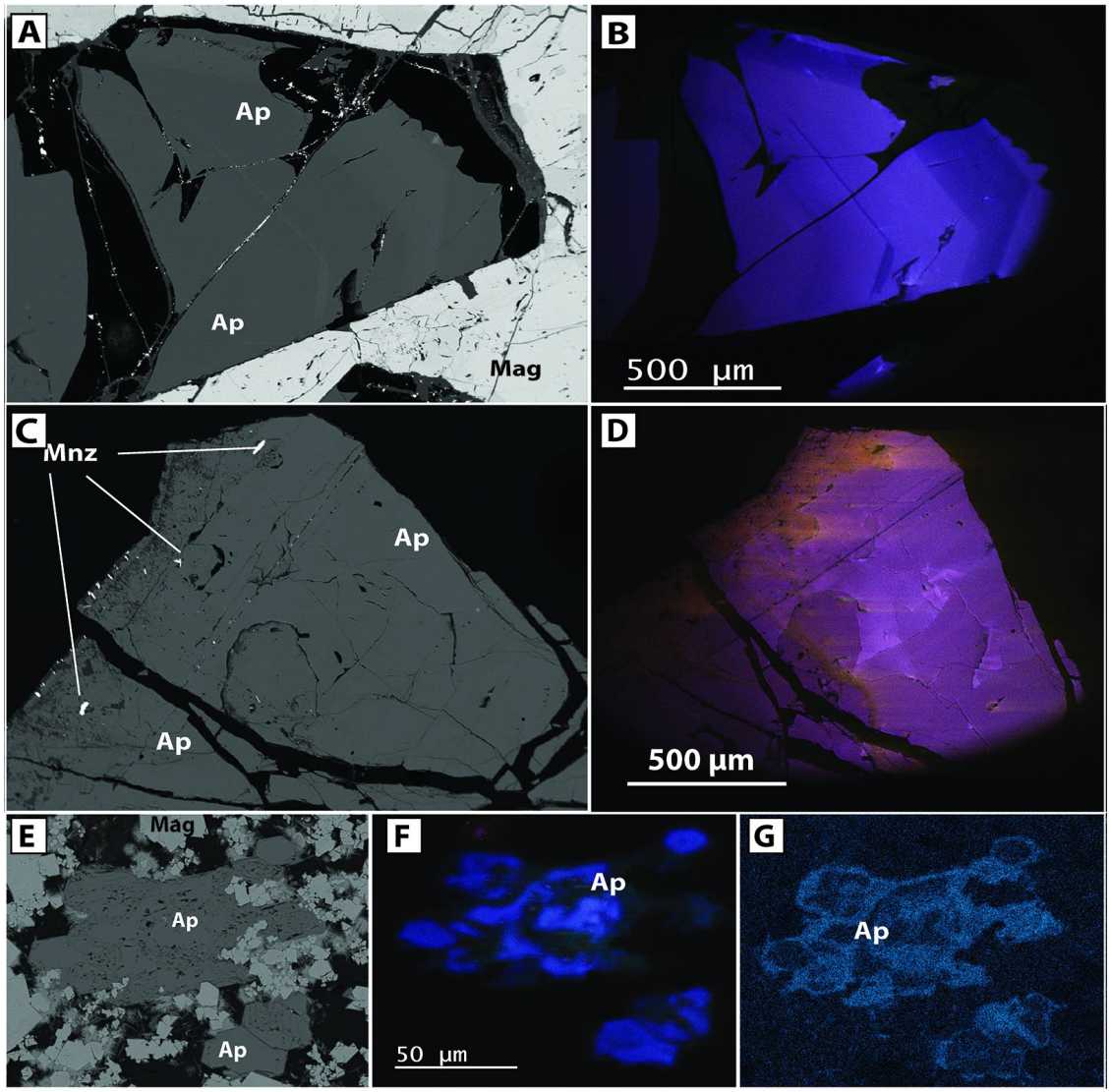

Figure 3.7. Representative BSE and cathodoluminescence (CL) images for apatite from the El Laco ore bodies. BSE (A) and CL (B) images, of apatite from Cristales Grandes. Areas of dark luminescence in (B) correspond to brighter regions in the BSE image. BSE (C) and CL (D) images for apatite from Rodados Negros. Monazite grains (Mnz) occur in cracks within grains and at grain boundaries. The

regions of orange luminescence in (D) correspond to regions within the apatite grains that have porous/mottled texture, higher Cl contents, and contain monazite inclusions. BSE image (E), CL image (F) and Sulfur Kα EDS element map (G) for apatite grains from Laco Sur. The S Kα map (G) reveals elevated S concentrations near grain rims and regions of the grains with porous/mottled texture. Regions of low S content in the apatite grains exhibit bright (purple) luminescence (F), while high S regions exhibit dark luminescence (F).

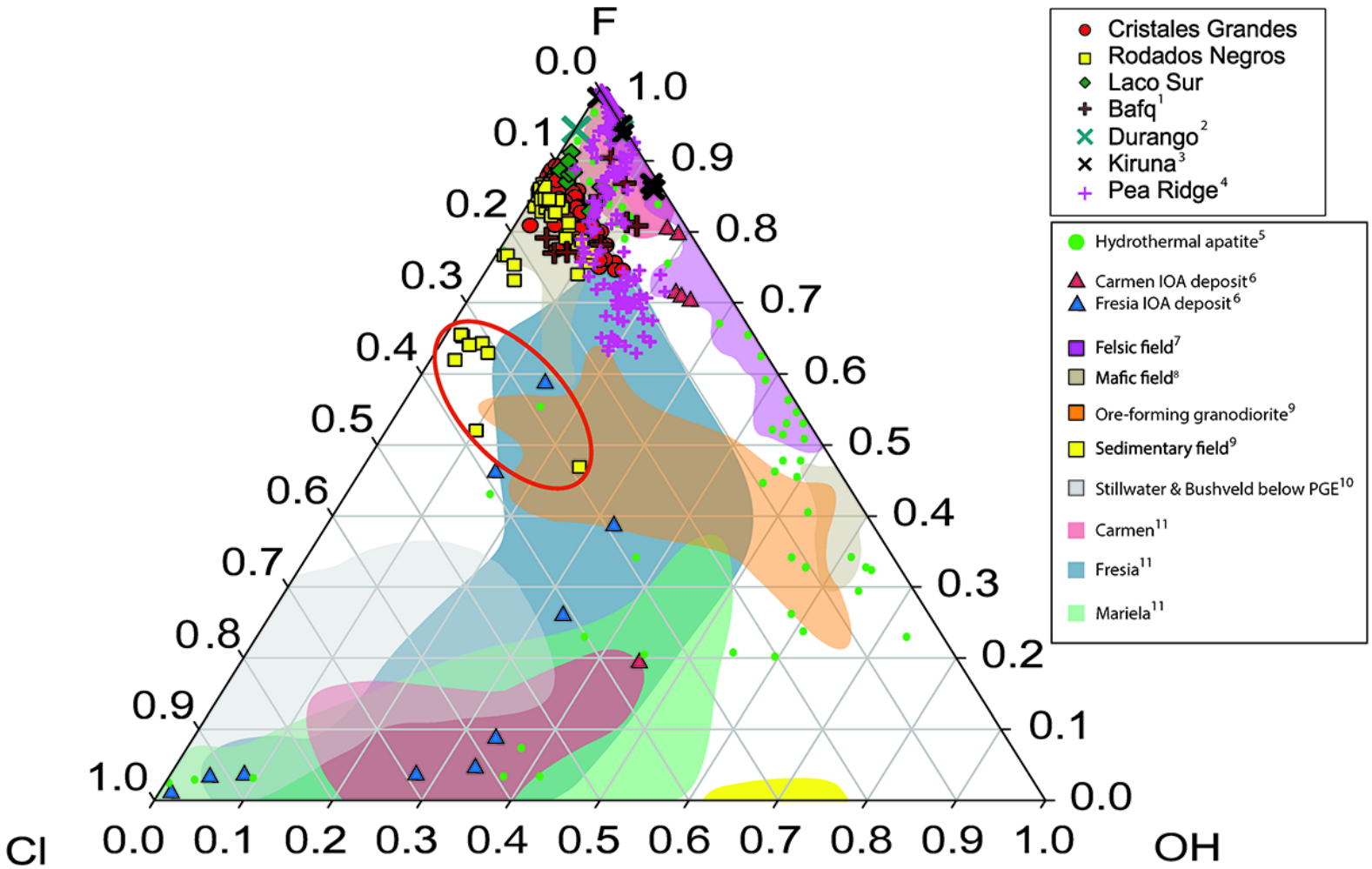

Figure 3.8. Comparison of F-Cl-OH compositions of apatite from Cristales Grandes, Rodados Negros and Laco Sur with published compositions of apatite from other IOA deposits, e.g., Cerro de Mercado (Durango, Mexico), Carmen (Chile), Fresia (Chile) and Pea Ridge (Missouri, USA), and those in the Kiruna (Sweden) and Bafq (Iran) districts, mafic, felsic, and intermediate rocks, hydrothermal and sedimentary environments, and below the PGE ore zones at the Stillwater (USA) and Bushveld (South Africa) complexes. The apatite at El Laco is fluorapatite and has a composition similar to primary apatite in Cretaceous IOA deposits from the Chilean Iron Belt and IOA deposits globally. The apatite chemistry is consistent with growth from magmatic and magmatic-hydrothermal fluids.

Comparison data obtained from [1]Torab and Lehman (2007); [2]Marks et al. (2012); [3]Harlov et al. (2002); [4]Harlov et al. (2016); [5]Webster and Piccoli (2015); [6]Treloar and Colley (1996); [7]Barth and Dorais (2000), Belousova et al. (2002), Krneta et al. (2016); [8]Marks et al. (2012); Patiño Douce et al. (2011); [9]Bao et al. (2016); [10]Boudreau et al. (1995); [11]Palma et al. (2019). The orange ellipse highlights Cl-enriched apatite from Rodados Negros (yellow squares), which has porous texture and contains monazite inclusions (Fig. 7C, D).

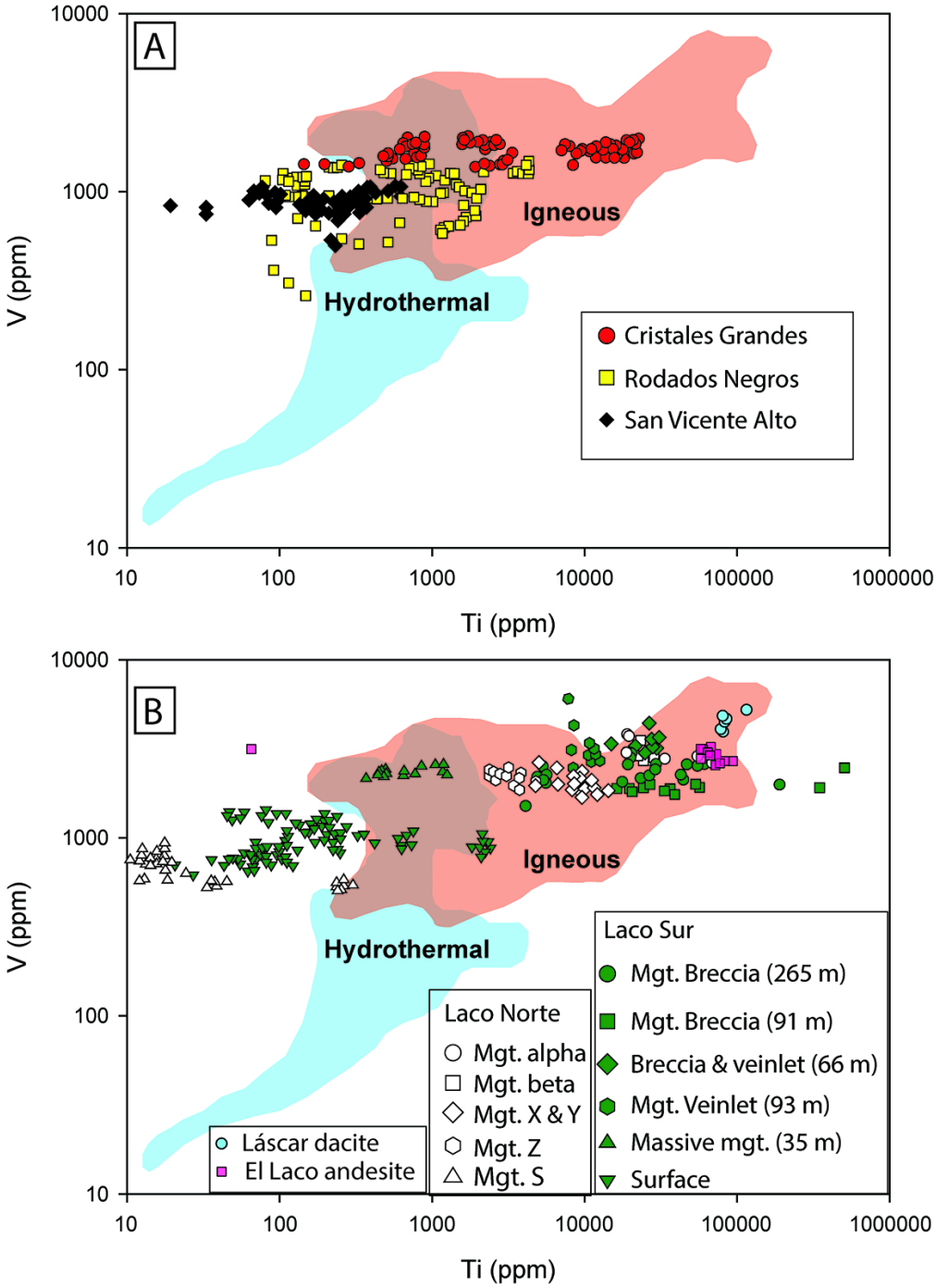

Figure 3.9. Comparison of V and Ti contents of magnetite from surface (A) and drill core (B) from the El Laco ore bodies, the El Laco andesite, and Láscar dacite (cf. Broughm et al., 2017) with fields for V and Ti content for magnetite from igneous and hydrothermal environments cf. Dare et al. (2014) and Knipping et al. (2015b). Magnetite from Cristales Grandes, Rodados Negros, and deep- to intermediate-levels of the ore bodies at Laco Sur and Laco Norte plot in the composition field seen in igneous magnetite, whereas data for magnetite from Cristales Grandes, Rodados Negros, San Vicente Alto, and the shallow levels of the ore bodies at Laco Sur and Laco

Norte plot in the region where the fields for hydrothermal and igneous magnetite overlap. A few data points from San Vicente Alto plot in the field seen in reference hydrothermal magnetite and data from all surface samples studied plot in the low Ti region of the field. These data are consistent with growth of magnetite from magmatic and magmatic-hydrothermal fluids.

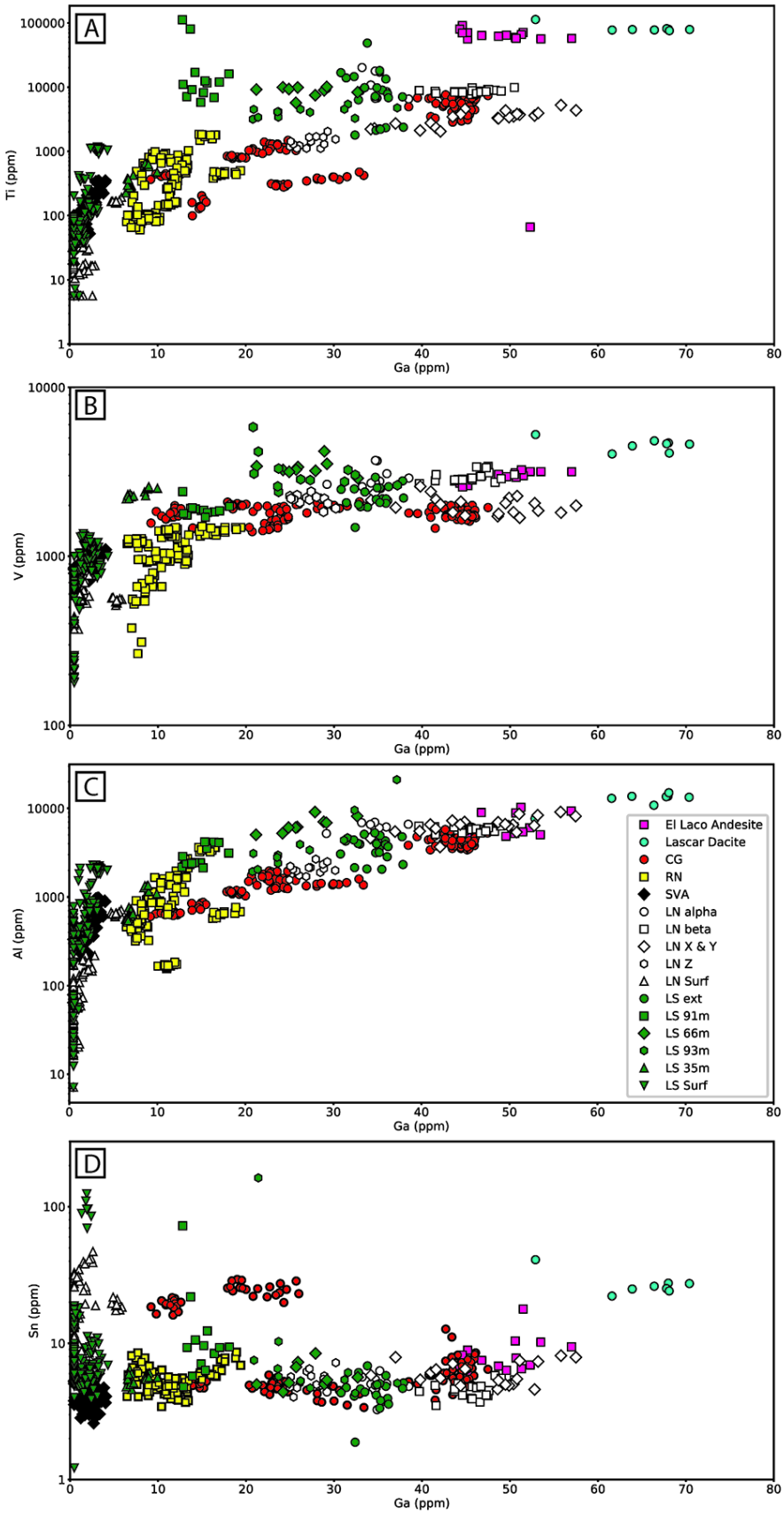
A
B
C
D
Ti (ppm)
V (ppm)
Al (ppm)
Sn (ppm)
Ga (ppm)
El Laco Andesite
Lascar Dacite
CG
RN
SVA
LN alpha
LN beta
LN X & Y
LN Z
LN Surf
LS ext
LS 91m
LS 66m
LS 93m
LS 35m
LS Surf

Figure 3.10. Comparison of (A) Ti, (B) V, (C) Al, (D) Sn, versus Ga contents in magnetite from surface and drill core from the El Laco ore bodies, the El Laco andesite and Láscar dacite host rocks (cf. Broughm et al., 2017). Igneous magnetite from the El Laco andesite and Láscar dacite host rocks have higher Ti, V, Al, and Ga contents. Generally, Ti, V, and Al contents decrease from deep to shallow regions in the deposit. This is consistent with growth of magnetite from a fluid that cools on ascent through the crust. The Sn contents are not as straightforward to interpret. Generally, there is a decrease in the Sn content of magnetite from Cristales Grandes, to Rodados Negros to San Vicente Alto for the surface samples. For drill core samples, the Sn content is highest in surface samples from Laco Sur but there are also 2 analyses of magnetite from deep breccias that have similarly high Sn contents. The surface samples from both Laco Norte and Laco Sur have higher Sn contents than the shallow, intermediate, and deep portions of these ore bodies. The increased Sn content of the surface samples from Laco Sur and Laco Norte, likely indicate metasomatic reactions of the ore minerals with hydrothermal fluids.

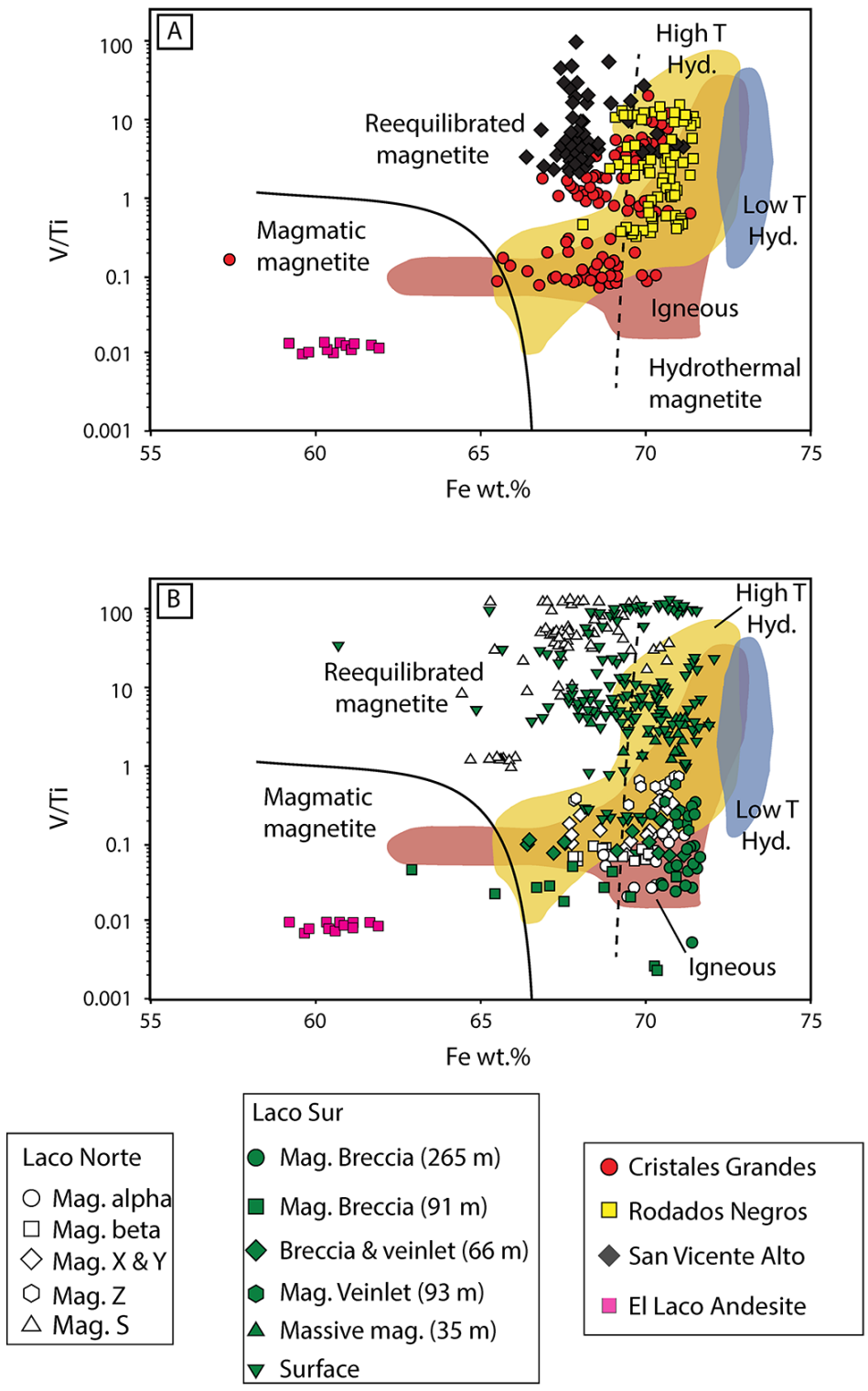

Figure 3.11. Comparison of V/Ti and Fe content of magnetite from surface outcrops (A) and drill core (B) from the El Laco ore bodies, and the El Laco andesite cf. Dare et al. (2015) with the fields for magmatic, reequilibrated, and hydrothermal magnetite (cf. Wen et al., 2017) and colored fields for igneous, high-temperature and low-temperature magnetite (cf. Nadoll et al., 2014). The

comparison indicates growth of magnetite in the ore bodies from magmatic and magmatic-hydrothermal fluids and is consistent with ore genesis at El Laco according to the model presented by Ovalle et al. (2018).

3.8 References

Alva-Valdivia, L.M., Rivas, M.L., Goguitchaichvili, A., Urrutia-Fucugauchi, J., Gonzalez, J.A., Morales, J., Gómez, S., Henríquez, F., Nyström, J.O. and Naslund, R.H., 2003, Rock-magnetic and oxide microscopic studies of the El Laco iron ore deposits, Chilean Andes, and implications for magnetic anomaly modeling: International Geology Review, v. 45, p.533-547.

Audétat, A. and Keppler, H., 2005, Solubility of rutile in subduction zone fluids, as Determined by experiments in the hydrothermal diamond anvil cell: Earth and Planetary Science Letter, v. 232, p. 393-402.

Balan, E., De Villiers, J. P., Eeckhout, S. G., Glatzel, P., Toplis, M. J., Fritsch, E., Allard, T., Galoisy, L., and Calas, G., 2006, The oxidation state of vanadium in titanomagnetite from layered basic intrusions: American Mineralogist, v. 91(5-6), p. 953-956.

Barra, F., Reich, M., Selby, D., Rojas, P., Simon, A.C., Salazar, E., Palma, G., 2017, Unraveling the origin of the Andean IOCG clan: A Re-Os approach: Ore Geology Reviews, v. 81, p. 62-78.

Barth, A.P., and Dorais, M.J., 2000, Magmatic anhydrite in granitic rocks: First occurrence and potential petrologic consequences: American Mineralogist, v. 85(3-4), pp.430-435.

Barton, M.D., 2013, Iron Oxide(-Cu-Au-REE-P-Ag-U-Co) Systems. In: Turekian KK, Holland HD (eds) Treatise on Geochemistry, 2nd ed.: Elsevier, Amsterdam, p. 515 - 541.

Barton, M.D., and Johnson, D.A., 1996, Evaporitic-source model for igneous-related Fe oxide–(REE-Cu-Au-U) mineralization: Geology 24(3):259-62.

Barton, M.D., and Johnson, D.A., 2004, Footprints of Fe-oxide(-Cu-Au) systems: University of Western Australia Special Publications, v. 33, p. 112-116.

Bao, B., Webster, J.D., Zhang, D.H., Goldoff, B.A, and Zhang, R.Z., 2016, Compositions of biotite, amphibole, apatite and silicate melt inclusions from the Tongchang mine, Dexing porphyry deposit, SE China: Implications for the behavior of halogens in mineralized porphyry systems: Ore Geology Reviews, v. 79, p.443-462.

Bell, A., and Simon, A.C., 2011, Evidence for the alteration of the $Fe^{3+}/\Sigma Fe$ of silicate melt caused by the degassing of chlorine-bearing aqueous volatiles: Geology, v. 39, p. 499-502.

Belousova, E.A., Griffin, W.L., O'Reilly, S.Y., and Fisher, N.I., 2002, Apatite as an indicator mineral for mineral exploration: Trace-element compositions and their relationship to host rock type: Journal of Geochemical Exploration, v. 7, p. 45–69.

Bilenker, L.D., Simon, A.C., Reich, M., Lundstrom, C.C., Gajos, N., Bindeman, I., Barra, F., and Munizaga, R., 2016, Fe-O stable isotope pairs elucidate a high-temperature origin of Chilean iron oxide-apatite deposits: Geochimica et Cosmochimica Acta, v. 177, p. 94–104.

Bonyadi, Z., Davidson, G.J., Mehrabi, B., Meffre, S., and Ghazban, F., 2011, Significance of apatite REE depletion and monazite inclusions in the brecciated Se-Chahun iron oxide apatite deposit, Bafq district, Iran: Insights from paragenesis and geochemistry: Chemical Geology, v. 281, p. 253–269.

Bordage, A., Balan, E., de Villiers, J. P., Cromarty, R., Juhin, A., Carvallo, C., Calas, G., Raju, P.V.S., and Glatzel, P., 2011, V oxidation state in Fe–Ti oxides by high-energy resolution fluorescence-detected X-ray absorption spectroscopy: Physics and Chemistry of

Minerals, v.38(6), p. 449-458.
Boudreau, A.E, Love, C., and Prendergast, M.D., 1995, Halogen geochemistry of the Great Dyke, Zimbabwe: Contributions to Mineralogy and Petrology, v. 122, p. 289-300.
Broman, C., Nyström, J.O., Henríquez, F, and Elfman, M., 1999, Fluid inclusions in magnetite-apatite ore from a cooling magmatic system at El Laco, Chile: Gff, v. 121(3), p.253-267.
Broughm, S.G., Hanchar, J.M., Tornos, F., Westhues, A., and Attersley, S., 2017, Mineral chemistry of magnetite from magnetite-apatite mineralization and their host rocks: examples from Kiruna, Sweden, and El Laco, Chile: Mineralium Deposita, v. 52 p. 1223-244.
Bouzari, F., Hart, C.J., Bissig, T., and Barker, S., 2016, Hydrothermal alteration revealed by apatite luminescence and chemistry: a potential indicator mineral for exploring covered porphyry copper deposits: Economic Geology, v. 111(6), p.1397-1410.;
Buddington, A. F., and Lindsley, D. H., 1964, Iron-Titanium Oxide Minerals and Synthetic Equivalents: Journal of Petrology, v. 5, p. 310–357.
CAP Minería, 2016, Annual Report, http://www.capmineria.cl/wp-content/uploads/2017/03/cap_mineria_memoria_2016.pdf (2016).
Childress, T., 2019, Fingerprinting Source Fluids of Iron Oxide-Copper-Gold and Iron Oxide-Apatite Deposits Using Traditional and Non-Traditional Stable Isotope Geochemistry: Unpublished Doctoral dissertation, Ann Arbor, Michigan, University of Michigan.Dare,
S.A.S., Barnes, S.J., and Beaudoin, G., 2015, Did the massive magnetite "lava flows" of El Laco (Chile) form by magmatic or hydrothermal processes? New constraints from magnetite composition by LA-ICP-MS: Mineralium Deposita, v. 50, p. 607–617.
Dare, S.A.S., Barnes, S.J., Beaudoin, G., Méric, J., Boutroy, E., and Potvin-Doucet, C., 2014, Trace elements in magnetite as petrogenetic indicators: Mineralium Deposita, v. 49, p. 785–796.
Deditius, A., Reich, M., Simon, A.C., Suvorova, A., Knipping, J., Roberts, M.P., Rubanov, S., Dodd, A., and Saunders, M., 2018, Nanogeochemistry of hydrothermal magnetite: Contributions to Mineralogy and Petrology, v. 123, p. 46-66.
de Jong, G., Rotherham, J., Phillips G.N., and Williams, P.J., 1998, Mobility of rare-earth elements and copper during shear-zone-related retrograde metamorphism: Geology en Mijnbouw, v. 76, p. 311-319.
Dupuis, C., and Beaudoin, G., 2011, Discriminant diagrams for iron oxide trace element fingerprinting of mineral deposit types: Mineralium Deposita, v. 46(4), p.319-335.
Edmonds, M., Brett, A., Herd, R.A., Humphreys, M.C.S. and Woods, A., 2014, Magnetite-bubble aggregates at mixing interfaces in andesite magma bodies: Geological Society, London Special Publication, v. 410, p. 95-121.
Frietsch, R., 1978, On the magmatic origin of iron ores of the Kiruna type: Economic Geology, v. 73, p. 478–485.
Frietsch, R., and Perdahl, J.A., 1995, Rare earth elements in apatite and magnetite in Kiruna-type iron ores and some other iron ore types: Ore Geology Reviews, v. 9, p. 489–510.
Giovanninia, A.L., Bastos, A.C., Porto, C.G., Pereira, V.P., Takehara, L., Barbanson, L., and Bastos, P.H.S., 2017, Mineralogy and geochemistry of laterites from the Morro dos Seis Lagos Nb (Ti, REE) deposit (Amazonas, Brazil): Ore Geology Reviews, v. 88, p. 461-480.
Götze, J., 2012, Application of cathodoluminescence microscopy and spectroscopy in

Geosciences: Microscopy and Microanalysis, v. 18, p. 1270–1284.
Götze, J., Plötze, and M., Habermann, D., 2001, Origin, spectral characteristics and practical applications of the cathodoluminescence (CL) of quartz - A review: Mineralogy and Petrology, 71: 225–250.
Gros, K., Słaby, E., Förster, H.J., Michalak, P.P., Munnik, F., Götze. J., and Rhede, D., 2016, Visualization Of trace-element zoning in fluorapatite using BSE and CL imaging, and EPMA and μPIXE/μPIGE mapping: Mineralogy and Petrology, v. 10(6), p. 809-821.
Groves, D.I., Bierlein, F.P., Meinert, L.D. and Hitzman, M.W., 2010, Iron oxide copper-gold (IOCG) deposits through Earth history: Implications for origin, lithospheric setting, and distinction from other epigenetic iron oxide deposits: Economic Geology, v. 105(3), p.641-654.
Harlov, D.E., 2015, Apatite: A Fingerprint for Metasomatic Processes: Elements, v.11, p. 171–176.
Harlov, D.E., Andersson, U.B., Förster, H.J., Nyström, J.O., Dulski, P., and Broman, C., 2002, Apatite – monazite relations in the Kiirunavaara magnetite – apatite ore, northern Sweden: Chemical Geology, v.191, p. 47–72.
Harlov, D.E. and Förster, H.J., 2003, High PT experimental metasomatism of a fluorapatite with significant britholite and fluorellestadite components: implications for LREE mobility during granulite-facies metamorphism: Mineralogical Magazine, v. 67, p. 61-72.
Harlov, D.E., Meighan, C.J., Kerr, I.D., and Samson, I.M., 2016, Mineralogy, chemistry, and fluid-aided evolution of the Pea Ridge Fe oxide-(Y+ REE) deposit, southeast Missouri, USA: Economic Geology, v. 111(8), p. 1963-1984.
Hedenquist, J.W., and Lowenstern, J.B., 1994, The role of magmas in the formation of hydrothermal ore deposits: Nature, v. 370(6490), p.519.
Henríquez, F., Naslund, H.R., Nyström, J.O., Vivallo, W., Aguirre, R., Dobbs, F.M., and Lledó, H, 2003, New field evidence bearing on the origin of the El Laco magnetite deposit, Northern Chile: Economic Geology, v.98(7), p. 1497–1502.
Hitzman, M.W., Oreskes, N., and Einaudi, M.T., 1992, Geological characteristics and tectonic setting of proterozoic iron oxide (Cu-U-Au-REE) deposits: Precambrian Research, v. 58, p. 241–287.
Hughes, J.M., and Rakovan, J.F., 2015, Structurally robust, chemically diverse: apatite and apatite supergroup minerals: Elements, v. 11, p.165–170.
Hurwitz, S., and Navon, O., 1994, Bubble nucleation in rhyolitic melts: Experiments at high pressure, temperature, and water content: Earth and Planetary Science Letters, v. 122(3-4), p.267-280.
Jochum, K.P., Weis, U., Stoll, B., Kuzmin, D., Yang, Q., Raczek, I., Jacob, D.E., Stracke, A., Birbaum, K., Frick, D.A., and Günther, D., 2011, Determination of reference values for NIST SRM 610–617 glasses following ISO guidelines: Geostandards and Geoanalytical Research, v. 35(4), p.397-429.
Jochum, K.P., Willbold, M., Raczek, I., Stoll, B., and Herwig, K., 2005, Chemical Characterisation of the USGS Reference Glasses GSA-1G, GSC-1G, GSD-1G, GSE-1G, BCR-2G, BHVO-2G and BIR-1G Using EPMA, ID-TIMS, ID-ICP-MS and LA-ICP-MS: Geostandards and Geoanalytical Research, v. 29(3), p.285-302.
Jonsson, E., Harlov, D.E., Majka, J., Högdahl, K., and Persson-Nilsson, K., 2016, Fluorapatite-monazite-allanite relations in the Grängesberg apatite-iron oxide ore district, Bergslagen, Sweden: American Mineralogist, v. 101(8), p. 1769-1782.

Jonsson, E., Troll, V.R., Högdahl, K., Harris, C., Weis, F., Nilsson, K.P., and Skelton, A., 2013, Magmatic origin of giant 'Kiruna-type' apatite-iron-oxide ores in central Sweden: Scientific Reports, v. 3 (1644), p. 1 – 8.

Ketcham, R.A., 2015, Technical Note: Calculation of stoichiometry from EMP data for apatite and other phases with mixing on monovalent anion sites: American Mineralogist, v. 100, p. 1620–1623. doi:10.2138/am-2015-5171

Knipping, J.L., Bilenker, L.D., Simon, A.C., Reich, M., Barra, F., Deditius, A.P., Lundstrom, C., Bindeman, I., and Munizaga, R., 2015a, Giant Kiruna-type deposits form by efficient flotation of magmatic magnetite suspensions: Geology, v. 43, p. 591–594.

Knipping, J.L., Bilenker, L.D., Simon, A.C., Reich, M., Barra, F., Deditius, A.P., Wälle, M., Heinrich, C.A., Holtz, F., and Munizaga, R., 2015b, Trace elements in magnetite from massive iron oxide-apatite deposits indicate a combined formation by igneous and magmatic-hydrothermal processes: Geochimica et Cosmochimica Acta, v. 171, p. 15–38.

Knipping, J.L., Webster, J.D., Simon, A.C., and Holtz, F., 2019, Accumulation of magnetite by flotation on bubbles during decompression of silicate magma: Scientific reports, v. 9 (1), p. 3852. doi.org/10.1038/s41598-019-40376-1

Konecke, B.A., Fiege, A., Simon, A.C., Parat, F., and Stechern, A., 2017a, Co-variability of S^{6+}, S^{4+} and S^{2-} in apatite as a function of oxidation state: Implications for a new oxybarometer: American Mineralogist, v. 102(3), p. 548-557. doi.10.2138/am-2017-5907

Konecke, B., Fiege, A., Simon, A.C., and Holtz, F., 2017b, Cryptic metasomatism during late-stage lunar magmatism implicated by sulfur in apatite: Geology, v. 45, p. 739-742.

Krneta, S., Ciobanu, C.L., Cook, N.J., Ehrig, K., and Kontonikas-Charos, A., 2016, Apatite at Olympic Dam, South Australia: A petrogenetic tool: Lithos, v. 262, p. 470–485.

La Cruz, N. L., Simon, A. C., Wolf, A. S., Reich, M., Barra, F., and & Gagnon, J. E., 2019, The geochemistry of apatite from the Los Colorados iron oxide–apatite deposit, Chile: implications for ore genesis: Mineralium Deposita, p. 1-14. doi.org/10.1007/s00126-019-00861-z

Lester, G.W., Kyser, T.K., and Clark, A.H., 2013a, Oxygen isotope partitioning between immiscible silicate melts with H_2O, P and S: Geochimica et Cosmochimica Acta, v. 109, p. 306–311.

Lester, G.W., Clark, A.H., Kyser, T.K., and Naslund, H.R., 2013b, Experiments on liquid immiscibility in silicate melts with H_2O, P, S, F and Cl: implications for natural magmas: Contributions to Mineralogy and Petrology, v. 166, p. 329 – 349.

Lindsley, D.H., 1991, Experimental studies of oxide minerals: Reviews in Mineralogy, v. 25, p. 69-106.

Mao, M., Rukhlov, A.S., Rowins, S.M., Spence, J., and Coogan, L.A., 2016, Apatite trace element compositions: A robust new tool for mineral exploration: Economic Geology, v. 111, p. 187–1222.

Marsh, B.D., 1989, Magma chambers: Annual Reviews of Earth and Planetary Science, v. 17, p. 439–474.

Marks, M.A., Wenzel, T., Whitehouse, M.J., Loose, M., Zack, T., Barth, M., Worgard, L., Krasz, V., Eby, G.N., Stosnach, H., and Markl, G., 2012, The volatile inventory (F, Cl, Br, S, C) of magmatic apatite: An integrated analytical approach: Chemical Geology, v. 291, p.241-255.

Martel, C., Pichavent, M., Holtz, F., and Scaillet, B., 1999, Effects of fO_2 and H_2O on andesite phase relations between 2 and 4 kbar: Journal of Geophysical Research, v. 104, p.

29453–29470
Mungall, J.E., Long, K., Brenan, J.M., Smythe, D. and Naslund, H.R., 2018, Immiscible shoshonitic and Fe-P-oxide melts preserved in unconsolidated tephra at El Laco volcano, Chile: Geology, v. 46, p. 255–258.
Nadoll, P., Angerer, T., Mauk, J.L., French, D., and Walshe, J., 2014, The chemistry of hydrothermal magnetite: a review: Ore geology reviews, v. 61, pp.1-32.Naranjo, J.A.,
Henríquez, F., and Nyström, J.O., 2010, Subvolcanic contact metasomatism at El Laco volcanic complex, central Andes: Andean Geology, v. 37(1), p. 110 – 120.
Naslund, H.R., Henríquez, F., Nyström, J.O., Vivallo, W., and Dobbs, F.M., 2002, Magmatic iron ores and associated mineralization: examples from the Chilean High Andes and Coastal Cordillera, in: Porter, T.M., ed., Hydrothermal iron oxide copper-gold and related deposits: A global perspective, 2nd ed.: Adelaide, PGC Publishing, p. 207-226.
Nielsen, R.L., Forsythe, L.M., Gallahan, W.E., and Fisk, M.R., 1994, Major-and trace-element magnetite-melt equilibria: Chemical Geology, v. 117, p.167-191.
Nyström, J.O., and Henríquez, F., 1994, Magmatic features of iron ores of the Kiruna type in Chile and Sweden: ore textures and magnetite geochemistry: Economic Geology, v. 89, p. 820–839.
Ovalle, J.T., La Cruz, N.L., Reich, M., Barra, F., Simon, A.C., Konecke, B.A., Rodriguez-Mustafa, M.A., Deditius, A.P., Childress, T.M., and Morata, D., 2018, Formation of massive iron deposits linked to explosive volcanic eruptions: Scientific reports, v. 8(1), p.14855.
Oyarzun, J., and Frutos, J., 1984, Tectonic and petrological frame of the Cretaceous iron deposits of north Chile: Mining Geology, v. 34, p. 21–31.
Palma, G., Barr, F., Reich, M., Valencia, V., Simon, A.C., Vervoort, J., Leisen, M., and Romero, R., 2019, Halogens (F, Cl, OH), trace element contents, and Sr-Nd isotopes in apatite from iron oxide-apatite (IOA) deposits in the Chilean iron belt: evidence for magmatic and hydrothermal stages of mineralization: Geochimica et Cosmochimica Acta, v. 246, p. 515–540.
Parat, F., Holtz, F., and Streck, M.J., 2011, Sulfur-bearing magmatic accessory minerals: Reviews in Mineralogy and Geochemistry, v. 73(1), p.285-314.
Park, C.F., 1961, A magnetite" flow" in northern Chile: Economic Geology, v. 56(2), p. 431-436.
Patiño Douce, A.E.P., Roden, M.F., Chaumba, J., Fleisher, C., and Yogodzinski, G., 2011, Compositional variability of terrestrial mantle apatites, thermodynamic modeling of apatite volatile contents, and the halogen and water budgets of planetary mantles: Chemical Geology, v. 288(1-2), p.14-31.
Piccoli, P.M., and Candela, P.A., 2002, Apatite in Igneous system: Reviews in Mineralogy and Geochemistry, v. 48(1), p. 255–292.
Pleše, P., Higgins, M.D., Baker, D.R., Lanzafame, G., Kudrna Prašek, M., Mancini, L., and Rooyakkers, S.M., 2019, Production and detachment of oxide crystal shells on bubble walls during experimental vesiculation of andesitic magmas: Contributions to Mineralogy and Petrology, v. 174 (3), p. 21. doi.org/10.1007/s00410-019-1556-8
Reed, M.J., Candela, P.A., and Piccoli, P.M., 2000, The distribution of rare earth elements between monzogranitic melt and the aqueous volatile phase in experimental investigations at 800 C and 200 MPa: Contributions to Mineralogy and Petrology, v. 140(2), p.251-262.
Reich, M., Simon, A.C., Deditius, A., Barra, F., Chryssoulis, S., Lagas, G., Tardani, D.,

Knipping, J., Bilenker, L., Sánchez-Alfaro, P., and Roberts, M.P., 2016, Trace element signature of pyrite from the Los Colorados iron oxide-apatite (IOA) deposit, Chile: A missing link between Andean IOA and iron oxide copper-gold systems?: Economic Geology, v. 111, p. 743–761.

Rhodes, A.L., and Oreskes, N., 1995, Magnetite deposition at El Laco, Chile: implications for Fe-oxide formation in magmatic-hydrothermal systems, in Clark, A.H., ed., Giant ore deposits-II: Controls on the scale of orogenic magmatic-hydrothermal mineralization, Proceedings of the Second Giant Ore Deposits Workshop: Kingston, Queen's University, p. 582-622.

Rhodes, A.L., and Oreskes, N., 1999, Oxygen isotope composition of magnetite deposits at El Laco, Chile: evidence of formation from isotopically heavy fluids: Society of Economic Geology Special Publications, v. 7, p. 333-351.

Rhodes A.L., Oreskes N., and Sheets S., 1999, Geology and rare earth element geochemistry of magnetite deposits at El Laco, Chile: Society of Economic Geology Special Publication, v. 7, p. 299-332.

Rudnick, R.L., and Gao, S., 2003, Composition of the continental crust: Treatise on geochemistry, v 3, p.659.

Sadove, G., Konecke, B., Fiege, A., and Simon, A. C., 2019, Structurally bound S2–, S1–, S4+, S6+ in terrestrial apatite: The redox evolution of hydrothermal fluids at the Phillips mine, New York, USA:Ore Geology Reviews, v. 107, p. 1084-1096.

Salazar, E., Barra, F., Reich, M., Simon, A.C., Leisen, M., Palma, G., Romero, R., and Rojo, M., 2019, Trace-element geochemistry of magnetite from the Cerro Negro Norte iron oxide-apatite deposit, northern Chile: Mineralium Deposita, p. 1-20.

Schettler, G., Gottschalk, M., and Harlov, D.E., 2011, A new semi-micro wet chemical method for apatite analysis and its application to the crystal chemistry of fluorapatite-chlorapatite solid solutions: American Mineralogist, v. 96, p. 138–152.

Sillitoe R.H., 2003, Iron oxide-copper-gold deposits: An Andean view: Mineralium Deposita, v. 38, p. 787–812.

Sillitoe, R.H., and Burrows, D.R., 2002, New field evidence bearing on the origin of the El Laco magnetite deposit, northern Chile.: Economic Geology, v. 97(5), p. 1101-1109.

Simon, A.C., Pettke, T., Candela, P.A., Piccoli, P.M., and Heinrich, C.A., 2007, The partitioning behavior of As and Au in S-free and S-bearing magmatic assemblages: Geochimica et Cosmochimica Acta, 71(7), p.1764-1782.

Simon, A.C., and Ripley, E.M., 2011, The role of magmatic sulfur in the formation of ore deposits: Reviews in Mineralogy and Geochemistry, 73(1), p.513-578.

Simon, A.C., Knipping, J., Reich, M., Barra, F., Deditius, A.P., Bilenker, L., Childress, T., 2018, Kiruna-Type Iron Oxide-Apatite (IOA) and Iron Oxide Copper-Gold (IOCG) Deposits Form by a Combination of Igneous and Magmatic-Hydrothermal Processes: Evidence from the Chilean Iron Belt. Society of Economic Geology Special Publication No. 21, p. 89-114.

Streck, M.J., and Dilles, J.H., 1998, Sulfur evolution of oxidized arc magmas as recorded in apatite from a porphyry copper batholith: Geology, v. 26, p. 523–526. doi: .1130/0091-7613(1998)026<0523: SEOOAM>2.3.CO

Tanis, E.A., Simon, A., Tschauner, O., Chow, P., Xiao, Y., Burnley, P., Cline, C.J., Hanchar, J.M., Pettke, T., Shen, G. and Zhao, Y., 2015, The mobility of Nb in rutile-saturated NaCl-and NaF-bearing aqueous fluids from 1–6.5 GPa and 300–800 C: American

Mineralogist, v. 100, p.1600-1609.
Toplis, M.J. and Carroll, M.R., 1995, An experimental study of the influence of oxygen fugacity on Fe-Ti oxide stability, phase relations, and mineral—melt equilibria in ferro-basaltic systems, Journal of Petrology, v. 36, p.1137-1170.
Torab, F.M., and Lehmann, B., 2007, Magnetite-apatite deposits of the Bafq district, Central Iran: apatite geochemistry and monazite geochronology: Mineralogical Magazine, v. 71, p. 347–363.
Tornos, F., Velasco, F., and Hanchar, J.M., 2016, Iron-rich melts, magmatic magnetite, and superheated hydrothermal systems: The El Laco deposit, Chile: Geology, v. 44, p. 427–430.
Treloar, P.J., and Colley, H., 1996, Variation in F and Cl contents in apatites from magnetite-apatite ores in northern Chile, and their ore-genetic implications: Mineralogical Magazine, v. 60, p. 285–301.
Velasco, F., Tornos, F., and Hanchar, J.M., 2016, Immiscible iron-and silica-rich melts and magnetite geochemistry at the El Laco volcano (northern Chile): Evidence for a magmatic origin for the magnetite deposits: Ore Geology Reviews, v. 79, p. 346-366.
Waychunas, G.A., 2002, Apatite Luminescence: Reviews in Mineralogy and Geochemistry, v.48, p. 701–742.
Webster, J.D., and Piccoli, P.M., 2015, Magmatic apatite: a powerful, yet deceptive, mineral: Elements, v. 11, p. 177–182.
Weis, F., 2013, Oxygen and Iron Isotope Systematics of the Grängesberg Mining District (GMD), Central Sweden: Unpublished M.Sc. thesis, Uppsala, Sweden, Uppsala University.
Wen, G., Li, J.W., Hofstra, A.H., Koenig, A.E., Lowers, H.A., and Adams, D., 2017, Hydrothermal reequilibration of igneous magnetite in altered granitic plutons and its implications for magnetite classification schemes: Insights from the Handan-Xingtai iron district, North China Craton: Geochimica et Cosmochimica Acta, v. 213, pp.255- 270.
Westhues, A., Hanchar, J.M., Whitehouse, M.J., and Martinsson, O., 2016, New constraints on the timing of host-rock emplacement, hydrothermal alteration, and iron oxide-apatite mineralization in the Kiruna District, Norrbotten, Sweden: Economic Geology, v. 111(7), p. 1595-1618.
Westhues, A., Hanchar, J.M., LeMessurier, M.J., and Whitehouse, M.J., 2017a, Evidence for hydrothermal alteration and source regions for the Kiruna iron oxide – apatite ore (northern Sweden) from zircon Hf and O isotopes: Geology, v. 45, p. 571-574.
Westhues, A., Hanchar, J.M., Voisey, C.R., Whitehouse, M.J., Rossman, G.R., and Wirth, R., 2017b, Tracing the fluid evolution of the Kiruna iron oxide apatite deposits using zircon, monazite, and whole rock trace elements and isotopic studies: Chemical Geology, v. 466, p. 303-322.
Williams, P.J., 1994, Iron mobility during synmetamorphic alteration in the Selwyn Range area, NW Queensland: implications for the origin of ironstone-hosted Au-Cu deposits: Mineralium Deposita, v. 29(3), p. 250-260.
Williams, P.J., Barton, M.D., Johnson, D.A., Fontboté, L., De Haller, A., Mark, G., Oliver, N.H. and Marschik, R., 2005, Iron oxide copper-gold deposits: Geology, space-time distribution, and possible modes of origin: Economic Geology, 100th Anniversary Volume, p.371-405.
Williams-Jones, A.E., and Heinrich, C.A., 2005, Vapor transport of metals and the formation of

magmatic-hydrothermal ore deposits. Economic Geology, 100th Anniversary Volume, p. 1287-1312.

Xie, Q., Zhang, Z., Hou, T., Cheng, Z., Campos, E., Wang, Z. and Fei, X., 2019. New insights for the formation of Kiruna-type iron deposits by immiscible hydrous Fe-P melt and high-temperature hydrothermal processes: evidence from El Laco deposit: Economic Geology,114(1), p.35-46.

Young, E.J., Myers, A.T., Munson, E.L., and Conklin, N.M., 1969, Mineralogy and geochemistry of fluorapatite from Cerro de Mercado, Durango, Mexico: US Geological Survey Professional Paper, v. 650, p. 84-93

Chapter 4

Using the Chemistry of Detrital Magnetite as an Exploration Tool in Densely Covered Terrains: A Case Study in the Greenstone Belts of Guyana

Co-authors: Aaron S. Wolf, Adam C. Simon, Chris Hunter, Marcus Harden, Georges Beaudoin

4.1 Abstract

Magnetite is a nearly ubiquitous phase in rocks and ore deposits, and its minor and trace element chemistry varies systematically depending on the environment in which it crystallizes. In this study, we developed a new statistical model that uses a global database of magnetite geochemistry measurements (n = 4600) for Cr, Ti, Mn, Al, V, Mg, Si, Ca, Cu, Ni, and Zn to discriminate magnetite from among the following ore deposit types: nickel copper platinum group element (Ni-Cu-PGE), orogenic gold, volcanogenic massive sulfide (VMS), iron oxide - copper - gold (IOCG), and porphyry copper (Au and Mo) deposits. We use this model, in addition to existing chemistry-based magnetite discriminant diagrams to identify the ore deposit source(s) (e.g., Ni-Cu-PGE, VMS, IOCG, etc.) of detrital magnetite in stream-sediment samples from catchments in Guyana. Comparisons of the chemistry of magnetite in outcrop and detrital grains from northwestern Guyana indicate that while the textural and physical characteristics of magnetite are partially preserved during weathering of rocks and stream transport, the minor and trace element chemistry of magnetite is only typically preserved if transported <1.5 km from the outcrop source. Notable exceptions are the concentrations of V and Al that remain unmodified during

stream transport (up to at least 5 km from the source outcrop). Application of our model to data for magnetite collected in Guyana indicates that the catchments sampled contain magnetite with chemistry characteristic of orogenic gold and Ni-Cu-PGE deposits. This work demonstrates the potential for detrital magnetite as an exploration tool for mineral systems in densely covered terrains, such as the Guiana Shield.

4.2 Introduction

Magnetite is a common iron oxide mineral and is ubiquitous in igneous, sedimentary, and metamorphic rocks, as well as in ore deposits. Magnetite has inverse spinel structure, Fe_3O_4, where ferrous iron (Fe^{2+}) is octahedrally coordinated and ferric iron (Fe^{3+}) is both tetrahedrally and octahedrally coordinated. Magnetite incorporates a large number of metals that substitute for both Fe^{2+} and Fe^{3+}, and results in the formation of solid solutions between magnetite, ulvöspinel, chromite, hercynite, magnesioferrite, trevorite, franklinite, and jacobsite as Ti^{4+}, Cr^{3+}, Al^{3+}, Mg^{2+}, Ni^{2+}, Zn^{2+}, and Mn^{2+} substitute for Fe in the magnetite structure (Deer et al., 1992; Dupuis and Beaudoin, 2011). Additionally, minerals such as coulsonite (FeV_2O_4,), cuprospinel ($CuFe_2O_4$), and harmunite ($CaFe_2O_4$), have the spinel structure and chemical formulas similar to magnetite with V^{3+} substituting for Fe^{3+}, and Ca^{2+} and Cu^{2+} substituting for Fe^{2+} (Galuskina et al., 2014). Ahrensite ($SiFe_2O_4$) also has spinel structure and is similar to ulvöspinel with Si substituting for Ti (Biagioni and Pasero, 2014). Given its compositional flexibility, magnetite is thus an invaluable geochemical tracer, reflecting the environmental conditions and processes present during the formation and processing of each grain. Magnetite geochemistry has been shown to be useful as an indicator of provenance and petrogenesis (Lovering and Hedal, 1987; Grigsby, 1990; Razjigaeva and Naumova, 1992; Singoyi et al., 2006), and to vary depending on the environment in which it

crystallizes (Dupuis and Beaudoin, 2011; Dare et al., 2012; Boutroy et al., 2014; Nadoll et al., 2014).

Variations in the composition of magnetites from different ore environments, including nickel copper platinum group element (Ni-Cu-PGE) deposits, chromitites, iron-titanium-vanadium (Fe-Ti-V) deposits, orogenic gold, porphyry copper (Au and Mo), epithermal, and skarn deposits, banded iron formations, volcanogenic massive sulfide (VMS) and sedimentary exhalative (SEDEX) deposits, iron oxide - apatite (IOA), and iron oxide - copper - gold (IOCG) deposits, have been used to identify the ore environment in which magnetite crystallized (Loberg and Horndahl, 1983; Dupuis and Beaudoin, 2011; Dare et al., 2012; Boutroy et al., 2014; Nadoll et al., 2014; Ward et al., 2018). Dupuis and Beaudoin (2011) showed that magnetite from ore environments, including Ni-Cu-PGEs, Cr deposits, VMS, Kiruna, porphyry Cu, BIF, IOCG, Skarn, and Fe-Ti-V deposits, can be identified using a combination of minor element concentrations. The authors report that Ni+Cr versus Si+Mg is useful for discriminating magnetite from Ni-Cu-PGE, Cr deposits; Al/(Zn+Ca) versus Cu/(Si+Ca) for identifying magnetite from Cu-Zn-Pb VMS deposits, and Ni/(Cr+Mn) versus Ti+V or Ca+Al+Mn versus Ti+V for discriminating magnetite from Kiruna, IOCG, porphyry Cu, BIF, skarn, and Fe-Ti-V deposits. Nadoll et al. (2014) suggested using Al+Mn versus Ti+V for discriminating magnetite from hydrothermal ore deposits (including Kiruna, IOCG, porphyry Cu, BIF, skarn, and Fe-Ti-V deposits) and plutonic igneous rocks. Additionally, Ward et al. (2018) showed that Ni versus Cr/V is useful for identifying magnetite from barren mafic and ultramafic rocks, mineralised ultramafic, and ore-related mafic rocks from the magmatic Ni-Cu-PGE sulfide deposits at Munali in Zambia. Recently, numerous researchers have shown that the use of a variety of statistical methods, which incorporate trace element geochemistry, improves geochemical discrimination methods for magnetite. Huang et al.

(2018, 2019) showed that the ability to discriminate between magnetite from hydrothermal ore deposits, including IOA, IOCG, porphyry copper deposits, and igneous rocks is improved by using partial least squares-discriminant analysis (PLS-DA) on geochemical datasets that include trace elements in addition to minor elements. Makvandi et al. (2016) also showed that PLS-DA allows discrimination of magnetite from VMS and BIF deposits. Pisiak et al. (2017) used linear discriminant analysis (LDA) to assess similarities between major, minor, and trace element compositions of magnetite in glacial till and known porphyry copper deposits in British Columbia. Dmitrijeva et al. (2018) demonstrated that the use of statistical methods on datasets which include both minor and trace elements allow discrimination of magnetite from BIF deposits in South Australia. While many studies discuss the utility of magnetite geochemistry as a tool for exploration, there are only a few published studies which investigate the magnetite geochemistry as a tool for exploration. Ward et al. (2018) compared the chemistry of magnetite in soil above known Ni-Cu-PGE deposits with magnetite from those deposits and found chemical signatures of mineralization in the detrital samples. The studies of Pisiak et al. (2017) and Makvandi et al. (2016) highlight the utility of investigating the geochemistry of glacially transported magnetite grains to assess ore deposit potential. To our knowledge, there is an overall absence of published studies that assess the viability of using the geochemistry of alluvial detrital magnetite as an exploration tool for the discovery of ore deposits in covered terrains.

The Guiana Shield in northern South America encompasses Guyana, Suriname, and French Guiana, much of western Venezuela, and parts of Colombia and Brazil (Gibbs and Barron, 1993). The Shield is primarily composed of early Proterozoic greenstones and metasediments that are overlain by conglomerates, quartzites, sandstones and shales, all of which are intruded by younger bimodal volcanic and intrusive rocks (Gibbs, 1987; Renner and Gibbs, 1987). Despite the long

history of mining in the Guiana Shield, it remains underexplored by modern exploration methods compared to other Precambrian cratons globally. Nonetheless, approximately 100 million ounces of gold have been discovered in the Guiana Shield (Goldfarb et al., 2017). Although gold is the major commodity mined in the Guiana Shield, it is an important producer of bauxite, and smaller deposits of manganese, diamonds, and iron have been discovered and/or mined (Bardoux et al., 2018). The Guiana Shield is hypothesized to have been contiguous with the Birimian Shield of West Africa prior to the opening of the Atlantic Ocean in the Cretaceous (Bullard et al., 1965; Delor et al., 2003; Tedeschi et al., 2019). Considering the ore deposit discoveries in the Birimian Shield, including >300 million ounces of gold as well as magmatic nickel deposits (Markwitz et al., 2016; Tedeschi et al., 2019), etc., similar deposits might be discovered in the Guiana Shield.

Though mining is an important contributor to Guyana's economy, it remains the most underexplored region in the Guiana Shield. Gold production in Guyana is dominated by the two major gold mines (Karouni and Aurora), however, there is also a significant contribution by small and medium scale miners, who collectively produce in excess of 300,000 ounces of gold annually GGMC, 2018, Go-Invest, 2019; Hook, 2019). Additionally, Guyana's mining sector comprises a bauxite mine (Bauxite Company of Guyana) and a manganese mine (Guyana Manganese Incorporated) in addition to small and medium scale alluvial diamond mining operations (GGMC, 2018). Currently, exploration methods that involve the use of geologic data are only employed by large scale miners and the (~6) junior mining companies doing exploration in Guyana. There is a dearth of recent geological data for Guyana; additionally, the thick forest cover and weathering profile and lack of outcrops make the collection of data challenging. Current exploration techniques are heavily focused on using: (1) data from geochemical surveys — mostly stream and soil sediments — to identify geochemical anomalies and targets for exploration, and (2) data from

legacy geophysical surveys (1960s) to gain insight about regional geology and structures. Exploration in Guyana, and the Guiana Shield, would benefit greatly from novel exploration techniques that could complement the regional datasets that exist by providing additional information about undiscovered deposits present under dense forest and soil cover and assist with the identification of targets.

In this study, we investigate the chemistry of magnetite and spinels from outcrop and stream sediment samples collected across Guyana in order to: (1) assess the effects of erosion, transport, and weathering on the chemistry of magnetite, and (2) to investigate the use of the geochemistry of detrital magnetite grains as a tool for regional exploration. We used a field emission scanning electron microscope (FE-SEM) to study samples at high magnification and acquire back scattered electron (BSE) images for textural characterization, and electron probe microanalysis (EPMA) to measure the abundance of major, minor, and trace elements in magnetite. Robust statistical methods were used to compare the chemistry of magnetite from Guyana with data from a global database of magnetite chemistry from Ni-Cu-PGE deposits, orogenic gold deposits, VMS deposits, IOCG deposits, porphyry - copper - gold (Cu-Au) deposits, and porphyry - copper - molybdenum (Cu-Mo) deposits. The mineralogical and geochemical data reveal that magnetite can be used as a robust exploration tool in areas that are heavily forested and have thick saprolite and soil cover.

4.3 Geological Background

4.3.1 Regional Geology

The Amazonian craton is divided into the Guiana Shield (north) and the Guaporé Shield (south). There are many open questions regarding the geologic evolution of the Guiana Shield. However, published works about the geology of the Shield indicate that it comprises rocks ranging

from Archean to Cenozoic in age (Fig 4.1A). The Imataca complex in Venezuela and the Cupixi formation in Brazil are both Archean in age. The Imataca complex contains banded iron formations and is likely the South American conjugate to the Archean nucleus in the Leo-Man Shield in Liberia/West Africa (Baratoux et al., 2019). The Cupixi formation is characterized as an allocthonous granitoid terrane (Sidder, 1990; Dardenne and Schobbenhaus, 2003; Klein and Rosa-Costa, 2003).

Paleoproterozoic units constitute the majority of the Guiana Shield. The oldest Paleoproterozoic rocks are greenstone belts formed during the Trans-Amazonian orogeny ~ 2.13 - 1.98 Ga (Daoust et al., 2011). The greenstone belts are distributed in the northwest of the Shield, in Guyana and Venezuela, and to the southeast in Suriname, French Guiana, and Brazil (Kroonenberg et al., 2016). The belts comprise bimodal mafic - ultramafic and felsic igneous rocks, in addition to clastic and chemical sedimentary rocks (Gibbs and Barron, 1993; Daoust et al., 2011). Gold mineralization has been discovered and mined in these belts in Venezuela (El Callao, Las Cristinas), Guyana (Aurora, Omai, Karouni), Suriname (Rosebel, Merian) and French Guiana (St. Elie) (Voicu et al., 1999; Daoust et al., 2011; Bassoo et al., 2018; Tedeschi et al., 2018a, b). The greenstone belts also contain diapiric tonalite-trondhjemite-granodiorite intrusions (TTGs) and gneisses with ages of 2.18 - 2.13 Ga (Kroonenberg et al., 2016; Tedeschi et al., 2018a, b). High grade metamorphic belts with ages ranging from 2.08 - 2.02 Ga are present in Suriname (Bakhuis and Coeroeni Belts), Guyana (Kanuku Group), and Brazil (Caurane belt) (Kroonenberg et al., 2016). The older felsic volcanic rocks and granitoids of the Orocaima belt (1.99 - 1.95 Ga) are present in Suriname, Guyana, Venezuela, and Brazil, while the younger felsic volcanics and granitoids of the Iricoumé belt (1.89 - 1.81 Ga) are present in Brazil and Guyana (Kroonenberg et al., 2016). The ~2000 m thick sandstones and conglomerates of the Roraima supergroup are

present in Venezuela, Guyana, and Brazil. This formation, dated to ~1.87 Ga (Kroonenberg et al., 2016), represents foreland basin sediments derived from the Trans-Amazonian mountains (Santos et al., 2003). The conglomerates in the Roraima are hypothesized to be similar to the gold-bearing Tarkwa formation in Ghana (Frimmel, 2014), and have also been investigated as a potential source of uranium in Guyana (Thompson, 2012). The Rio Negro Belt (1.86 - 1.72 Ga) is present in Venezuela, Colombia, and Brazil (Kroonenberg et al., 2016). The youngest Paleoproterozoic rocks are the ~1.79 Ga mafic intrusives and younger Avanavero and other Proterozoic mafic and alkaline intrusives in Guyana and Venezuela.

Mesoproterozoic intrusive rocks (1.59 - 1.51 Ga) and Platform Covers (1.3 - 1.2 Ga) are present in Brazil, Colombia, and Venezuela (Kroonenberg et al., 2016). Sedimentary rocks formed from the Paleozoic onwards are present in all 6 countries that constitute the Guiana Shield (Kroonenberg et al., 2016).

4.3.2 Local Geology

Of the countries that make up the shield, the geology of Guyana is the least well-constrained. Based on geological mapping, the major lithologic formations in Guyana formed in the Precambrian, Mesozoic, and Cenozoic (Fig. 1B; Heesterman and Nadeau, 2010). Proterozoic formations include: (1) Lower Proterozoic supracrustals, i.e., the greenstone belts of the Barama - Mazaruni supergroup and the high grade gneisses, granulites, and charnockites of the Kanuku group; (2) rocks formed during the Trans-Amazonian tectono-thermal event, i.e., the granitoids of the Younger Granites, the gneissose granites, diorites, and the migmatites of the Bartica Assemblage; and (3) ultramafic intrusives, layered gabbros, and the Kaburi anorthosite of the Badidku Suite/Older Basic Rocks. Other Proterozoic geologic units of interest include: (1) manganese deposits of the Matthew's Ridge Formation, (2) Middle Proterozoic gabbro-norite sills

and dikes of the Avanavero Suite; (3) fluviatile sands and conglomerates of the Roraima Group; (4) sub-volcanic granites and acid/intermediate volcanics of the Iwokrama and Kuyuwini Formations; (5) fluviatile sands and cherty mudstones of the Muruwa Formation; and (6) Upper Proterozoic nepheline syenites and inferred carbonatites of the Muri Alkaline Suite (Heesterman and Nadeau, 2010). Mesozoic formations include: (1) continental sands and silts of the Takutu Formation and (2) andesite flows of the Apoteri Volcanics, which constitute the Rewa Group (Heesterman and Nadeau, 2010). The Takutu graben formed during a failed rifting event that was a precursor to the opening of the Atlantic Ocean (Burke and Dewey, 1973; Choudhuri, 1980). The Cenozoic units include: (1) fluviatile and marine sands of the White Sand formation and (2) marine clays (Heesterman and Nadeau, 2010).

The catchment areas sampled are shown in Figure 4.1B. The intrusions sampled in northwestern Guyana belong to the Barama - Mazaruni Supergroup, and the detrital samples collected in this region, likely sample rocks from both the Barama - Mazaruni Supergroup and the Younger Granites (Fig. 4.1B). The detrital samples collected in the rest of the country additionally sample the Badidku Suite/Older Basic Rocks and the Avanavero Suite (Fig. 4.1B). The southernmost detrital grains likely sample the charnockites of the Kanuku Group (Fig. 4.1B).

4.4 Methods

4.4.1 Sample collection and preparation

We collected 14 outcrop samples and 84 detrital samples in the greenstone belts in Guyana. Sample locations for outcrops were identified by targeting regions with positive magnetic anomalies and coincident anomalous concentrations of Cr, Cu, and Ni in rock and soil geochemistry. In northwestern Guyana, stream sediment samples were collected from streams of different sizes/orders within 5 km of the intrusions sampled (Fig. 4.1C). Additionally, stream

sediment samples were collected during regional stream geochemistry surveys in the other regions of northwestern Guyana and in mining districts throughout the rest of the country (Fig. 4.1B). Outcrop samples were cut into billets and 100 μm thick sections were made. Heavy mineral separates were obtained by panning of stream sediments using a plastic pan to avoid contamination. The magnetic fractions of these heavy mineral separates were extracted using a hand magnet and mounted in epoxy resin to make 1 inch rounds, which were polished to a 0.3 μm finish using aluminum oxide polishing paper.

4.4.2 Phase identification and quantitative analyses

Mineral phases were identified and characterized via energy-dispersive X-ray spectrometry (EDS) spot analyses and backscattered electron (BSE) imaging by using the JEOL JSM – 7800FLV Field-Emission Scanning Electron Microscope (FE-SEM) at the University of Michigan Electron Microbeam Analysis Laboratory (EMAL) with an accelerating voltage of 15 kV.

The major, minor, and trace element chemistry of mineral phases was determined using a CAMECA SX-100 electron probe micro-analyzer (EPMA) in wavelength-dispersive X-ray spectrometry (WDS) mode in EMAL. For each outcrop and detrital sample, the concentrations of Fe, Ti, V, Mn, Ca, Mg, Cr, Al, Si, Ni, Cu, and Zn in representative magnetite and Fe-Cr-Ti oxide grains were measured by using an accelerating voltage of 20 keV, a beam current of 30 nA, and a focused electron beam. The counting times and standards used are presented in Table 4.1. Vanadium measurements were corrected for the spectral overlap of the V Kα X-ray line by the Ti Kβ. The average detection limits obtained for Fe, Ti, V, Mn, Ca, Mg, Cr, Al, Si, Ni, Cu, and Zn are 607 ppm, 101 ppm, 46 ppm, 82 ppm, 71 ppm, 86 ppm, 125 ppm, 74 ppm, 65 ppm, 83 ppm, 115 ppm, and 275 ppm, respectively. A total of 1100 individual EPMA spot analyses were

conducted on ~ 600 representative iron oxide grains from rock and stream sediment samples collected throughout Guyana.

4.4.3 Statistical analyses

In order to assess the ore deposit potential of the catchments sampled, we compared the chemistry of magnetite from Guyana with data from a global database that contains ~24,000 analyses of oxides (magnetite, titanomagnetite, hematite, chromite) from 13 ore deposit types (Ni-Cu-PGE, chromitites, Fe-Ti-V deposits, orogenic gold, porphyry copper (Au and Mo), epithermal, and skarn deposits, banded iron formations, VMS, SEDEX, IOA, and IOCG). We selected analyses from the global database that reported the concentrations of Ti, Cr, Mn, Al, Mg, Zn, Ni, V, Si, and Ca measured via EPMA, since we measured the concentrations of these elements in our samples from Guyana. This produced a global dataset that contained ~9,000 analyses. Next, we identified well-represented ore deposit types (with more than 300 analyses) to avoid issues associated with small number statistics. This produced a dataset of ~6,000 analyses from 6 ore deposit types (Ni-Cu-PGEs, VMS, orogenic gold, IOCG, porphyry Cu-Au, and porphyry Cu-Mo). Prior to the development and application of the model, data from both the Guyana and global datasets were screened to exclude data that were not representative of magnetite or spinel group minerals. We imposed concentration upper-limits (in wt. %) based on spinel group stoichiometry for Ti, Cr, Mn, Al, Mg, Zn, Ni, V, and Fe of 21.4, 46.5, 26.6, 31.1, 12.2, 16.6, 16.7, 46.5, and 72.4, respectively. Analyses were also removed if they had concentrations of Si and Ca greater than 5.5 and 0.4 wt. %, as these are the maximum concentrations of these elements reported in magnetite from natural samples (Newberry et al., 1982; Shimazaki, 1998; Dupuis and Beaudoin, 2011). The final global dataset used in the statistical analyses contained ~4,600 analyses, and 99% of these analyses had compositions with mole fractions of magnetite greater than 0.75. The remaining

analyses had compositions between endmember magnetite, chromite, ulvöspinel, and hercynite. The Guyana dataset contained ~700 analyses with mole fractions of magnetite greater than 0.75 and an additional 140 analyses with magnetite fraction less than 0.75.

The data were analyzed using scripts developed in the open-source Python programming language. We first developed a normative calculation scheme that attributes the measured concentrations to endmember spinel group minerals, which contain the elements of interest (Ti, Cr, Mn, Al, Mg, Zn, Ni, V, Si, and Ca), and calculates the mole fraction of magnetite. Next, the data from the global dataset were used to develop a multivariate normal distribution model (using tools from the Scikit-Learn module including quadratic discriminant analysis; see Pedregosa et al., 2011) to distinguish magnetite from Ni-Cu-PGE, VMS, orogenic gold, IOCG, and porphyry copper (i.e., Cu-Au and Cu-Mo) ore environments (Appendix 4.1). The model was developed using >400 analyses of magnetite from multiple individual ore deposits belonging to the aforementioned ore deposit types. We grouped analyses for magnetite from porphyry Cu-Au and porphyry Cu-Mo deposits and treat them as a single ore deposit type, referred to as porphyry copper deposits (PCD). The model characterizes the distinct chemical signatures of magnetite from each of these deposit types, allowing us to predict the likely parent ore deposit type for a grain from an unknown source. To quantify the accuracy of this model for deposit type predictions, we determine the number of true and false positives and true and false negatives and used these values to calculate the sensitivity and precision for each deposit type in the model (this type of accuracy assessment is typical in diagnostic medical testing, e.g. Drum and Christacopoulos, 1972). The sensitivity indicates how likely the method is to correctly identify a sample from a given deposit type, while the precision reflects the accuracy of identifications made; they are calculated as follows:

$$Sensitivity = \frac{True\ Positive}{True\ Positive + False\ Negative}$$ (Equation 1)

$$Precision = \frac{True\ Positive}{True\ Positive + False\ Positive}$$ (Equation 2).

For this study, true positives for a deposit type, e.g., Ni-Cu-PGEs, are the analyses from Ni-Cu-PGE deposits that are correctly identified as being from the Ni-Cu-PGE deposit type; false positives are those analyses from other deposit types (e.g., VMS, IOCG) that are wrongly identified as Ni-Cu-PGEs; true negatives are analyses from other deposit types (e.g., VMS, IOCG) that are identified as not being from Ni-Cu-PGEs; and false negatives are analyses from Ni-Cu-PGEs that are incorrectly identified as belonging to another deposit type (e.g., VMS, IOCG). The normal distribution model thus provides a prediction of the relative likelihood that a single sample is derived from each of the five deposit types, and is well characterized in terms of its identification accuracy.

In most cases, when we have a collection of samples from a given region, we can infer the likely mixture of ore deposit source types that produced the sample set. We used a non-negative least squares regression model to compare the multivariate normal model results of data from unknown samples and the characteristic geochemical signatures of the five classes of deposits to infer which deposit type or mixture of deposit types is required to produce the chemical signature obtained when the model is applied to the data. Lastly, the model was applied to the 700 analyses for magnetite from Guyana (generated in this study) to investigate if the chemistry of magnetite in intrusions and stream sediment samples are typical of Ni-Cu-PGE, VMS, orogenic gold, IOCG, and/or porphyry copper mineralization.

4.5 Results

4.5.1 Mineral chemistry and descriptions

4.5.1.1 Outcrop samples

The sampled intrusions were identified as pyroxenites (GY-RC-03, GY-RC-07, GY-RC-10, GY-RC-11, GY-RC-13, GY-RC-14) and iron-titanium (Fe-Ti) poor mafic rocks (GY-RC-01, GY-RC-12) using whole rock geochemistry and the rock-type classification calculations in the ioGAS software (Fig. 4.1C). Scanning electron microscope investigations of thin sections from the intrusions indicate that the investigated grains have chemistries equivalent to magnetite, hematite and spinel minerals that have compositions between endmember magnetite, ulvöspinel, and chromite. EPMA indicate that magnetite grains have a range of compositions, including low Cr-Ti magnetite, Cr-rich titanomagnetite, and Cr-poor titanomagnetite, and that the samples also contained chromium-rich spinels, titanomagnetite and hematite. Mafic outcrop samples contain Cr-poor titanomagnetite, hematite, and titanomagnetite. Pyroxenite outcrop samples contain the aforementioned phases present in the mafic outcrops, in addition to Cr-Ti poor magnetite, Cr-rich magnetite, Cr-rich titanomagnetite, and Cr-rich spinels. The chemistry of magnetite in the intrusions is presented in box and whisker plots in Fig. 4.4 and in Table 4.2. Generally, Cu and Zn concentrations are below or close to the detection limit for most of the analyses. The analyzed grains exhibit a variety of textures (Table 4.A1) and the observed textural differences correlate with chemical differences.

Chromium-poor titanomagnetite from mafic rocks have median Fe, Cr, Ti, Mg, V, and Al contents (± 1σ) of 67.2 ± 2.4 wt%, 0.05 ± 0.04 wt.%, 1.7 ± .1.3 wt.%, 0.03 ± 0.1 wt.%, 0.6 ± 0.5 wt.%, and 0.5 ± 0.3 wt.%, respectively. These grains have well-developed sandwich-textured ilmenite exsolution lamellae and cloth-textured ilmenite exsolution lamellae are present in the

magnetite between the sandwich-textured ilmenite lamellae (Fig. 4.2A). A subset of these magnetite grains also contains fluorapatite and sulfide grains as inclusions, and ilmenite granules are present in cracks within the magnetite grains and at their grain boundaries (Fig. 4.2B). Additionally, some of these magnetite grains are adjacent to ilmenite grains, which sometimes contain magnetite and/or sulfide inclusions (Fig. 4.2A, C, D). A subset of these grains are identified as titanomagnetite, and have median concentrations (± 1σ) of Fe, Cr, Ti, Mg, V, and Al of 58 ± 3.5 wt.%, 0.1 ± 0.02 wt.%, 8 ± 2.3 wt.%, 0.07 ± 0.1 wt.%, 0.6 ± 0.2 wt.%, and 1.1± 2.5 wt.%, respectively.

Chromium-Ti poor magnetite from pyroxenite sample GY-RC-07 have median concentrations (± 1σ) of Fe, Ti, and Mg of 70 ± 0.5 wt.%, 0.05 ± 0.02 wt.%, and 0.1 ± 0.2 wt.%, respectively, and Cr, Al and V below the limit of detection. These grains are small and inclusion-poor. Chromium-rich titanomagnetite from the pyroxenite samples have median concentrations (± 1σ) of Fe, Cr, Ti, Mg, V, and Al of 64.8 ± 6.9 wt.%, 3.2 ± 1.9 wt.%, 1 ± 1 wt.%, 0.1 ± 1.5 wt.%, 0.2 ± 0.6 wt.%, and 0.2 ± 1.5 wt.%, respectively. Some Cr-rich titanomagnetite grains exhibit a wavy or spongy texture, which characterizes entire grains or is present only in the rims of some grains (Fig. 4.2E, F). Other grains are inclusion-poor and contain ilmenite or hercynite granules within grains or at grain boundaries (Fig. 4.2G, H). Additionally, some of these magnetite grains contain very thin trellis-textured ilmenite exsolution lamellae (Fig. 4.2I). Both the inclusion-poor grains and those that contain ilmenite exsolution lamellae sometimes meet at triple junctions. Cr-poor titanomagnetite in the pyroxenite outcrops have median concentrations (± 1σ) of Fe, Cr, Ti, Mg, V, and Al of 68.9 ± 2 wt.%, 0.2 ± 0.1 wt.%, 0.5 ± 0.5 wt.%, 0.02 ± 0.4 wt.%, 0.3 ± 0.1 wt.%, and 0.04 ± 0.1 wt.%, respectively. These grains also exhibit wavy texture, contain small, irregularly shaped cloth-textured ilmenite exsolution lamellae, or contain visible ilmenite

exsolution lamellae or ilmenite granules (Fig. 4.1C; 4.2J). Chromium-rich magnetite from the pyroxenite intrusions have median Fe, Cr, Ti, Mg, V, and Al contents (± 1σ) of 62.6 ± 6.7 wt.%, 2 ± 1.2 wt.%, 0.07 ± .01wt%, 0.7 ± 3.2 wt.%, 0.2 ± 0.1 wt.%, and 0.4 ± 1 wt.%, respectively. This magnetite is inclusion-poor, has lower Z than the previously described magnetite grains and is present between the cores and rims of zoned spinel grains in the intrusions (Fig. 4.2F). Chromium-rich spinels from the pyroxenite samples have median Fe, Cr, Ti, Mg, V, and Al contents (± 1σ) of 44 ± 10 wt.%, 19 ± 6 wt.%, 1.8 ± 1.2 wt.%, 0.05 ± 2 wt.%, 0.3 ± 0.1 wt.%, and 0.8 ± 7 wt.%, respectively. These grains are present in three intrusions (GY-RC-10, GY-RC-11, GY-RC-14) and are zoned, with cores and rims of different compositions as indicated by differences in color BSE images (Fig. 4.1C; 4.2F). Titanomagnetite present in pyroxenite samples have median concentrations (± 1σ) of Fe, Cr, Ti, Mg, V, and Al of 57.2 ± 3.5 wt.%, 0.2 ± 1.9 wt.%, 7.9 ± 2.3 wt.%, 0.05 ± 0.1 wt.%, 0.3 ± 0.2 wt.%, and 0.2 ± 1.9 wt.%, respectively. These grains, like the titanomagnetite grains in the mafic outcrops, contain visible ilmenite exsolution lamellae (Fig. 4.2K).

Hematite in the intrusion samples have median concentrations (± 1σ) of Fe, Cr, Ti, Mg, V, and Al of 68.5 ± 1 wt.%, 0.01 ± 0.1 wt.%, 0.02 ± 0.02 wt.%, 0.4 ± 0.2 wt.%, 0.04 ± 0.02 wt.%, and 0.03 ± 0.01 wt.%, respectively. Hematite grains are typically small and somewhat porous and meet at triple junctions (Fig. 4.2L). Additionally, hematite in GY-RC-07 contains millerite as an inclusion (Fig. 4.2M). Many intrusions contain ilmenite with patchy texture, which contain magnetite exsolution lamellae, and sometimes sulfide inclusions (Fig. 2C, 2N). Sulfide grains were observed in all sampled intrusions (Table 4.A1). Sulfides observed include pyrrhotite, pentlandite, chalcopyrite, pyrite, cubanite, bornite, sphalerite, covellite, chalcocite, and some grains contained multiple sulfide phases within the same grain (Fig. 4.2A, D, O, P, Q). Pentlandite, pyrrhotite,

sphalerite, chalcopyrite, and pyrite were observed in the mafic and ultramafic rocks (Fig. 4.2A, M, and O). Small (10s μm) sulfide grains are present in the groundmass of some intrusions; however, larger grains, (100s μm) were observed in other intrusions (Fig. 4.2P).

4.5.1.2 Detrital samples

The detrital grains present in the stream sediments samples include magnetite, hematite, chromium-rich spinels, and chromite, in addition to ilmenite, zircon, monazite, xenotime, and free gold grains. Magnetite in detrital grains exhibit the compositional variability described for the outcrop samples, i.e., low Cr-Ti poor magnetite, Cr-rich and Cr-poor titanomagnetite, and Cr- rich magnetite. Ilmenite is common in many samples and some detrital samples contain ilmenite and other phases, but no magnetite. Most mineral grains are angular to sub-angular, and only a few grains were rounded/subrounded (Fig. 4.3A). A summary of the chemical data for magnetite from the streams are presented in Fig. 4.4.

The grains in the stream sediment samples contain many of the textures described for grains in the intrusion samples, however, the majority of the grains exhibit the inclusion-poor texture and some of these grains contain visible pits (Figure 4.3B). Inclusion-poor detrital grains have chemical compositions classified as Cr-Ti poor magnetite, Cr-rich magnetite, and Cr-rich titanomagnetite. The Cr-Ti poor magnetite grains have median concentrations (± 1σ) of Fe, Cr, Ti, V, and Al of 71.4 ± 1 wt.%, 0.02 ± 0.1 wt.%, 0.03 ± 0.03 wt.%, 0.1 ± 0.1 wt.%, and 0.02 ± 0.06 wt.%, respectively and Mg below the limit of detection. Additionally, some Cr-Ti poor magnetite grains contain crevices along the (111) planes which appear to represent trellis and sandwich textured ilmenite exsolution lamellae that have been weathered or reacted away; this texture is referred to as magnetite with relic ilmenite exsolution lamellae (Fig. 4.3C). Detrital Cr-rich titanomagnetite have median concentrations (± 1σ) of Fe, Cr, Ti, Mg, V, and Al of 65.6 ± 3.5 wt.%,

3.6 ± 2.3 wt.%, 0.6 ± 1 wt.%, 0.1 ± 0.2 wt.%, 0.1 ± 0.1 wt.%, and 0.1 ± 0.6 wt.%, respectively. Some Cr-rich titanomagnetite grains have lower Z than the other magnetite grains in the samples (Fig. 4.3D). Chromium-rich magnetite grains have median Fe, Cr, Ti, Mg, V, and Al contents (± 1σ) of 69.3 ± 5.3 wt.%, 0.5 ± 1.9 wt.%, 0.05 ± 0.02wt%, 0.03 ± 0.3 wt.%, 0.1 ± 0.1 wt.%, and 0.1 ± 0.7 wt.%, respectively. This group of magnetite grains is dominated by the inclusion-poor texture, however, some grains also contain thin trellis- and/or sandwich-textured ilmenite exsolution lamellae (Fig. 4.3E, F, G). Detrital Cr-poor titanomagnetite exhibits a variety of textures and have median Fe, Cr, Ti, V, and Al contents (± 1σ) of 68.1 ± 3.3 wt.%, 0.03 ± 0.06 wt.%, 0.6 ± 1.5 wt.%, 0.2 ± 0.2 wt.%, and 0.1 ± 0.5 wt.%, respectively, and Mg below the limit of detection. These magnetite grains contain visible trellis and sandwich textured or cloth-textured ilmenite exsolution lamellae and relic ilmenite exsolution lamellae (Fig. 4.3C, H, I). A few Cr-poor titanomagnetite grains also exhibit the wavy/ spongy texture observed in outcrop samples (Fig. 4.3J). Detrital hematite grains have median concentrations (± 1σ) of Fe, Cr, Ti, V, and Al of 68.9 ± 0.4 wt.%, 0.02 ± 0.03 wt.%, 0.03 ± 0.02 wt.%, 0.1 ± 0.1 wt.%, and 0.04 ± 0.05 wt.%, respectively, and Mg below the limit of detection. These grains also appear inclusion-poor and contain visible pits (Fig. 4.3B). Chromium-rich spinels have median Fe, Cr, Ti, Mg, V, and Al contents (± 1σ) of 40 ± 12 wt.%, 22 ± 9 wt.%, 0.7 ± 1 wt.%, 0.3 ± 1 wt.%, 0.2 ± 0.1 wt.%, and 1 ± 3 wt.%, respectively. Some of these grains were zoned with cores and rims of different compositions as observed in some intrusions samples (Fig. 4.3K, L). These grains are characterized by much lower Z or darker color in BSE images compared to the magnetite grains. Detrital titanomagnetite grains have median concentrations (± 1σ) of Fe, Cr, Ti, Mg, V, and Al of 61 ± 4 wt.%, 0.04 ± 0.2 wt.%, 7.3 ± 2 wt.%, 0.01 ± 0.03 wt.%, 0.2 ± 0.2 wt.%, and 0.1 ± 0.3 wt.%, respectively. These grains have visible ilmenite exsolution lamellae (Fig. 4.3M).

Generally, a few magnetite grains have sharp, polygonal boundaries (Fig. 4.3B) and some magnetite grains contain sulfide inclusions, e.g., chalcocite and bornite (Fig. 4.3N, O, P, Q). Many ilmenite grains have patchy texture and contain magnetite exsolution lamellae (Fig. 3R) and ilmenite granules are present within cracks in some magnetite grains and on the edges of some grains (Fig. 4.3O). Pyrrhotite, pentlandite, chalcopyrite, bornite, sphalerite, pyrite, polymineralic sulfide assemblages, cobaltite, gersdorffite, and barite are present as inclusions in magnetite, ilmenite, quartz, and clinopyroxene in samples collected during regional stream sediment surveys, i.e., not in the samples proximal to the sampled outcrops (Fig. 4.3R, S, T, U, V).

4.5.1.3 Chemical and textural comparison of outcrop and detrital samples collected in the same catchment

Detrital sample C-12174 was collected in a third order stream that drains rock samples GY-RC-10 and GY-RC-11, and samples C-12170 and C-12171 were collected further downstream from C-12174 (Fig. 4.1C). Sample C-12170 was collected about 1 km from C-12174, while C-12170 was ~0.1 km downstream from C-12171. Sample C-12174 contained inclusion-poor magnetite, magnetite with trellis-textured ilmenite exsolution lamellae, and magnetite with wavy/spongy texture (Fig. 4.5E-H). Magnetite with wavy/spongy texture was observed in GY-RC-10, while the inclusion poor-magnetite and magnetite with thin ilmenite exsolution lamellae were observed in both GY-RC-10 and GY-RC-11 (Fig. 4.2E, 4.5A-D). Both rock samples and C-12174 contain Cr-rich spinels. C-12174 contains magnetite with relic ilmenite exsolution lamellae (Fig. 4.5E). Sample C-12171 contains Cr-rich spinels, inclusion-poor magnetite, and magnetite with visible and relic ilmenite exsolution lamellae (Fig. 4.5I-M). The magnetite grains with relic ilmenite exsolution lamellae in samples C-12174 and C-12171 have similar appearance; however, the grains in C-12171 are more rounded (Fig. 4.5E, M). Sample C-12170 contains inclusion-poor

magnetite and magnetite with relic ilmenite exsolution lamellae (Fig. 4.5). Chemically, magnetite grains from the outcrop and detrital samples are similar, even though all textural types of magnetite observed in the outcrops are not observed in the detrital grains in this catchment (Fig 4.5; Table 4.2). All three detrital samples contain Cr-Ti poor magnetite and Cr-poor titanomagnetite. All outcrop and detrital samples in this catchment contain Cr-rich titanomagnetite. Chromium-rich magnetite is present in GY-RC-10 and C-12170; titanomagnetite is present in GY-RC-11 and detrital samples C-12174 and C-12171. The V and Al content of the magnetite in C-12174 is lower than that in the rocks, however, the decrease in the concentrations of these elements is much smaller than for other elements, i.e., Cr, Ti, Mg, Mn, and Ni (Fig. 4.6C). Sample C-12171, collected about 1 km from C-12174, has similar median Si, Cr, V, and Ti concentrations, lower Ni concentrations, and higher Al and Mn concentrations relative to this sample. The magnetite grains in C-12170, generally have lower median concentration of Al, similar median concentrations of Si, V, Mn, Ni, and higher median concentrations of Cr and Ti relative to those in sample C-12171. The chemistry of the magnetite in C-12170 is generally similar to that for magnetite for C-12174, however, there are minor differences, including higher median Si, Cr, and Ti (Fig. 4.6C, E).

Generally, the concentrations of all elements in detrital magnetite grains are lower than those from outcrop samples. The concentrations of Cr, Ca, Ti, Mn, Mg, and Ni in magnetite decrease in stream sediment samples as stream order/size increases (Fig. 4.4). The concentrations of V and Al are lower in magnetite from streams, however, the (median) concentrations of these elements are mostly constant in streams of all orders/sizes (Fig. 4.4).

4.6 Discussion

4.6.1 Insights from compositions and textures of magnetite and Fe-Cr-Ti oxides in outcrop and detrital samples

The chemical and textural analyses of grains from outcrop samples indicate the presence of multiple generations of magnetite and Cr-rich spinels in the samples. Magnetite grains from outcrop and detrital samples contain ilmenite exsolution lamellae, which form due to the oxy-exsolution of the ulvöspinel component of magnetite-ulvöspinel$_{ss}$ (Buddington and Lindsley, 1964). This texture is an indication that the magnetite grains are igneous in nature. Magnetite with well-developed thick (10 - 200 μm) and thin (1-5 μm) ilmenite exsolution lamellae with trellis and sandwich textures, and ilmenite exsolution with cloth texture (Fig 4.2A) were observed by Arguin et al. (2018) in their study of vanadiferous titanomagnetite from the Lac Doré Complex in Québec, Canada. The authors note that the various textural forms of ilmenite exsolution lamellae provide insight about when the oxy-exsolution of ulvöspinel occurred. Arguin et al (2018) note that thick ilmenite exsolution lamellae form as a result of oxy-exsolution of ulvöspinel from magnetite-ulvöspinel$_{ss}$ above the solvus temperature (450-600 °C) and that cloth-textured and thin ilmenite exsolution lamellae form as a result of oxy-exsolution of ulvöspinel from magnetite-ulvöspinel$_{ss}$ below the solvus temperature (Vincent et al., 1957; Duchense, 1970; Lindsley, 1981; Lilova et al., 2012; Arguin et al., 2018). The occurrence of ilmenite exsolution lamellae formed via both super and sub-solvus oxy-exsolution of the ulvöspinel in a single mineral grain (Fig. 4.2A) are consistent with changes in the oxidation state of the silicate melt during cooling of intrusion after emplacement. We note that this texture was also observed by Ward et al. (2018) in the poikilitic gabbro in the Munali Igneous Complex. Ilmenite exsolution lamellae are observed in magnetite grains which terminate at triple junctions; similar observations were also made by Von

Gruenewaldt et al. (1985) and Arguin et al. (2018). They interpret this texture to indicate that oxy-exsolution of ulvöspinel and the formation of ilmenite occurred after compaction and annealing of magnetite grains during cooling and accumulation in the rock mass (Von Gruenewaldt et al., 1985; Arguin et al. 2018). If the ilmenite lamellae had exsolved prior to re-equilibration, they would have diffused and migrated to the grain boundaries and eventually be expelled out of the grains to form granules (Buddington and Lindsley, 1964; Von Gruenewaldt et al., 1985; Arguin et al. (2018). Alternatively, re-equilibration of igneous magnetite — which contained ilmenite exsolution lamellae — with hydrothermal fluids (during or after cooling of the intrusions) via coupled dissolution reprecipitation reactions can also produce this texture (Hu et al., 2015; 2016).

Chromium-rich spinels and Cr-rich magnetite were observed in outcrop and detrital samples (Fig. 4.2F, G; 4.3K, L). Chromite and Cr-spinels are the dominant oxide minerals in ultramafic rocks being the first spinels to crystallize from a primitive silicate melt (Irvine, 1965; Roeder, 1994; Abzalov, 1998; Barnes and Roeder, 2001). The compositions of spinels change as a result of compositional changes of parental magmas due to fractional crystallization such that the most primitive spinels are Al-Ti chromites, and later spinels have increasing Ti and Fe contents resulting in the formation of titanomagnetite and eventually magnetite (Roeder, 1994; Abzalov, 1998; Barnes and Roeder, 2001). Spinel compositions can also be changed due to reactions of the earliest spinels with the evolving intercumulus silicate liquid during post-cumulus processes, and Cr-spinels can be altered to/or replaced by ferritchromite (chromian magnetite) and magnetite during metamorphism (Abzalov, 1998; Barnes and Roeder 2001; Merlini et al., 2005; 2009). Abzalov (1998) noted the crystallization of three generations of spinels in ultramafic (gabbro-wehrlite) intrusions in the Proterozoic Pechenga greenstone belt in Russia. The earliest spinels were Al-Ti chromites, the second generation of spinels had composition ranging from Ti-rich

chromite to Ti-rich chrome magnetite and often contained ilmenite exsolution lamellae, and the third generation of spinel was Cr-poor titanomagnetite — this phase was common in pyroxenites and gabbros (Abzalov, 1998).

The Cr contents measured in the Cr-rich spinel grains observed in this study (below the limit of detection to ~ 45 wt. %), overlap those reported by Abzalov (1998). Additionally, oxide grains from three intrusions showed zonations in Cr contents with highest Cr in the cores, intermediate Cr contents between the core and rim and very low Cr content in the rims (Fig. 4.2H). The chemical formulas of the phases in the distinct domains of this grain are $Fe^{2+}_{0.9}(Cr^{3+}Fe^{3+}_{0.5}Al^{3+}_{0.5})O_4$, $Fe^{2+}_{1}(Cr^{3+}_{0.9}Fe^{3+}_{0.8}Al^{3+}_{0.07})O_4$, $Fe^{2+}_{1}(Cr^{3+}_{0.3}Fe^{3+}_{1.6}Al^{3+}_{0.01})O_4$, and $Fe^{2+}_{1}(Cr^{3}_{0.03}{}^{+}Fe^{3+}_{1.9}Al^{3+}_{0.004})O_4$ from core to rim. The compositions of the cores of the zoned grains are similar to those reported for chromite by Abzalov (1998), consistent with the growth of these grains from silicate melts of primitive composition. The core to rim zonation of Cr and Fe in the grains is consistent with growth from or reaction with an evolving silicate liquid (Roeder, 1994; Abzalov, 1998; Barnes and Roeder, 2001).

Additionally, we observed Cr-rich titanomagnetite containing thin ilmenite exsolution lamellae, attributed to sub-solvus oxy-exsolution of ulvöspinel, in sampled pyroxenite intrusions (Fig. 4.2I); Cr-rich magnetite grains were not observed in the mafic rocks. These grains have compositions similar to the second generation of spinels reported by Abzalov (1998), which were ascribed to growth from evolved parental melts or intercumulus melts. Pyroxenite samples also contained inclusion-poor Cr-rich titanomagnetite with elevated minor and trace elements, and these grains are sometimes associated with hercynite or ilmenite granules (Fig. 4.2G). The chemical and textural characteristics of these grains indicate that they are igneous in nature (Arguin et al., 2018). Further, the pyroxenites contain inclusion-poor Cr-Ti-poor magnetite that is

characterized by low minor and trace element contents that are consistent with precipitation from hydrothermal fluids (Nadoll et al., 2014; Dare et al., 2015; Fig. 4.2J). Hematite, which is sometimes associated with secondary sulfide minerals (e.g., millerite, Fig. 4.2M), is also present in intrusion samples. This provides further evidence of hydrothermal alteration of outcrop samples. The sampled outcrops were collected in a greenstone belt, where metamorphism to greenschist facies is common (Gibbs and Barron, 1993). Thus, it is likely that Cr-Ti-poor magnetite formed due to metamorphism/hydrothermal activity; these fluids, or later fluids, could have also produced the hematite observed (Abzalov, 1998; Mellini et al., 2005; Merlini et al., 2009; Nadoll et al., 2014).

Notable textural similarities are found in magnetite and spinel grains from outcrops and detrital samples, indicating that we can gain insights about the geology of the sampled catchments using the detrital grains (Fig. 4.5). Some detrital grains from northwestern Guyana have Fe and Cr contents expected for endmember chromite, while others are characterized by elevated Al and Cr contents, similar to the earliest formed chrome spinels described by Abzalov (1998). Moreover, we observe the compositional zonation observed in spinel from intrusion samples in detrital grains despite weathering and transport of these grains by streams. The detrital grains typically contain 2 distinct compositional zones (Fig. 4.3K); however, these observations are enough to allow us to infer that the grains grew from a silicate fluid of evolving composition. Ilmenite exsolution lamellae are observed in detrital Cr-rich titanomagnetite grains in some sampled catchments (Fig. 4.3D). However, the ilmenite exsolution lamellae in the detrital Cr-rich titanomagnetite grains are much thicker (up to 10 μm) than those observed in the Cr-rich titanomagnetite from the pyroxenite outcrops (Fig. 4.2I). The thin (<5 μm) trellis-textured ilmenite exsolution lamellae observed in outcrops was rarely observed (~ 1%) among detrital grains (Fig. 4.3G, F). The overlap in

compositions of the ilmenite-bearing and inclusion-poor Cr-rich titanomagnetite may indicate that the inclusion-poor grains represent a weathered form of the ilmenite-bearing Cr-rich titanomagnetite grains. The term weathering in this paper is used to describe chemical and physical processes. Physical weathering in this environment results is likely responsible for the formations of pits in grains, and the disintegration and removal of ilmenite exsolution lamellae. Consequently, this physical disintegration of magnetite likely also results in changes to the chemistry of magnetite grains (Fig. 4.4).

Many investigated magnetite grains preserve evidence of the presence of trellis-textured ilmenite exsolution lamellae that have been lost due to weathering and erosion (Fig. 4.3G, 4.5E, M, V). Comparison of the chemistry of magnetite associated with ilmenite exsolution lamellae in sampled outcrops, and detrital grains with visible and relic ilmenite exsolution lamellae indicate decreasing concentrations of minor and trace elements (i.e., Ti, Cr, Mn, Mg, Ca) and increasing concentrations of Fe from the ilmenite-bearing magnetite in intrusions to magnetite with relic ilmenite exsolution lamellae in streams. This comparison further illustrates that magnetite grains are texturally and chemically altered during weathering and transport. Inclusion-poor magnetite is the most common textural variety of magnetite observed in the detrital samples, though this texture was not very common in outcrop samples. The prevalence of this texture is likely the result of loss of texture and changes in the composition of magnetite during weathering and transport. Despite the textural changes to detrital grains, the overlap in the chemical signatures of oxide grains from outcrops and detrital samples indicate that the chemical signatures of magnetite and spinels are preserved for transport up to 2 km within catchments, and that detrital grains can still be used as petrogenetic indicators at the local, catchment scale (Fig. 4.6). Generally, the detrital grains investigated in this study indicate that the grains are sourced from outcrops of mafic to ultramafic

compositions, which have been hydrothermally altered; this interpretation is consistent with the understanding of the geology of the regions sampled (Fig. 4.1B; Gibbs and Barron, 1993).

4.6.2 A new model for inferring ore deposit potential from magnetite geochemistry

We developed a new predictive model that identifies which of 5 types of ore deposits (Ni-Cu-PGEs, orogenic gold, VMS, IOCG, and porphyry copper deposits) magnetite grains are likely sourced from by assessing chemical similarities with a global geochemical database for these deposit types. The attribution of measured compositions to endmember spinels proved important since it reduced the effects of outliers in the raw geochemical data. To predict the source of magnetite from unknown sources, the model compares individual analyses to the multivariate normal distributions for the global geochemical data. Thus, the probability for each deposit type for an unknown sample is predicted based on chemical similarity. Since we know the actual deposit source of each analysis from the training data, we are able to test the accuracy of the model for the global database by comparing the true and inferred deposit indices for each analysis; these results are presented in Fig. 4.7. The sensitivity of the model (which indicates the probability of detection) varies by deposit type: 59% for Ni-Cu-PGEs, 50% for orogenic gold, 16% for VMS, 37% for IOCG, and 76% for PCDs. The precision for each deposit type (which indicates the identification accuracy) is 76% for Ni-Cu-PGEs, 56% for orogenic gold deposits, 71% for VMS deposits, 25% for IOCGs, and 28% for porphyry copper deposits.

The underlying premise of our model is that data for magnetite from the 5 ore deposit types are normally distributed and that the normal distributions for each deposit type are sufficiently distinct to enable clear identification. The precision and sensitivity for each deposit type measure the distinctness of the multivariate normal distributions for each deposit type. The high precision and sensitivity for Ni-Cu-PGEs suggest that for the elements considered (Si, Al, Mg, Ti, Cr, Mg,

Mn, V, Ca, Cu, Zn) there is minimal overlap between the multivariate normal distribution — the size and shape of the cluster of data points — for data from this and other deposit types. The low precision and high sensitivity for PCDs suggest that the multivariate normal distribution for this deposit type is not distinct in the geochemical space considered. In fact, the plot in figure 4.7A shows that the normal distribution for the data from PCDs overlaps the normal distributions for data from other deposit types. Based on the precision and sensitivity for each deposit type in our model, the model satisfactorily identifies analyses for magnetite from Ni-Cu-PGE and orogenic gold deposits, and does a less satisfactory job of identifying analyses for magnetite from VMS, IOCG, and porphyry copper deposits (Fig. 4.7A). When applied to a dataset, the model returns the proportion of the data that is identified as being from each deposit class, e.g., proportions of 57% Ni-Cu-PGE, 13% orogenic gold, 4% VMS, 13% IOCG, and 12% PCD are returned when the model is applied to the global Ni-Cu-PGE deposit dataset. This result reflects misidentification of analyses due to the overlap between the normal distributions for the ore deposits in the chemical space considered.

The overlap between the chemical signatures for magnetite in the chemical space considered hampers our ability to accurately identify individual analyses as belonging to a particular deposit type. Therefore, to improve the predictive nature of our model, we use the characteristic overlap between the chemical signatures of magnetite from different deposit classes to infer the likely contribution of each deposit type to the signature obtained for a collection of samples gathered from a particular region. This is carried out using non-negative least squares regression (NNLS), by comparing the maximum likelihood model results for the unknown samples to that of the global training data. Due to compositional overlap, some deposit types are often confused for one another, but in a collection of samples, the fraction of grains assigned to each

deposit type is itself diagnostic of the mixture of deposits in the source region. NNLS thus determines the proportion of each deposit type that best reproduces the model results for the entire collection of grains. The NNLS regression model was utilized because it allows us to determine the contributions of individual deposit type signatures to the mixed stream signature with the constraint that the proportion of each deposit type is non-negative, since it represents the fractional contribution of magnetite grains, making negative numbers unphysical. When the NNLS model is applied to the global Ni-Cu-PGE data, the inferred source proportions are 94% Ni-Cu-PGE, 1% orogenic gold, 0% VMS, 0% IOCG, and 5% PCD (Fig. 4.7B). Comparison of the results for the multivariate normal distribution and NNLS model for the global Ni-Cu-PGE dataset indicate that by using the NNLS model, we are able to reduce the contamination/overlap in the signatures for magnetite from the other types of ore deposits, when we are provided a collection of magnetite samples.

The effectiveness of the NNLS model was further assessed by applying it to individual deposits from the global database (Fig. 4.A1-A). The result indicates that magnetite grains from some individual deposits have chemistry that deviates from the bulk chemistry of the overall deposit type. The plot indicates that for some Ni-Cu-PGE, orogenic gold, and IOCG deposits, we can correctly identify the source deposit type with less than 20% contamination from other deposit types. Additionally, we applied the NNLS model to the results for a binary mixture of a Ni-Cu-PGE deposit (Pipe Mine) and an orogenic gold deposit (Kittila) (Fig. 4.A1-B). The result indicates that the model does an acceptable job of identifying the signatures from individual deposit types in an input dataset that contains data from mixed ore deposit sources. This allows us to apply both aspects of the model to data for a sample that contains magnetite from unknown sources, e.g.,

grains collected in a stream and to use each analysis in the sample, in addition to the collective sample signature to infer the ore deposit source(s) of the magnetite grains.

4.6.3 Existing discriminant diagrams for magnetite from different ore environments

The overlap of the composition of magnetite from Ni-Cu-PGE, VMS, orogenic gold, IOCG, and porphyry copper deposits is apparent when data from global datasets for individual classes of ore deposits are plotted on the existing discriminant plots (Fig. 4.8). We calculated the proportion of the data that plot in each field on the discriminant plots and the sensitivity (Equation 1) for each plot for the respective target deposits. In figure 4.8A, we plot data from the global Ni-Cu-PGE dataset on the discriminant plots and 24% of the data plot in the Ni-Cu-PGE field, even though all of the data are from known Ni-Cu-PGE deposits. This 24% represents the sensitivity of the discriminant plot. The plot indicates that 6% of the data from Ni-Cu-PGE deposits plots in the field for VMS deposits, while some data also plot in the porphyry and IOCG fields (Fig. 4.8A). The mean compositions for individual Ni-Cu-PGE deposits are plotted in Fig. A2-A; approximately half the deposit means plot in the Ni-Cu-PGE field, while the remainder plot in other fields, including VMS, IOCG, porphyry and BIF. When plotted on the Ward et al. (2018) discriminant plot (Ni versus Cr/V), 18% of the data plot in the field for ore-related mafic rocks while the remainder plot in the field for barren mafic rocks (Fig. 4.9). The existing discriminant plots do not identify magnetite from orogenic gold deposits; however, when data from the global dataset of orogenic gold deposits are plotted on the discriminant plots, up to 10% of the data plot in the fields for Ni-Cu-PGE, VMS, IOCG, and PCDs (Fig. 4.8C). The Al+Mn versus Ti+V discriminant plot has a sensitivity of 26% for IOCGs, while that for the Ni/(Cr+Mn) versus Ti+V plot has sensitivity of 11% (Fig. 4.8D). As observed for other global datasets, data from the global IOCG dataset plot in the field for other deposits (Fig. 4.8D). We plotted data for porphyry Cu-Au

and porphyry Cu-Mo deposits separately on the discriminant plot to assess how the deposits are discriminated by the plots. Figure 8E indicates that the Al+Mn versus Ti+V discriminant plot has a sensitivity of 48% for porphyry Cu-Au deposits, while that for the Ni/(Cr+Mn) versus (Ti+V) plot has sensitivity of 13%. The sensitivity of the Al+Mn versus Ti+V discriminant plot for porphyry Cu-Mo deposits is about half that for porphyry Cu-Au deposits (21%), while the sensitivity of the Ni/(Cr+Mn) versus Ti+V is similar for the two deposit types (Fig. 4.8F).

4.6.4 Assessing the ore deposit potential of sampled catchments in Guyana

Application of the models developed in this study to the Guyana dataset indicate that the chemistry of magnetite in most samples is consistent with being sourced from orogenic gold and/or Ni-Cu-PGE deposits. The results when the models are applied to data for magnetite from rocks and 1st to 5th order streams from northwestern Guyana are presented in Fig. 4.10. The model pie chart for the rocks indicates that the combined chemical signatures of all intrusions sampled are dominated by signatures for orogenic gold (37%) and Ni-Cu-PGEs (31%), with the remaining 32% indicating signatures for other deposit types (Fig. 4.10A). This result is confirmed and strengthened by the inferred source/NNLS model, which weighs the proportion of these two deposit types more heavily (i.e., 58% orogenic gold, 38% Ni-Cu-PGE) while removing the contamination from other deposit types (Fig. G). In Fig. 4.11, we plot the geochemistry for the rocks and ordered streams from northwestern Guyana on the discriminant plots of Dupuis and Beaudoin (2011), Nadoll et al. (2014), and Ward et al. (2018). Magnetite from the sampled intrusions plot in the fields for Ni-Cu-PGE, Fe-Ti-V, porphyry, and IOCGs (Fig. 4.11A), and in fields for magnetite from ore-related and barren mafic rocks (Fig. 4.11B). The results from the existing plots and the new model indicate that the magnetite in the ordered streams have chemistry consistent with being sourced from multiple ore deposit types (Fig. 4.10G, 4 11A, B).

The results for outcrop samples GY-RC-10 and GY-RC-11 and proximal detrital samples C-12174, C-12171, and C-12170 are presented in Fig. 4.12. Model results indicate that 36% and 32% of the data from GY-RC-10 and GY-RC-11, respectively, are identified as having chemical signatures consistent with being from a Ni-Cu-PGE deposit, while 50% and 57% of the data from the rocks have chemistry consistent with being from an orogenic gold deposit. The inferred source model suggests that the chemical signatures of magnetite grains in the rocks are more consistent with 32% Ni-Cu-PGE and 68% orogenic gold for GY-RC-10 and 20% Ni-Cu-PGE and 80% orogenic gold for GY-RC-11. Detrital sample C-12174 is chemically and texturally similar to GY-RC-10 and GY-RC-11 (Fig. 4.5Y, Z), and the model results indicate that 69% of its chemical signature has character to similar to that for orogenic gold deposits and 27% is similar to that for porphyry copper deposits (Fig. 4.12C). The inferred source model indicates that the chemical signature of this stream sediment sample is more consistent with all of the grains being sourced from an orogenic gold deposit (100%) (Fig. 4.12F). The chemical and textural observations of sample C-12171 indicate that the magnetite grains in this sample are similar to those seen in rock samples GY-RC-10 and GY-RC-11, and in C-12174, but that it contained magnetite from an additional source in the catchment (Fig. 4.5I). The model results suggest that the signature of this sample is dominated by PCD (57%) and orogenic gold (32%) but shows minor contribution from Ni-Cu-PGE (11%). The inferred source model indicates that the chemical signature of the grains are similar to orogenic gold (32%), PCD (43%), VMS (17%) and Ni-Cu-PGE (8%) (Fig. 4.11D, F). Sample C-12170 was chemically and texturally similar to sample C-12174, and the inferred source model result indicates that the chemical signatures of grains in this sample are very similar to those from orogenic gold deposits (100%; Fig. 4.5E, M, N; 4.12E, G). The disparity between the results of the multivariate normal model (e.g., pie charts in Fig. 4.12) and the inferred source

model (e.g., Fig. 4.12F) reflect the overlap in compositions of magnetite from the 5 ore deposit types considered. The results of the multivariate normal model is the average of the chemical signature for every analysis for a sample and it reflects the prevalence of misidentifications due to the overlap in the compositions of magnetite from the 5 ore deposit types. The NNLS inferred source model compares the chemical signature for all the analyses in an unknown sample with the chemical signatures of magnetite from all analyses of the individual class specific datasets and determines what proportion(s) of the signature for each global deposit type is responsible for the unknown sample signature obtained using the multivariate normal model. The NNLS model, therefore, reduces the effect of the overlap between the compositions of magnetite from the individual ore deposit types and improves the predictive nature of the model.

The existing discriminant plots of Dupuis and Beaudoin (2011) and Ward et al. (2018) also indicate Ni-Cu-PGE potential of the samples and highlight changes in the chemistry of magnetite grains during weathering and transport (Fig. 4.13). Magnetite from both intrusions plot in the fields for Ni-Cu-PGE deposits, Fe-Ti-V, porphyry, and Kiruna deposits (Fig. 4.13A). Data for samples C-12174 and C-12171, like the intrusions, plot in the fields for Ni-Cu-PGE deposits, Fe-Ti-V, porphyry and Kiruna deposits (Fig. 4.13A). The data for C-12170 plot outside most of the fields on the discriminant diagrams of Dupuis and Beaudoin et al. (2011) and Nadoll et al. (2014), and our model results suggest that the chemistry of this sample is most similar to that from an orogenic gold source. Data for magnetite from the intrusions and sample C-12174 plot in the field for ore-related mafic rocks on the Ward et al., (2018) plot (Fig. 4.13B). Both rock samples 10 and 11 are pyroxenites. This result, therefore, suggests that the ultramafic rocks in this study have higher Cr/V ratios than those at the Munali Ni-Cu-PGE deposits in Zambia. There is overlap between the data for the three detrital samples, however, the plot also highlights the decrease in the Ni and Cr

content of the detrital grains as they are transported further away from their source intrusions. (Fig. 4.13B).

Both the existing discriminant plots and the new model presented in this study indicate porphyry copper deposit potential for the samples from Guyana (Fig. 4.12A, 4.13G, 4.A3). Porphyry copper deposits are hydrothermal ore deposits that are typically associated with intermediate to felsic rocks and found in arc environments (Richards, 2013). Magnetite in porphyry copper deposits is characterized by low minor and trace element contents compared to magnetite from igneous environments (Nadoll et al., 2014). The rock samples from Guyana are mafic and ultramafic rocks collected in greenstone belts, and contain magnetite with chemical and textural characteristics that suggest that they are hydrothermal in nature (Table 4.1; Fig. 4.2J). Therefore, while Archean-aged porphyry gold deposits have been discovered in greenstone belts (e.g., the Abitibi in Canada; Jébrak and Doucet, 2002; Jébrak, 2011), the indications of porphyry copper mineralization in the sampled intrusions likely reflect hydrothermal alteration of the outcrop samples. Additionally, our data indicate that minor and trace element concentrations in magnetite decrease with weathering and transport. Thus, it is possible that indications of PCD potential also reflect the effects of weathering and transport on detrital grains. Further, the results of the multivariate normal distribution and NNLS models and the discriminant plots indicate that there is overlap between the concentrations of Si, Al, Mg, Ca, Cr, Ti, Mn, Ni, V, Cu, and Zn in magnetite from porphyry copper deposits and the other deposit classes considered in this study. As such, the indication of porphyry copper deposit potential is likely indication of the potential for other classes of deposits, i.e., Ni-Cu-PGE, orogenic gold, or VMS, typically found in greenstone belt environments. The presence of other phases, e.g., sulfides, in the samples can likely be utilized to improve the interpretation of the model results.

4.6.5 Model results for samples containing sulfides

Sulfide minerals are not necessarily diagnostic for the ore deposits considered in this study as many of them can be present in all the deposits considered, and in barren rocks. However, the combination of the model results (based on magnetite geochemistry) and the presence of visible sulfides provide useful information that can improve exploration efforts in particular catchments. Sulfides are the ore minerals in Ni-Cu-PGEs, porphyry, IOCG, and VMS deposits, and are present in orogenic gold deposit environments. The typical hypogene sulfide assemblage in Ni-Cu-PGEs include pyrrhotite, pentlandite, and chalcopyrite, however, cubanite and troilite may be present in lesser amounts; supergene enrichment in these environments results in a sulfide assemblage which may include bravorite, violarite, pyrite, millerite, and marcasite (Barnes and Lightfoot, 2005; Schulz et al., 2010). Porphyry copper deposits contain chalcopyrite, bornite, chalcocite, pyrite, pyrrhotite, and marcasite (Fontboté et al., 2017). Volcanogenic massive sulfide deposits contain sphalerite, galena, chalcopyrite, bornite, barite, pyrite, and pyrrhotite (Taylor et al., 1995). Iron oxide - copper - gold deposits usually contain chalcopyrite, bornite, chalcocite, and pyrite (Williams et al., 2010). Sulfides commonly present in orogenic gold deposits include pyrrhotite, pyrite, and arsenopyrite (Groves et al., 1998); however, the presence of sphalerite, chalcopyrite, bornite, marcasite, and galena has also been reported (Hammond and Tabata, 1997; Niroomand et al., 2011). Many of the aforementioned sulfides were observed in magnetite, ilmenite, and silicates in intrusions and detrital samples from Guyana.

Sampled intrusions contain a variety of sulfide minerals present in Ni-Cu-PGE and other deposits, and by comparing the chemistry of magnetite in the samples with that from modeled ore deposits, we are able to narrow down the ore deposit source of the sulfide and magnetite grains. Rock samples GY-RC-01 and GY-RC-12 contain magnetite that is chemically and texturally very

similar, in addition to pyrite and chalcopyrite; sample 1 also contains pyrrhotite and cubanite (Fig. 4.2A, B, D). The model results indicate that these rocks have magnetite with chemistry similar to that present in VMS and porphyry copper deposits; the sulfide mineralogy observed is consistent with the model results (Table 4.3). GY-RC-13 contained pyrrhotite and pentlandite, in addition to polymineralic sulfide grains comprising pyrrhotite, chalcopyrite, and pentlandite (Fig, 4.2O). The magnetite in this sample have chemistry similar to that from Ni-Cu-PGE deposits (86%), globally (Table 4.3) and also have non-negligible similarity to magnetite from orogenic gold deposits (14%). The model result for sample 3 indicates prospectivity for orogenic gold deposits and the sulfide assemblage in this rock was predominantly pyrrhotite, pyrite, and pentlandite (Table 4.3). Samples 11 and 14 contained pentlandite, pyrrhotite, and sphalerite; model results indicate that magnetite in these samples are compositionally similar to magnetite from Ni-Cu-PGE and orogenic gold deposits (Fig. 4.12B, F; Table 4.3). Sample 7 contained pyrrhotite, pentlandite, chalcopyrite, a Ni sulfide (millerite?) inclusion in a hematite grain, in addition to polymineralic sulfide grains. One polymineralic sulfide grain chalcopyrite, pentlandite, and pyrrhotite, and two other polymineralic grains contained pentlandite, magnetite, chalcopyrite, and bornite (Fig. 4.2Q). The chemical signatures of magnetite in this sample are similar to that from Ni-Cu-PGE (64%), orogenic gold (32%), and IOCG (4%) deposits (Table 4.3). The mixed source signatures observed for magnetite from the intrusions likely reflects both the overlap in chemistry of magnetite from the various classes of ore deposits, and the hydrothermal/metamorphic alteration of these outcrop samples which resulted in the formation of hydrothermal magnetite.

The model results indicate Ni-Cu-PGE, orogenic gold, VMS, porphyry Cu-Mo, and porphyry Cu-Au ore deposit potential for sampled catchments and that the sulfide inclusions in detrital grains do not specify which type of mineralization they are sourced from. Detrital sample

83037 contained 4 magnetite grains with bornite inclusions, and one of these grains contained 4 bornite inclusions (Fig. 4.3Q); the chemistry of magnetite in this stream indicates that the grains were sourced from an orogenic gold deposit (Table 4.3). Numerous chalcocite inclusions were present in clinopyroxene grains in sample 22503; the model suggests that the chemistry of magnetite in this sample are consistent with being sourced from a Ni-Cu-PGE deposit (Fig. 4.3U; Table 4.3). Chalcocite is present in the ore at Noril'sk Talnakh deposit (Sluzhenikin and Mokhov, 2015) and as an accessory phase in Ni-Cu-PGE deposits in the Sudbury camp (Farrow and Watkinson, 1992). However, sample C-12178 contained a chalcocite inclusion in a magnetite grain and the model indicates that its source is a mixture of Ni-Cu-PGE (23%), VMS (26), and PCD (51%) (Fig. 4.2N; Table 4.3). Chalcocite is also a common supergene mineral in porphyry copper deposits and an accessory mineral in VMS deposits (Marshall et al., 2018). The model result for C-12178 likely indicates Ni-Cu-PGE and VMS potential. Sample 83108 contained chalcopyrite as an inclusion in ilmenite (Fig. 4.3V); the chemistry of magnetite is consistent with mixed source of 34% Ni-Cu-PGE, 16% VMS and 50% PCD (Table 4.3). Sample 83117 contains pentlandite and pyrrhotite inclusions in clinopyroxene and a pyrrhotite inclusion in ilmenite, which had patchy texture that contained magnetite exsolution lamellae (Fig. 4.3R, S). Magnetite grains in this sample showed high prospectivity for orogenic gold deposits (100%). Sample 83103 contained multiple polymineralic sulfide grains as inclusions in ilmenite; two of the polymineralic grains comprise magnetite, sphalerite and pyrrhotite, and the other two grains comprise sphalerite and pyrite (Fig. 4.3I). The model indicates that magnetite in this sample is sourced from Ni-Cu-PGE (27%), VMS (27%) and PCD (46%) (Table 4.3). Sample 83110 contained a chalcopyrite inclusion in magnetite, in addition to cubanite inclusions in ilmenite and clinopyroxene. Magnetite in this sample indicated mixed ore deposit potential: VMS (24%) and PCD (76%) (Table 4.3). Sample AH007 contained

chalcopyrite and pentlandite in ilmenite, in addition to a free gold grain ~50 μm long (Fig. 4.3W). The inferred source model suggests that magnetite grains in this sample are sourced from orogenic gold (5%), VMS (30%) and porphyry copper (65%) deposits (Table 4.3). Sample C-12180 also contained a visible gold grain; magnetite grains in this sample were identified as having chemical signatures similar to Ni-Cu-PGE (10%), VMS (29%), and porphyry copper deposits (61%) (Table 4.3). Visible gold is common in orogenic gold deposits, and since the samples were collected in greenstone belts, known to host orogenic gold deposits, the observation of visible gold is expected to indicate orogenic gold mineralization. The model result for AH007 indicates orogenic gold potential but this is not the case for C-12180. Native gold grains have been reported in both gold rich VMS and porphyry copper deposits, though the bulk of the gold in these deposits is typically present in the lattice of sulfides (Kesler et al., 2002; Dube et al., 2007). The gold grains in both C-12180 and AH007 were present as inclusions in quartz, which is typical for orogenic gold deposits. An interpretation of the model results is that the magnetite grains and auriferous quartz grains were derived from different sources or that the magnetite grains have been weathered to an extent such that their compositions no longer reflect their true ore deposit source. Generally, the sulfides present in samples from analysed catchments are common or present in the ore deposits predicted by the model in this study. Our results highlight that while the sulfide assemblages in catchments are similar, the ore deposit potential inferred for the catchments based on magnetite geochemistry can be very different. Therefore, while the presence of sulfides in detrital grains upgrades the prospectivity of a catchment during exploration, it is not a direct indicator of the type of mineralization that may be present in that catchment.

4.6.6 Samples with Ni-Cu-PGE potential

Dare et al. (2012) and Boutroy et al. (2014) showed that for Ni-Cu-PGE deposits globally, the chemistry of magnetite, which crystallizes in equilibrium with a fractionating sulfide liquid, depends on the fractionation history of the sulfide liquid. Those studies showed that binary plots of Ni, Ti, V versus Cr identify magnetite that crystallized in equilibrium with primitive Fe-rich monosulfide solution (MSS), evolved, Fe-rich MSS, and residual Cu-rich intermediate solid solution (ISS), respectively. Since our data indicate that the Cr, Ti, and Ni contents of magnetite decrease with increasing transport distance from the host intrusion, we decided to ascertain the changes in Al and V contents of magnetite which crystallize in equilibrium with the aforementioned sulfide liquid compositions. Following Dare et al. (2012), we plotted data for magnetite from the Creighton and McCreedy East Ni-Cu-PGE deposits, both located in the Sudbury Igneous Complex that crystallized in equilibrium with sulfide liquids of different compositions (Fig. 4.14). Despite a paucity of data for magnetite that crystallizes from a sulfide liquid with composition equivalent to residual Cu-rich ISS, the plot indicates that the V and Al content of magnetite decreases with continued fractionation of a sulfide liquid (Fig. 4.14). This is the expected behavior as V and Al are lithophile elements, thus have high concentrations in magnetite crystallizing in equilibrium with the early forming monosulfide solid solution, and lower concentrations in magnetite crystallizing with the more evolved sulfide liquid (Dare et al., 2012). The plot indicates that there is some overlap in the V and Al signatures for magnetite from primitive and evolved MSS, however, the magnetite from the three sulfide liquid compositions generally plot in distinct regions in V and Al space. In Fig. 4.14, we also include the concentrations of V and Al for magnetite from 4 samples with chemical signatures most similar to those for Ni-Cu-PGEs. The majority of the analyses overlap magnetite that crystallizes in equilibrium with

primitive/early MSS, and a few analyses from GY-RC-07 plot closer to the data for residual Cu-rich ISS samples (Fig. 4.14). The observations of pentlandite, pyrrhotite, and chalcopyrite in GY-RC-13 and GY-RC-07 support the composition of the sulfide liquid (primitive MSS) inferred from magnetite chemistry. Additionally, the presence of bornite in GY-RC-07 explains the overlap with the data for residual Cu-rich ISS. Thus, from an exploration perspective, if the chemistry of magnetite in an area is indicative of Ni-Cu-PGE potential, the V and Al plot may be used to gain insights about the tenor of ore in that area (i.e., Cu versus Ni rich). This can assist with target generation in covered terrains as it would provide insights about which geochemical anomalies would be most indicative of mineralization.

4.6.7 Insights about ore deposit potential inferred from magnetite geochemistry

Direct comparison of results for the global magnetite database indicates that the new model achieves better results for magnetite from Ni-Cu-PGE, VMS, IOCG, and porphyry Cu deposits than existing discriminant plots. Additionally, the new model allows discrimination of magnetite from orogenic gold deposits and other deposits, which were left unmodeled by prior discriminant methods. Of the existing discriminant plots, the Al+Mn versus Ti+V does an acceptable job of discriminating magnetite from porphyry Cu-Au deposits; 48% of the data plot in the porphyry field (Fig. 4.8E). The decreased ability of this diagram to discriminate magnetite from porphyry Cu-Mo deposits indicates that there are differences in the composition of magnetite from porphyry Cu-Au and porphyry Cu-Mo deposits for the elements considered (Fig. 4.7E, F). When the datasets for porphyry Cu-Au and porphyry Cu-Mo deposits are combined and plotted on the Al+Mn versus Ti+V diagram, 35% of the data are correctly identified as being from a porphyry copper deposit (Fig. 4.A3).

The success of the recent studies of Makvandi et al. (2016), Pisiak et al. (2017), Dmitrijeva et al. (2018), and Huang et al. (2018, 2019), indicate the utility of incorporating trace element geochemistry into statistics-based discrimination models for magnetite. Thus, by incorporating trace element compositions of magnetite into our model will likely be able to decrease the overlap of the normal distributions for the deposit classes in our model and improve its ability to discriminate magnetite from Ni-Cu-PGEs, orogenic gold, VMS, IOCG, and porphyry copper deposits. Additionally, the research outlined above, and the results of this study indicate that care must be taken when interpreting the results of the existing discriminant plots and that our ability to discriminate magnetite from different environments increases as we increase the number of elements considered.

4.6.8 Implications and application to exploration in covered terrains

The observations outlined above indicate that while the physical/textural signatures of magnetite from intrusions are somewhat retained during weathering and transport, the chemical signatures of magnetite grains change during weathering and transport (Fig. 4.4, 4.5). Our data suggest that the chemical signatures of magnetite in intrusions, is retained in detrital magnetite grains provided that the grains are transported less than 1.5 km from the source intrusions. The data presented also indicate that the V and Al contents of magnetite in intrusions can be retained in magnetite that has travelled up to 5 km away from the source intrusions. An important implication of these findings is that care must be taken when selecting elements to use in models to discriminate magnetite from different ore environments.

We found that sulfide inclusions can be preserved in detrital magnetite, ilmenite, quartz, and clinopyroxene grains and while they are useful for identifying areas for targeted exploration, they are not indicative of the type of mineralization in a particular catchment. Due to the

importance of sulfides in many classes of ore deposits, including the 5 considered in this study, the presence of visible sulfides in detrital grains can be used to upgrade the prospectivity of an area during regional exploration, especially if that area was previously identified as prospective using other geologic information, e.g., geochemical and geophysical anomalies. Further, the observation of sulfides in detrital grains collected blindly in areas for which there was little to no prior geologic information, increases the prospectivity of that area and necessitates mapping to elucidate the geology of that catchment. This is especially important since the observed sulfide assemblages may not be diagnostic for a particular type of ore deposit. This approach is potentially valuable in countries like Guyana, and in regions like the Guiana Shield, where stream and soil sediment sampling are routinely done. Heavy minerals samples can be collected during stream sampling surveys and the grains can be observed by using a petrographic microscope to ascertain whether sulfides are present in an effort to identify catchments for prospecting and target generation. Investigation of the chemistry of magnetite from these catchments can additionally be used ascertain the ore deposit potential of the catchments and to identify geochemical tracers that will be useful for identifying targets in the region.

Despite evidence of past and current drainage inversions in the regions sampled, the angular nature of the grains investigated indicate that they were sourced locally from the catchments where they were collected. Drainage inversions are very common in tropical environments, and they are often the result of duricrusts, e.g., ferricrete, silicrete, calcrete, and gypcretes (Pain and Ollier, 1995). Ferricrete observed in sampled catchments, therefore, provide evidence of past drainage inversion. Additionally, the bulk of the small and medium scale mining in Guyana targets gold in alluvium; so the land that is being mined likely represents old river channels and the streams have since migrated to new locations. Current gold mining in Guyana is

a major cause of drainage inversions or alterations to the courses of rivers/streams, and there is likely minimal drainage inversion due to tectonic activity since Guyana is located in the stable Amazonian craton. Thus, given the angular nature of the grains and the lack of evidence of recent mining activities, or other evidence of stream channel migration at sample locations, we assume that the samples collected are sourced locally.

Though we observe sulfides in many of the rocks and detrital grains investigated, and the chemistry of magnetite in the samples indicate Ni-Cu-PGE potential, we do not encounter mineralization. The presence of sulfides in the intrusions indicate that they attained sulfide saturation, which is an important first step in the formation of ore deposits, such as Ni-Cu-PGEs. While Ni-Cu-PGE potential is inferred from magnetite in the sampled outcrops, the lack of mineralization in these samples indicates that ore forming processes aside from sulfide saturation did not occur. Ni-Cu-PGE deposits are not heavily pursued in Guyana and the Guiana Shield. However, the results of this study are encouraging for Ni-Cu-PGE exploration in the region because it indicates that the right geological processes have occurred in intrusions in the greenstone belts. Additionally, the observations of Cr-rich spinels in the detrital samples indicate the presence of primitive rocks in the sampled catchments. Thus, with continued mapping and exploration, we will likely be able to ascertain areas where more of the important ore-forming processes have occurred, and this can lead to the discovery of new ore deposits.

4.7 Conclusions

We investigated the chemistry of magnetite in outcrop and detrital samples from Guyana and compared them with geochemical data for magnetite from known ore environments using existing discriminant plots based on major and minor element chemistry and a new geochemical discriminant model developed in this study. Our new model improves the ability to discriminate

magnetite from Ni-Cu-PGE, orogenic gold, VMS, IOCG, and porphyry copper deposits using Cr, Ti, Al, V, Mn, Mg, Ca, Si, Ni, Cu, and Zn. Our results indicate that the concentrations of Ti, Cr, Ni, Mn, Mg, and Ca in magnetite decrease as magnetite is weathered and transported by streams to distances exceeding 1.5 km from the host intrusions, while the concentration of V and Al in magnetite remain mostly unchanged provided that the transport distance does not exceed 5 km. We found that the physical and textural signatures of magnetite from rocks, including sulfide inclusions, and mineral exsolutions, are partially preserved in detrital grains. Our model results — based on magnetite chemistry — indicate orogenic gold and/or Ni-Cu-PGE potential in the catchments investigated; this is supported by the presence of sulfide inclusions in detrital grains. This study indicates that petrographic and chemical investigations of detrital magnetite grains can be a useful tool for exploration in covered terrains. This work demonstrates the potential for detrital magnetite as an exploration tool for mineral systems in densely covered terrains, such as the Guiana Shield.

Table 4.1. EPMA Conditions for magnetite analyses.

Element/ X-ray line	Crystal	Standard	Counting Time (s)
Fe Kα	LIF	USMN Magnetite	20
Ti Kα	PET	USMN Ilmenite	100
Cr Kα	PET	Cr_2O_3	100
V Kα	LLIF	V_2O_5	150
Ca Kα	PET	CaF_2	100
Ni Kα	LLIF	Ni-olivine	150
Mn Kα	LLIF	$MnFe_2O_4$	150
Si Kα	LTAP	SiO_2	100
Mg Kα	LTAP	MgO	100
Al Kα	LTAP	Al_2O_3	100
Cu Kα	LLIF	Dioptase	150
Zn Kα	LIF	Gahnite	280

Table 4.2: Median compositions of magnetite and spinel phases from sampled catchments.

	Hematite				Cr-Ti-poor Magnetite			
Concentrations	Detrital		Pyroxenite		Detrital		Pyroxenite	
(wt%)	Median (N=22)	σ	Median (N=5)	σ	Median (N=9)	σ	Median (N=160)	σ
Si	0.04	0.03	0.38	0.32	0.02	0.15	0.08	0.13
Mg	0.00	0.02	0.43	0.25	0.00	0.05	0.11	0.23
Al	0.04	0.05	0.03	0.01	0.02	0.06	0.00	0.01
Cr	0.02	0.03	0.01	0.10	0.02	0.06	0.01	0.02
Ti	0.03	0.02	0.02	0.02	0.03	0.03	0.05	0.02
Ca	0.00	0.00	0.12	0.11	0.00	0.01	0.01	0.11
V	0.09	0.11	0.04	0.02	0.13	0.13	0.00	0.00
Mn	0.01	0.02	0.02	0.01	0.01	0.07	0.03	0.03
Fe	68.94	0.36	68.53	0.97	71.35	0.95	69.96	0.53
Ni	0.00	0.01	0.05	0.11	0.00	0.01	0.10	0.15
Cu	0.01	0.00	0.00	0.00	0.00	0.45	0.00	0.30
Zn	0.01	0.00	0.01	0.00	0.01	0.00	0.01	0.00

	Cr-poor titanomagnetite						Cr-rich titanomagnetite			
Concentrations	Detrital		Mafic		Pyroxenite		Detrital		Pyroxenite	
(wt.%)	Median (N=246)	σ	Median (N=31)	σ	Median (N=27)	σ	Median (N=66)	σ	Median (N=98)	σ
Si	0.05	0.61	0.18	0.30	0.10	0.29	0.02	0.16	0.02	1.53
Mg	0.00	0.18	0.03	0.12	0.02	0.39	0.10	0.17	0.11	1.51
Al	0.07	0.52	0.48	0.33	0.04	0.13	0.09	0.61	0.15	1.82
Cr	0.03	0.06	0.05	0.04	0.16	0.11	3.64	2.29	3.17	1.91
Ti	0.63	1.52	1.68	1.28	0.52	0.55	0.59	0.87	0.98	0.99
Ca	0.00	0.17	0.03	0.14	0.03	0.02	0.00	0.03	0.03	0.33
V	0.15	0.15	0.63	0.54	0.25	0.11	0.13	0.10	0.20	0.55
Mn	0.03	0.09	0.05	0.08	0.04	0.07	0.17	0.33	0.28	0.21
Fe	68.12	3.33	67.17	2.36	68.94	2.02	65.64	3.52	64.84	6.87
Ni	0.00	0.01	0.01	0.00	0.06	0.03	0.09	0.12	0.07	0.09
Cu	0.00	0.01	0.00	0.04	0.00	0.01	0.00	0.00	0.00	0.00
Zn	0.01	0.03	0.01	0.05	0.01	0.01	0.04	0.09	0.01	0.12

	Cr-rich magnetite				Titanomagnetite					
Concentrations	Detrital		Pyroxenite		Detrital		Mafic		Pyroxenite	
(wt%)	Median (N=12)	σ	Median (N=3)	σ	Median (N=75)	σ	Median (N=8)	σ	Median (N=10)	σ
Si	0.11	0.85	0.88	1.02	0.01	0.21	0.05	0.22	0.03	0.11
Mg	0.03	0.35	0.73	3.17	0.01	0.03	0.07	0.09	0.04	0.11
Al	0.08	0.74	0.36	0.93	0.06	0.27	1.14	2.48	0.08	0.12
Cr	0.54	1.88	1.98	1.21	0.04	0.19	0.05	0.02	1.40	2.13
Ti	0.05	0.02	0.07	0.01	7.29	2.36	8.14	2.36	7.54	2.42
Ca	0.02	0.12	0.08	0.01	0.00	0.06	0.01	0.02	0.04	0.05
V	0.09	0.07	0.19	0.08	0.17	0.22	0.58	0.20	0.22	0.09
Mn	0.02	0.20	0.04	0.06	0.24	0.46	0.17	0.09	1.09	0.48
Fe	69.28	5.31	62.65	6.69	60.86	3.60	57.98	3.50	56.42	3.69
Ni	0.03	0.03	0.09	0.12	0.00	0.01	0.01	0.01	0.05	0.01
Cu	0.01	0.02	0.00	0.00	0.00	0.00	0.00	0.01	0.00	0.00
Zn	0.01	0.02	0.01	0.01	0.01	0.03	0.11	0.13	0.01	0.09

	Chrome spinel			
Concentrations	Detrital		Mafic	
(wt%)	Median (N=89)	σ	Median (N=18)	σ
Si	0.02	0.02	0.01	0.28
Mg	0.27	1.17	0.05	1.97
Al	1.13	2.71	0.77	6.73
Cr	22.36	9.33	18.90	5.97
Ti	0.70	0.96	1.79	1.18
Ca	0.00	0.01	0.02	0.08
V	0.17	0.09	0.26	0.14
Mn	0.68	0.47	0.88	0.48
Fe	39.97	12.42	43.98	10.35
Ni	0.07	0.07	0.06	0.04
Cu	0.00	0.00	0.00	0.00
Zn	0.43	0.70	0.49	0.41

Table 4.3. Inferred deposit sources for magnetite from rocks and detrital samples that contain sulfides as inclusions in magnetite and other phases.

Sample ID	Ni-Cu-PGE	Orogenic Gold	VMS	IOCG	Porphyry Copper Deposit
GY-RC-01	0	0	27	0	73
GY-RC-03	0	100	0	0	0
GY-RC-07	64	32	0	4	0
GY-RC-12	0	0	25	0	75
GY-RC-13	86	14	0	0	0
GY-RC-14	44	56	0	0	0
C-12180	10	0	29	0	61
C-12186	96	4	0	0	0
AH007	0	5	30	0	65
C12178	23	0	26	0	51
83037	0	100	0	0	0
83039	0	72	0	21	7
83047	0	100	0	0	0
22503	71	0	0	0	29
83108	34	0	16	0	50
83110	0	0	24	0	76
83103	27	0	27	0	46
83117	0	100	0	0	0

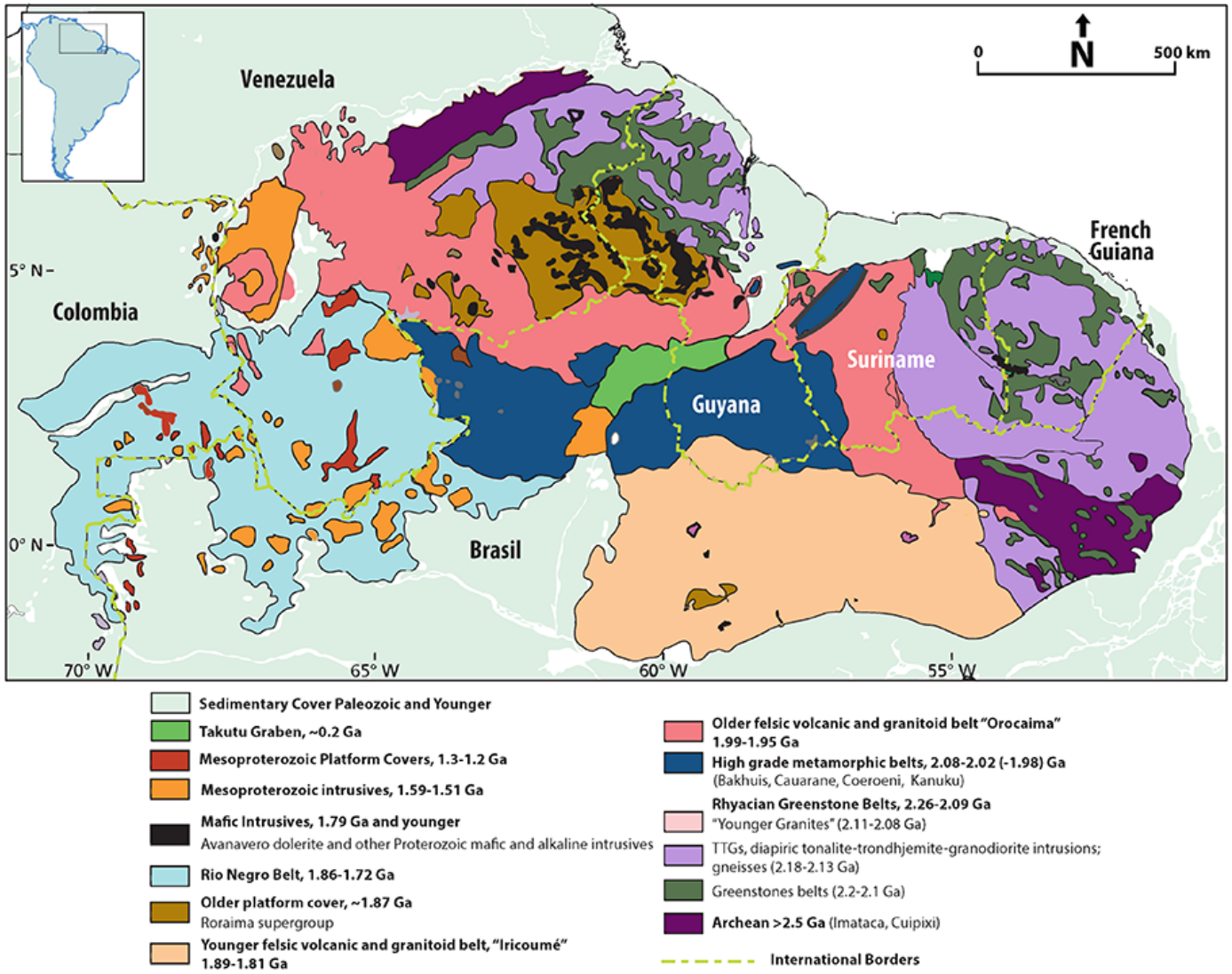

Figure 4.1. (A) Regional map showing the major geologic units of the Guiana Shield and their ages. This map is modified from Tedeschi et al., 2018 a,b.

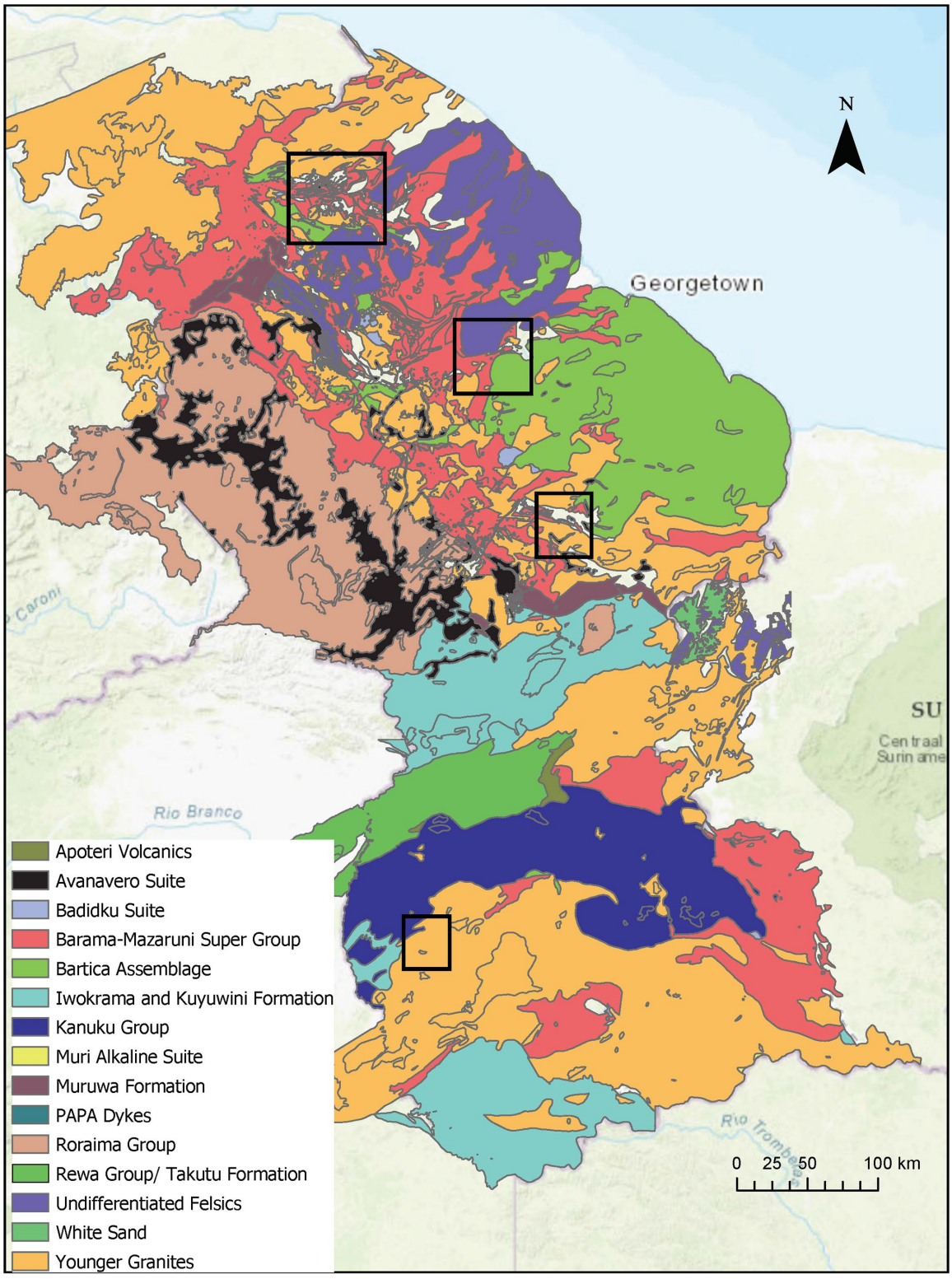

Figure 4.1. (B) Geological map of Guyana with boxes outlining the regions where samples were collected for this study.

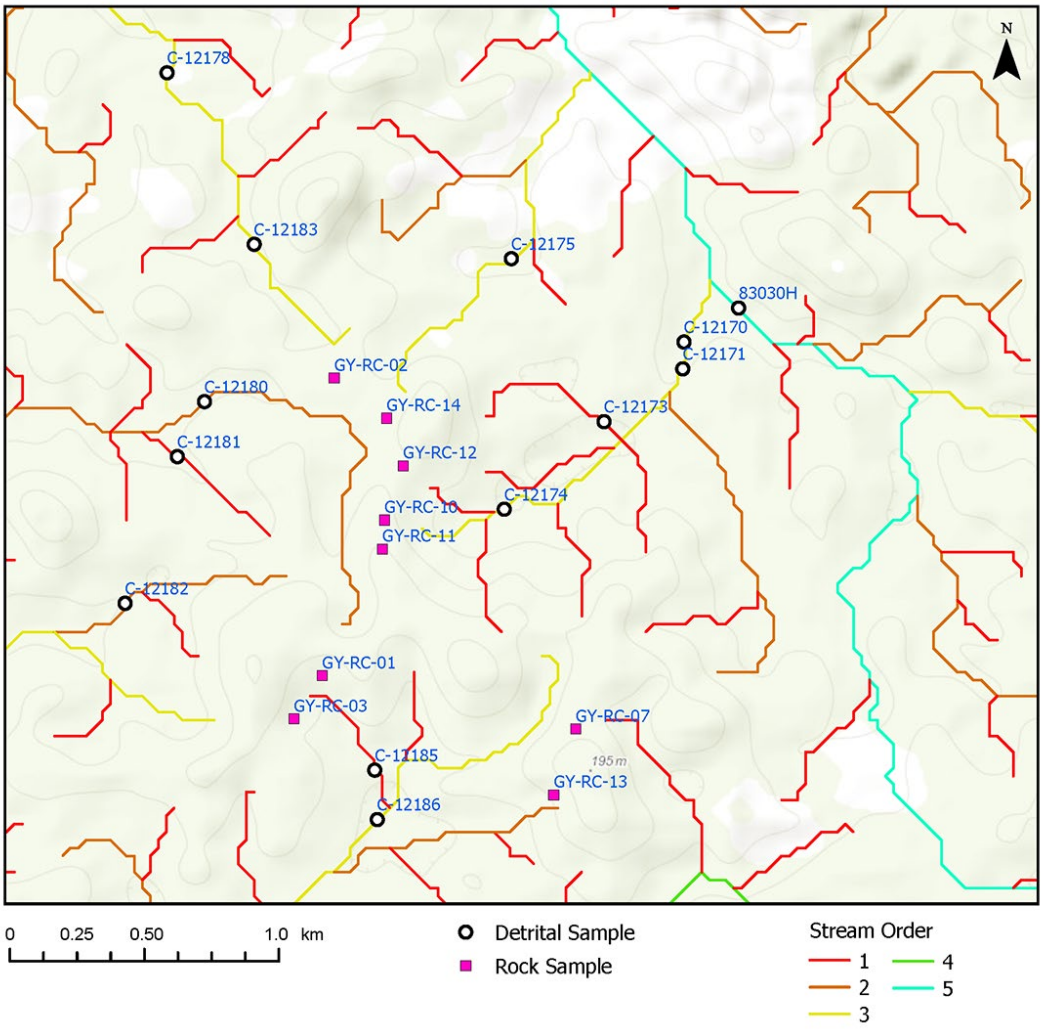

Figure 4.1. (C) Map showing primary collection locations of rocks (pink squares) and detrital samples (white circles) in northwestern Guyana.

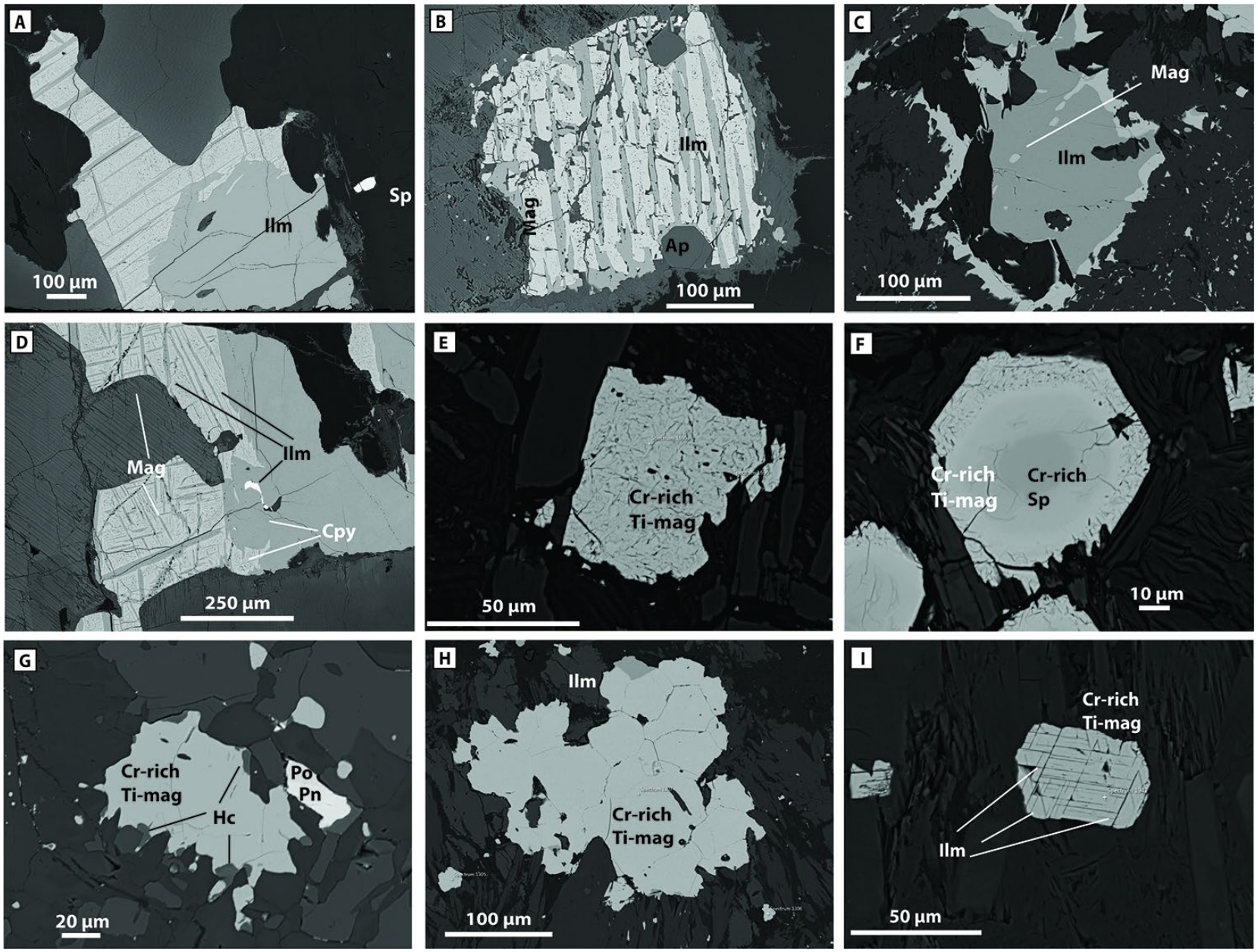
A
Sp
Ilm
100 µm
B
Ilm
Mag
Ap
100 µm
C
Mag
Ilm
100 µm
D
Mag
Ilm
Cpy
250 µm
E
Cr-rich
Ti-mag
50 µm
F
Cr-rich
Ti-mag
Cr-rich
Sp
10 µm
G
Cr-rich
Ti-mag
Po
Pn
Hc
20 µm
H
Ilm
Cr-rich
Ti-mag
100 µm
I
Cr-rich
Ti-mag
Ilm
50 µm

Figure 4.2. Representative backscattered electron (BSE) images of grains from outcrop samples. Magnetite and Fe-Cr-Ti oxides display a variety of textures which indicate that the sampled outcrops are igneous in nature and have been altered by hydrothermal fluids. (A) BSE image of a magnetite grain from intrusion sample GY-RC-01 containing well developed ilmenite exsolution lamellae with sandwich texture and ilmenite overgrowth. Ilmenite exsolution lamellae with cloth texture are present in magnetite that exists in the regions between the ilmenite exsolutions with sandwich texture. Two small sphalerite (Sp) grains are also visible in the image. (B) Magnetite grain from a mafic intrusion showing texture dominated by sandwich-textured ilmenite exsolution lamellae. This grain contains fluorapatite and small sulfide grains (white phases in the grain). (C) Ilmenite from mafic intrusions contains magnetite as inclusions or magnetite at the boundaries of some grains. (D) Magnetite and ilmenite, which contains a chalcopyrite inclusion, from a mafic intrusion. (E) Magnetite with wavy/spongy texture; this texture was observed in grains from 2 of the pyroxenite outcrops. (F) Zoned magnetite grain with domains that contain differing Cr contents. The cores have highest Cr content and Cr content decreases towards the rim. (G) Inclusion-poor magnetite grain with hercynite (Hc) granules at the grain boundaries that is proximal to a sulfide grain, which contains pyrrhotite and pentlandite. (H) Agglomeration of magnetite grains from a pyroxenite intrusion. The grains terminate at triple junctions and an ilmenite granule is observed at the boundary of two grains. (I) Magnetite from pyroxenite intrusion with sub-micrometer trellis-textured ilmenite exsolution lamellae.

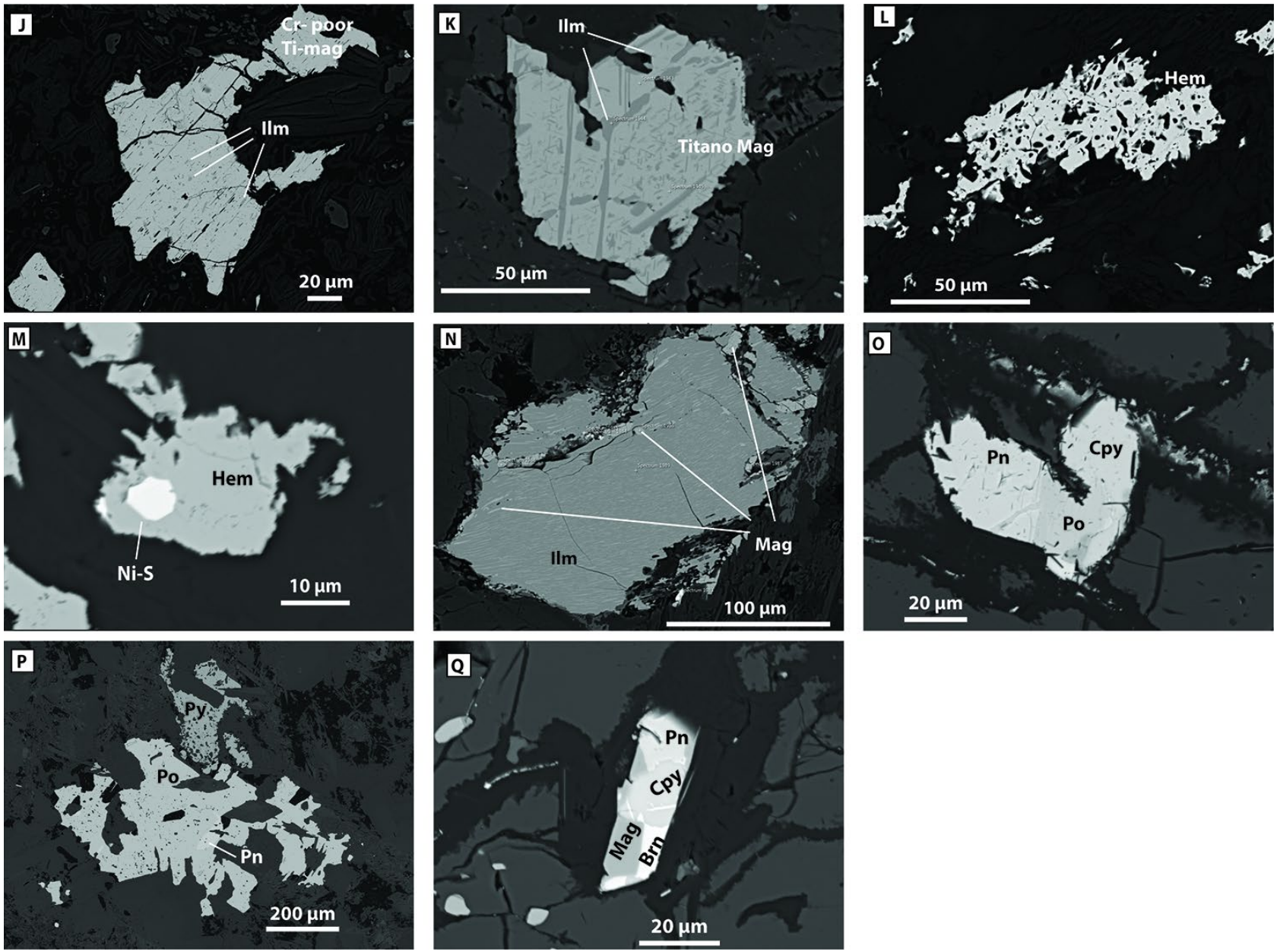
J
Cr- poor
Ti-mag
Ilm
20 µm
K
Ilm
Titano Mag
50 µm
L
Hem
50 µm
M
Hem
Ni-S
10 µm
N
Ilm
Mag
100 µm
O
Pn
Cpy
Po
20 µm
P
Py
Po
Pn
200 µm
Q
Pn
Cpy
Mag
Brn
20 µm

Figure 4.2. (J) Magnetite from pyroxenite outcrop containing cloth-textured ilmenite exsolution lamellae. (K) Titanomagnetite grain from pyroxenite intrusion. (L) Hematite grains that meet at triple junctions. These grains were observed in three sampled outcrops. (M) Hematite grain from GY-RC-07 with Ni-S (millerite?) inclusion. (N) Ilmenite from pyroxenite samples contains magnetite exsolution lamellae and magnetite granules. (O) Polymineralic sulfide grain comprising pentlandite, pyrrhotite and chalcopyrite; this grains was observed in GY-RC-13. (P) Pyrrhotite and pyrite (Py) observed in a sampled intrusion. Exsolved pentlandite observed in the pyrrhotite grain. (Q) Polymineralic assemblage of magnetite, chalcopyrite, pentlandite and bornite (Bn) in a pyroxenite intrusion. This grain likely represents a crystallized sulfide liquid globule.

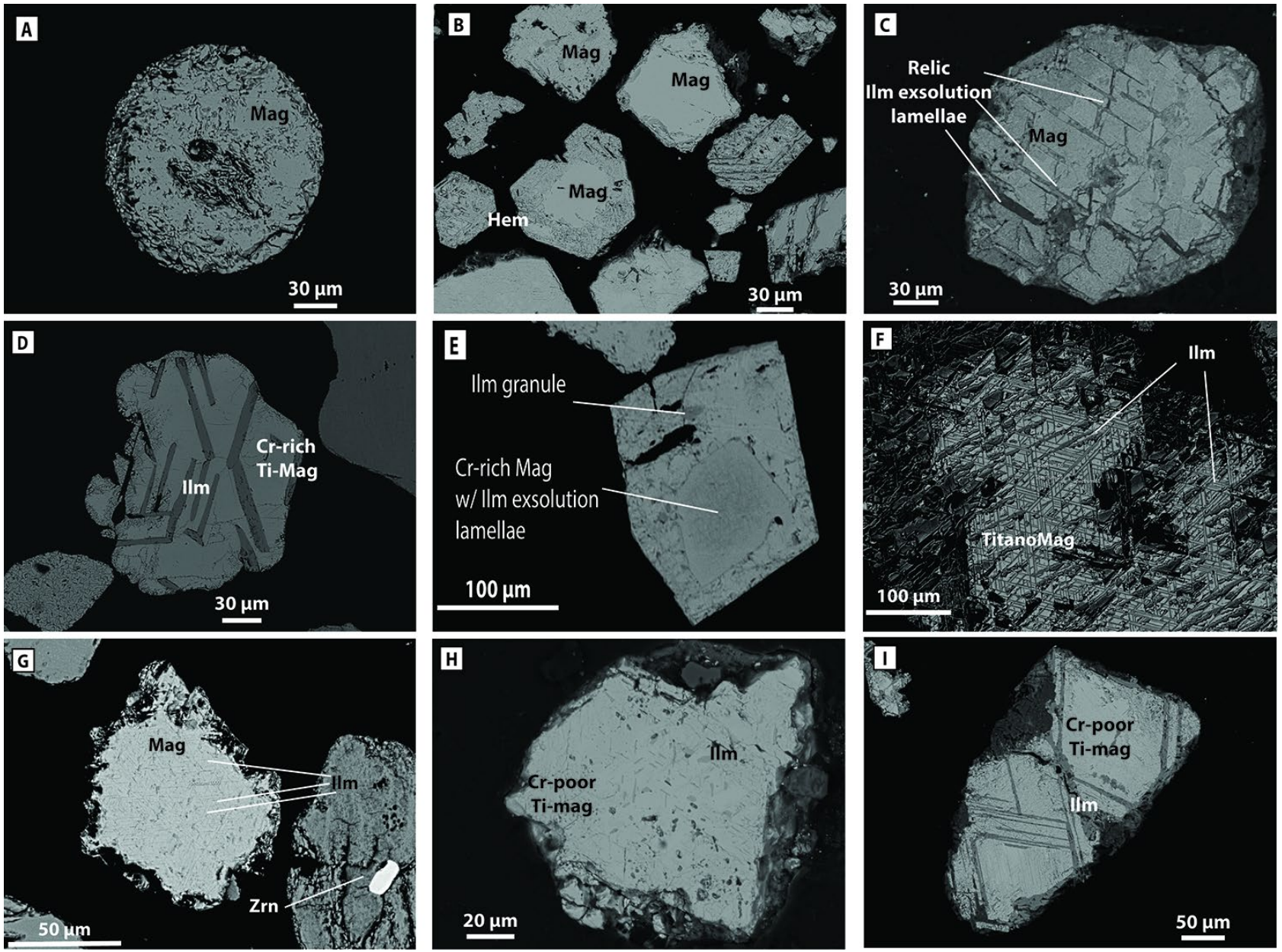
A
Mag
30 µm
B
Mag
Mag
Mag
Hem
30 µm
C
Relic
Ilm exsolution
lamellae
Mag
30 µm
D
Cr-rich
Ti-Mag
Ilm
30 µm
E
Ilm granule
Cr-rich Mag
w/ Ilm exsolution
lamellae
100 µm
F
Ilm
TitanoMag
100 µm
G
Mag
Ilm
Zrn
50 µm
H
Ilm
Cr-poor
Ti-mag
20 µm
I
Cr-poor
Ti-mag
Ilm
50 µm

Figure 4.3. This figure contains representative backscattered electron images of Fe-Cr-Ti oxides from detrital samples collected throughout Guyana. Generally, the detrital grains are texturally similar to those in the outcrop samples but also show loss of texture caused by weathering. (A) Rounded magnetite grain collected from a catchment in north-central Guyana. (B) Angular to sub-angular detrital magnetite grains collected in Guyana; inclusion-poor magnetite is the dominant texture observed in detrital grains; however, ilmenite exsolution lamellae are sometimes preserved. Some inclusion poor grains also contain hematite rims. (C) Magnetite grain with visible crevices that appears to have contained ilmenite exsolution lamellae that have been lost due to weathering; these are referred to as relic ilmenite exsolution lamellae in this study. (D) Cr-rich titanomagnetite with ilmenite exsolution lamellae. (E) Magnetite grain containing a Cr-rich titanomagnetite core, with visible ilmenite exsolution lamellae, and a Cr-poor titanomagnetite rim. An ilmenite granule is observed within the Cr-poor rim. (F, G) Detrital magnetite grains with thin (<5 μm) trellis-textured ilmenite exsolution lamellae. (H) Magnetite grain with cloth-textured ilmenite exsolution lamellae. (I) Magnetite with sandwich-textured ilmenite exsolution lamellae.

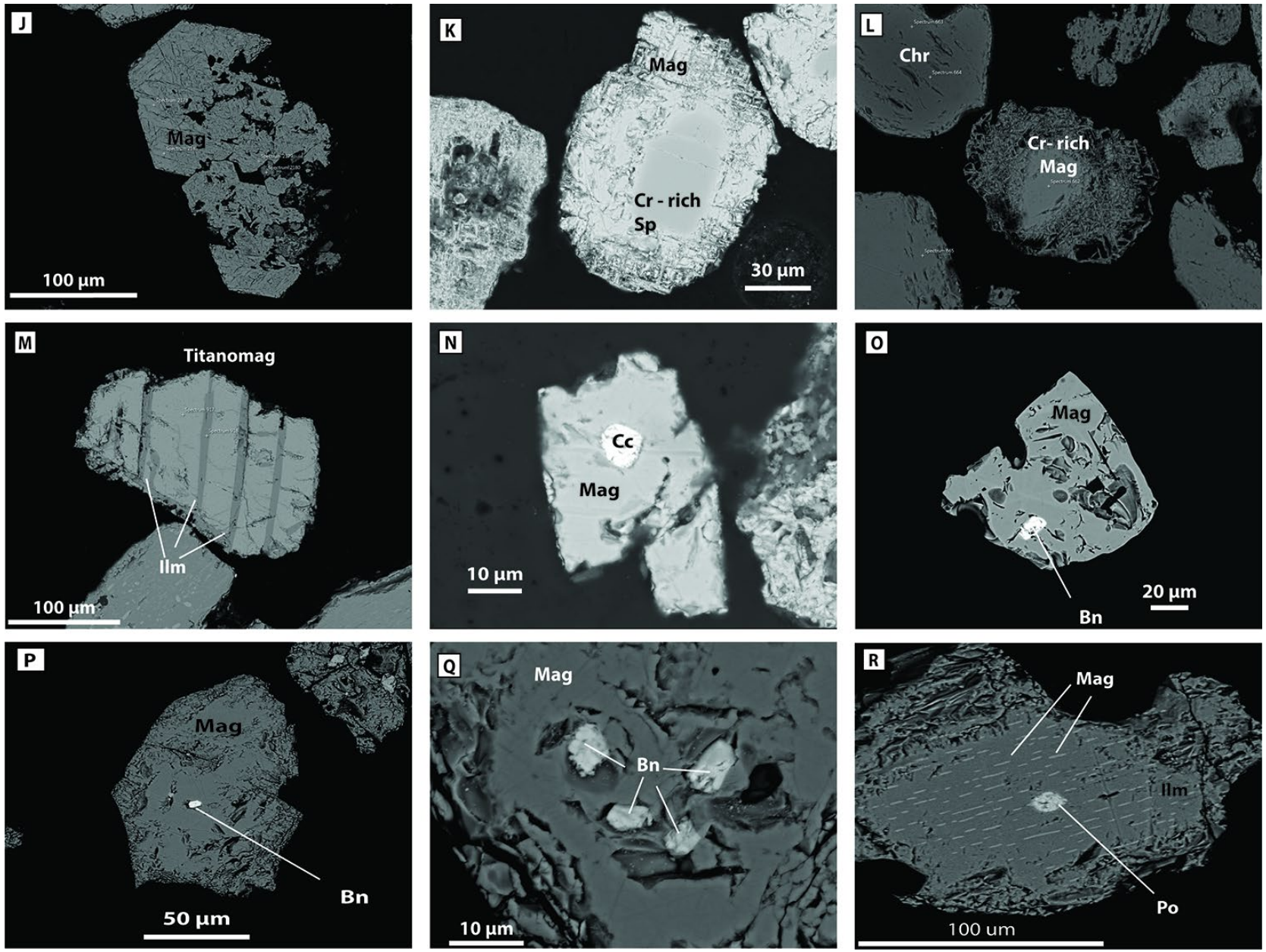
J
Mag
100 µm
K
Mag
Cr - rich
Sp
30 µm
L
Chr
Cr- rich
Mag
M
Titanomag
Ilm
100 µm
N
Cc
Mag
10 µm
O
Mag
Bn
20 µm
P
Mag
Bn
50 µm
Q
Mag
Bn
10 µm
R
Mag
Ilm
Po
100 um

Figure. 4.3. (J) Magnetite with wavy/spongy texture. L) Detrital chromite and weathered Cr-rich magnetite. (M) Detrital titanomagnetite grain with visible sandwich-textured ilmenite exsolution lamellae. Angular magnetite grains containing (N) chalcocite and bornite (O, P) inclusions. (Q) Magnetite grain containing multiple bornite inclusions. (R) Ilmenite grain with pyrrhotite and tiny magnetite exsolution lamellae inclusions.

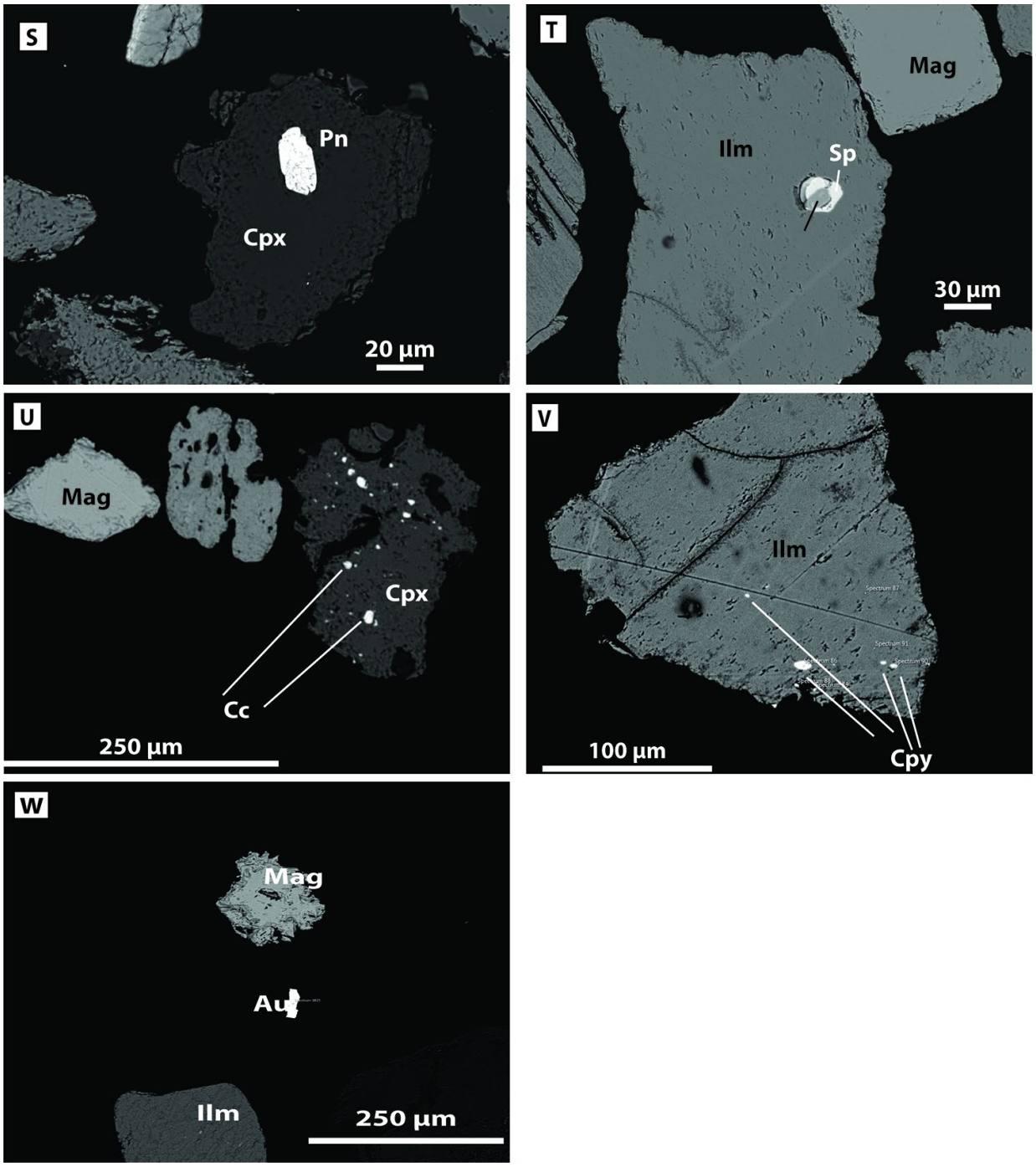

Figure 4.3. (S) Pentlandite inclusion in detrital clinopyroxene grain. (T) Ilmenite grain containing polymineralic sulfide assemblage, comprising pyrite and sphalerite. (U) Chalcocite inclusions in clinopyroxene. (V)Ilmenite grain containing multiple chalcopyrite inclusions. (W) Visible gold grain, magnetite, and ilmenite.

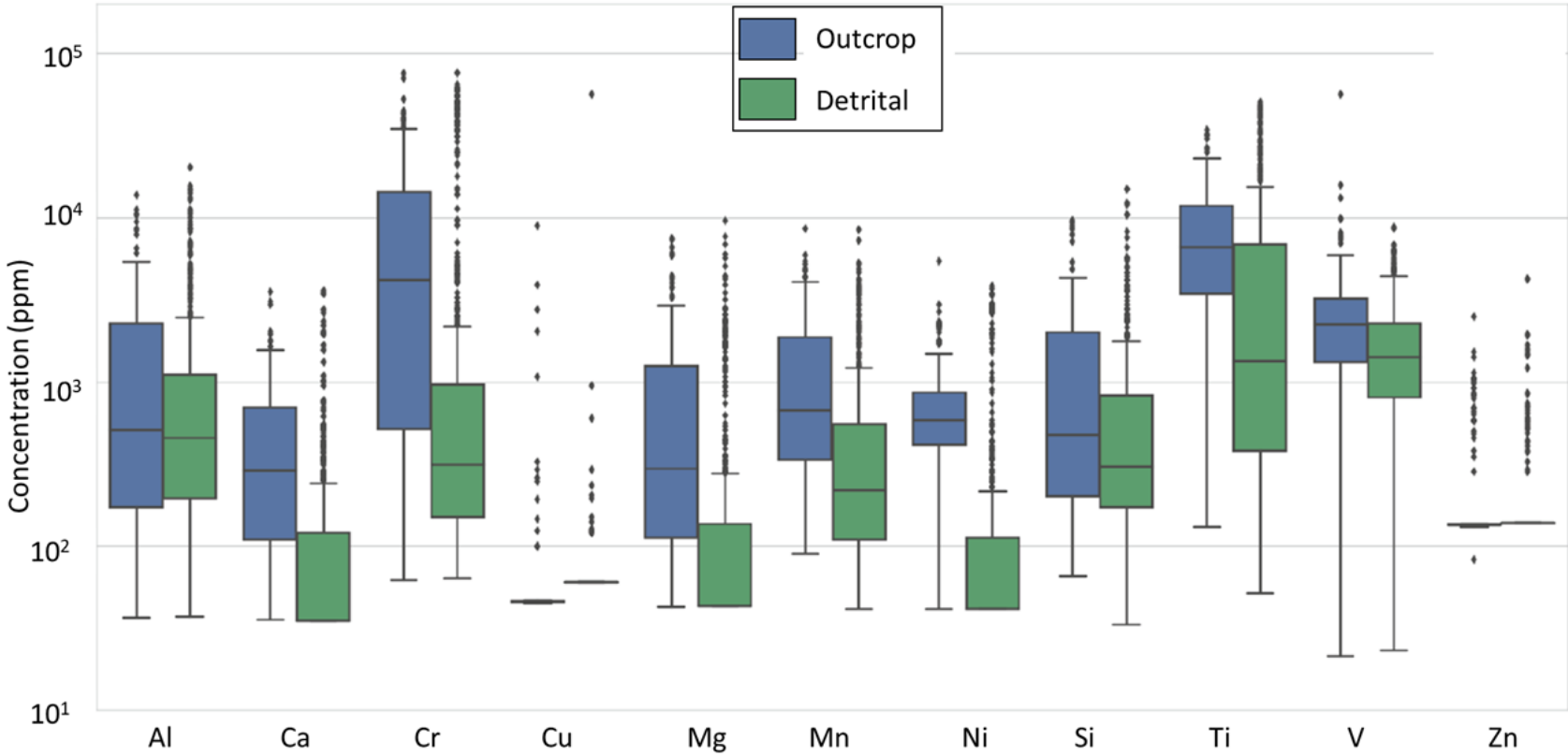

Figure 4.4. Box and whisker plots showing the composition of magnetite in outcrop and detrital samples. The whiskers encompass 95 percent of the data for each element, while the box covers the interquartile range (25% to 75%). The black line within each box represents the median concentration, and the diamonds represent outliers for samples.

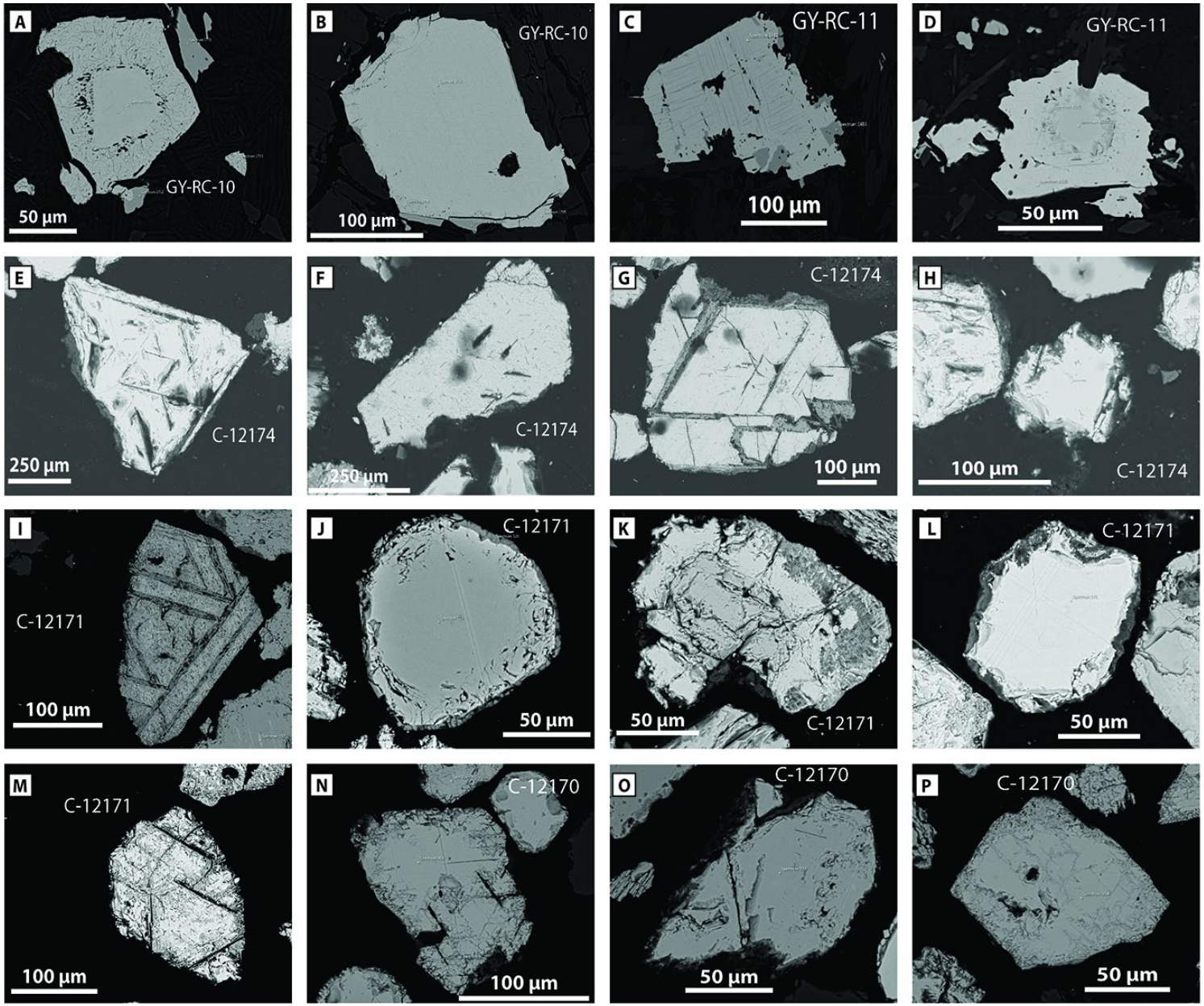
A
GY-RC-10
50 µm
B
GY-RC-10
100 µm
C
GY-RC-11
100 µm
D
GY-RC-11
50 µm
E
C-12174
250 µm
F
C-12174
250 µm
G
C-12174
100 µm
H
100 µm
C-12174
I
C-12171
100 µm
J
C-12171
50 µm
K
50 µm
C-12171
L
C-12171
50 µm
M
C-12171
100 µm
N
C-12170
100 µm
O
C-12170
50 µm
P
C-12170
50 µm

Figure 4.5. Backscattered electron (BSE) images of representative spinel grains from outcrop and detrital samples from a catchment in northwestern Guyana (A - P).

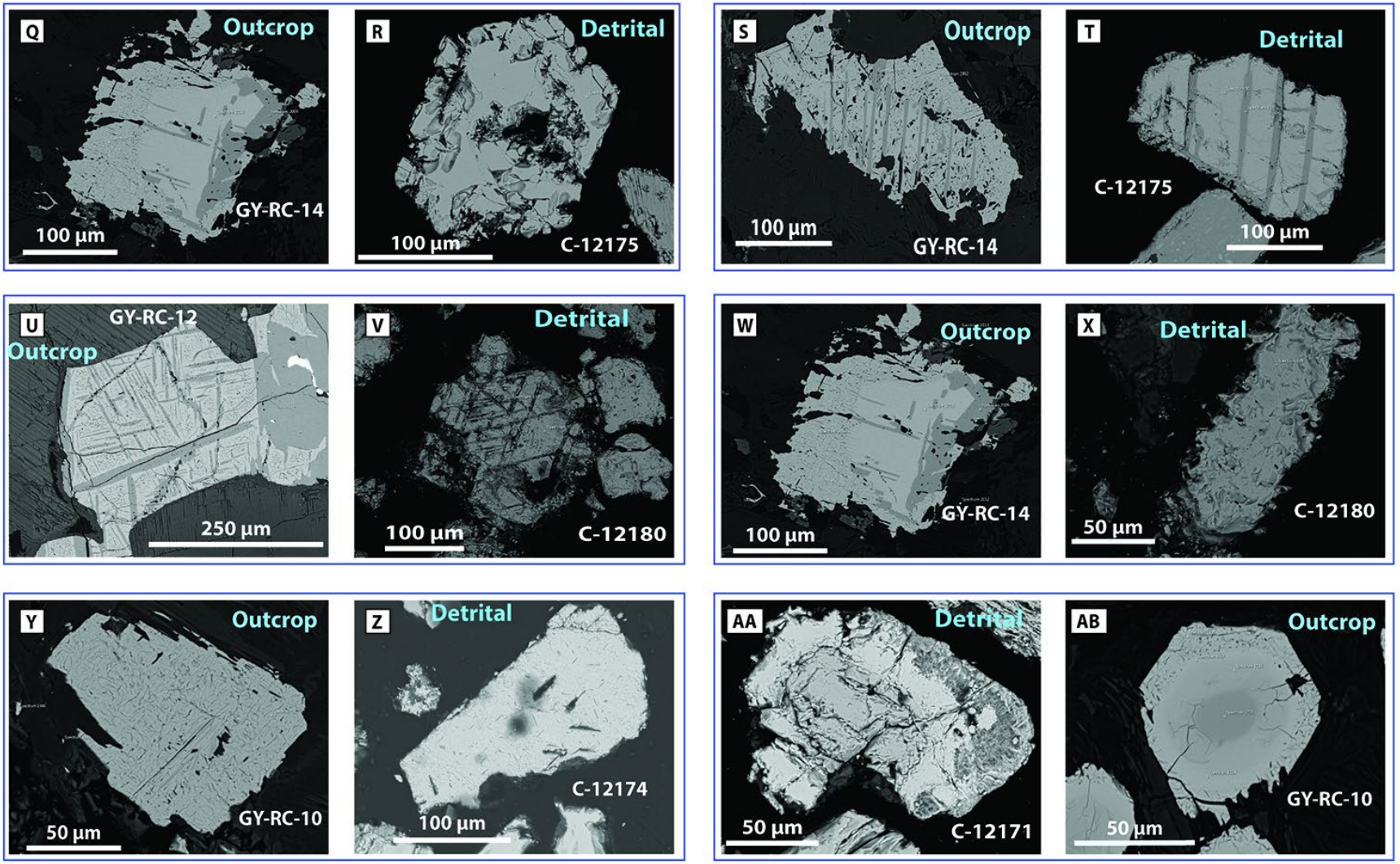

Figure 4.5. Additionally, we compare BSE images for Fe-Cr-Ti oxides from outcrop and detrital samples highlighting the textural similarities in grains from these sample types (Q - AB). The comparisons indicate that while some textural types persist during weathering and erosion (e.g., A,I, S,T, Y, Z, AA, AB), textures are altered and eventually lost due to weathering (E, G, M , V).

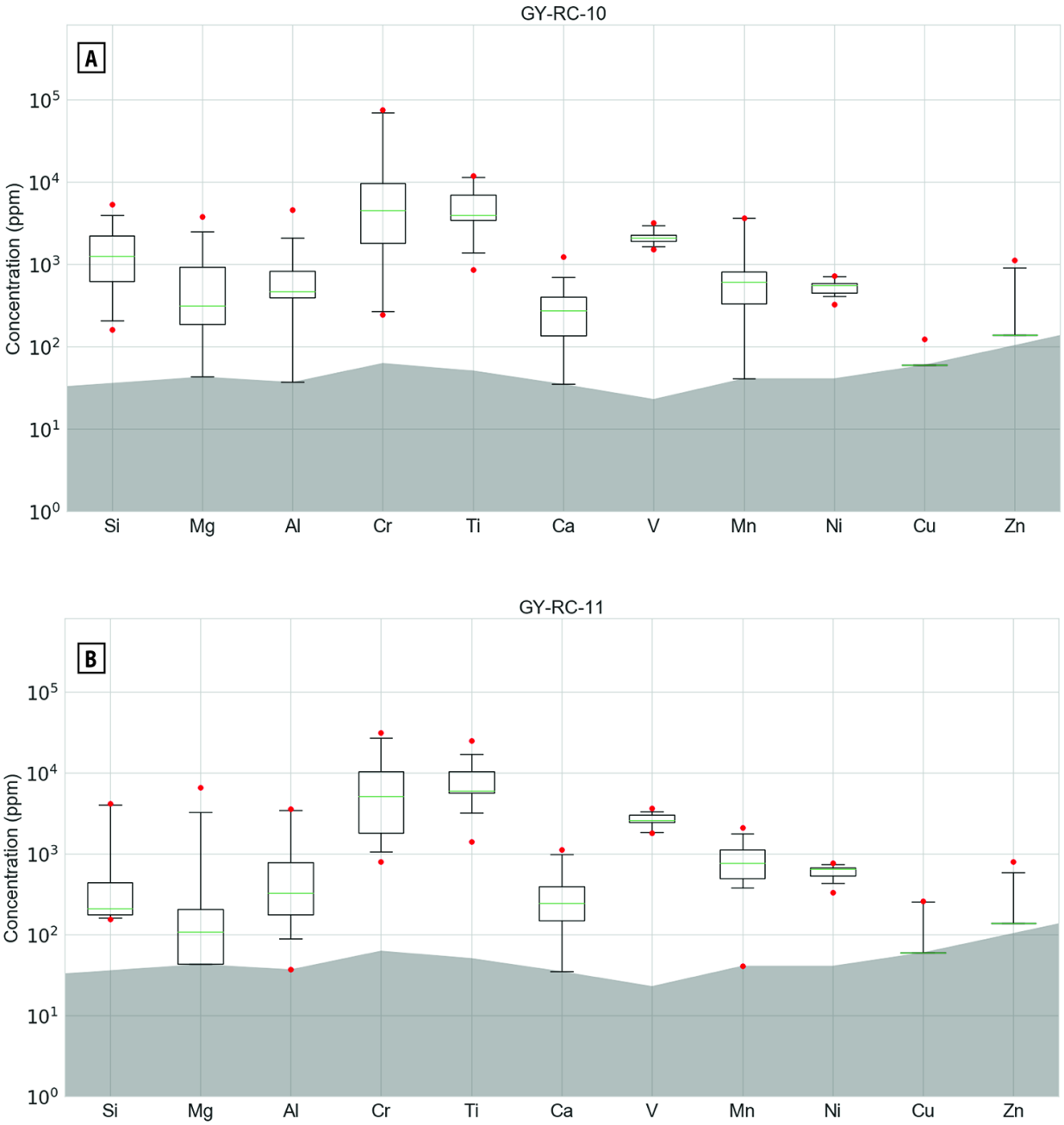

Figure 4.6. Box and whisker plots comparing the compositions of magnetite from outcrop samples GY-RC-10 (A), GY-RC-11 (B).

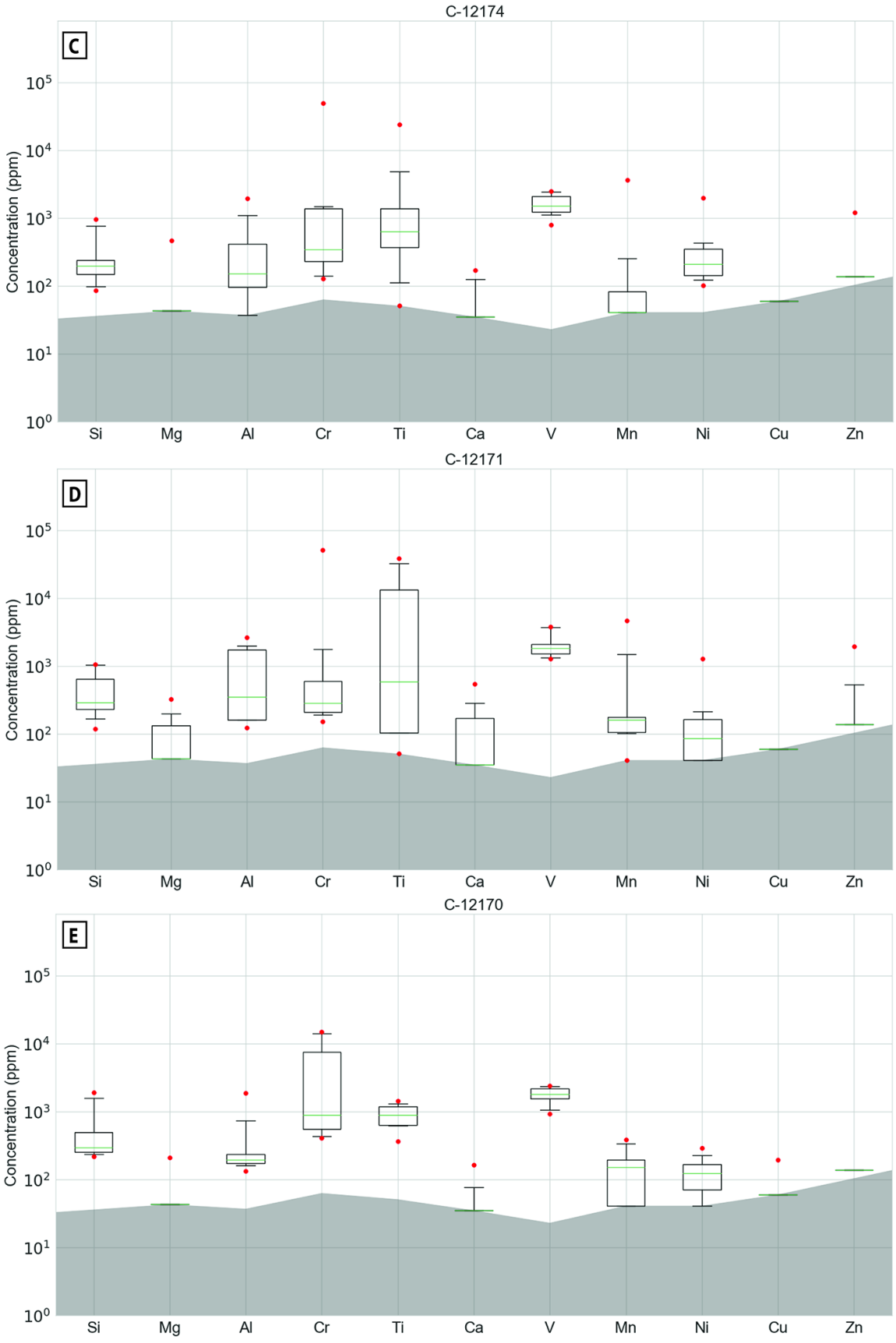
C-12174
C
Concentration (ppm)
10^5
10^4
10^3
10^2
10^1
10^0
Si
Mg
Al
Cr
Ti
Ca
V
Mn
Ni
Cu
Zn
C-12171
D
Concentration (ppm)
10^5
10^4
10^3
10^2
10^1
10^0
Si
Mg
Al
Cr
Ti
Ca
V
Mn
Ni
Cu
Zn
C-12170
E
Concentration (ppm)
10^5
10^4
10^3
10^2
10^1
10^0
Si
Mg
Al
Cr
Ti
Ca
V
Mn
Ni
Cu
Zn

Figure 4.6. Box and whisker plots comparing the compositions of magnetite from detrital samples C-12174 (C), C-12171 (D), and C-12170 (E). The outcrop and detrital samples are within 2 km of each other. Median concentrations of all elements are lower in the detrital samples compared to rock samples indicating change in the chemical composition of Fe-Cr-Ti oxides as they are chemically weathered. The concentrations of V and Al show less change than the other elements

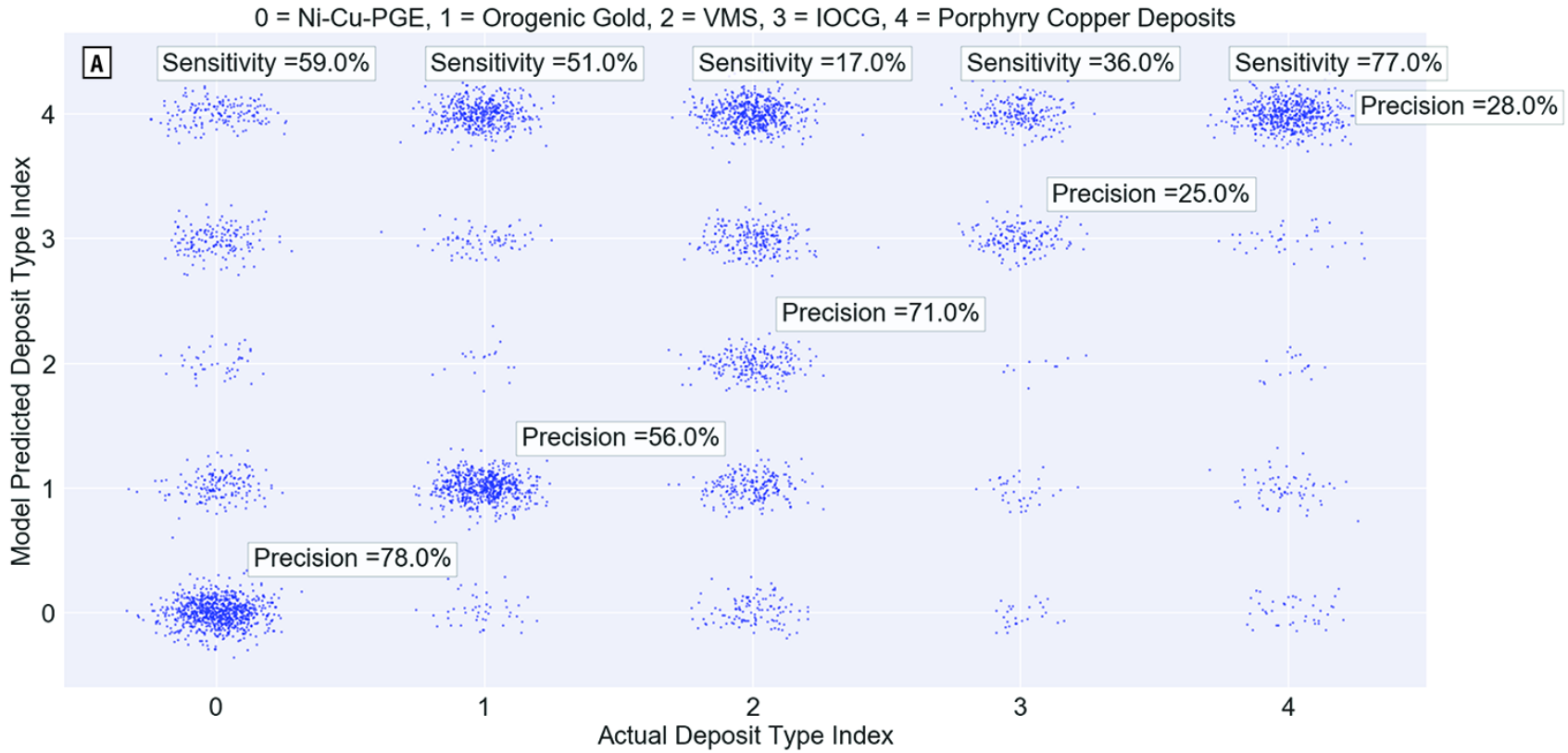

B

Input Data	Ni-Cu-PGE	Orogenic Gold	VMS	IOCG	Porphyry Copper
Global Ni-Cu-PGE	94	1	0	0	5
Global OGD	0	82	0	0	18
Global VMS	4	0	48	0	48
Global IOCG	0	0	10	44	46
Global PCD	0	0	33	0	67

Figure 4.7. Model classification results for global magnetite data, comparing true and inferred deposit types along with model accuracy metrics. In (A) we plot of the actual versus inferred deposit type of global Fe-Cr-Ti oxide data used to train the model for 5 major ore deposits types. Analyses that plot along the diagonal are correctly classified, while off-diagonal points are misclassified. Model accuracy

is reported for each deposit type in two ways: sensitivity (or probability of detection) shows how often a sample from a particular deposit type is correctly identified, and precision shows how frequently an inferred classification label is correct. IOCGs and PCDs are hampered by high false positive rates, yielding low precision values, but the model shows informatively high precision for Ni-Cu-PGE, orogenic gold, and VMS deposits. Combined with sizeable detection probabilities, the model is especially diagnostic for Ni-Cu-PGE and orogenic gold deposits. By using a non-negative least squares regression (NNLS) model that compares the characteristic overlap between the chemical signatures of magnetite from the 5 ore deposit types with that obtained when the multivariate normal model is applied to data from an unknown source, we are able to reduce the effects of the chemical overlap and determine the ore deposit source of the input data. In (B) we show the corrected/improved ore deposit source proportions obtained when the NNLS model is applied to the characteristic chemical signatures for Fe-Cr-Ti oxides from the 5 ore deposit types when they are treated as data from unknown sources. The combined use of the multivariate normal and NNLS models improves our ability to identify magnetite from the 5 ore deposit types.

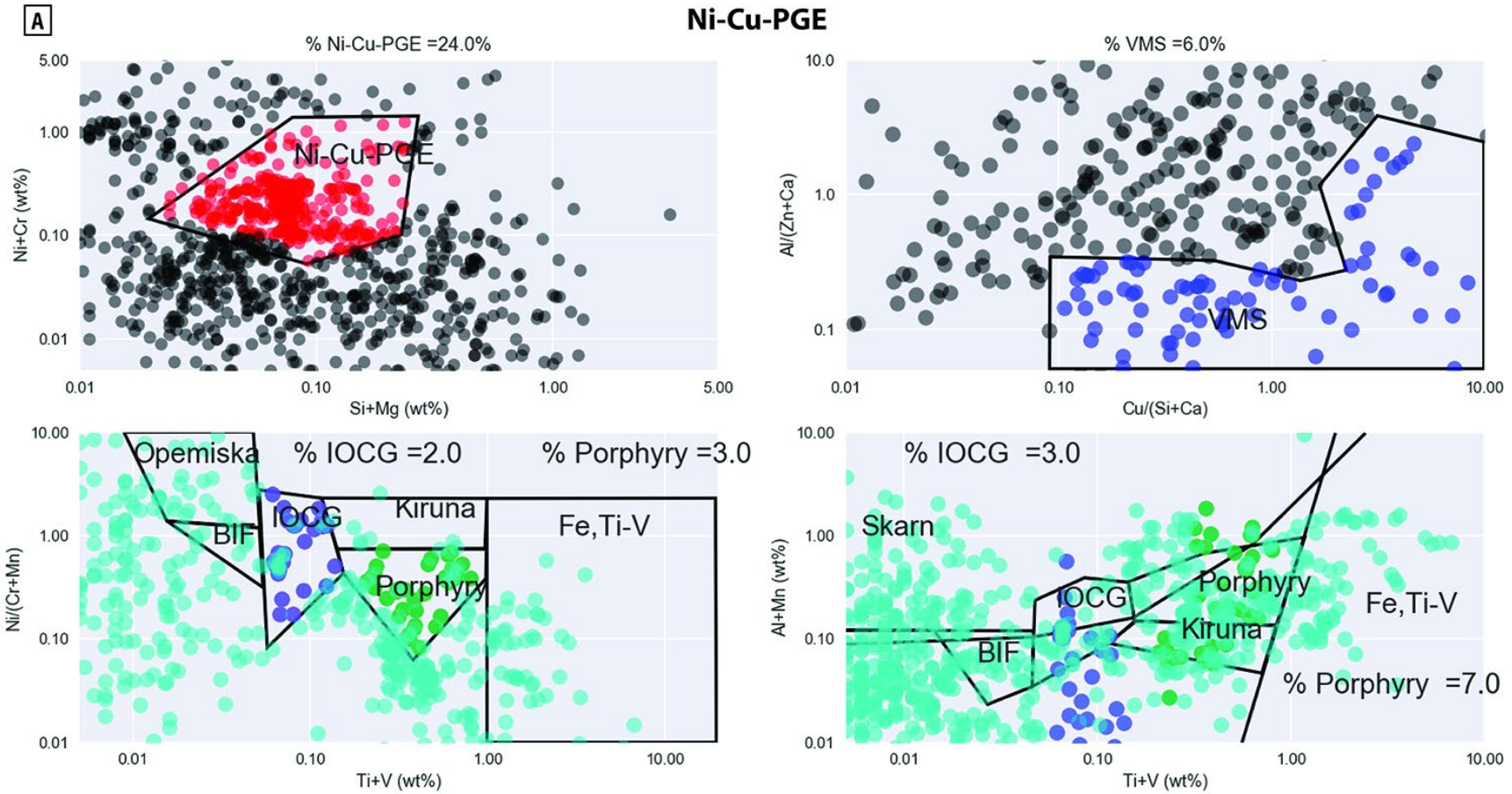

Figure 4.8. Global compilations of magnetite geochemical data from individual samples for (A) Ni-Cu-PGE, (B) VMS, (C) orogenic gold, (D) porphyry Cu-Au, and (E) porphyry Cu-Mo deposits are visualized using the discriminant plots of Dupuis and Beaudoin (2011) and Nadoll et al. (2014), where compositional fields are labeled according to nominal deposit type. When applied to individual analyses from ore deposits globally, only 24% and 5% of the global (A) Ni-Cu-PGE and (B) VMS deposit data are identified by those fields, respectively.

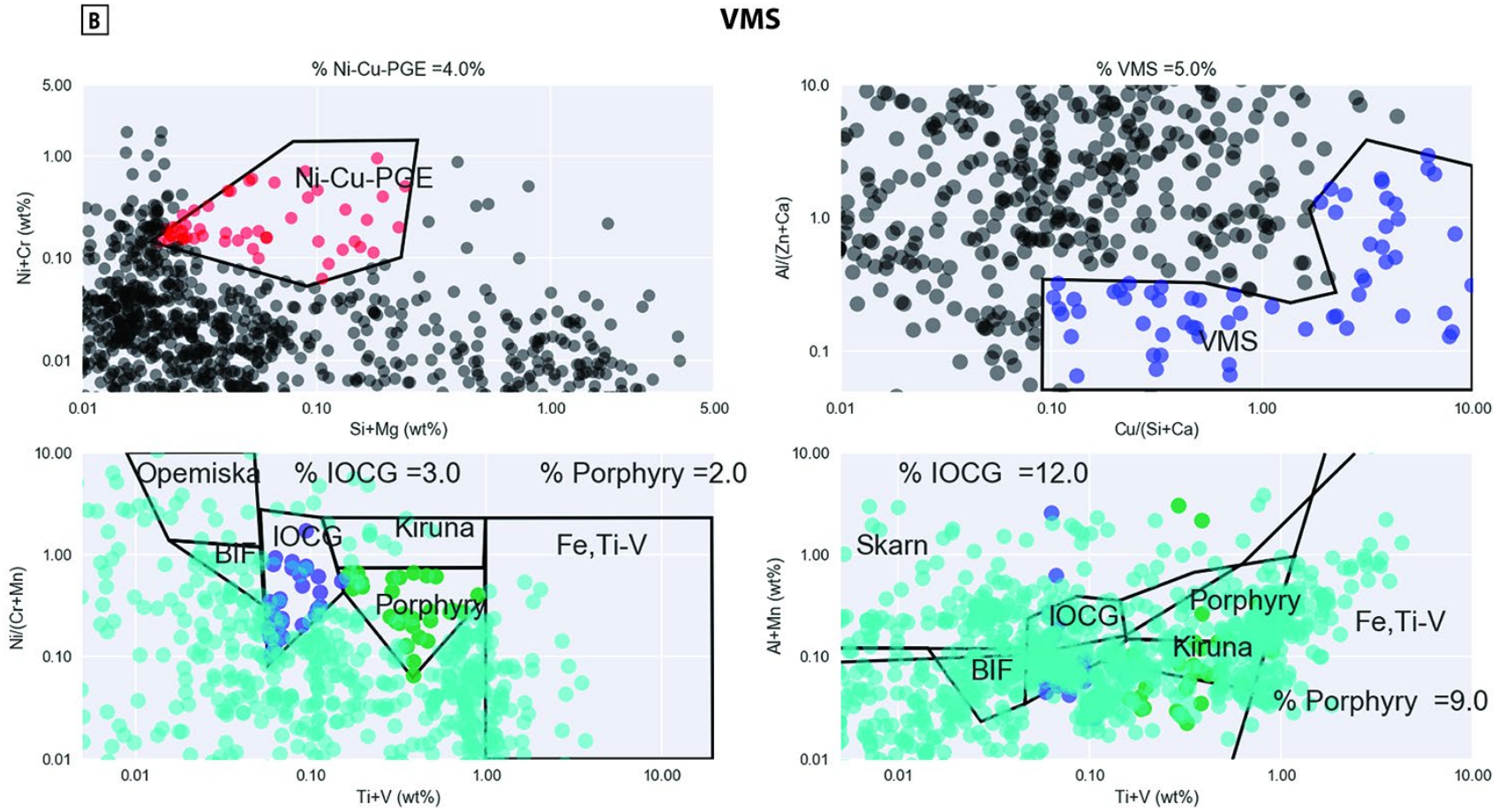

Figure 4.8. (B) Global compilation of magnetite from VMS deposits.

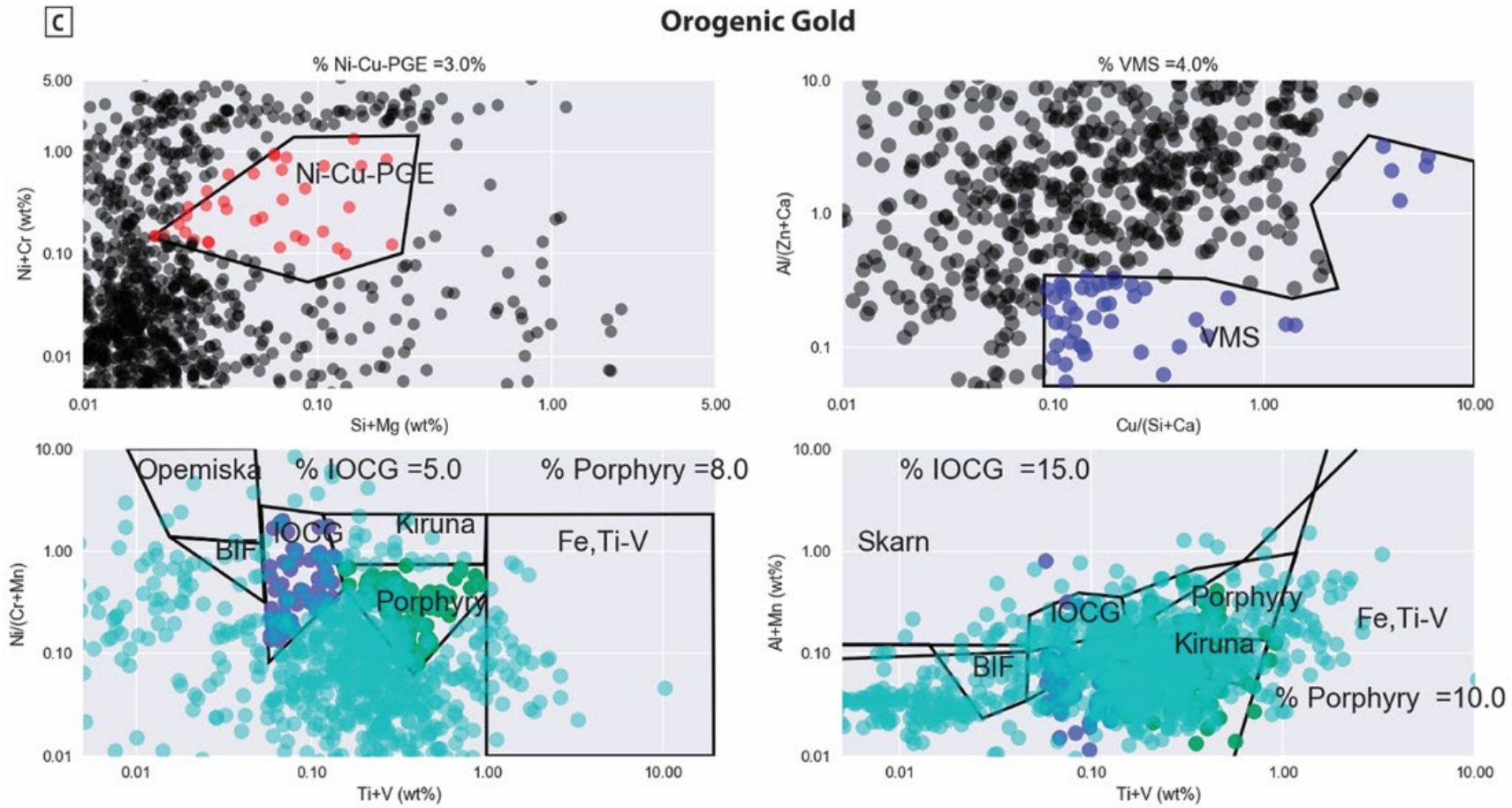

Figure 4.8. Global compilation of magnetite from (C) orogenic gold deposits.

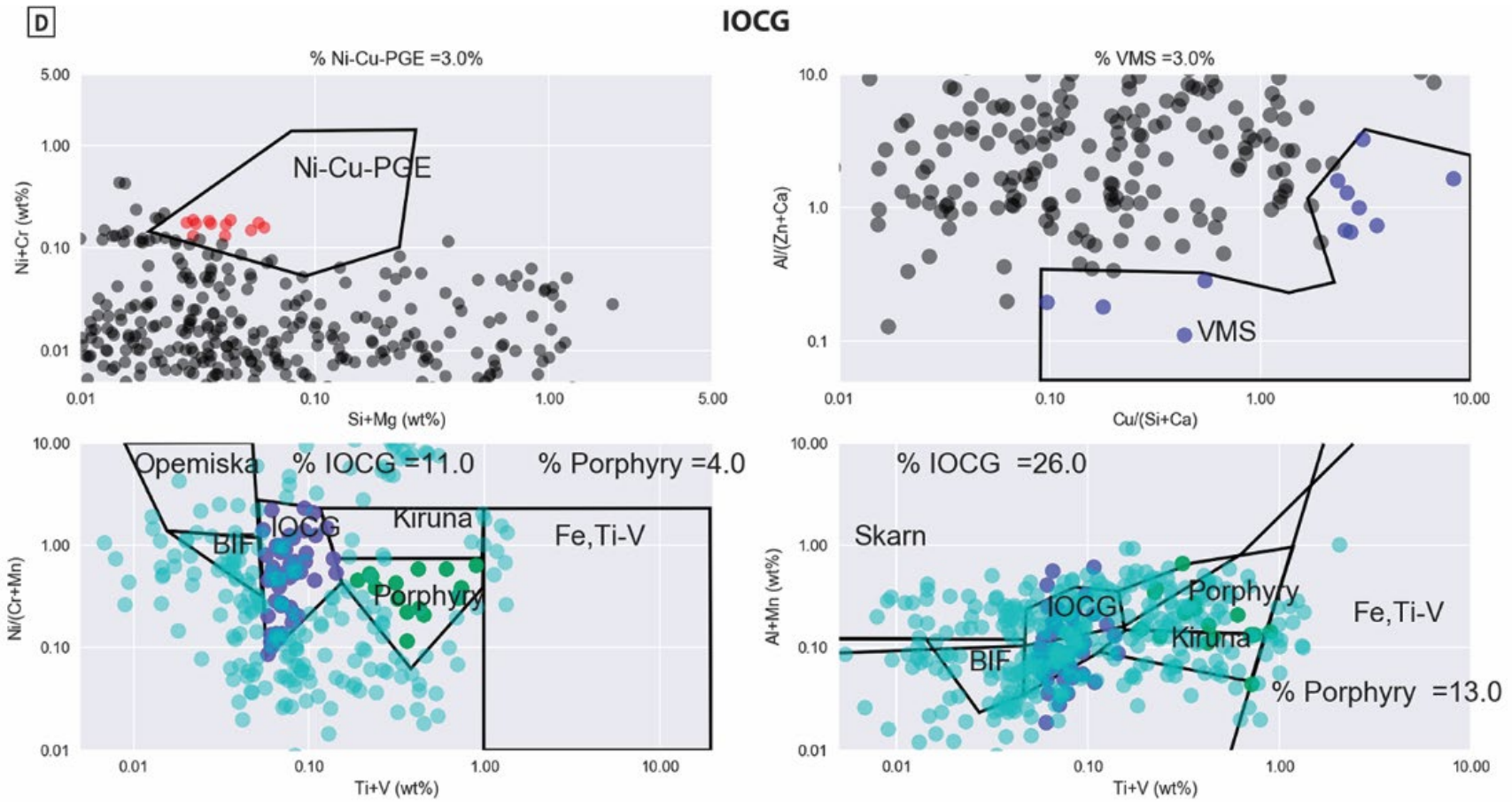

Figure 4.8. Global compilation of magnetite from (D) iron oxide – copper – gold deposits.

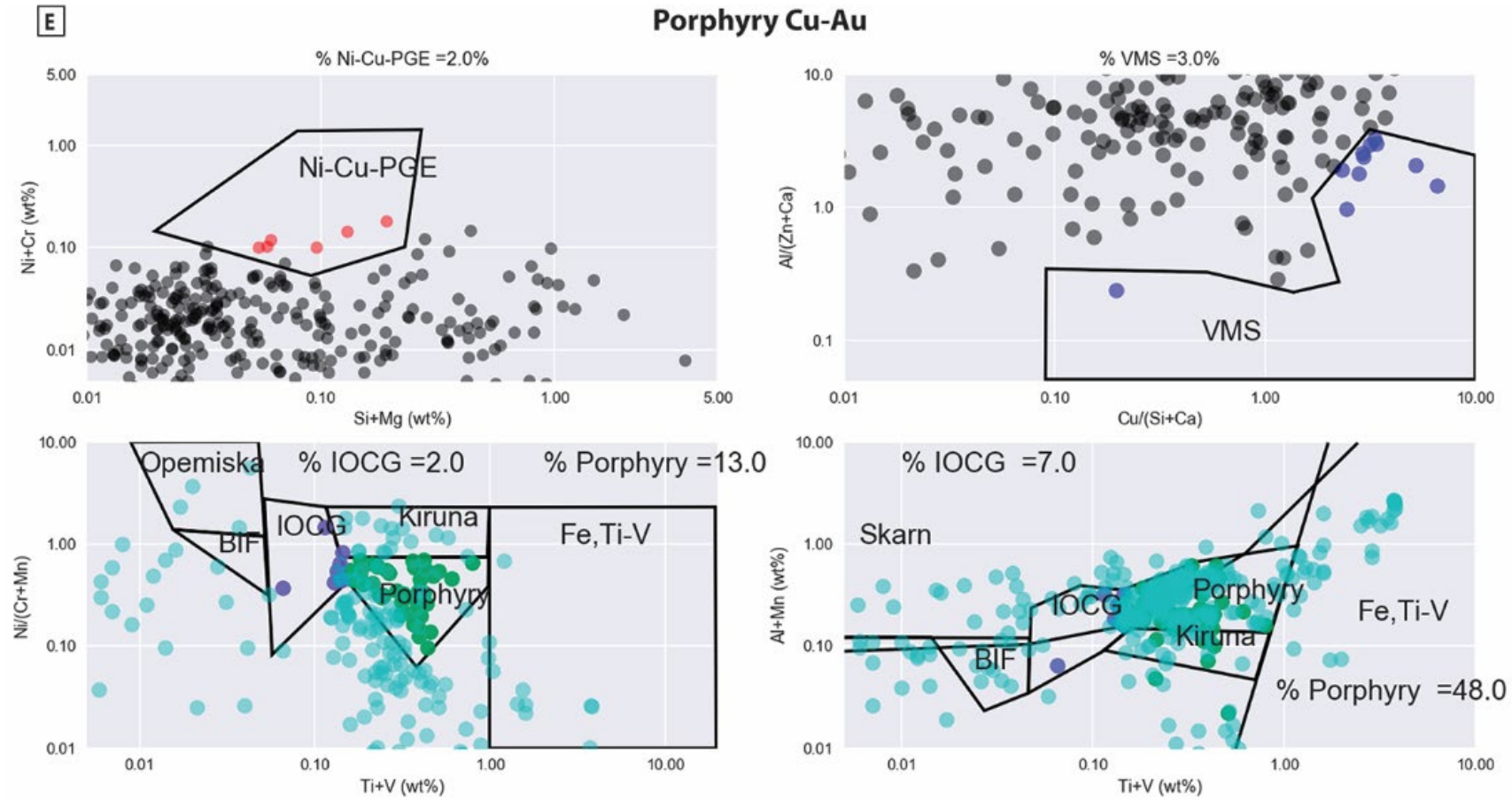

Figure 4.8. Global compilation of magnetite from (E) porphyry Cu-Au deposits.

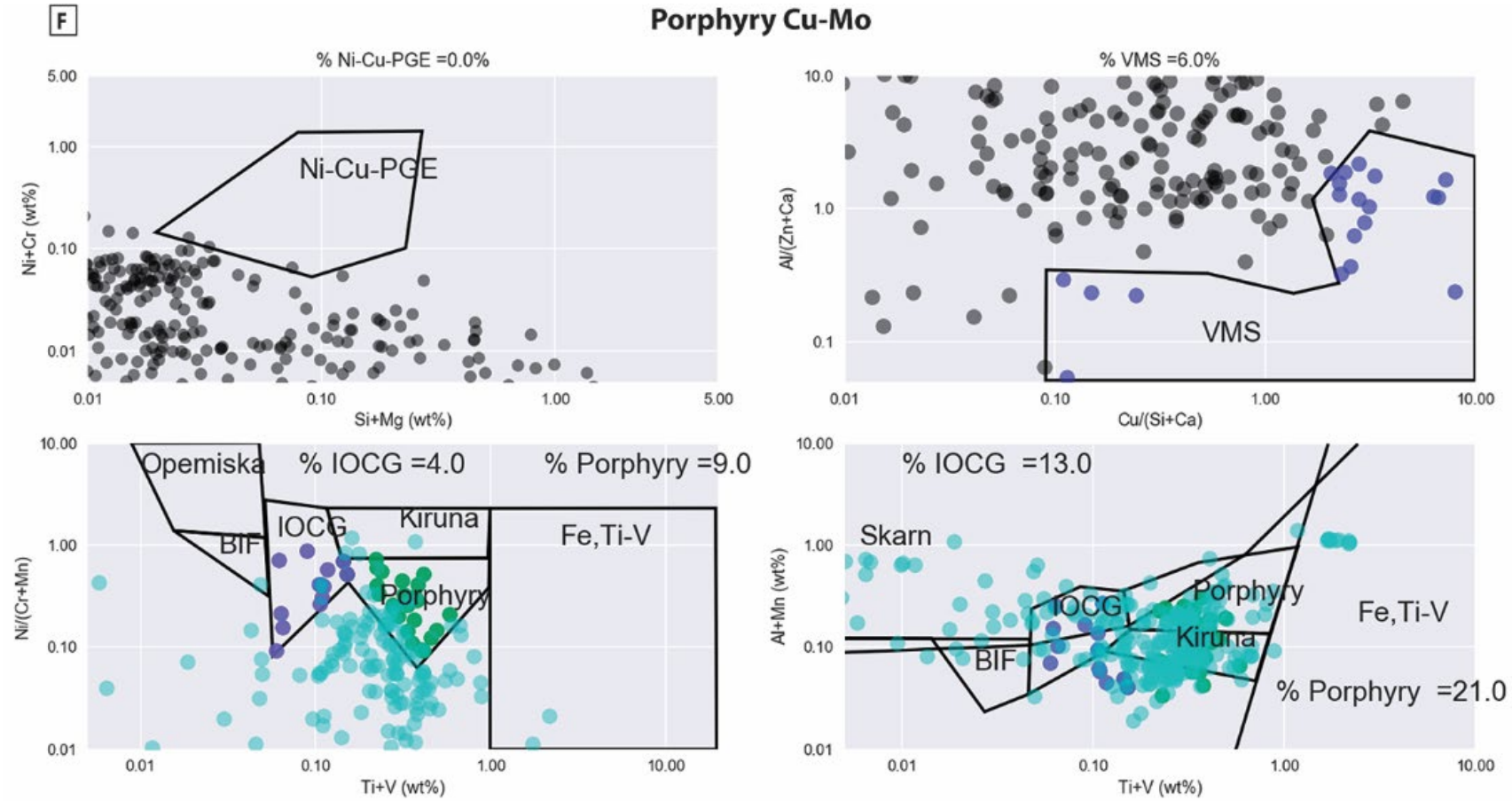

Figure 4.8. Global compilation of magnetite from (F) porphyry Cu-Mo.

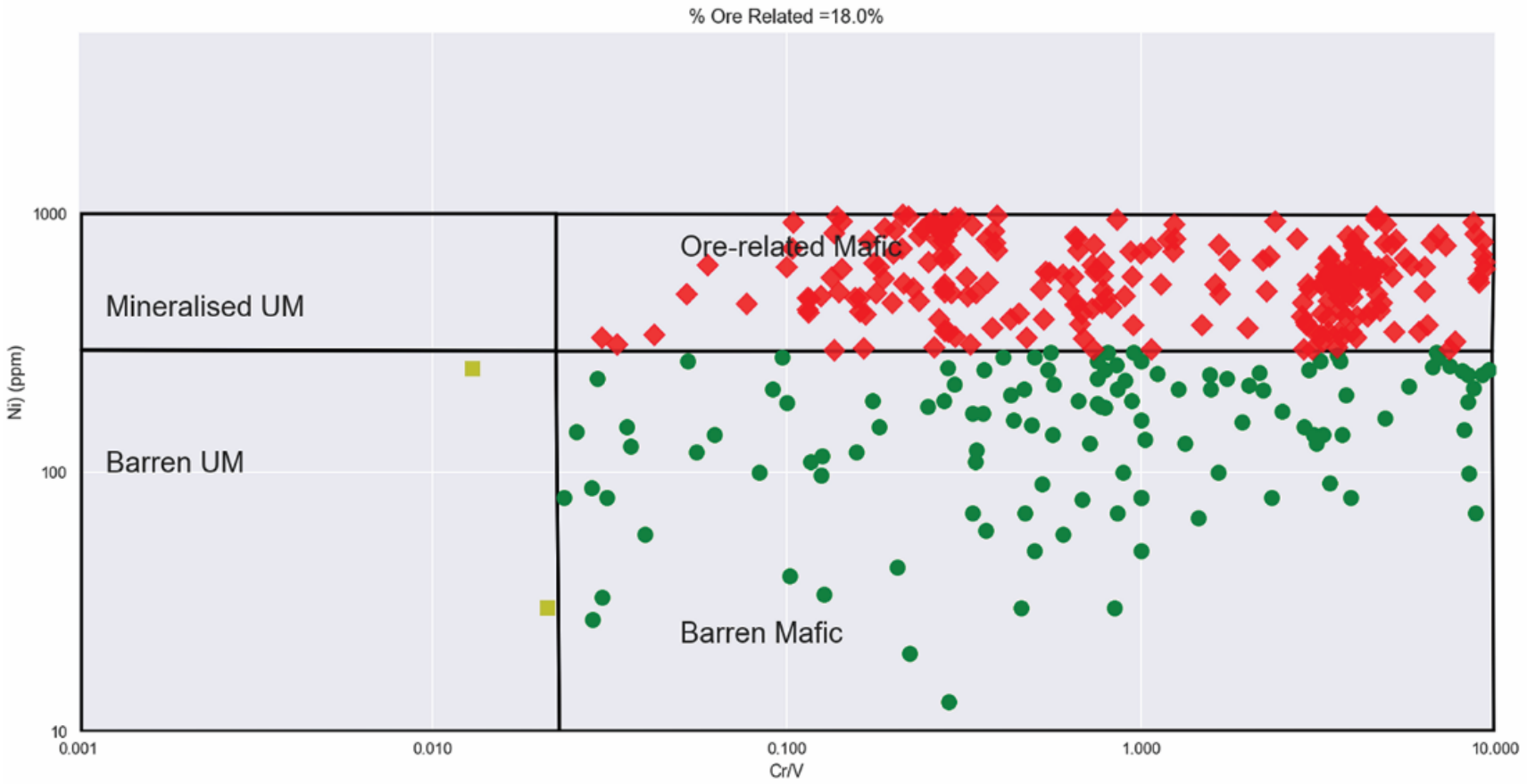

Figure 4.9. Global magnetite data for Ni-Cu-PGE deposits are plotted as in Figure 5 but in Ni versus Cr/V geochemical space, according to Ward et al. (2018), who showed that magnetite from mineralised and unmineralised ultramafic rocks and ore-related and barren mafic rocks nominally display distinct compositions in this space. Eighteen percent of the data plot in the field for magnetite from ore-related mafic rocks, while the majority of the data plot in the field for barren mafic rocks.

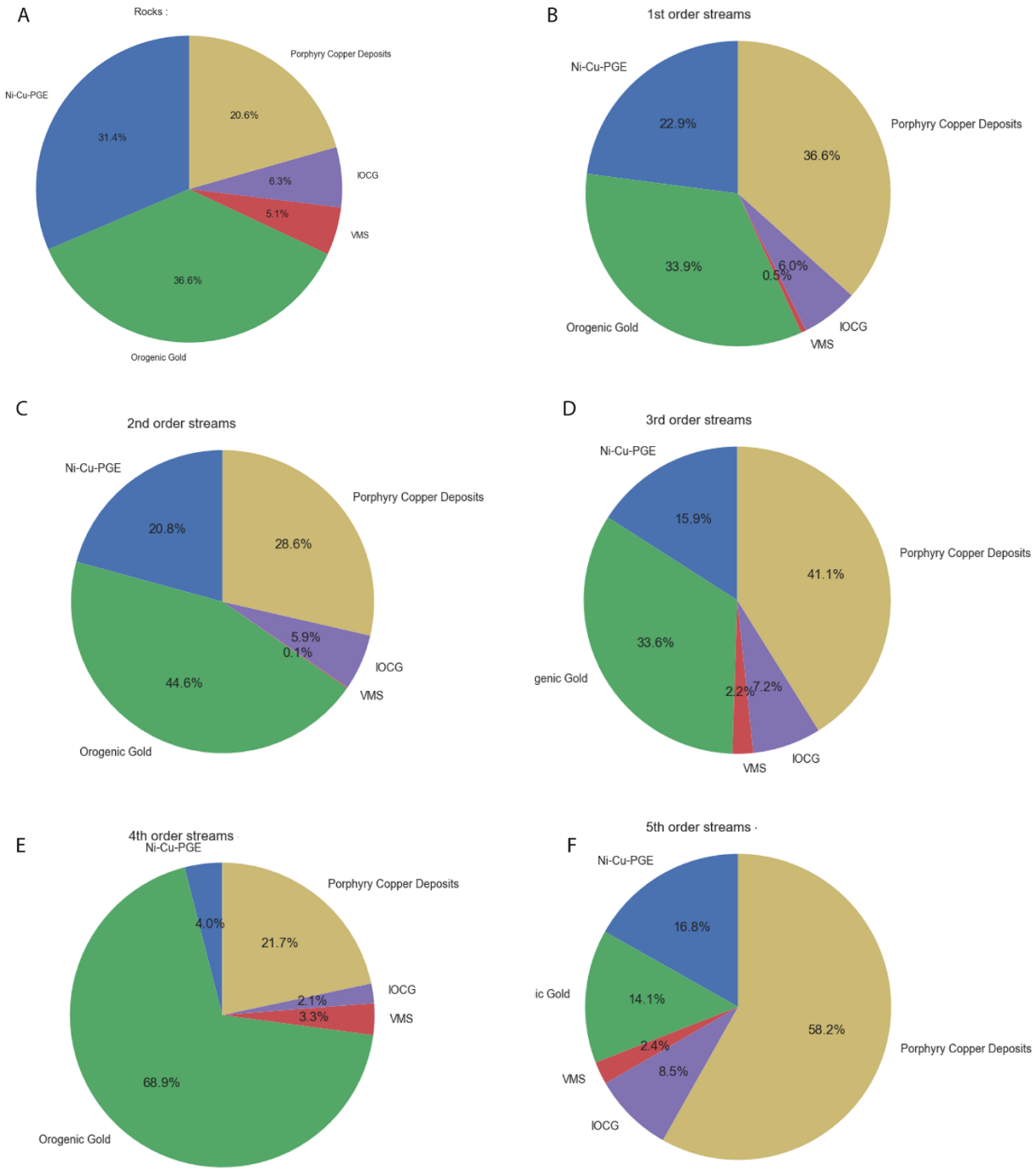

G

Sample ID	Ni-Cu-PGE	Orogenic Gold	VMS	IOCG	Porphyry Copper Deposit
Guyana Rocks	72	28	0	0	0
Guyana 1st order	30	48	0	0	22
Guyana 2nd order	18	74	0	0	8
Guyana 3rd order	17	44	10	0	29
Guyana 4th order	0	100	0	0	0
Guyana 5th order	23	0	24	0	53

Figure 4.10. Inferred proportions of magnetite from (A) outcrop, (B) 1st , (C) 2nd, (D) 3rd, (E) 4th, and (F) 5th order streams that are identified as being similar to Fe-Cr-Ti oxides from Ni-Cu-PGE (blue), orogenic gold (green), VMS (red), IOCG (purple), and porphyry copper deposits

(gold) using the multivariate normal model developed in this study. The pie charts represent the collective chemical signature obtained when individual analyses of grains from these samples are compared to the distribution of data from the 5 ore deposit types. Comparison of these collective signatures with those for magnetite from the (5) modeled ore deposit types, using the non-negative least squares (NNLS) model, reduces the effect of misidentification of analyses due to overlapping chemical signatures between ore deposit types and improves the predictive ability of the model (G). For instance, application of the NNLS model to data from outcrop samples downweighs the effect of the overlap between the chemical signatures for VMS, IOCG and porphyry copper deposits, and reveals that the chemical signature of the sample is most similar to Fe-Cr-Ti oxides from Ni-Cu-PGE (72%) and orogenic gold (28%) deposits.

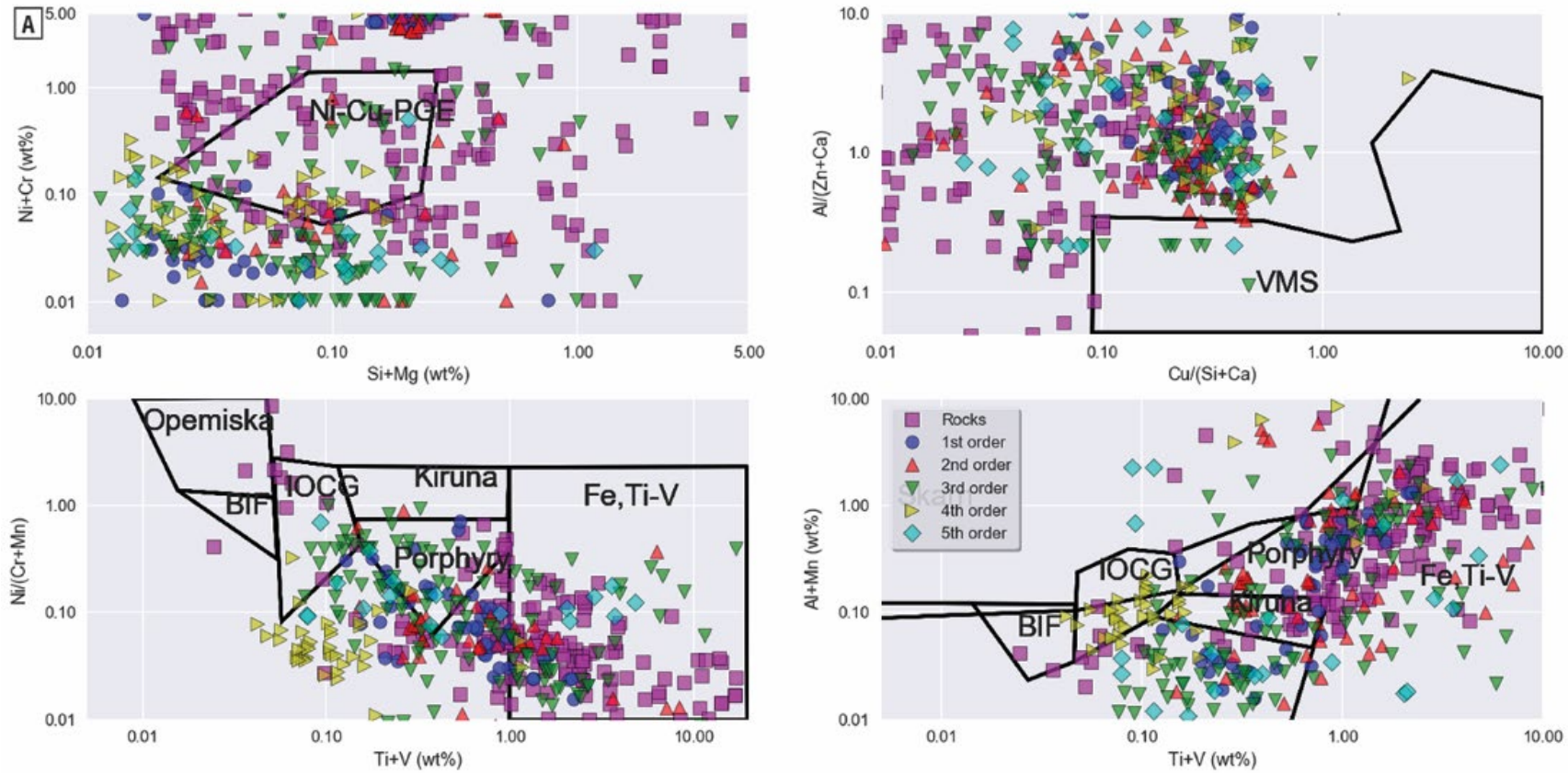

Figure 4.11. Visualization of geochemical data for rocks (pink squares), 1st (blue circles), 2nd (red upward triangles), 3rd (green downward triangles), 4th (yellow right-facing triangles), and 5th (cyan diamonds) order streams on the discriminant plots of (A) Dupuis and Beaudoin (2011) and Nadoll et al. (2014) and (B) Ward et al. (2018). The samples plot in many fields in the discriminant plots but generally indicate the potential for Ni-Cu-PGE, Fe-Ti-V, porphyry, and IOCG deposits in the sampled catchments.

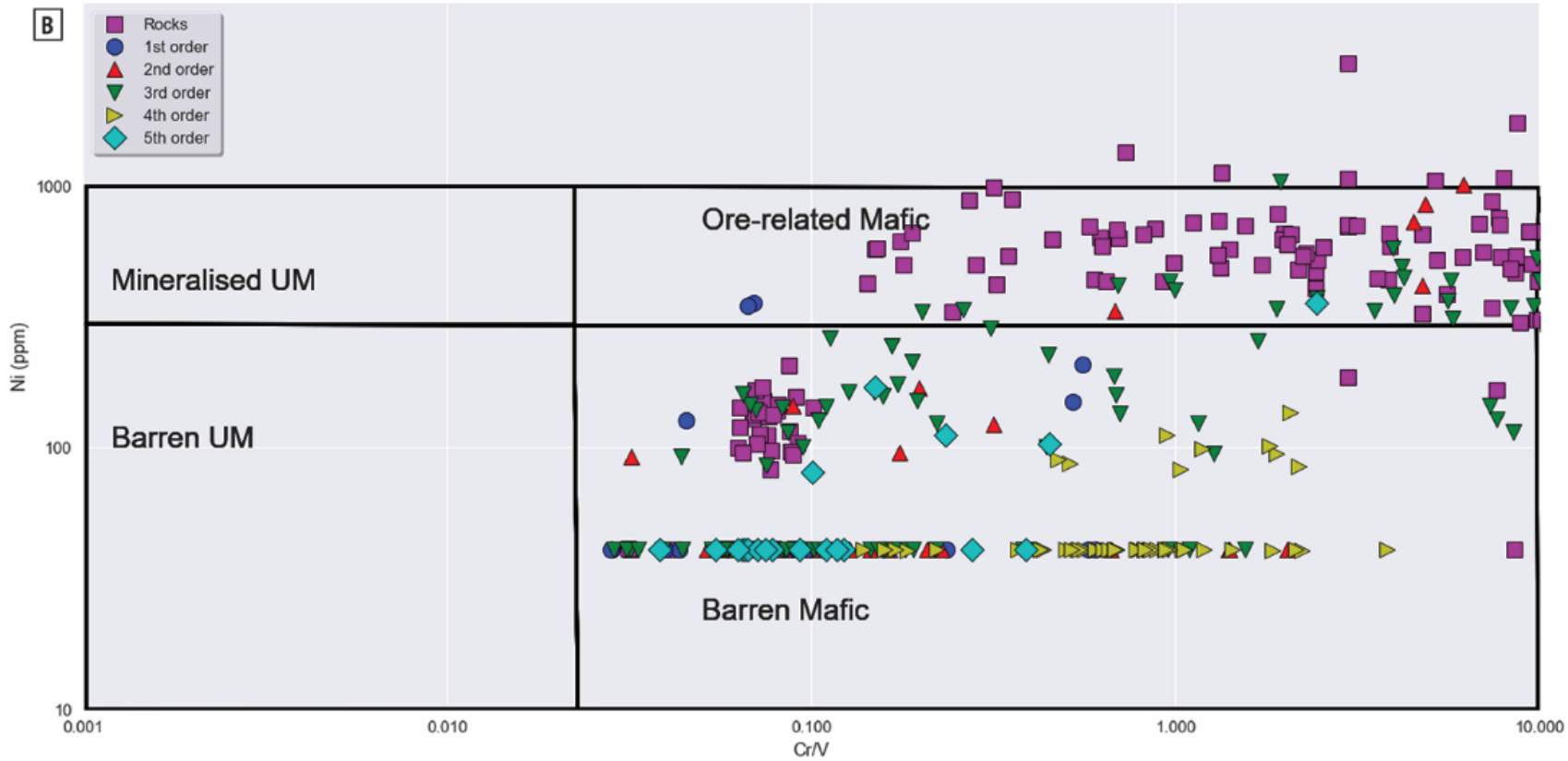

Figure 4.11. (B) Visualization of geochemical data for rocks (pink squares), 1st (blue circles), 2nd (red upward triangles), 3rd (green downward triangles), 4th (yellow right-facing triangles), and 5th (cyan diamonds) order streams on the discriminant plot of Ward et al. (2018).

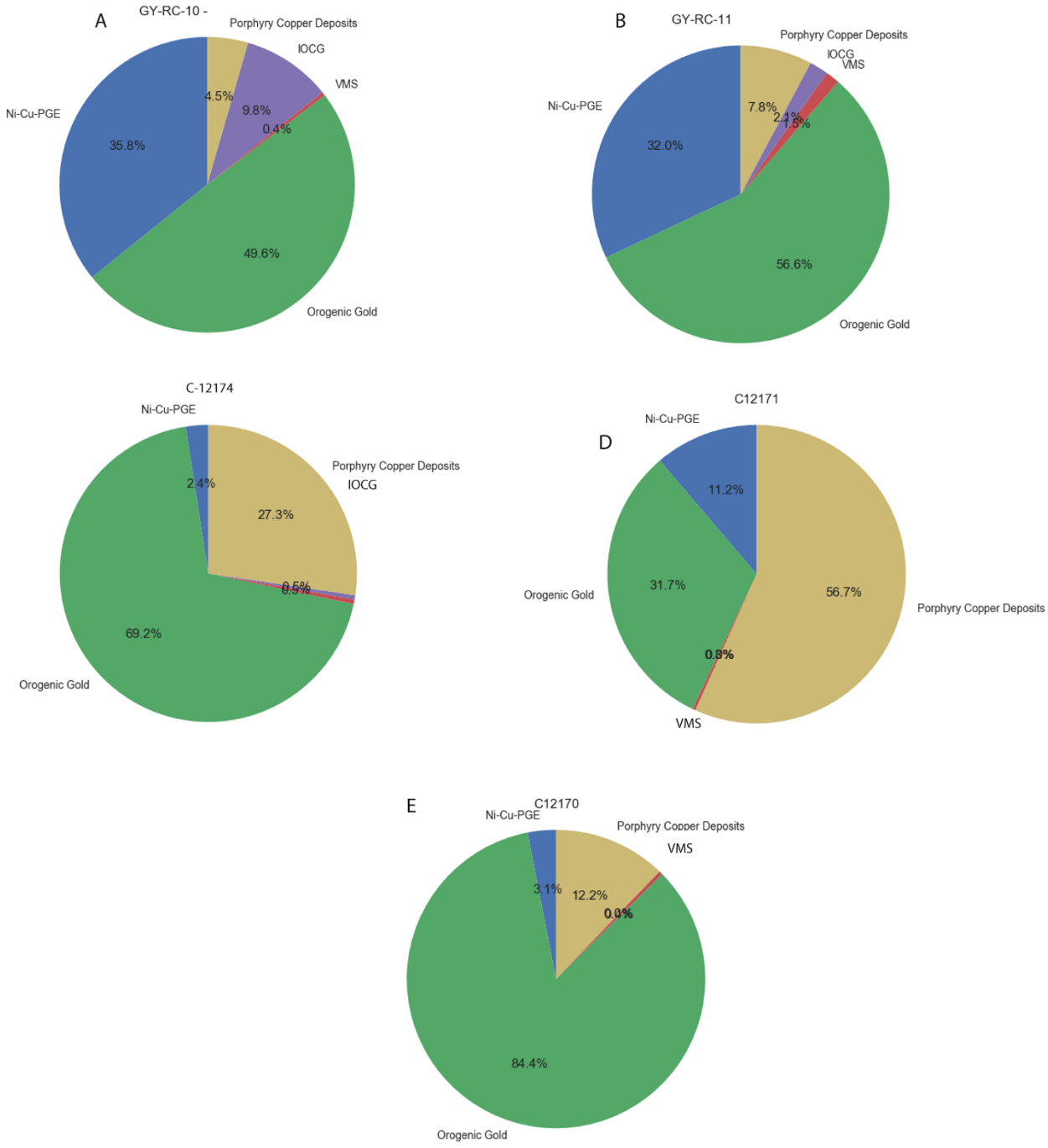

F

Sample ID	Ni-Cu-PGE	Orogenic Gold	VMS	IOCG	Porphyry Copper Deposit
GY-RC-10	32	68	0	0	0
GY-RC-11	20	80	0	0	0
C-12174	0	100	0	0	0
C-12171	9	32	16	0	43
C-12170	0	100	0	0	0

Figure 4.12. Inferred ore deposit source results obtained when the multivariate normal model is applied to rock (10 (A) and 11 (B)) and detrital (C-12174 (C), C-12171 (D), and C-12170 (E)) samples from a catchment in northwestern Guyana. (F) Application of the NNLS model to the

collective chemical signatures of these samples indicate that the grains in this catchment are chemically similar to Fe-Cr-Ti oxides from global Ni-Cu-PGE and orogenic gold deposits.

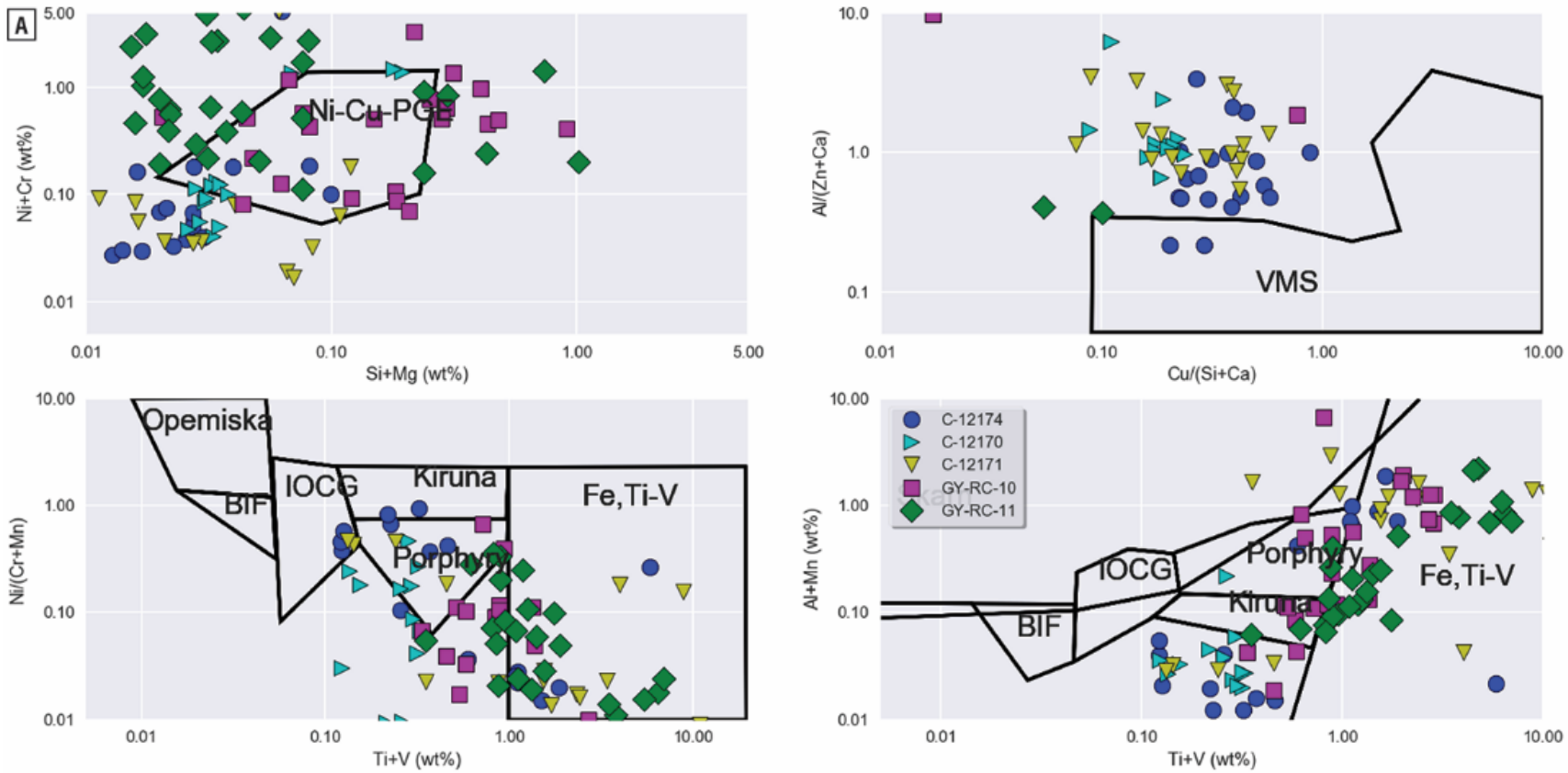

Figure 4.13. Visualization of the data for the rocks and stream sediment samples from the catchment in Figure 4.12 on the discriminant plots of (A) Dupuis and Beaudoin (2011), Nadoll et al. (2014).

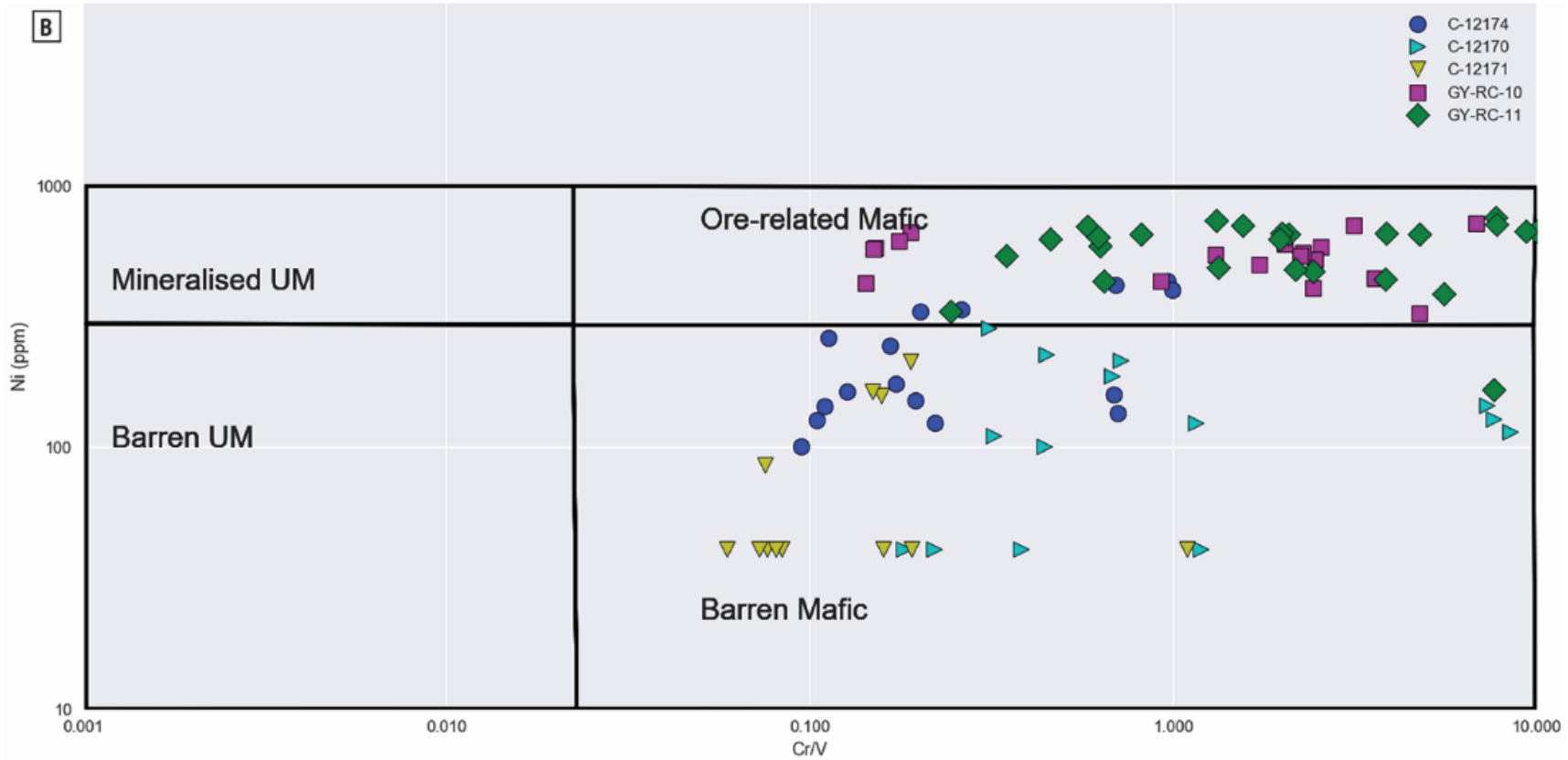

Figure 4.13. Visualization of the data for the rocks and stream sediment samples from the catchment in Figure 4.12 on the discriminant plot (B) Ward et al. (2018).

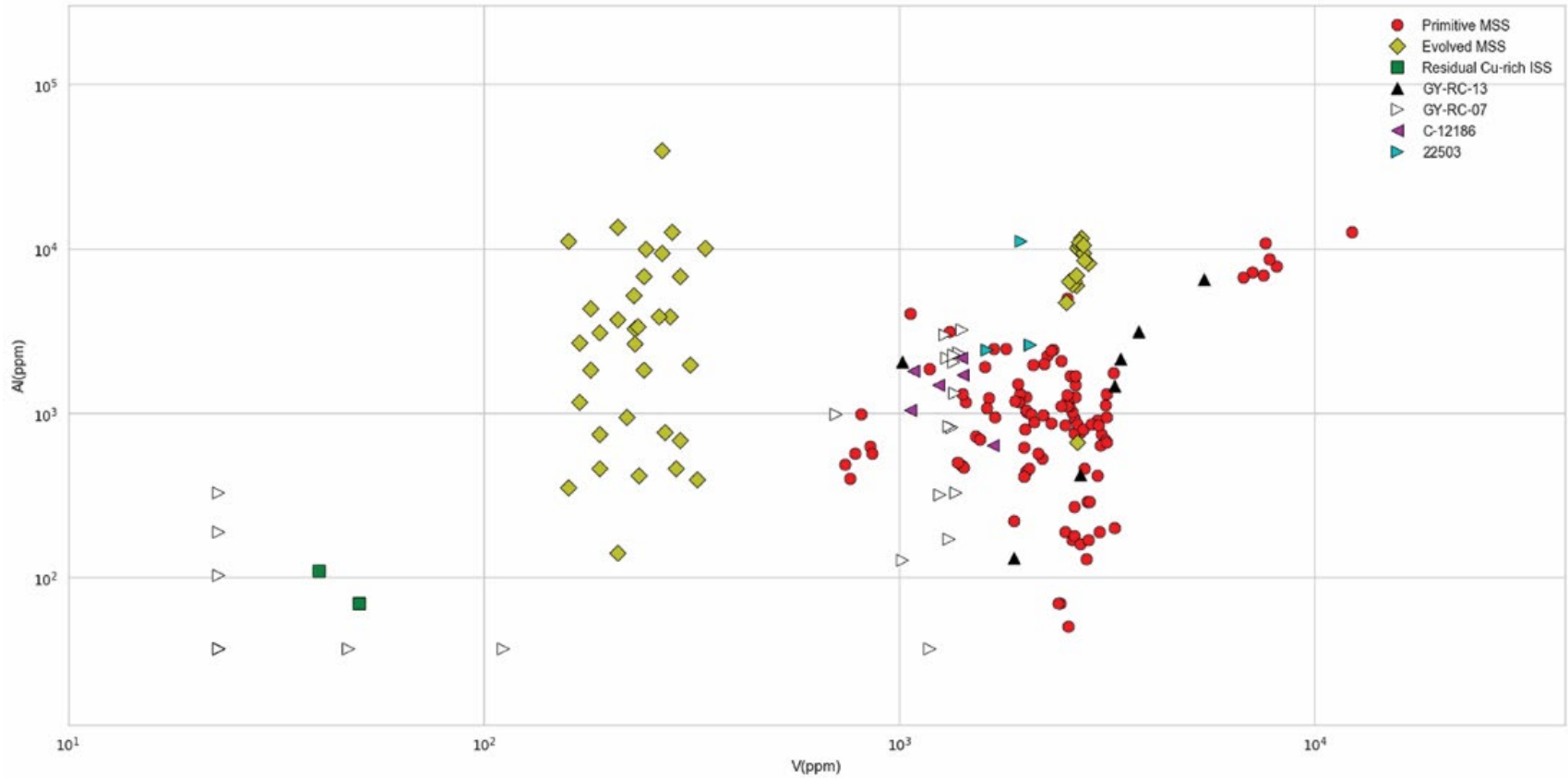

Figure 4.14. Comparison of the concentrations of V and Al in magnetite that crystallizes in equilibrium with sulfide liquids of different compositions; i.e., primitive monosulfide solid solution (red circles), evolved monosulfide solid solution (yellow diamonds), and Cu-rich intermediate solid solution (green squares). We also plot the V and Al contents for magnetite from samples with chemical signatures that are very similar to magnetite from Ni-Cu-PGE deposits, according to the multivariate normal and NNLS models developed in this study.

4.8 References

Abzalov, M.Z., 1998, Chrome–spinels in gabbro–wehrlite intrusions of the Pechenga area, Kola Peninsula, Russia: emphasis on alteration features: Lithos, 43(3), p.109-134.

Arguin, J.P., Pagé, P., Barnes, S.J., Girard, R., and Duran, C., 2018, An integrated model for ilmenite, al-spinel, and corundum exsolutions in titanomagnetite from oxide-rich layers of the Lac Doré Complex (Québec, Canada): Minerals, 8(11), p. 476.

Baratoux, L., Jessell, M.W., and Ernst R.E., 2019, Mapping and correlation of West African and South American mafic dykes: Inter-Guiana Geological Convention, Paramaribo, Suriname, Extended Abstracts, p. 19-22.

Bardoux, M., Moroney, M., and Robert, F., 2018, Gold mineralization in the Guiana Shield, Guiana and Suriname, South America: a field trip to the 14th biennial Society for Geology Applied to Mineral Deposits (SGA) meeting: Geological Survey of Canada, Open File 8351, p. 28 https://doi.org/10.4095/306546

Barnes, S.J., and Roeder, P.L., 2001, The range of spinel compositions in terrestrial mafic and ultramafic rocks: Journal of petrology, 42(12), p. 2279-2302.

Barnes, S.J., and Lightfoot, P.C., 2005, Formation of magmatic nickel-sulfide ore deposits and processes affecting their copper and platinum-group element contents: Economic Geology 100th Anniversary, p. 179-213.

Bassoo, R., and Murphy, J.B., 2018, The 9 Mile Deposit of the Barama-Mazaruni Greenstone Belt of the Guiana Shield: geochemistry, geochronology and regional significance: Brazilian Journal of Geology, 48(4), p. 671-683.

Biagioni, C., and Pasero, M., 2014, The systematics of the spinel-type minerals: An overview: American Mineralogist, 99(7), p. 1254-1264.

Boutroy, E., Dare, S.A., Beaudoin, G., Barnes, S.J., and Lightfoot, P.C., 2014, Magnetite composition in Ni-Cu-PGE deposits worldwide: application to mineral exploration: Journal of Geochemical Exploration, 145, p. 64-81.

Bullard, E., Everett, J.E., and Gilbert Smith, A., 1965, The fit of the continents around the Atlantic: Philosophical Transactions of the Royal Society of London. Series A, Mathematical and Physical Sciences, 258(1088), p. 41-51.

Buddington, A.F., and Lindsley, D.H., 1964, Iron-titanium oxide minerals and synthetic equivalents: Journal of petrology, 5(2), p. 310-357.

Burke, K., and Dewey, J.F., 1973, Plume-generated triple junctions: key indicators in applying plate tectonics to old rocks: The Journal of Geology, 81(4), p. 406-433.

Choudhuri, A., 1980, The early Proterozoic greenstone belt of the northern Guiana Shield, South America: Precambrian Research, 13(4), p. 363-374.

Daoust, C., Voicu, G., Brisson, H., and Gauthier, M., 2011, Geological setting of the Paleoproterozoic Rosebel gold district, Guiana Shield, Suriname: Journal of South American Earth Sciences, 32(3), p. 222-245.

Dardenne, MA., and Schobbenhaus, C., 2003, Mineral deposits in geological time and

metallogenetic times: BIZZI, l. THE.; SCHoBBENHAuS, C .; VIDottI, RM , p. 365-447.
Dare, S.A., Barnes, S.J. and Beaudoin, G., 2012, Variation in trace element content of magnetite crystallized from a fractionating sulfide liquid, Sudbury, Canada: implications for provenance discrimination: Geochimica et Cosmochimica Acta, 88, p. 27-50.
Dare, S.A., Barnes, S.J. and Beaudoin, G., 2015, Did the massive magnetite "lava flows" of El Laco (Chile) form by magmatic or hydrothermal processes? New constraints from magnetite composition by LA-ICP-MS: Mineralium Deposita, 50(5), p. 607-617.
Deer W.A., Howie R.A., and Zussman, J., 1992, An introduction to rock forming minerals, 2nd edn. Longman, Harlow, Wiley, New York
Delor, C., de Roever, E.W.F., Lafon, J-M., Lahondère, D., Rossi, P., Cocherie, A., Guerrot, and C., Potrel, A., 2003, The Bakhuis ultra-high-temperature granulite belt (Suriname): II. Implications for the late Transamazonian crustal stretching in a revised Guiana Shield framework: Geologie de la France, v. 2-3-4, p. 207-230.
Dmitrijeva, M., Metcalfe, A.V., Ciobanu, C.L., Cook, N.J., Frenzel, M., Keyser, W.M., Johnson, G., and Ehrig, K., 2018, Discrimination and variance structure of trace element signatures in Fe-Oxides: A Case Study of BIF-Mineralisation from the Middleback Ranges, South Australia: Mathematical Geosciences, 50(4), p. 381-415.
Drum, D.E., and Christacopoulos Sdougou J., 1972, Hepatic scintigraphy in clinical decision making: Journal of Nuclear Medicine 13, no. 12, p. 908-915.
Dubé, B., Gosselin, P., Mercier-Langevin, P., Hannington, M., and Galley, A., 2007, Gold-rich volcanogenic massive sulphide deposits: Geological Association of Canada, Mineral Deposits Division, p. 75-94.
Duchesne, J.C., 1970, Microtextures of Fe-Ti oxide minerals in the South-Rogaland anorthositic complex (Norway): Annales de la Société Géologique de Belgique, 935, p. 527-544.
Dupuis, C., and Beaudoin, G., 2011, Discriminant diagrams for iron oxide trace element fingerprinting of mineral deposit types: Mineralium Deposita, 46(4), p. 319-335.
Farrow, C.E., and Watkinson, D.H., 1992, Alteration and the role of fluids in Ni, Cu and platinum-group element deposition, Sudbury Igneous Complex contact, Onaping-Levack area, Ontario: Mineralogy and Petrology, 46(1), p. 67-83.
Fontboté, L., Kouzmanov, K., Chiaradia, M., and Pokrovski, G.S., 2017, Sulfide minerals in hydrothermal deposits: Elements, 13(2), p. 97-103.
Frimmel, H.E., 2014, A giant Mesoarchean crustal gold-enrichment episode: Possible causes and consequences for exploration.
Galuskina, I.O., Vapnik, Y., Lazic, B., Armbruster, T., Murashko, M., and Evgeny V., Galuskin; Harmunite $CaFe_2O_4$: A new mineral from the Jabel Harmun, West Bank, Palestinian Autonomy, Israel. American Mineralogist ; 99 (5-6): 965–975. doi: https://doi.org/10.2138/am.2014.4563
Gibbs, A.K., 1987, Proterozoic volcanic rocks of the northern Guiana Shield, South America: Geological Society, London, Special Publications, 33(1), p. 275-288.
Gibbs, A.K., and Barron, C.N., 1993, The geology of the Guiana Shield: Oxford University Press, USA.
Grigsby, J.D., 1990, Detrital magnetite as a provenance indicator: Journal of Sedimentary Research, 60(6), p. 940-951
Groves, D.I., Goldfarb, R.J., Gebre-Mariam, M., Hagemann, S.G., and Robert, F., 1998, Orogenic gold deposits: a proposed classification in the context of their crustal distribution and relationship to other gold deposit types: Ore geology reviews, 13(1-5), p. 7-27.

Guyana Geology and Mines Commission, 2018, The mining sector in Guyana 2018.
Guyana Office for Investment, 2019, Mining Sector.(http://goinvest.gov.gy/sectors/mining/)
Hammond, N.Q., and Tabata, H., 1997, Characteristics of ore minerals associated with gold at the Prestea mine, Ghana.
Heesterman, L.H., and Heesterman and Nadeau, 2010, S., 2010, Geological map of Guyana at a scale of 1:1,000,000.: Guyana, Geo-Services Department, Guyana Geology and Mines Commission p.1.
Holtrop, J.F., 1965, The manganese deposits of the Guiana Shield: Economic Geology, 60(6), p. 1185-1212.
Hook, A., 2019, Fluid formalities: Insights on small-scale gold mining dynamics, informal practices, and mining governance in Guyana: Resources Policy, 62, p. 324-338.
Huang, X.W., Boutroy, É., Makvandi, S., Beaudoin, G., Corriveau, L. and De Toni, A.F., 2018, Trace element composition of iron oxides from IOCG and IOA deposits: relationship to hydrothermal alteration and deposit subtypes: Mineralium Deposita, v. 54(4), p. 525-552.
Huang, X.W., Sappin, A.A., Boutroy, É., Beaudoin, G. and Makvandi, S., 2019, Trace Element Composition of Igneous and Hydrothermal Magnetite from Porphyry Deposits: Relationship to Deposit Subtypes and Magmatic Affinity: Economic Geology, v. 114(5), p.953-979. doi.org/10.5382/econgeo.4651.
Hu, H., Lentz, D., Li, J.W., McCarron, T., Zhao, X.F., and Hall, D., 2015, Reequilibration processes in magnetite from iron skarn deposits: Economic Geology, 110(1), p. 1-8.
Irvine, T.N., 1965, Chromian spinel as a petrogenetic indicator: Part 1. Theory: Canadian Journal of Earth Sciences, 2(6), p. 648-672.
Jébrak, M., and Doucet, P., 2002, Geology and gold–molybdenum porphyry mineralisation of the Archean Taschereau–Launay plutons, Abitibi, Quebec: Precambrian Research, 115(1-4), p. 329-348.
Jébrak, M., 2011, Archean gold porphyry deposits of the Abitibi greenstone belt. In Québec, Canada, SGA-11 th biennial meeting: Antofagasta, Chile.
Kesler, S.E., Chryssoulis, S.L., and Simon, G., 2002, Gold in porphyry copper deposits: its abundance and fate: Ore Geology Reviews, 21(1-2), p. 103-124.
Klein, E.L., Moura, C.A., and Pinheiro, B.L., 2005, Paleoproterozoic crustal evolution of the São Luís Craton, Brazil: evidence from zircon geochronology and Sm-Nd isotopes: Gondwana Research, 8(2), p. 177-186.
Klein, E.L., and Rosa-Costa, L.T.D., 2003, Geology of quartz-vein gold deposits in the Ipitinga Auriferous District, northern Brazil, southeastern Guiana Shield.
Kroonenberg, S.B., De Roever, E.W.F., Fraga, L.M., Reis, N.J., Faraco, T., Lafon, J.M., Cordani, U., and Wong, T.E., 2016, Paleoproterozoic evolution of the Guiana Shield in Suriname: A revised model: Netherlands Journal of Geosciences, 95(4), p. 491-522.
Lilova, K.I., Pearce, C.I., Gorski, C., Rosso, K.M., and Navrotsky, A., 2012, Thermodynamics of the magnetite-ulvöspinel (Fe3O4-Fe2TiO4) solid solution: American Mineralogist, 97(8-9), p. 1330-1338.
Lindsley, D.H., 1981, Some experiments pertaining to the magnetite–ulvöspinel miscibility gap: American Mineralogist, 66(7-8), p. 759-762.
Loberg, B.E., and Horndahl, A.K., 1983, Ferride geochemistry of Swedish Precambrian iron ores: Mineralium Deposita, 18(3), p. 487-504.
Lovering, T.G., and Hedal, A., 1987, Trace Elements in MagneticConcentrates from Stream

Sediments in Southwestern New Mexico- A Potential Tool for Reconnaissance Geochemical Exploration in Arid Lands: United States Geological Survey Bulletin 1566.
Makvandi, S., Ghasemzadeh-Barvarz, M., Beaudoin, G., Grunsky, E.C., McClenaghan, M.B., and Duchesne, C., 2016, Principal component analysis of magnetite composition from volcanogenic massive sulfide deposits: Case studies from the Izok Lake (Nunavut, Canada) and Halfmile Lake (New Brunswick, Canada) deposits: Ore Geology Reviews, 72, p. 60-85.
Markwitz, V., Hein, K.A., Jessell, M.W., and Miller, J., 2016, Metallogenic portfolio of the West Africa craton: Ore geology reviews, 78, p. 558-563.
Marshall, D., Nicol, C.A., Greene, R., Sawyer, R., Stansell, A., and Easterbrook, R., 2018, Precious Metal Enrichment at the Myra Falls VMS Deposit, British Columbia, Canada: Geosciences, 8(11), p. 422.
Mellini, M., Rumori, C., and Viti, C., 2005, Hydrothermally reset magmatic spinels in retrograde serpentinites: formation of "ferritchromit" rims and chlorite aureoles: Contributions to Mineralogy and Petrology, 149(3), p. 266-275.
Merlini, A., Grieco, G., and Diella, V., 2009, Ferritchromite and chromian-chlorite formation in mélange-hosted Kalkan chromitite (Southern Urals, Russia): American Mineralogist, 94(10), p.1459-1467.
Nadoll, P., Angerer, T., Mauk, J.L., French, D., and Walshe, J., 2014, The chemistry of hydrothermal magnetite: a review: Ore geology reviews, 61, p. 1-32.
Newberry, N.G., Peacor, D.R., Essene, E.J. et al., 1982, Contr. Mineral. and Petrol. 80: 334. https://doi.org/10.1007/BF00378006
Niroomand, S., Goldfarb, R.J., Moore, F., Mohajjel, M., and Marsh, E.E., 2011, The Kharapeh orogenic gold deposit: geological, structural, and geochemical controls on epizonal ore formation in West Azerbaijan Province, Northwestern Iran: Mineralium Deposita, 46(4), p. 409-428.
Pain, C.F., and Ollier, C.D., 1995, Regolith stratigraphy: principles and problems: AGSO Journal of Australian Geology and Geophysics, 16(3), p. 197-202.
Pedregosa, F., Varoquaux, G., Gramfort, A., Michel, V., Thirion, B., Grisel, O., Blondel, M., Prettenhofer, P., Weiss, R., Dubourg, V., and Vanderplas, J., 2011, Scikit-learn: Machine learning in Python: Journal of machine learning research, 12(Oct), p. 2825-2830.
Pisiak, L.K., Canil, D., Lacourse, T., Plouffe, A., and Ferbey, T., 2017, Magnetite as an indicator mineral in the exploration of porphyry deposits: a case study in till near the Mount Polley Cu-Au deposit, British Columbia, Canada: Economic Geology, 112(4), p. 919-940.
Razjigaeva, N.G., and Naumova, V.V., 1992, Trace element composition of detrital magnetite from coastal sediments of northwestern Japan Sea for provenance study: Journal of Sedimentary Research, 62(5), p. 802-809.
Renner, R., and Gibbs, A.K., 1987, Geochemistry and petrology of metavolcanic rocks of the early Proterozoic Mazaruni greenstone belt, northern Guyana: Geological Society, London, Special Publications, 33(1), p. 289-309.
Richards, J.P., 2013, Giant ore deposits formed by optimal alignments and combinations of geological processes: Nature geoscience, 6(11), p. 911.
Roeder, P.L., 1994, Chromite; from the fiery rain of chondrules to the Kilauea Iki lava lake: The Canadian Mineralogist, 32(4), p. 729-746.
Santos, J.O.S., Potter, P.E., Reis, N.J., Hartmann, L.A., Fletcher, I.R., and McNaughton, N.J., 2003, Age, source, and regional stratigraphy of the Roraima Supergroup and

Roraima-like outliers in northern South America based on U-Pb geochronology: Geological Society of America Bulletin, 115(3), p. 331-348.
Schulz, K.J., Chandler, V.W., Nicholson, S.W., Piatak, N., Seal, R.R., Woodruff, L.G., and Zientek, M.L., 2010, Magmatic sulfide-rich nickel-copper deposits related to picrite and (or) tholeiitic basalt dike-sill complexes: A preliminary deposit model: US Department of the Interior, US Geological Survey.
Shimazaki, H., 1998, On the occurrence of silician magnetites: Resource Geology, 48(1), p. 23-29.
Sidder, G.B., 1990, Geologic province map of the Venezuelan Guiana Shield (No. 90-73): US Dept. of the Interior, Geological Survey.
Singoyi, B., Danyushevsky, L., Davidson, G.J., Large, R., and Zaw, K., 2006, Determination of trace elements in magnetites from hydrothermal deposits using the LA ICP-MS technique: Oral and Poster Presentations from the SEG 2006 Conference Society of Economic Geologists, Keystone, USA, p. 367-368.
Sluzhenikin, S.F., and Mokhov, A.V., 2015, Gold and silver in PGE–Cu–Ni and PGE ores of the Noril'sk deposits: Russia. Mineralium Deposita, 50(4), p. 465-492.
Taylor, C.D., Zierenberg, R.A., Goldfarb, R.J., Kilburn, J.E., Seal II, R.R., and Kleinkopf, M.D., 1995, Volcanic-Associated massive sulfide deposits (MODELS 24a-b, 28a; Singer, 1986a, b; Cox, 1986).
Tedeschi, M., Hagemann, S.G., and Davis, J., 2018, The Karouni Gold Deposit, Guyana, South America: Part I. Stratigraphic Setting and Structural Controls on Mineralization: Economic Geology, 113(8), p. 1679-1704.
Tedeschi, M., Hagemann, S.G., Roberts, M.P., and Evans, N.J., 2018, The Karouni Gold Deposit, Guyana, South America: Part II. Hydrothermal Alteration and Mineralization: Economic Geology, 113(8), p. 1705-1732.
Tedeschi, M.T., Hagemann, S.G., Kemp, A.I.S., Kirkland, C.L., and Ireland, T.R., 2019, Geochronological constraints on the timing of magmatism, deformation and mineralization at the Karouni orogenic gold deposit: Guyana, South America: Precambrian Research, p.105329.
Thompson, P., 2012, Ore resource model of the Aricheng North Uranium Deposit: Unpublished B.Sc. Thesis, Turkeyen, Guyana, The University of Guyana, 106 p.
Vincent, E.A., Wright, J.B., Chevallier, R., and Mathieu, S., 1957, Heating experiments on some natural titaniferous magnetites: Mineralogical Magazine and Journal of the Mineralogical Society, 31(239), p. 624-655.
Von Gruenewaldt, G., Klemm, D.D., Henckel, J., and Dehm, R.M., 1985, Exsolution features in titanomagnetites from massive magnetite layers and their host rocks of the Upper Zone, Eastern Bushveld Complex: Economic Geology, 80(4), p. 1049-1061.
Voicu, G., Bardoux, M., Jebrak, M., and Crepeau, R., 1999, Structural, mineralogical and geochemical studies of the Paleoproterozoic Omai gold deposit, Guyana: Economic Geology, 94(8), p. 1277-1303.
Ward, L.A., Holwell, D.A., Barry, T.L., Blanks, D.E., and Graham, S.D., 2018, The use of magnetite as a geochemical indicator in the exploration for magmatic Ni-Cu-PGE sulfide deposits: A case study from Munali, Zambia: Journal of Geochemical Exploration, 188, p. 172-184.
Williams, P.J., Kendrick, M.A., and Xavier, R.P., 2010, Sources of ore fluid components in IOCG deposits: PGC Publishing

Chapter 5
Conclusions

This dissertation demonstrates the utility of using the geochemistry of apatite, magnetite, and Fe-Ti-Cr oxides as a tool for investigating geological processes, including the fluid histories in Kiruna-type iron oxide apatite (IOA) deposits. The second and third chapters of my dissertation build on the work of Knipping et al. (2015a) that focused on using the chemistry of magnetite to investigate ore forming processes at the Los Colorados IOA deposit. Those authors hypothesized that since the minerals in ore deposits have the ability to record their fluid histories, and those fluid histories can be ascertained by using new (e.g., combined stable Fe and O isotopes of magnetite) and existing geochemical tools (e.g., major, minor, and trace element geochemistry), investigations of magnetite geochemistry are ideal for elucidating ore formation processes. After compiling the geochemical data for magnetite in the deposit, the researchers developed a new genetic model to explain the formation of IOA deposits that explains the geochemical data, and remains consistent with the field observations.

Chapter 2 of this dissertation investigated the chemistry of apatite from the Los Colorados IOA deposit. Investigating the chemistry of apatite allows us to attain additional insights about the fluid history during ore genesis because apatite is a common gangue mineral found among the ore in these deposits. Additionally, investigating the chemistry of apatite from Los Colorados allows us to rigorously test the genetic model proposed by Knipping et al. (2015a) which was developed without considering the chemistry of apatite in the deposit. The analyses in *Chapter 2* indicate that individual apatite grains contain distinct domains that have statistically significant differences in

chemical compositions that cannot be explained by growth from a single fluid (La Cruz et al., 2019). These apatite grains are intergrown with magnetite grains that have cores enriched in Ti, V, Al, and Mn, and the concentrations of these elements decrease towards the rims of these grains (Knipping et al., 2015a, b). The geochemistry of apatite and magnetite from Los Colorados indicates growth of mineral cores from a silicate melt and growth of the rims from a magmatic-hydrothermal fluid; these observations are most consistent with the formation of the Los Colorados IOA deposit according to the magmatic/magmatic-hydrothermal flotation model of Knipping et al. (2015a). An important takeaway from the study of apatite in this chapter is the usefulness of imaging the grains with techniques such as cathodoluminescence (CL) imaging, backscattered electron (BSE) imaging, and energy dispersive X-ray spectroscopy (EDS) element mapping, prior to quantitative analyses. Backscattered electron imaging is commonly done during EPMA analyses, so compositional zonations in grains can usually be ascertained using this technique during quantitative analyses. The apatite grains investigated in this chapter are compositionally zoned, despite not being obviously zoned in BSE images. The chemical variability in the grains, therefore, would not have been observed if CL imaging and EDS element mapping were not utilized.

In *Chapter 3*, I investigate the chemistry of magnetite and apatite from multiple ore bodies at the El Laco IOA deposit. In addition to investigating magnetite from surface samples from 5 of the 7 ore bodies that constitute the ore deposit, I also studied drill core samples from 2 ore bodies in order to obtain a holistic understanding of the ore system at this deposit. Prior to this study, the bulk of the magnetite geochemical data for this deposit indicated that magnetite in the deposit has low Ti content (Nyström and Henríquez, 1994; Dare et al., 2015; Velasco, 2016; Broughm et al., 2017). However, investigations of magnetite from outcrop and drill core samples from multiple

ore bodies indicate that the range of Ti content is much larger than the range of 200 - 300 ppm, reported by the aforementioned authors. The study of Ovalle et al., (2018), in addition to the study in *Chapter 3* report Ti contents > 1 wt%, in addition to the presence of ilmenite exsolution lamellae in magnetite from the deepest samples at El Laco. The presence of ilmenite exsolution lamellae indicates that magnetite from the deep portions of the deposit grew from a silicate melt (Buddington and Lindsley, 1964; Ovalle et al., 2018). Additionally, the high Ti contents in the magnetite grains are consistent with growth of magnetite from magmatic/magmatic-hydrothermal fluids (Nadoll et al., 2014; Ovalle et al., 2018). Ovalle et al. (2018) concluded that the ore bodies at El Laco formed due to shallow emplacement and/or venting of magmatic/magmatic-hydrothermal fluid suspensions that contain igneous magnetite microlites, and the chemistry of magnetite and apatite reported in this study agree with this conclusion. The F, Cl, and calculated OH contents for apatite from the sampled ore bodies at El Laco overlap those for apatite from many other IOA deposits, and igneous rocks. However, apatite grains from the Rodados Negros ore body have increased Cl content, relative to that from the other ore bodies, and the other global IOA deposits. The increased Cl content of apatite from Rodados Negros is, however, lower than the high Cl contents reported for apatite from IOA deposits in the Chilean Iron Belt (CIB), i.e. Los Colorados, Carmen and Fresia (Treloar and Colley, 1996; La Cruz et al., 2019; Palma et al., 2019). The chemistry of magnetite in the deposits from the CIB is similar to that for magnetite from IOA deposits in many global districts, and is consistent with ore genesis in these deposits from fluids that are magmatic/magmatic-hydrothermal in nature. However, apatite in the deposits of the CIB are relatively more Cl-enriched compared to apatite in the other IOA deposits. More work needs to be done to explain the difference in apatite chemistry and to assess what this difference reveals about the IOA deposits in the CIB.

In *Chapter 4,* I demonstrate that detrital magnetite geochemistry is a useful tool for exploration in covered terrains, such as Guyana, located in the Guiana Shield. An important aspect of this research was the development of a discriminant model that assists in the identification of ore deposit sources of magnetite grains of unknown origin; in particular, the model focuses on deposit types which are common in greenstone belt environments, specifically orogenic gold and nickel copper platinum group element (Ni-Cu-PGE). The multivariate normal distribution model developed allows discrimination of magnetite from orogenic gold deposits, and it more successfully identifies magnetite from Ni-Cu-PGE, volcanogenic massive sulfide (VMS), iron - oxide copper gold (IOCG), and porphyry copper gold and porphyry copper molybdenum deposits than the discriminant diagrams that existed previously. Application of the model to data for detrital magnetite from stream catchments throughout the greenstone belts of Guyana indicate the potential presence of orogenic gold and/or Ni-Cu-PGE deposits in the sampled catchments. Sulfide grains present in detrital grains from the sampled catchments support the inferred ore deposit potential from the model. This work demonstrates that weathering and transport of magnetite grains by streams result in changes to the chemistry and textures of detrital grains. The data indicate that grains maintain their chemical and textural character when transported to distances <1.5 km from source outcrops, but that the concentrations of V and Al are preserved for transport up to 5 km. The current model uses 11 elements measured via electron-probe micro-analyses (EPMA) to identify magnetite from the 5 ore deposit types, but despite outperforming the existing discriminant models, the model can be improved by increasing the number of elements included in the model as indicated by recent studies (Makvandi et al., 2016; Pisiak et al., 2017; Dmitrijeva et al., 2018; Huang et al., 2019). To this end, I will incorporate trace element contents of magnetite into the model, reassess its accuracy and apply the model to recently collected trace element compositions

for magnetite from Guyana. The findings of *Chapter 4* are encouraging from an exploration perspective because it has demonstrated the potential presence of Ni-Cu-PGE mineralisation in the sampled catchments, while confirming the potential for the discovery of new orogenic gold deposits. During this study, I analysed the composition of ilmenite, which has been used in the exploration for diamonds (Mitchell, 1986; Haggerty, 1991a,b; Wyatt et al., 2004; Robles-Cruz et al., 2009; Castillo-Oliver et al., 2017). For instance, the Mg content of ilmenite has been shown to be an indicator of diamond-bearing kimberlite lavas (Mitchell, 1978). Alluvial diamonds are mined in Guyana, but no kimberlites have been discovered to date. Thus, assessing the geochemistry of ilmenite in the sampled and other catchments countrywide, may allow for the identification of catchments prospective for diamond exploration in Guyana. The detrital samples also contained zircon, monazite, and xenotime grains; these grains can also be utilized to gain insights about the geological processes that occurred in the sampled catchments. The use of the chemistry of detrital phases to identify regions for targeted exploration is advantageous since outcrops are scarce in this terrain.

The data presented in this dissertation demonstrate that the geochemistry of minerals can be utilized to improve our understanding of the processes that result in the formation of ore deposits, and as a tool for finding ore deposits in regions where exploration for ore deposits is challenging. This research aims at ensuring that our global society has access to the required metals and non-metals for its survival. As we work to make these resources available, we must ensure that they are harvested in a manner that is environmentally and socially responsible.

5.1 References

Broughm, S.G., Hanchar, J.M., Tornos, F., Westhues, A., and Attersley, S., 2017, Mineral chemistry of magnetite from magnetite-apatite mineralization and their host rocks: examples from Kiruna, Sweden, and El Laco, Chile: Mineralium Deposita, v. 52(8), p.1223-1244.

Buddington, A.F., and Lindsley, D.H., 1964, Iron-titanium oxide minerals and synthetic equivalents. Journal of petrology, v. *5*(2), p.310-357.

Castillo-Oliver, M., Melgarejo, J.C., Galí, S., Pervov, V., Gonçalves, A.O., Griffin, W.L., Pearson, N.J., and O'Reilly, S.Y., 2017, Use and misuse of Mg-and Mn-rich ilmenite in diamond exploration: a petrographic and trace element approach: Lithos, v. 292, p.348-363.

Dare, S.A., Barnes, S.J. and Beaudoin, G., 2015, Did the massive magnetite "lava flows" of El Laco (Chile) form by magmatic or hydrothermal processes? New constraints from magnetite composition by LA-ICP-MS: Mineralium Deposita, v. 50(5), p.607-617.

Dare, S.A., Barnes, S.J., Beaudoin, G., Méric, J., Boutroy, E., and Potvin-Doucet, C., 2014, Trace elements in magnetite as petrogenetic indicators., Mineralium Deposita, v. 49, p. 785–796.

Dmitrijeva, M., Metcalfe, A.V., Ciobanu, C.L., Cook, N.J., Frenzel, M., Keyser, W.M., Johnson, G., and Ehrig, K., 2018, Discrimination and variance structure of trace element signatures in Fe-Oxides: A Case Study of BIF-Mineralisation from the Middleback Ranges, South Australia: Mathematical Geosciences, v. 50(4), p. 381-415.

Haggerty, S.E., 1991a, Oxide mineralogy of the upper mantle. Oxide Minerals. Mineralogical Society of America Reviews in Mineralogy, v. 25, p. 355–416.

Haggerty, S.E., 1991b. Oxide textures; a mini-atlas. Reviews in Mineralogy and Geochemistry v. 25, 129–219.

Huang, X.W., Boutroy, É., Makvandi, S., Beaudoin, G., Corriveau, L., and De Toni, A.F., 2019, Trace element composition of iron oxides from IOCG and IOA deposits: relationship to hydrothermal alteration and deposit subtypes: Mineralium Deposita, v. 54(4), p. 525-552.

Knipping, J.L, Bilenker, L.D, Simon, A.C., Reich, M., Barra, F., Deditius, A.P., Lundstrom, C., Bindeman, I., and Munizaga, R., 2015a, Giant Kiruna-type deposits form by efficient flotation of magmatic magnetite suspensions: Geology, v. 43, p. 591–594.

Knipping, J.L., Bilenker, L.D., Simon, A.C., Reich, M., Barra, F., Deditius, A.P., Wälle, M., Heinrich, C.A., Holtz, F., and Munizaga, R., 2015b, Trace elements in magnetite from massive iron oxide-apatite deposits indicate a combined formation by igneous and magmatic-hydrothermal processes: Geochimica et Cosmochimica Acta, v. 171, p. 15–38.

La Cruz, N.L., Simon, A.C., Wolf, A.S., Reich, M., Barra, F., and Gagnon, J.E., 2019, The geochemistry of apatite from the Los Colorados iron oxide–apatite deposit, Chile: implications for ore genesis: Mineralium Deposita, p. 1-14. doi.org/10.1007/s00126-019-00861-z.

Makvandi, S., Ghasemzadeh-Barvarz, M., Beaudoin, G., Grunsky, E.C., McClenaghan, M.B., and Duchesne, C., 2016, Principal component analysis of magnetite composition from volcanogenic massive sulfide deposits: Case studies from the Izok Lake (Nunavut, Canada) and Halfmile Lake (New Brunswick, Canada) deposits: Ore Geology Reviews, v. 72, p. 60-85.

Mitchell, R.H., 1978, Manganoan magnesian ilmenite and titanian clinohumite from the Jacupiranga carbonatite, Sao Paulo, Brazil: American Mineralogist, v. 63(5-6), p.544-547.

Mitchell, R.H., 1986, Kimberlites mineralogy, geochemistry and petrology.

Nadoll, P., Angerer, T., Mauk, J., French, D., and Walshe, J., 2014, The chemistry of hydrothermal magnetite: a review. Ore Geology Reviews, v. 61, p. 1-32.

Nyström, J.O. and Henríquez, F., 1994, Magmatic features of iron ores of the Kiruna type in Chile and Sweden: ore textures and magnetite geochemistry: Economic Geology, v.89, p. 820–839.

Ovalle, J.T., La Cruz, N.L., Reich, M., Barra, F., Simon, A.C., Konecke, B.A., Rodriguez-Mustafa, M.A., Deditius, A.P., Childress, T.M., and Morata, D., 2018, Formation of massive iron deposits linked to explosive volcanic eruptions: Scientific reports, v. 8(1), p.14855.

Palma, G., Barr, F., Reich, M., Valencia, V., Simon, A.C., Vervoort, J., Leisen, M., and Romero, R., 2019, Halogens (F, Cl, OH), trace element contents, and Sr-Nd isotopes in apatite from iron oxide-apatite (IOA) deposits in the Chilean iron belt: evidence for magmatic and hydrothermal stages of mineralization: Geochimica et Cosmochimica Acta, v. 246, p. 515–540.

Pisiak, L.K., Canil, D., Lacourse, T., Plouffe, A., and Ferbey, T., 2017, Magnetite as an indicator mineral in the exploration of porphyry deposits: a case study in till near the Mount Polley Cu-Au deposit, British Columbia, Canada: Economic Geology, 112(4), p. 919-940.

Robles-Cruz, S.E., Watangua, M., Isidoro, L., Melgarejo, J.C., Galí, S., and Olimpio, A., 2009, Contrasting compositions and textures of ilmenite in the Catoca kimberlite, Angola, and implications in exploration for diamond: Lithos, v. 112, p.966-975.

Treloar, P.J. and Colley, H., 1996, Variations in F and Cl contents in apatites from magnetite—apatite ores in northern chile, and their ore-genetic implications: Mineralogical Magazine, v. 60(399), p.285-301.

Wyatt, B.A., Baumgartner, M., Anckar, E., and Grutter, H., 2004, Compositional classification of "kimberlitic" and "non-kimberlitic" ilmenite: Lithos, v. 77(1-4), p.819-840.

Velasco, F., Tornos, F., Hanchar, J.M., 2016, Immiscible iron-and silica-rich melts and magnetite geochemistry at the El Laco volcano (northern Chile): Evidence for a magmatic origin for the magnetite deposits: Ore Geology Reviews, v. 79, p. 346-366.

Appendices

Appendix 2.1 Detailed Explanation of Data Analysis Methodology

Python programming language scripts used in the image and statistical analyses of apatite grains from the Los Colorados IOA deposit can be accessed from the Los Colorados IOA apatite repository on github.com. (user name: nlacruz).

Data Analysis Methods

We quantitatively assessed the observed spatial variability of F and Cl concentrations within individual apatite grains by using customized analysis scripts written in the Python programming language. We applied a Gaussian smoothing filter to the chemical (EDS) maps for P Kα and Cl Kα to improve signal- to-noise and reveal the local spatially-averaged composition of each grain. Individual grain boundaries were then identified automatically using the smoothed EDS P Kα maps, which provide masks that clearly distinguish apatite grains from other phases in the grain mounts and thin sections (Fig. 2.A11). The frequency distribution of Cl within each apatite grain was analyzed using histograms of the smoothed Cl maps, which revealed the presence of distinct Cl-rich and Cl-poor domains within each grain. The smoothed Cl maps were then used to assign each EPMA and LA-ICP-MS analytical spot to one of three possible grain regions: core, rim, or intermediate boundary zone. This assignment was- based upon the smoothed Cl intensity value at each analytical spot location, reflecting how the local Cl value compared to the histogram-derived ranges for the Cl-poor, Cl-rich, and intermediate Cl populations. Elemental concentrations of apatite cores and rims were analyzed by using sample means, standard deviations, and elemental correlations. We found that the data for apatite from both drill core samples are statistically indistinguishable for all analyzed elements; hence, we combined them for subsequent statistical analyses to avoid misinterpretations arising from small sample size.

Next, we conducted statistical tests to investigate the chemical variability within the apatite grains. For these analyses, we used the data for the Cl-rich (rim) and Cl-poor (core) populationsof the apatite grains from the pit sample and from the combined drill core dataset. First, we investigated the behavior of F and Cl in the Cl-rich and Cl-poor populations of apatite from the pit and drill core. The concentrations of F and Cl were visualized and found to covary, thus we determined the best-fit linear trends. Visual analysis showed that there were abundant outliers that might affect the best fit line in the drill core dataset; thus, robust linear estimators were necessary to assess the correlated behavior of F and Cl in the Cl-rich and Cl-poor regions of the grains.

To investigate the statistical significance of the linear relationship between F and Cl in the cores and rims of the apatite grains, we performed a bootstrap Monte Carlo simulation to assess the uncertainties on the robust slope estimate, which properly downweighs the effect of outliers. The simulation (using 3000 Monte Carlo draws) produced uncertainty estimates for each region in the apatite grains. These results are summarized in histograms, shown in Fig. 2.A6, which estimate the probability distribution for the true slope of the data. To assess the significance of the fitted negative correlation, we evaluate the probability that the true slope is actually zero or positive based on the proportion of simulations that return a non- negative fitted value. A probability value ≤ 0.05 suggests that the robust slope has a value that is significantly different than zero, i.e., the slope is likely negative. A probability value ≥ 0.05 suggests that the robust slope has a value that is not significantly different than zero, i.e., the slope is positive.

Systematic differences between the behavior of minor and trace elements in core and rim regions, as well as between the pit and drill core samples, were observed in the data. To assess the significance of these observations, we performed statistical tests to determine whether there are statistically significant differences between the minor (Na, S, Si) and trace element concentrations

(Sr, Mn, As, La, Ce, Nd, Dy, Yb, Lu, Y, Ti, V) in the Cl-rich and Cl-poor regions of the apatite grains from the pit and drill core. The t-test was used to assess differences in the mean values, while the Levene test was used to assess differences in the spread (or standard deviation) of the concentration data. Since robust estimators were required for the statistical assessment of the major elements, we also used them in the statistical assessment of the minor and trace elements. Unlike the major elements, the use of robust versus non-robust estimators did not change the results obtained for the minor and trace elements, indicating that they were less affected by outliers as compared to F and Cl.

Appendix 3.1 Detailed Explanation of the LA-ICP-MS Analytical Protocol

Details of LA-ICP-MS Analyses

Magnetite

The spot analyses were performed by using a beam diameter of 40 μm, a repetition rate of 5 Hz, and energy density of 4 J/cm^2. Each individual analysis consisted of first measuring the gas background for 20 s followed by ablation of magnetite for 60 s (300 pulses) and subsequent measuring of the gas background for at least 20 s between analyses. Different dwell times were used to optimize the analyses. For instance, 40 ms were for Cu and Cr, 30 ms were used for Mn, Ti, Ni, Pb, Ge and Mo, 20 ms were used for Ga, Zn and Sn, and 10 ms were used for all the other elements. The concentrations of most elements measured in the secondary reference glasses, when treated as unknowns, agree within analytical error to the concentrations reported by Jochum et al. (2005, 2011).

Apatite

A beam energy of ~8 J/cm^2, a repetition rate of 10 Hz and a beam diameter of 30 μm were used during the analyses. Each spot analysis consisted of first measuring the gas background for 20 s, followed by ablation of apatite for 60 s (600 pulses) and measuring of the gas background for at least 20 s between analyses. A dwell time of 10 ms was used for all elements except As for which we used dwell times of 30 ms. The concentrations of all elements measured in the Durango apatite, when treated as an unknown, agree within analytical error to the concentrations reported by Chew et al. (2016).

Appendix 4.1 Additional Explanation of the New Predictive Model

Explanation of Model

An underlying premise of the model is that the concentrations of various elements in magnetite can provide insights about the geological processes and environments in which magnetite crystallized. The elements that substitute into magnetite reflect conditions such as temperature, fluid composition, oxygen and sulfur fugacity, and silicate and sulfide activity in the environments in which magnetite formed (Nadoll et al., 2014). Thus by combining the concentrations of various elements — like Ti and Ni which have differential characteristics in magmatic and hydrothermal fluids that give rise to the formation of ore deposits — in magnetite, we are able to identify magnetite sourced from different ore deposit types. This model was developed as a way to improve our ability to identify magnetite from different ore deposit environments based on chemical composition. We found that the existing discriminant diagrams of Dupuis and Beaudoin (2011), Nadoll et al. (2014), and Ward et al. (2018), who used a few elements (<6) to identify magnetite from different ore deposit environments, do not sufficiently identify magnetite from different ore deposit environments. To this end, we developed a model that considers the concentrations of 11 elements measured via EPMA to assess whether we can improve the ability to identify magnetite from different ore deposit environments by increasing the chemical dimensions considered. Another fundamental difference with previous methods is that we consider the correlations amongst all 11 elements. In contrast, discriminant diagram methods consider only a few elements at a time, thereby projecting down into a much lower dimensional space and losing most of the information about the complex correlated compositional properties of magnetites, resulting from their formation histories. We found that by considering the concentrations of these 11 elements in magnetite, we are able to more satisfactorily identify

magnetite from different ore deposit environments. Despite our significant improvements over existing methods, there are still overlaps in the chemistry of magnetite from these 5 ore deposit types for the elements considered. By increasing the number of elements modeled, we will likely be able to reduce these chemical overlaps and better identify magnetite from different deposit types.

In the first part of the model, the geochemical data of magnetite from unknown sources are compared to the multivariate normal distributions of magnetite from the 5 ore deposit types. This model is applied to a single analysis independently. The result of the multivariate normal model is a probability score for each analysis that represents the likely ore deposit source for that analysis. Application of the model to data for magnetite from individual ore deposit types indicate that the compositional ranges for magnetite from each deposit type overlap each other, thereby hindering precise identification. The overlaps, however, generate characteristic signatures for magnetite from each deposit type in the chemical space considered. This chemical signature, obtained by applying the model to data from the global database, reflects how frequently our multivariate normal model identifies individual analyses as belonging to each of the considered deposit types. Even when the identification of an individual analysis is incorrect, the combined results for a collection of analyses of magnetite from a particular ore deposit type is diagnostic of the chemistry of magnetite from that individual ore deposit types. This information can, therefore, be leveraged to improve the model's ability to infer the ore deposit sources of a collection of magnetite analyses.

For instance, the chemical signature for a collection of magnetite analyses from the streams/catchments in Guyana represents the combined signatures for magnetite from different sources; thus, the chemical signature is the weighted sum of the chemical signatures of magnetite from individual deposit sources in that catchment. If we assume that magnetite in the catchment is

sourced from the 5 modeled ore deposit types, then we can compare the combined catchment signature with the characteristic signature for each modeled ore deposit type and determine the proportions of the characteristic signatures from each ore deposit that constitutes the catchment signature. This is accomplished using a non-negative least squares (NNLS) regression model. The NNLS model was chosen because it allows us to determine the contributions of individual deposit type signatures to the mixed stream signature with the constraint that the proportion of each deposit type is non-negative, since it represents the fractional contribution of magnetite grains, making negative numbers unphysical.

We can better understand the chemical signature of each deposit type with a concrete example. When the multivariate normal model is applied to individual analyses of magnetite from Ni-Cu-PGE deposits, for instance, 59% of the data are correctly identified as being from this deposit type, and the remaining 41% are misidentified as belonging to other ore deposit types with a particular characteristic distribution due to geochemical overlap. The NNLS model then compares with combined signature for a collection of magnetite grains to the characteristic signature for each deposit type. We can analyze the accuracy of this process by considering, for instance, the collection of all magnetite grains from Ni-Cu-PGE deposits, to see how much our identification rate has improved. Using the NNLS model, we find that 94% of the analyses in the global dataset are correctly identified as being sourced from Ni-Cu-PGE deposits. Given this huge increase in modeling accuracy, we can therefore confidently apply this two-stage model to samples of unknown origin, like those collected in this study from stream catchments in Guyana.

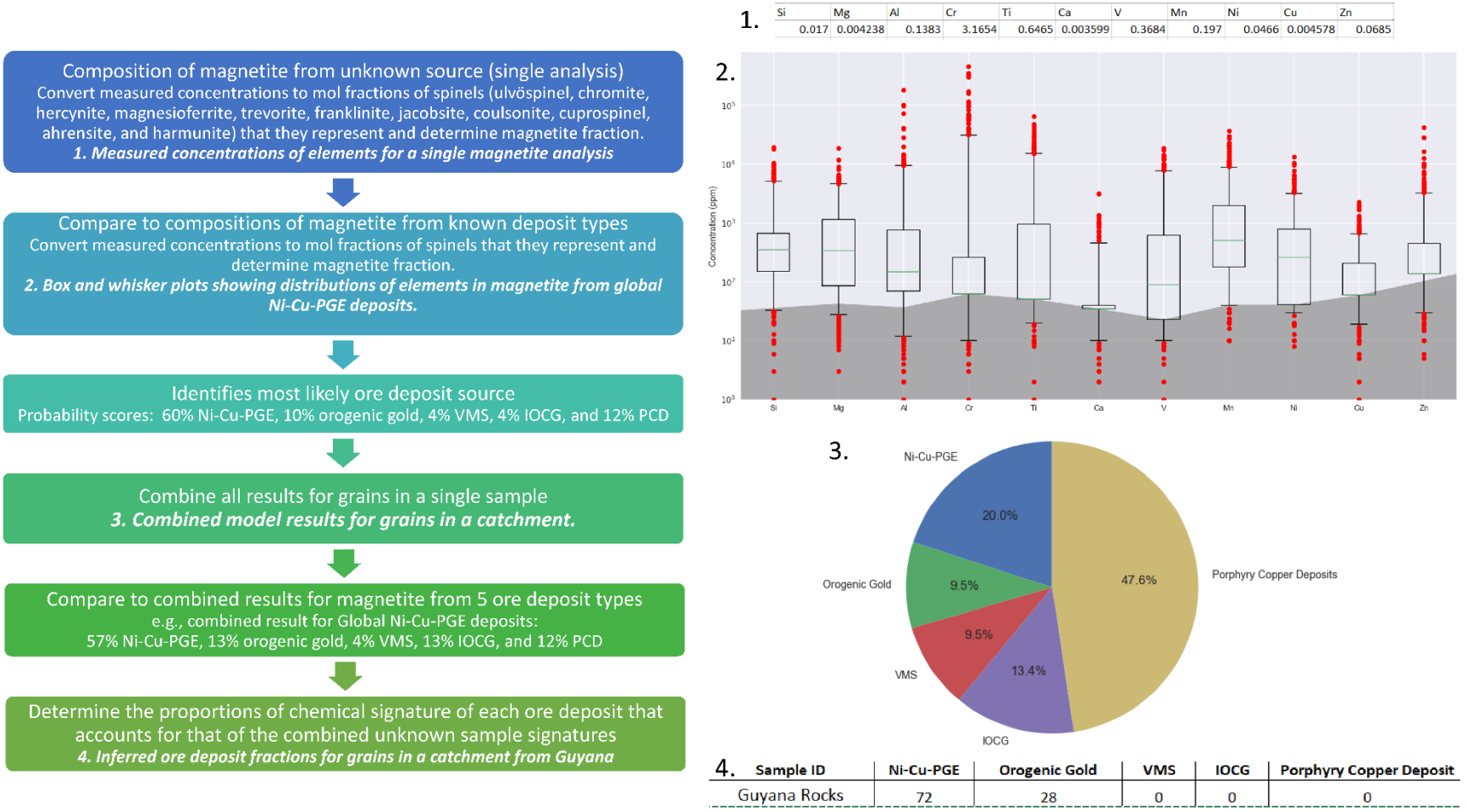

Flowchart and figures illustrating how the newly developed predictive model magnetite geochemistry works.

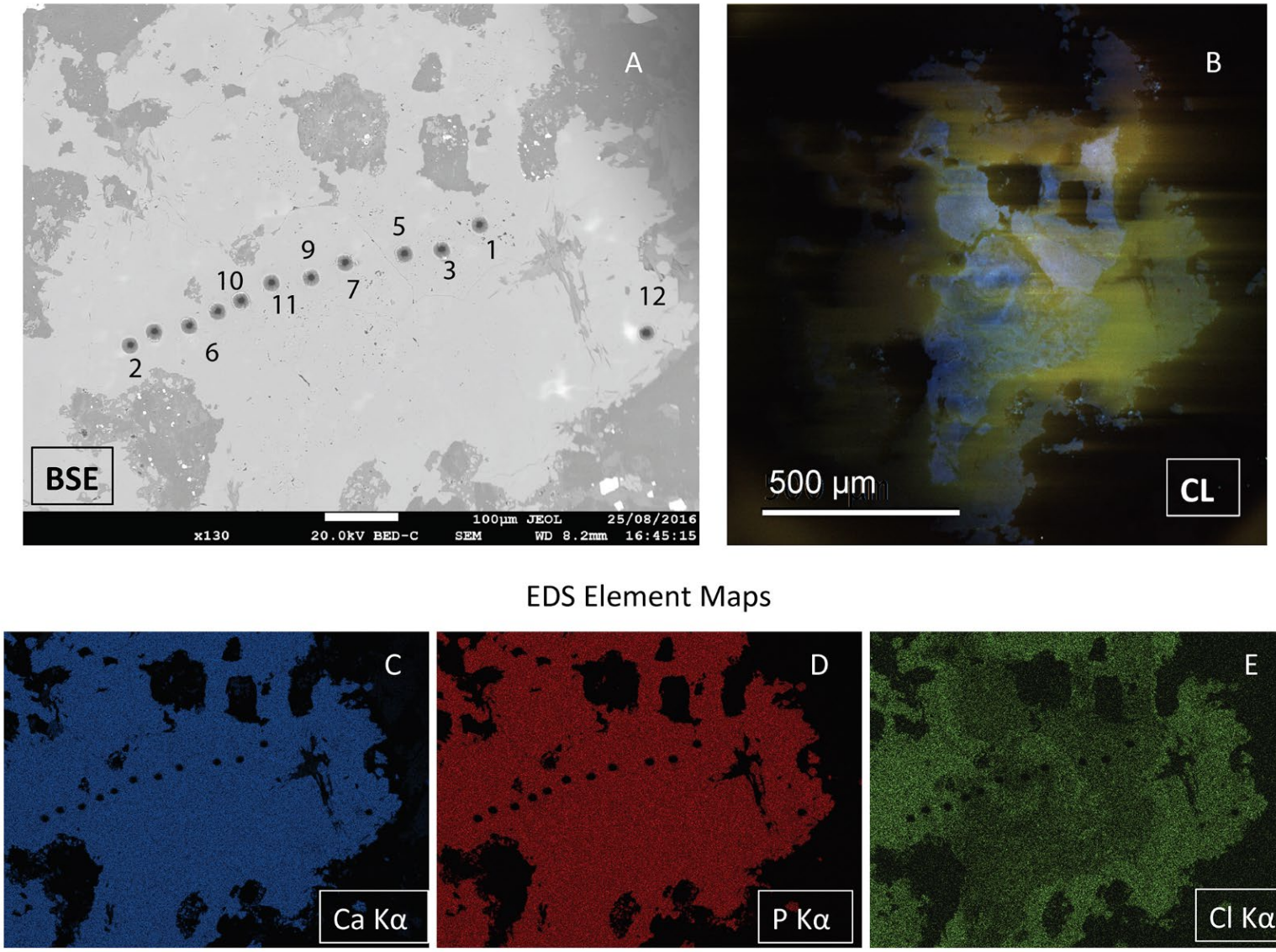

Figure 2.A1. Apatite grain maps as in Figure 2.2 for a representative sample from the pit. Similar to Figure 2.2, in this grain areas of bright luminescence correspond to the areas of low Cl concentration

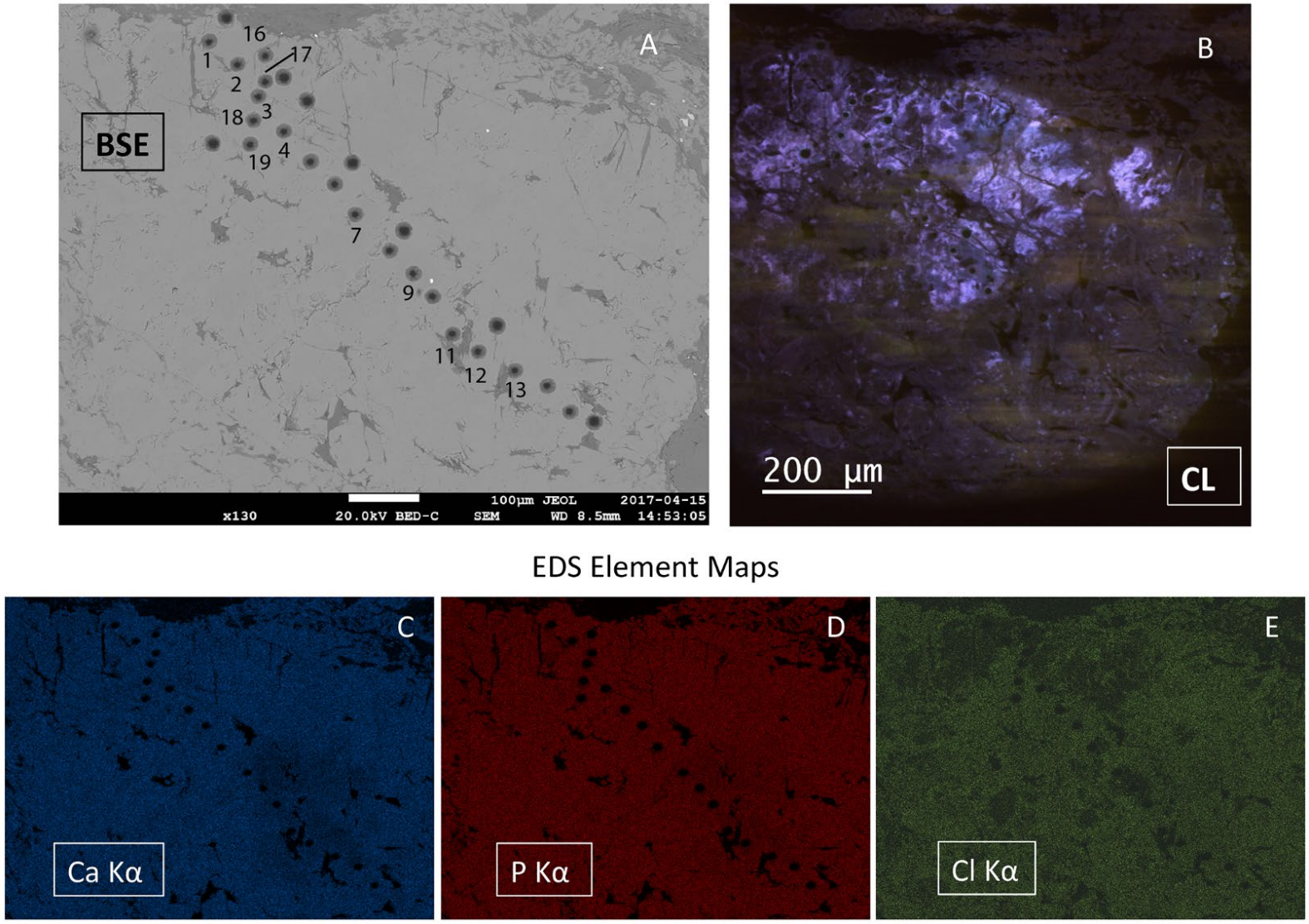

Figure 2.A2. Apatite grain maps as in Figure 2.2 for a representative sample from the drill core LC-04 in a massive magnetite dike (sample 04-99.5B in Knipping et al., 2015a, b). In this grain, areas of bright luminescence correspond to the areas of high Cl concentration.

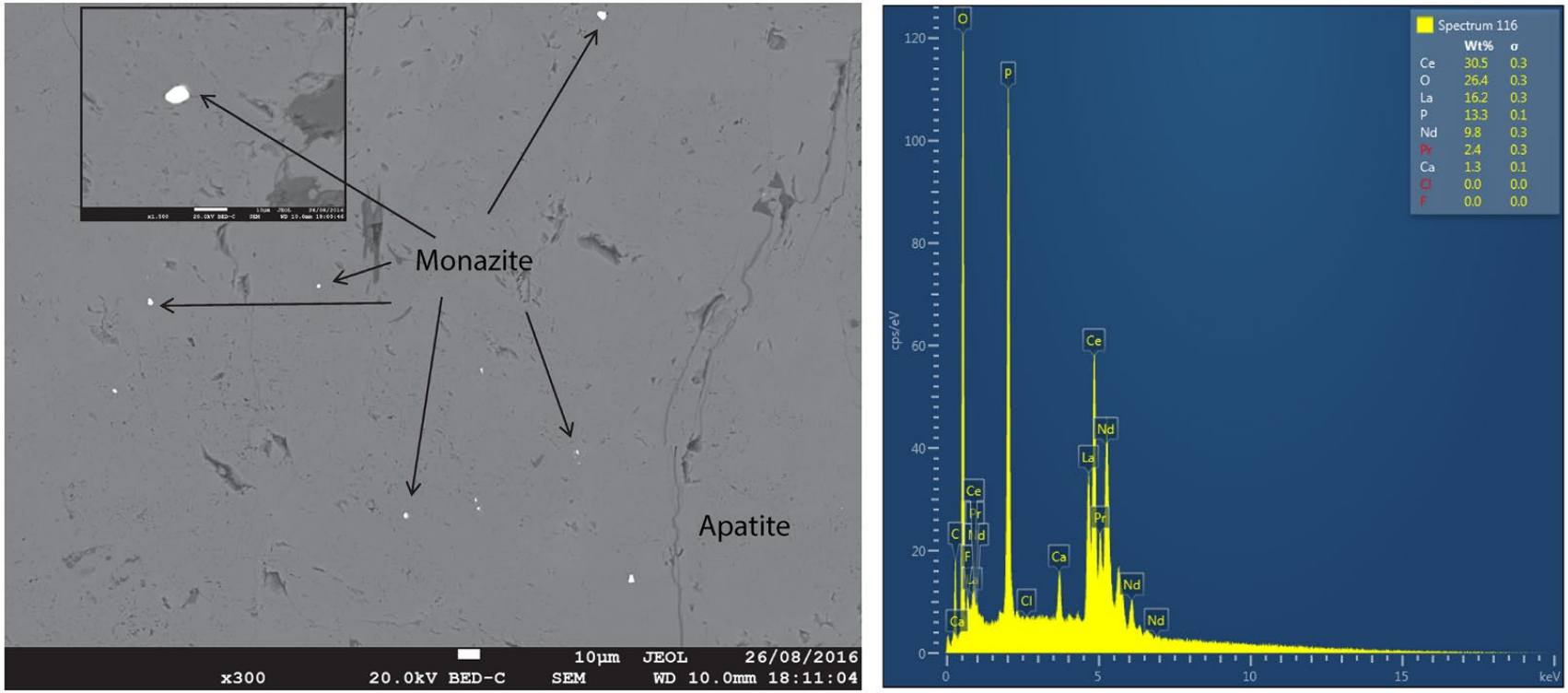

Figure 2.A3. (A) BSE image showing the distribution of monazite grains within apatite from Los Colorados. (B) Representative EDS spectrum for $REEPO_4$ inclusions in apatite grains from drill core samples at Los Colorados.

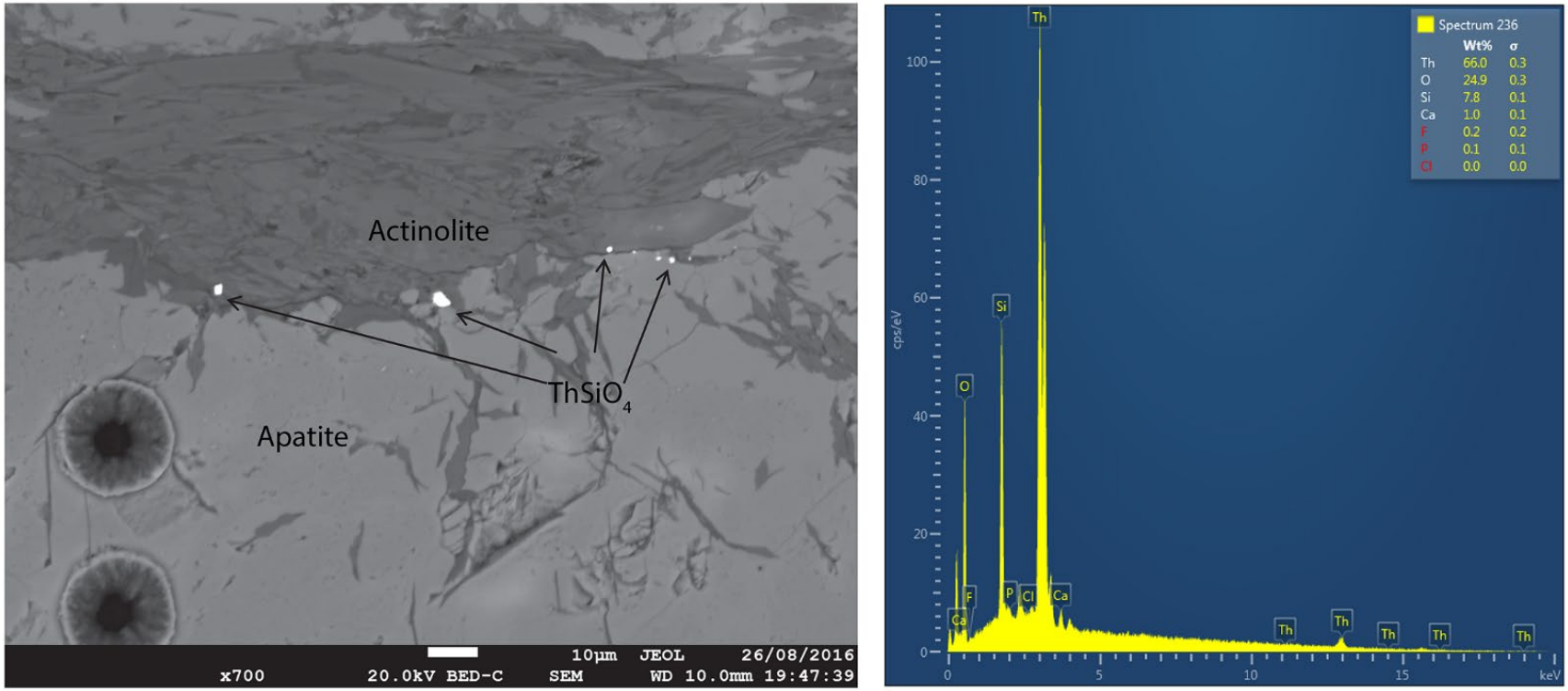

Figure 2.A4. (A) Distribution of thorite grains at the interface between apatite and actinolite. (B) Representative EDS spectrum for $ThSiO_4$ inclusions in apatite grains from the pit and drill core samples at Los Colorados.

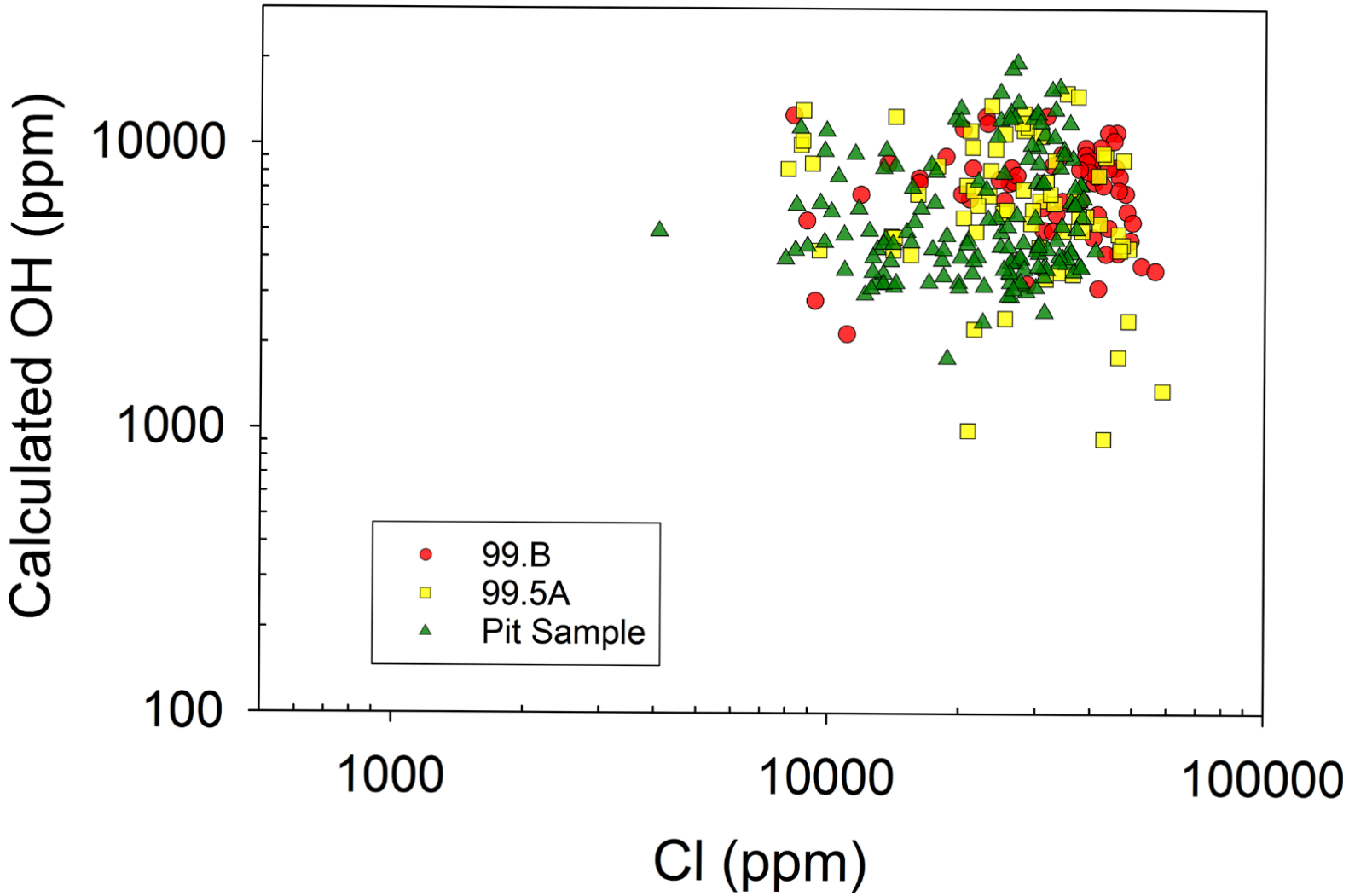

Figure 2.A5. Calculated OH concentration versus Cl concentration among all apatite grains from Los Colorados. Each sample is denoted by the same color and shape, and each point corresponds to an individual spot analysis. It is difficult to discern the relationship between calculated OH and Cl in the apatite grains.

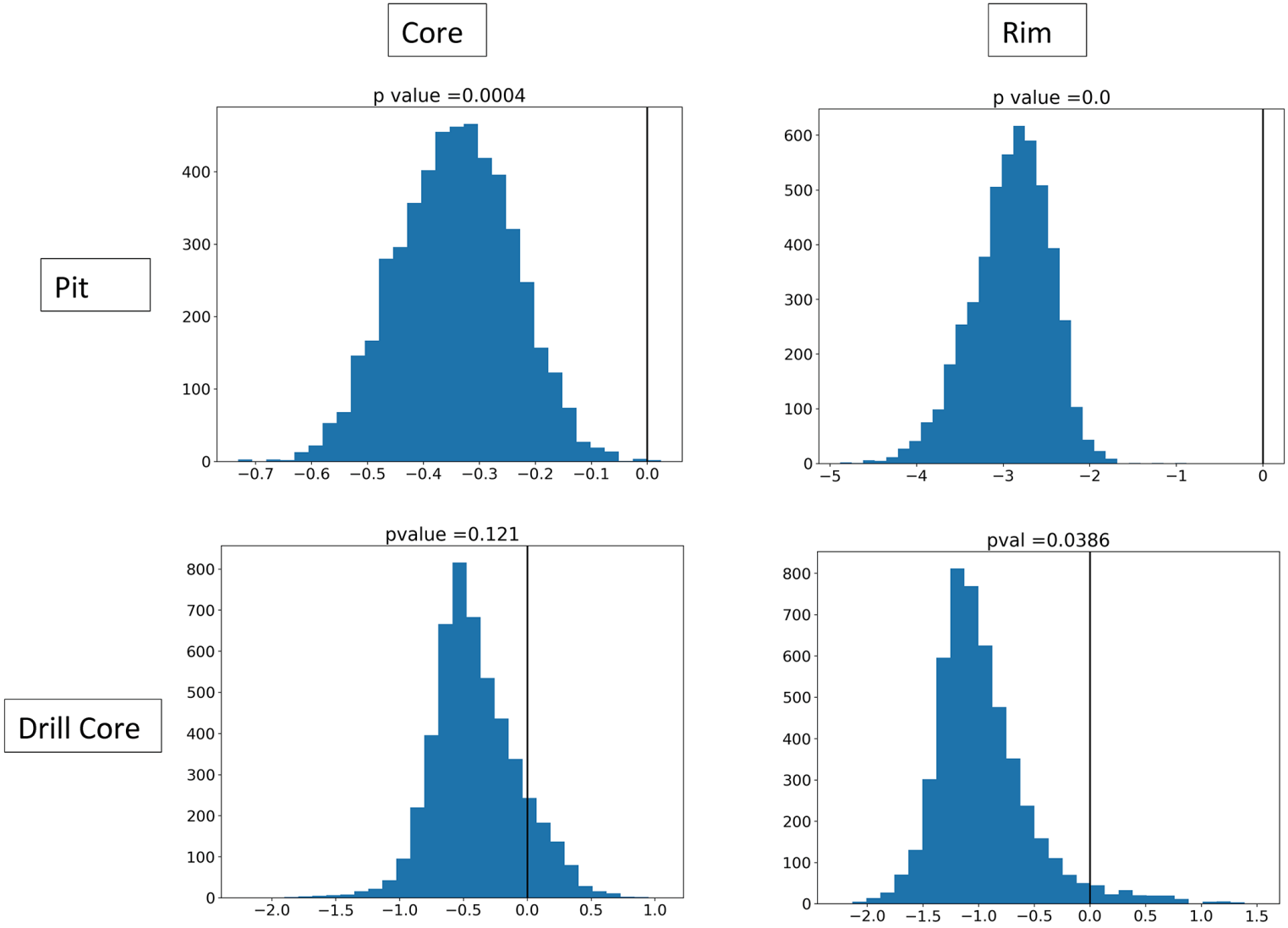

Figure 2. A6. Histograms summarizing the distribution of the slopes of best fit lines for the cores and rims of apatite grains from the pit and drill core samples during the bootstrap Monte Carlo simulation. The p values indicate the proportion of slopes (out of 3000 Monte Carlo draws) that had a positive value.

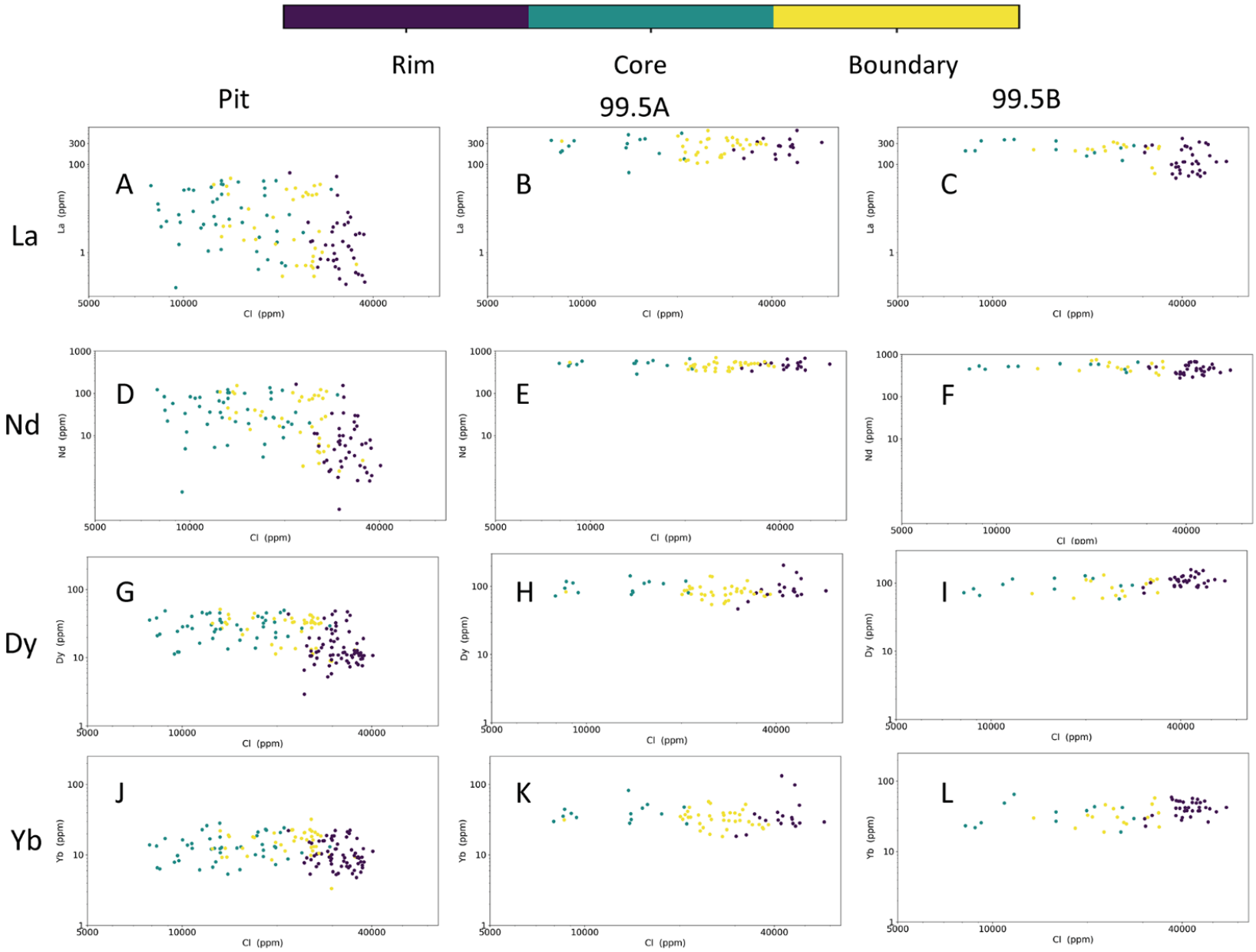
Rim
Core
Boundary
Pit
99.5A
99.5B
La
Nd
Dy
Yb
A
B
C
D
E
F
G
H
I
J
K
L
La (ppm)
Nd (ppm)
Dy (ppm)
Yb (ppm)
Cl (ppm)
5000
10000
40000
1
10
100
300
1000

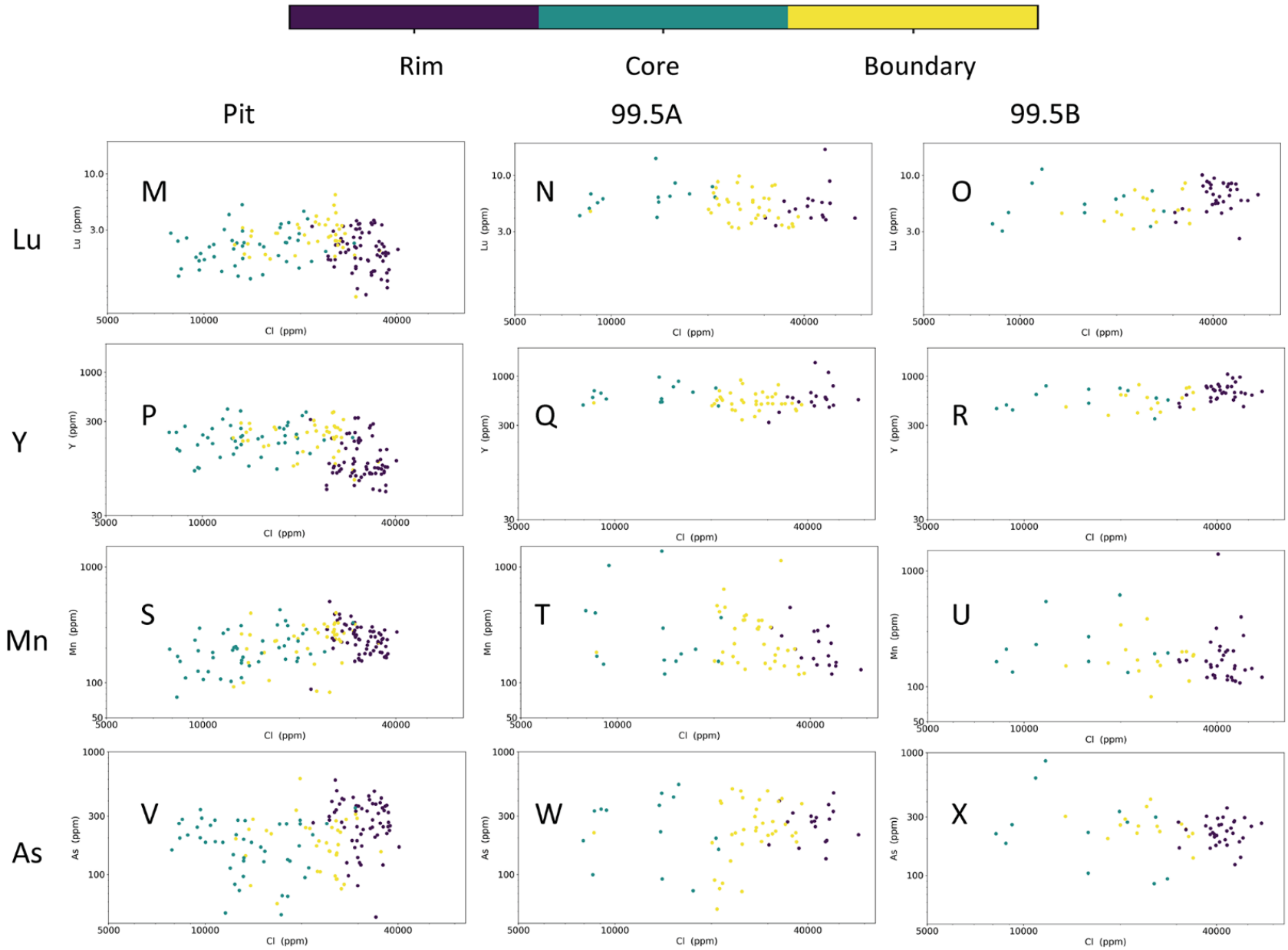
Rim
Core
Boundary
Pit
99.5A
99.5B
Lu
Y
Mn
As
M
N
O
P
Q
R
S
T
U
V
W
X
Cl (ppm)
Lu (ppm)
Y (ppm)
Mn (ppm)
As (ppm)

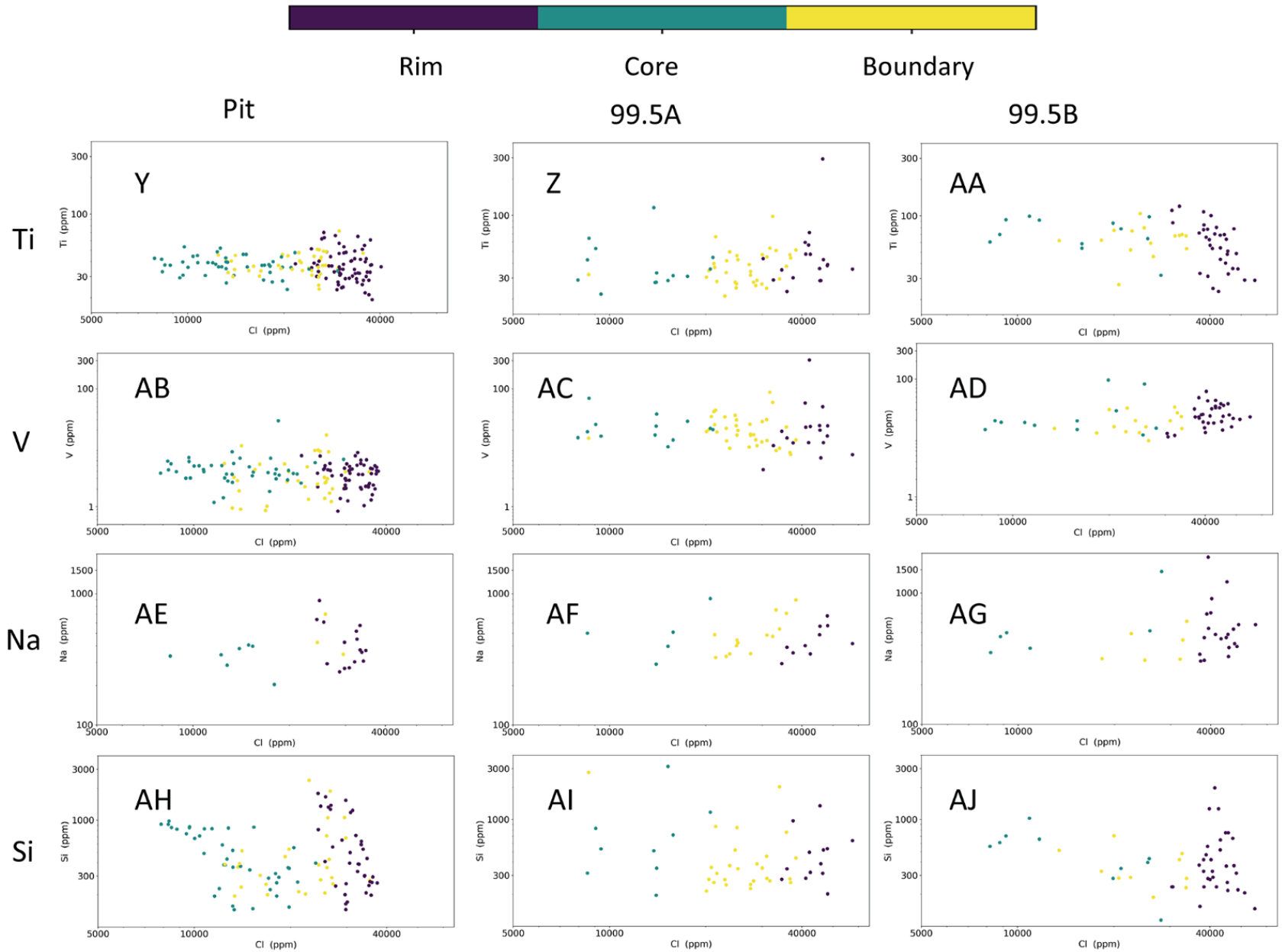
Rim
Core
Boundary
Pit
99.5A
99.5B
Ti
V
Na
Si
Y
Z
AA
AB
AC
AD
AE
AF
AG
AH
AI
AJ
Ti (ppm)
V (ppm)
Na (ppm)
Si (ppm)
Cl (ppm)

Rim Core Boundary

Pit 99.5A 99.5B

S

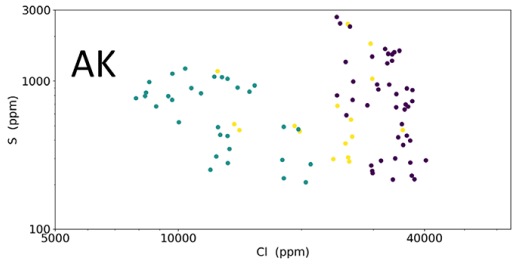

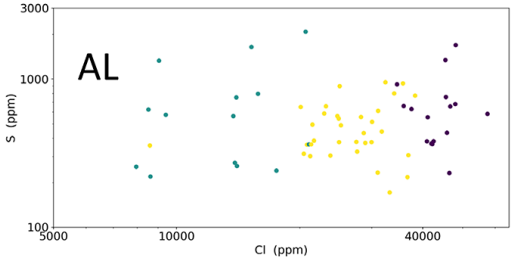

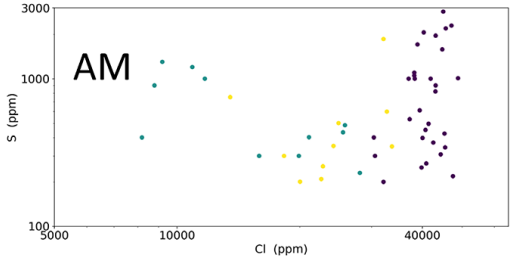

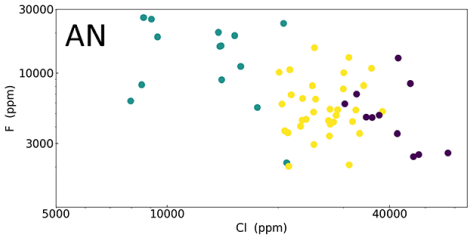

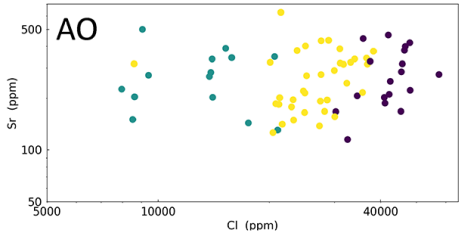

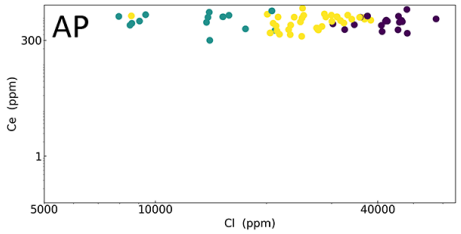

Figure 2.A7. The concentrations of minor and trace elements versus the concentration of Cl. Each spot represents an individual EPMA and LA-ICP-MS analysis and the color of the spot indicates whether it was located in the core (teal), rim (plum) or boundary zone (yellow). The labels above the columns indicate if the data are for the pit or drill core A or B sample, while the label on the left side of each row indicates the element plotted on the y-axis of the plots in that row.

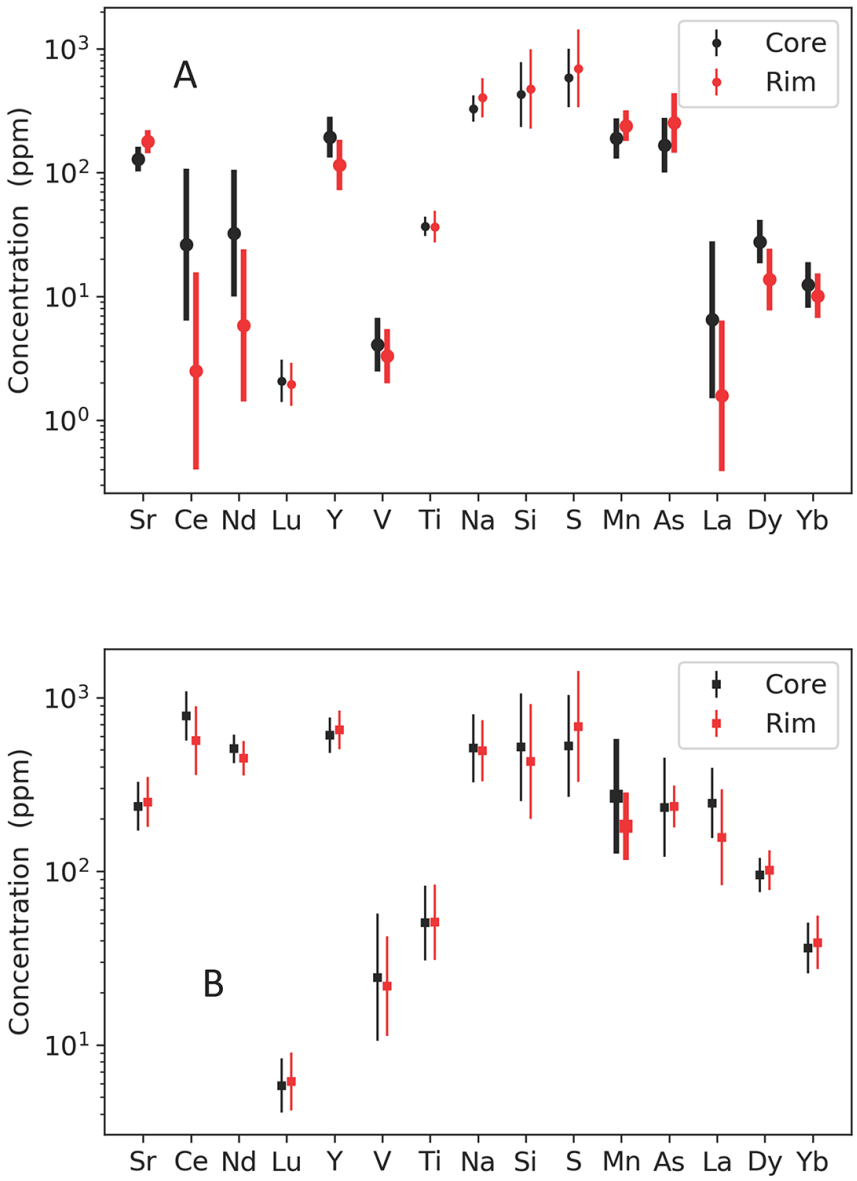

Figure 2.A8. Comparison of mean concentrations of minor and trace elements in the cores (black) and rims (red) of apatite grains from pit (A) and drill core (B) samples. Symbols with error bars represent the mean and 1σ standard deviations in measured concentrations. Elements with statistically distinct ($p<0.05$) elemental concentrations in cores and rims are shown in bold. The cores and rims of apatite from the pit sample generally show numerous distinct elemental distributions (Sr, Ce, Nd, Y, V, Mn, La, Dy, Yb and As), while the cores and rims of apatite from the drill core samples are statistically indistinguishable for all elements, except Mn.

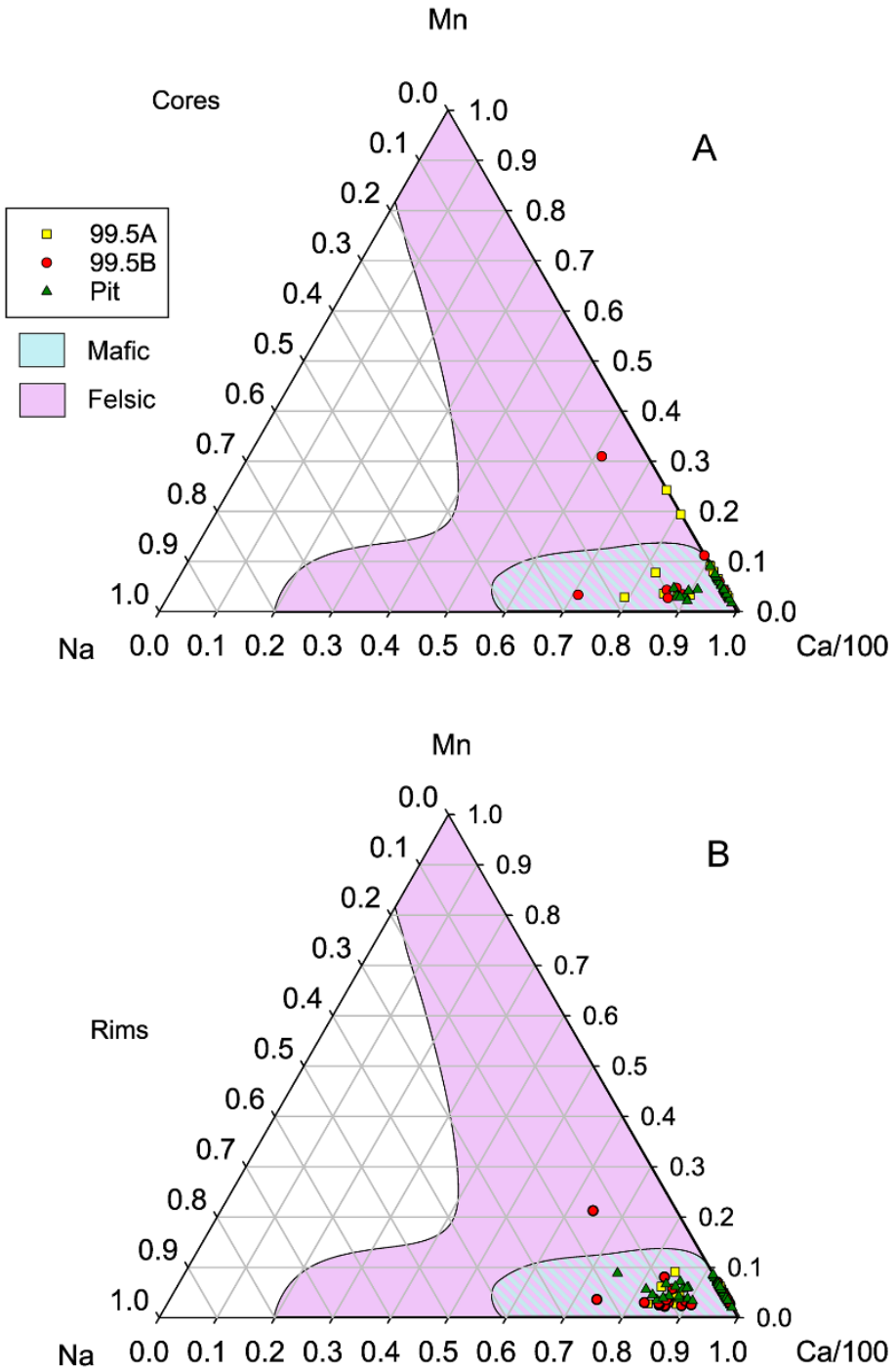

Figure 2.A9. The concentrations of Mn, Na, and Ca in apatite cores (A) and rims (B) from Los Colorados plotted along with the fields that represent the compositions of apatite from mafic rocks (cyan) and felsic rocks (pink), associated and not associated with ore deposits, from the global compilation of Piccoli and Candela (2002). The symbols for apatite grains from the different samples at Los Colorados are the same as in previous figures (red circle: drill core 99.5B; yellow squares: drill core 99.5A; green triangles: pit sample). The concentrations of these elements in the cores and rims of apatite from Los Colorados overlap those for apatite from mafic and felsic rocks. Note that the mafic field from Piccoli and Candela (2002) plots within the felsic field.

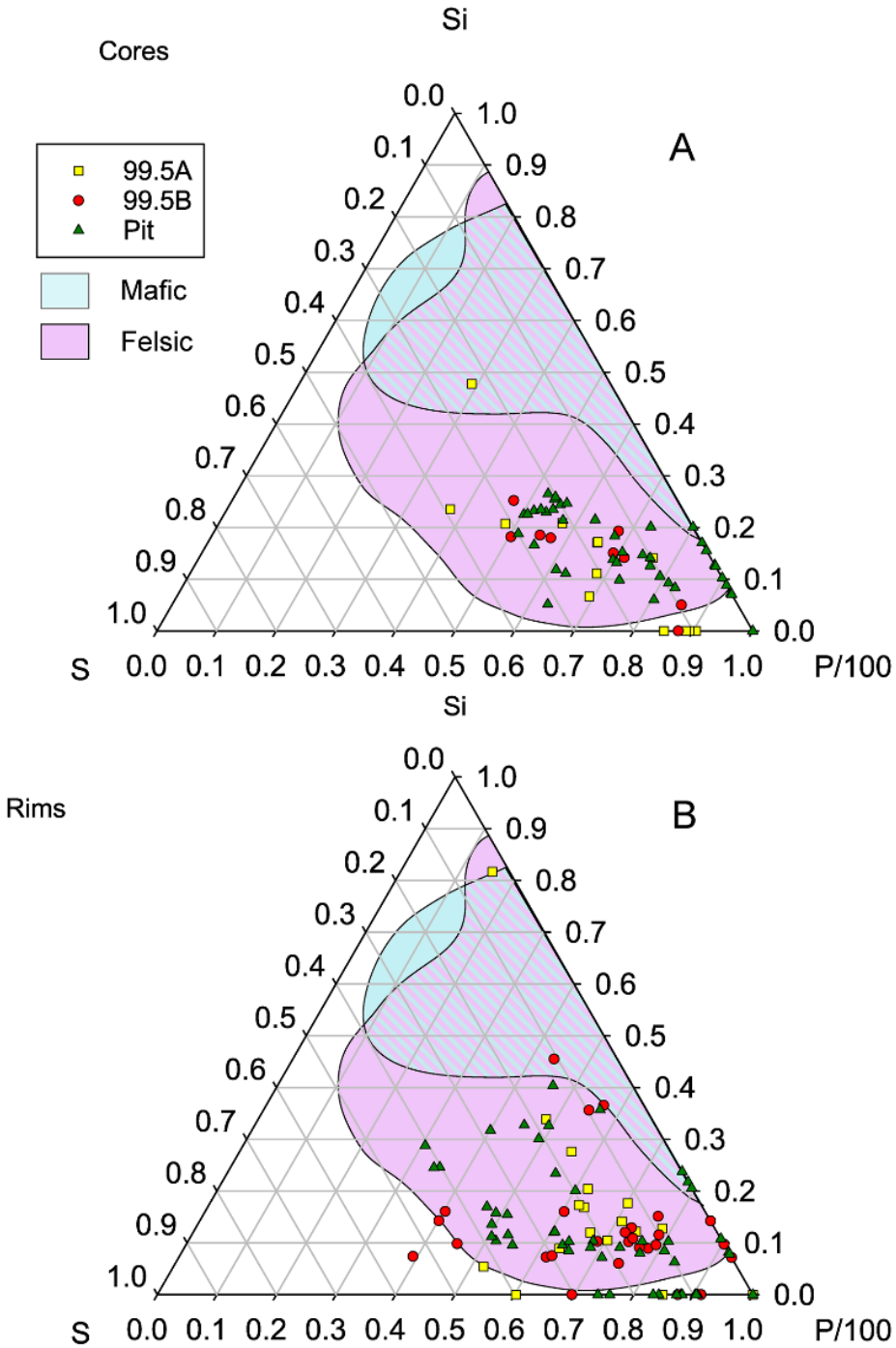

Figure 2.A10. The concentrations of Si, S, and P in apatite cores (A) and rims (B) from Los Colorados plotted along with fields that represent the compositions of apatite from mafic rocks and felsic rocks, associated and not associated with ore deposits, from the global compilation of Piccoli and Candela (2002). The colors representing the fields and symbols for apatite grains from the different localities are the same as Figure 15. Most of the data for both the cores and rims of apatite from Los Colorados overlap those for apatite from felsic rocks, while a small subset of the data overlap those for mafic rocks. Note that the mafic field from Piccoli and Candela (2002) plots within the felsic field.

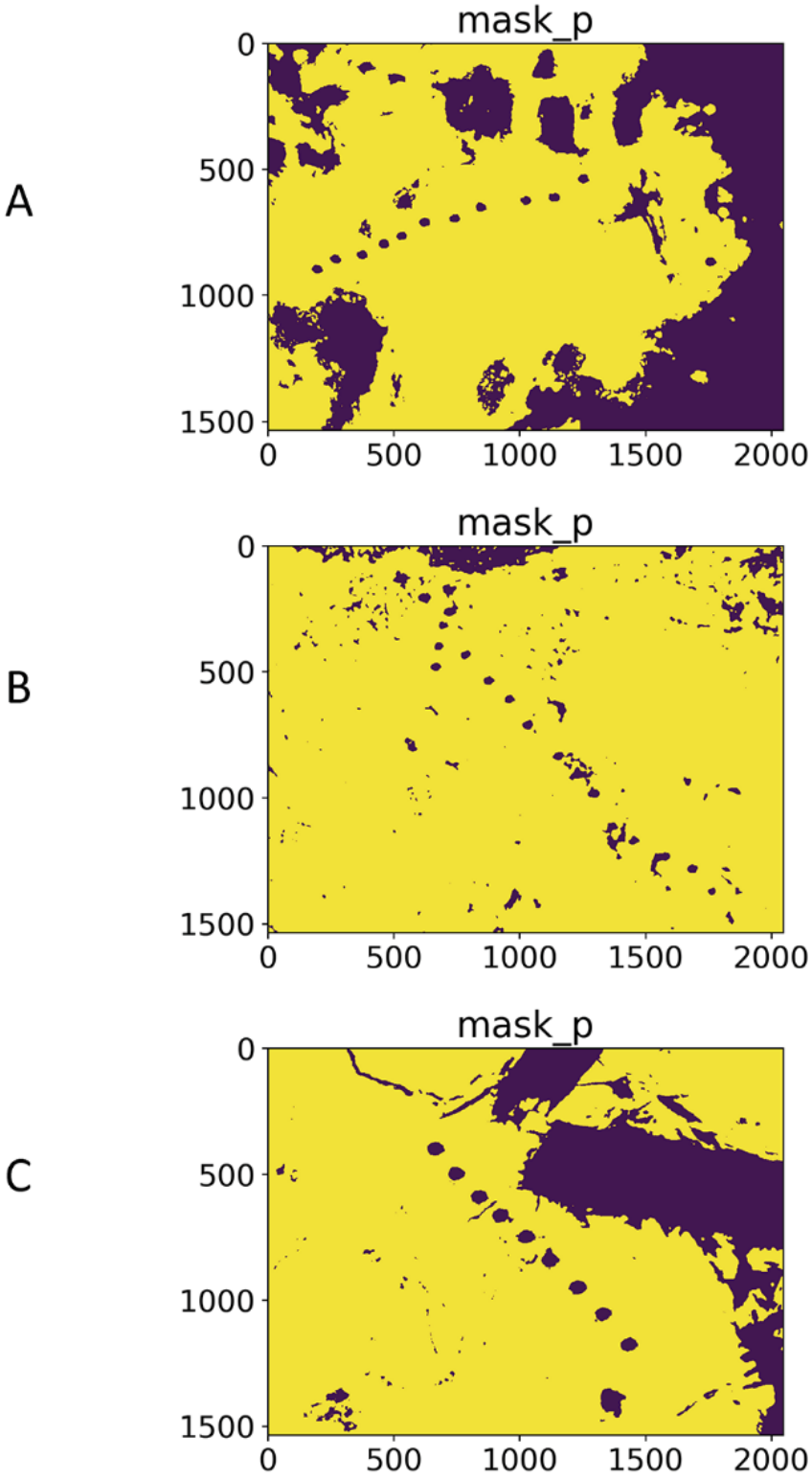

Figure 2.A11. Smoothed (pixel averaged) EDS P Kα maps for representative apatite grains from the pit (A), drill core A (B) and drill core B (C) samples. These masks were used to differentiate between apatite and other phases prior to the assessment of the distribution of Cl intensity in the apatite grains.

Table 2A.1. EPMA Conditions. (*APS-21 and APS-26 are synthetic apatite characterized and described by Schettler et al., 2011)

Element/ X-ray line	Crystal	Standard	Counting Time (s)
Ca Kα	PET	*APS – 26	20
P Kα	LPET	APS – 26	20
Cl Kα	LPET	APS – 26	20
F Kα	PC1	*APS – 21	20
Na Kα	LTAP	Jadeite	30
S Kα	LTAP	Anhydrite	30
Mg Kα	LTAP	Diopside	30
Al Kα	LTAP	Sillimanite	30

Table 2.A2. EPMA and LA-ICP-MS composition data for all 43 apatite grains analyzed from the pit and drill core samples at the Los Colorados IOA deposit.

Google drive folder link for Table 2.A2:

https://drive.google.com/open?id=1-YLev-FFwUBIyAiFdNpBSOQrrGkMCmsZ

Table 2A.3. p values obtained from the Levene test for the variance/ spread of the concentration data for elements in the cores and rims of apatite grains from the pit and drill core samples at Los Colorados.

Element	p value	
	Pit	Drill core
Sr	0.541	0.453
Mn	0.057	0.053
As	0.898	0.003
Na	0.195	0.933
Si	0.222	0.746
S	0.164	0.501
V	0.350	0.989
Ti	0.001	0.508
Y	0.237	0.873
La	0.578	0.495
Ce	0.048	0.313
Nd	0.263	0.044
Dy	0.143	0.632
Yb	0.961	0.802
Lu	0.712	0.640

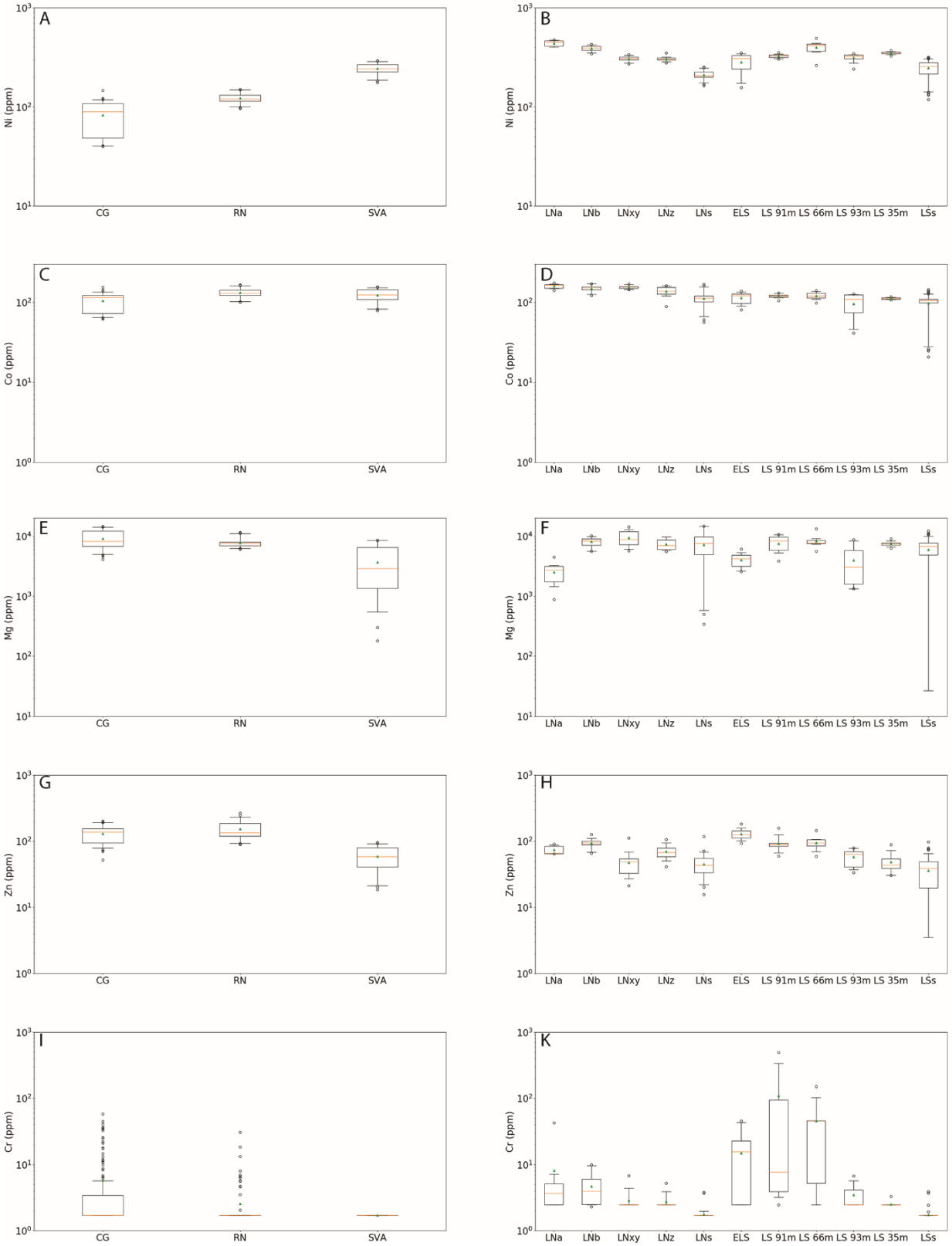

Figure 3.A1. Box and whisker plots displaying the range of concentrations of Ni, Co, Mg, Zn, and Cr in magnetite from surface outcrops (A, C, E, G, I) and drill core (B, D, F, H, J) at the El Laco deposit. The orange line in the boxes represents the median concentration and the green triangles

represent the mean values. The upper and lower margins of the box identify the upper and lower fifty percent of the data, while the whiskers show the range of concentrations for ninety-five percent of the data.

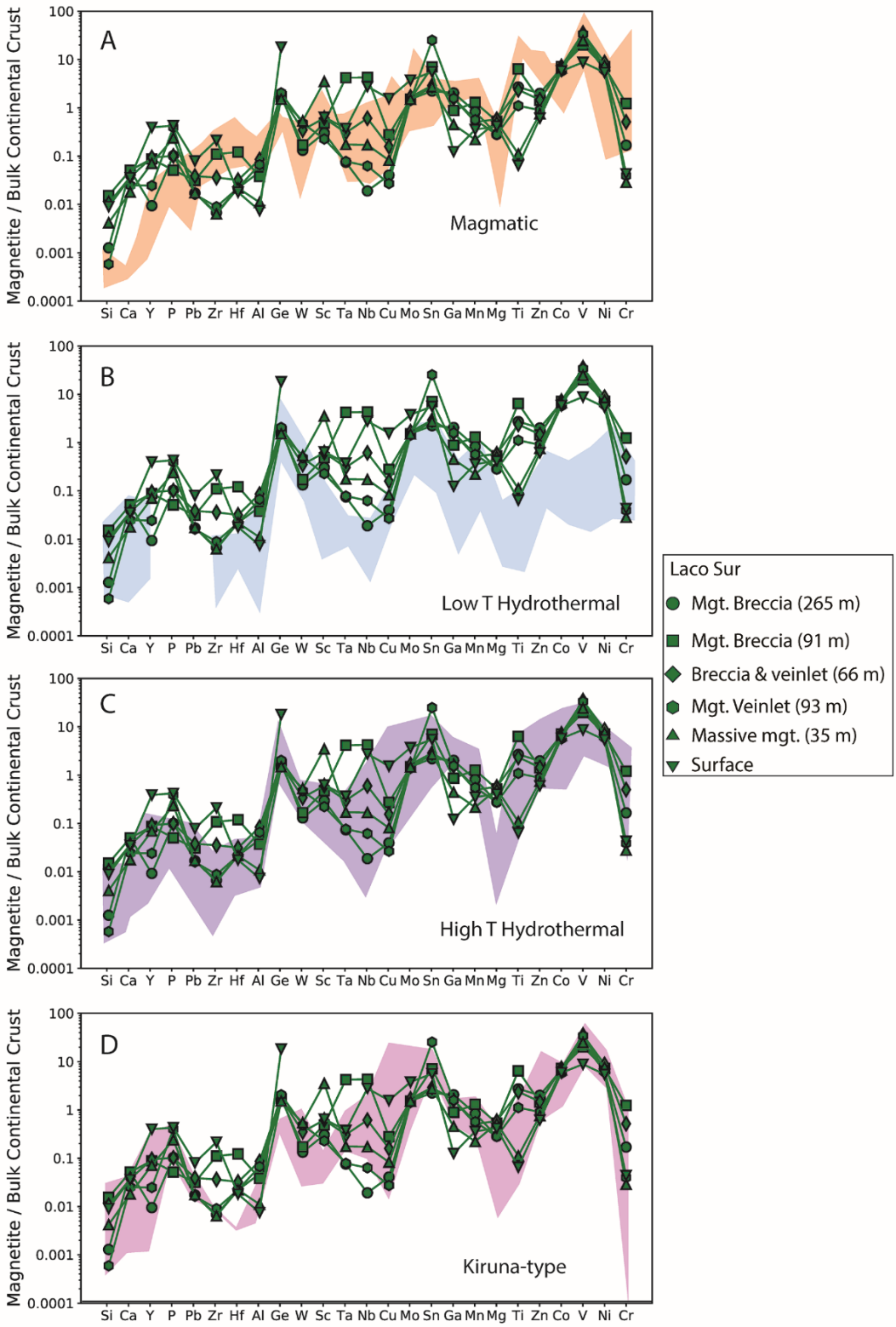

Figure 3.A2. The average bulk continental crust normalized compositions of magnetite samples from magnetite breccias at deep (265 m) and intermediate (91 m, 66 m) depths, magnetite veinlets at intermediate (93 m, 61 m) depths, and massive magnetite from shallow (35 m) depths of the drill core and surface outcrops at Laco Sur compared to the same fields as shown in Figs. 4 and 5.

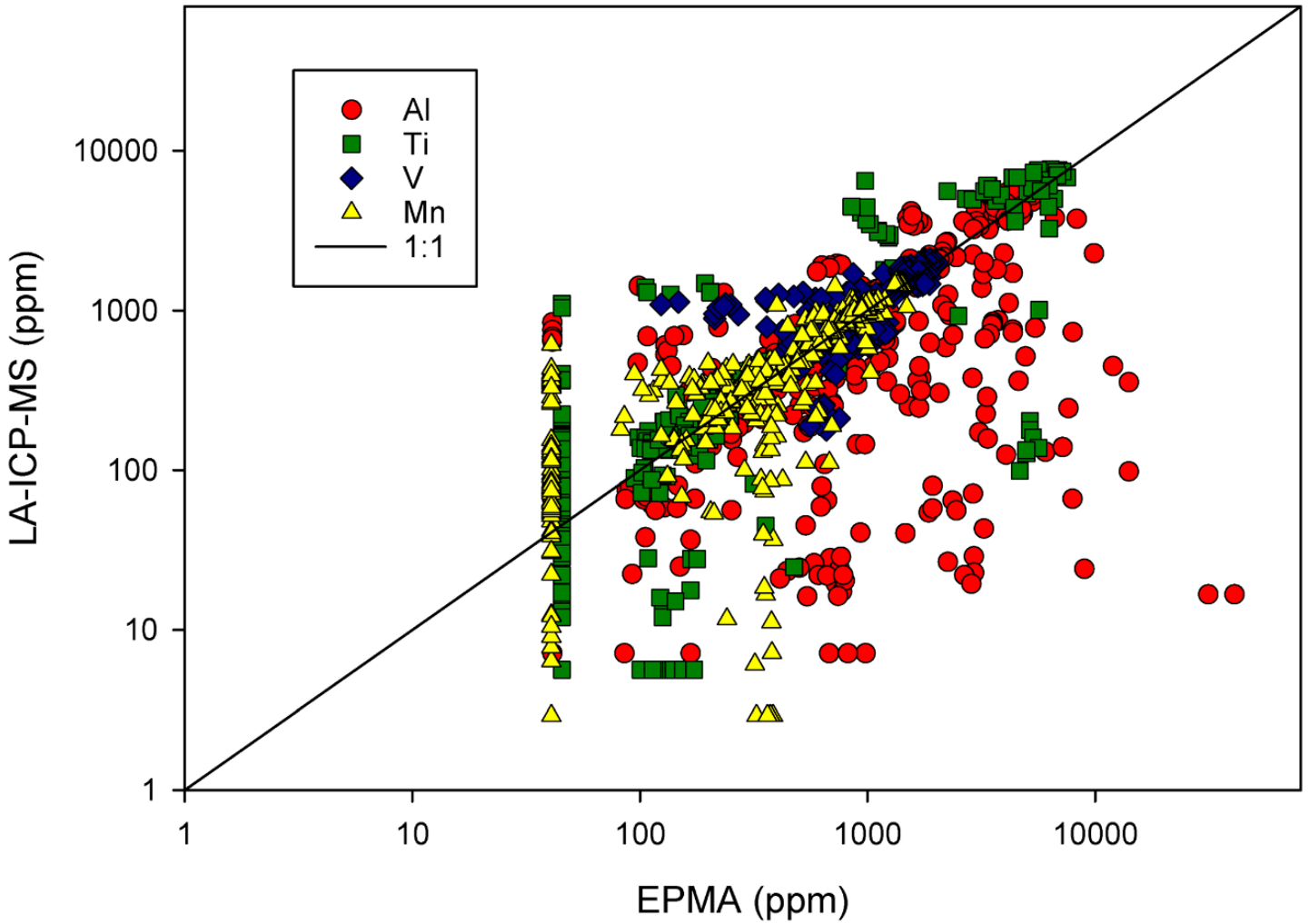

Figure 3.A3. Comparison of the Ti, V, Mn, and Al contents measured via LA-ICP-MS and EPMA. While there is some variability between the measurements, the plot indicates good agreement between measurements via the two methods.

Table 3.A1. EPMA Conditions for magnetite.

Element/ X-ray line	Crystal	Standard	Counting Time (s)
Fe Kα	LLIF	USMN Magnetite	20
Ti Kα	PET	USMN Ilmenite	120
Cr Kα	LLIF	Cr_2O_3	100
V Kα	LLIF	V_2O_5	120
Ca Kα	PET	Wollastonite	100
P Kα	LTAP	BaCl	100
Mn Kα	LPET	Rhodonite (BHRH)	100
Si Kα	LTAP	Wollastonite	100
Mg Kα	TAP	Geikielite (GEIK)	100
Al Kα	TAP	Jadeite	100

Table 3.A2. EPMA Conditions for apatite.

Element/ X-ray line	Crystal	Standard	Counting Time (s)
F Kα	PC1	MgF_2	20
Cl Kα	LPET	BaCl	20
Ca Kα	PET	APS 21	20
P Kα	LPET	APS 21	20
S Kα	LPET	Anhydrite	30
Fe Kα	LLIF	FESI	30
Na Kα	LTAP	Jadeite	30
Si Kα	LTAP	FOBO	30
Mg Kα	LTAP	PX69	30
Al Kα	LTAP	Sillimanite	30

Table 3.A3. EPMA and LA-ICP-MS compositional data for magnetite and apatite from the ore bodies at the El Laco IOA deposit.

Google drive folder link for Table 3.A3:

https://drive.google.com/open?id=1fa4BxH87dfdUSj7nZ41ZQJi9QHusj0tU

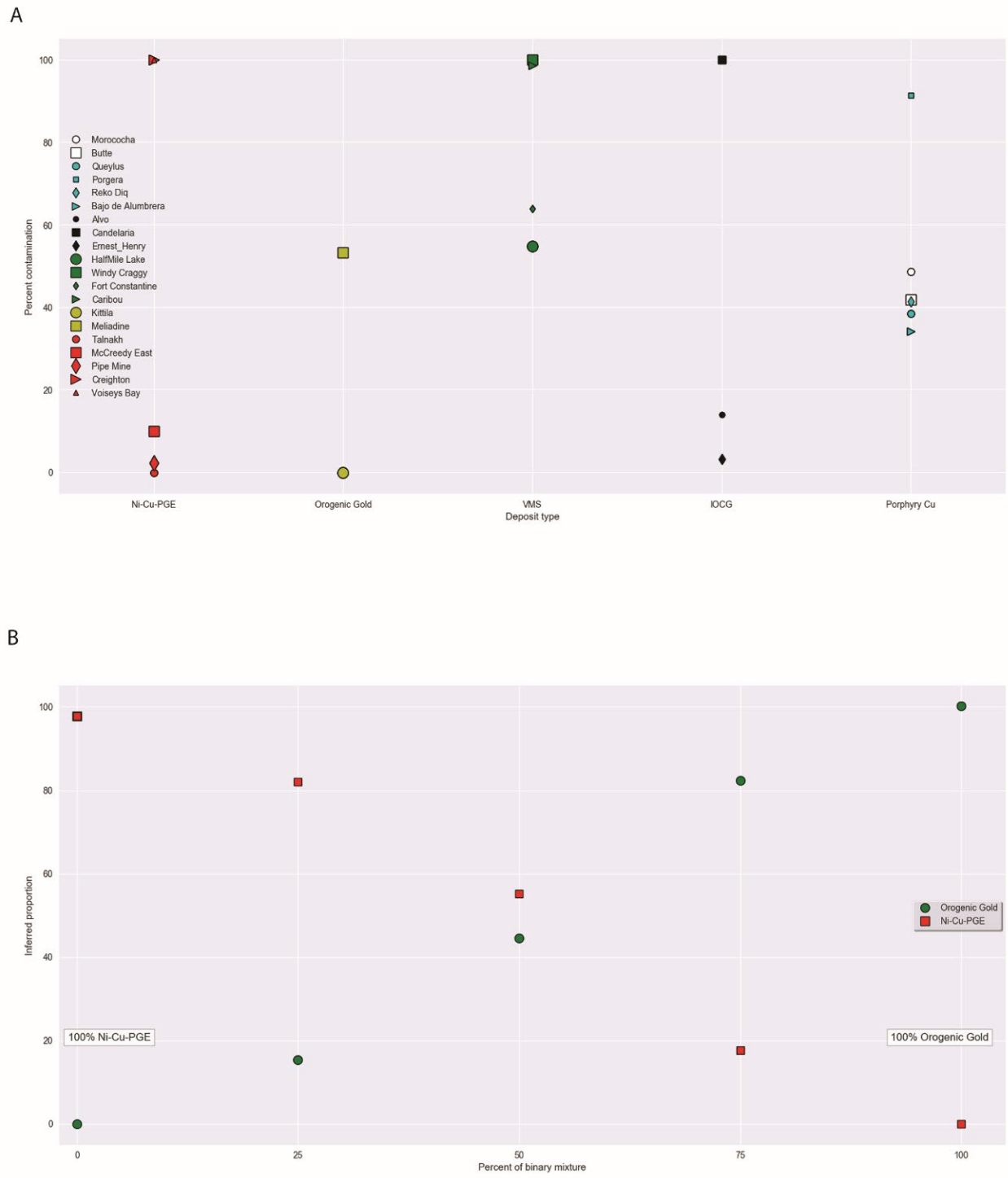

Figure 4. A1: Inferred sources for magnetite from (A) individual ore deposits from each deposit type and (B) a binary mixture comprising magnetite from an orogenic gold deposit and a Ni-Cu-PGE deposit. The percent contamination in (A) is an indication of the proportion of the sample signature that is identified as belonging to another deposit class. The size of the symbols in (A) reflect the number of analyses for the particular deposit; the smallest symbol reflects deposits with <10 analyses, the intermediate symbol indicates deposits with 10 to 100 analyses, and the largest symbol indicates deposits with >100 analyses. The plot indicates that for the elements considered,

individual ore deposits from each class have magnetite chemistry that deviate from the magnetite compositions of the global dataset for the particular deposit class. This deviation results in the individual ore deposit having a chemical signature similar to that for another deposit type, and high percentage of inferred contamination when the signature is compared to the chemical signature for the five deposit types using the non-negative least squares model. The non-negative least squares model reasonably identifies the proportions of the data that constitute the binary mixture of data from orogenic gold and Ni-Cu-PGE deposits (B).

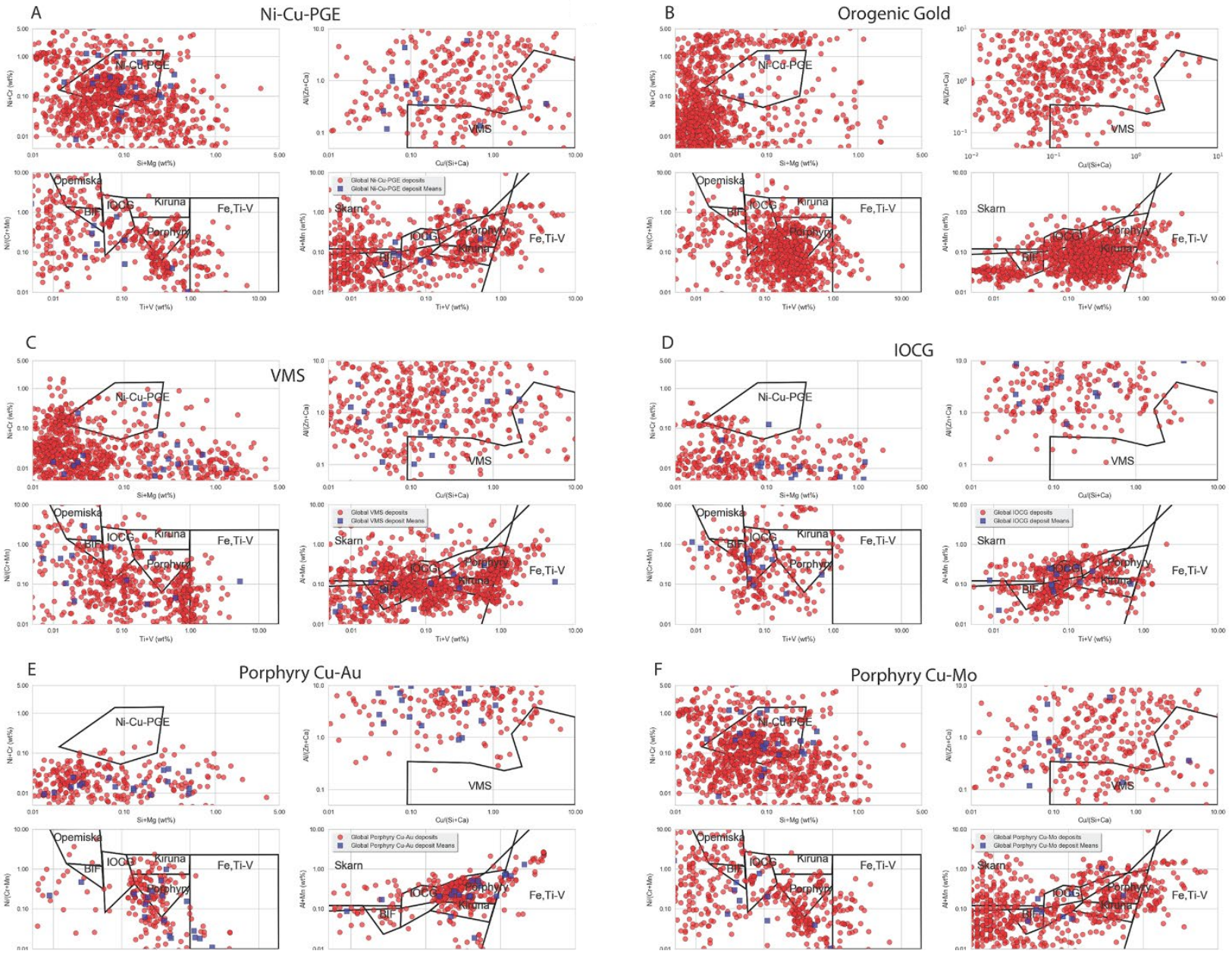
A
Ni-Cu-PGE
Ni-Cu-PGE
VMS
Opemiska
BIF
IOCG
Kiruna
Fe,Ti-V
Porphyry
Skarn
Global Ni-Cu-PGE deposits
Global Ni-Cu-PGE deposit Means
B
Orogenic Gold
C
VMS
Global VMS deposits
Global VMS deposit Means
D
IOCG
Global IOCG deposits
Global IOCG deposit Means
E
Porphyry Cu-Au
Global Porphyry Cu-Au deposits
Global Porphyry Cu-Au deposit Means
F
Porphyry Cu-Mo
Global Porphyry Cu-Mo deposits
Global Porphyry Cu-Mo deposit Means
Ni+Cr (wt%)
Si+Mg (wt%)
Al/(Zn+Ca)
Cu/(Si+Ca)
Ni/(Cr+Mn)
Ti+V (wt%)
Al+Mn (wt%)

Figure 4. A2. Global compilations of magnetite geochemical data from individual samples (red circles) for (A) Ni-Cu-PGE, (B) VMS, (C) orogenic gold, (D) porphyry Cu-Au, and (E) porphyry Cu-Mo deposits are visualized using the discriminant plots of Dupuis and Beaudoin (2011) and Nadoll et al. (2014), where compositional fields are labeled according to nominal deposit type. Additionally, we plot the mean compositions (blue squares) for magnetite for the individual ore deposits represented in the global compilation for the 5 ore deposit types. The deposit means, like the individual sample analyses plot in multiple fields within the discriminant diagrams.

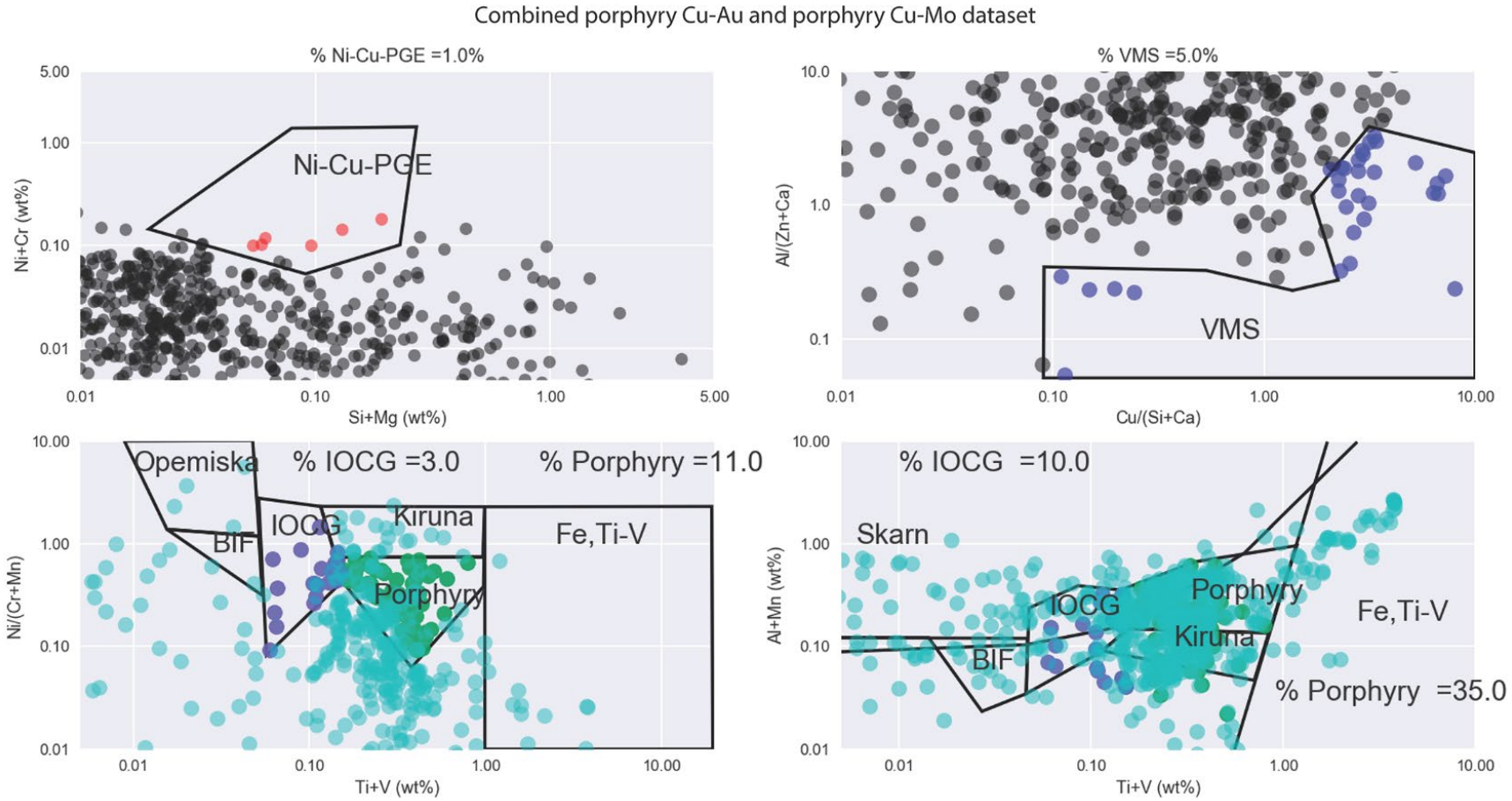

Figure 4. A3. A global compilation of magnetite geochemical data from porphyry Cu-Au and porphyry Cu-Mo deposits is visualized using the discriminant plots of Dupuis and Beaudoin (2011) and Nadoll et al. (2014), where compositional fields are labeled according to nominal deposit type. When data from these two types of porphyry copper deposits are combined, 35% of the data are correctly identified as being sourced from a porphyry copper deposit by the Al+Mn versus Ti+V discriminant plot compared to 11% by the Ni/(Cr+Mn) versus Ti+V discriminant plot.

Table 4.A1. Identification of mineral phases and textures observed sampled catchments.

Google drive folder link for Table 4.A1:
https://drive.google.com/open?id=1Fl5x9jd2oj71sqoHkGXAOcX7UxbgUiVZ